

https://dspace.org/

Antibody functionalized nanoliposomes to slow the progression of ovarian cancer

Hoosen, Yasar

2021

https://hdl.handle.net/10539/32074

Downloaded from a DSpace repository. https://dspace.org/

Antibody Functionalized Nanoliposomes to Slow the Progression of Ovarian Cancer

YASAR HOOSEN

RESEARCH GROUP: THE WITS ADVANCED DRUG DELIVERY PLATFORM



Supervisors

Professor Viness Pillay
University of the Witwatersrand, Department of Pharmacy and Pharmacology, Johannesburg, South Africa

Co-Supervisors

Professor Yahya. E. Choonara
University of the Witwatersrand, Department of Pharmacy and Pharmacology, Johannesburg, South Africa

Associate Professor Pradeep Kumar
University of the Witwatersrand, Department of Pharmacy and Pharmacology, Johannesburg, South Africa

Associate Professor Lisa. C. du Toit
University of the Witwatersrand, Department of Pharmacy and Pharmacology, Johannesburg, South Africa

Dr Clement Penny

University of the Witwatersrand, Department Internal Medicine, Medical Oncology, Johannesburg, South Africa

DECLARATION

I, Yasar Hoosen, declare that this thesis is my own work. It is being submitted for the degree of Doctor of Philosophy in the Faculty of Health Sciences at the University of the Witwatersrand, Johannesburg, South Africa. It has not been submitted before for any degree or examination at this or any other University.

Signature ……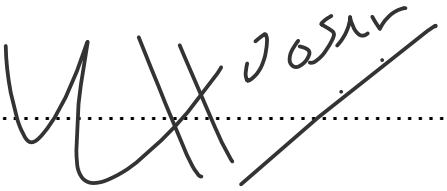……

This …….**22**……. day of …**October 2020**….....

DEDICATIONS

This PhD is dedicated to my mum, Fameeda Hoosen who lost her sister, Farhana Ahmed, to cancer in 2011. It is also dedicated to my dad, Ashruf Hoosen. I finally would like to dedicate this work to all women globally who are terminally ill from gynaecological malignancies, physical and sexual abuse and gender-based inequalities.

RESEARCH PRESENTATIONS ARISING FROM THIS WORK

1. Yasar Hoosen, Pradeep Kumar, Priyamvada Pradeep, Thashree Marimuthu, Lisa C Du Toit, Yahya E Choonara, Clement Penny and Viness Pillay. “On the Spot” Arresting of Chondroitin Sulphate for Inhibition of Glycosaminoglycan Activity in Ovarian Cancer. University of the Witwatersrand, School of Therapeutic Science 2018 Research Day, Johannesburg, South Africa (Poster Presentation).

2. Yasar Hoosen, Pradeep Kumar, Priyamvada Pradeep, Thashree Marimuthu, Lisa C Du Toit, Yahya E Choonara, Clement Penny and Viness Pillay. Anti-MUC 16 Functionalized Cationic Nanoliposomes, for “Arresting” of Chondroitin Sulphate in Ovarian Cancer. University of the Witwatersrand, Wits Cross faculty Research Day 2018, Johannesburg, South Africa (Poster Presentation).

3. Yasar Hoosen, Pradeep Kumar, Priyamvada Pradeep, Thashree Marimuthu, Lisa C Du Toit, Yahya E Choonara, Clement Penny and Viness Pillay. Anti-MUC 16 Functionalized Cationic Nanoliposomes, for “Arresting” of Chondroitin Sulphate in Ovarian Cancer. South African Chemical Institute, 43rd National Convention 2018, Pretoria, South Africa (Podium Presentation)

4. Yasar Hoosen, Pradeep Kumar, Priyamvada Pradeep, Thashree Marimuthu, Lisa C Du Toit, Yahya E Choonara, Clement Penny and Viness Pillay. Anti-MUC 16 Functionalized Cationic Nanoliposomes, for “Arresting” of Chondroitin Sulphate in Ovarian Cancer. University of the Witwatersrand, 10th Wits Cross Faculty Postgraduate Symposium 2019, Johannesburg, South Africa (Podium Presentation).

5. Yasar Hoosen, Pradeep Kumar, Priyamvada Pradeep, Thashree Marimuthu, Lisa C Du Toit, Yahya E Choonara, Clement Penny and Viness Pillay. Anti-MUC 16 Functionalized Cationic Nanoliposomes, for “Arresting” of Chondroitin Sulphate in Ovarian Cancer. University of the Witwatersrand, School of Therapeutic Science Research Day 2019, Johannesburg, South Africa (Podium Presentation).

RESEARCH PUBLICATIONS ARISING FROM THIS WORK

1. Nanotechnology and glycosaminoglycans: Paving the Way Forward for Ovarian Cancer Intervention. Yasar Hoosen, Priyamvada Pradeep, Pradeep Kumar, Lisa. C. du Toit, Yahya. E. Choonara, Viness Pillay, Int. J. Mol. Sci. 19 (2018). doi:10.3390/ijms19030731.

2. Synthesis, and Evaluation of Chondroitin Sulphate-Didodecyldimethyl Ammonium Bromide Nanoconjugates for Potentially Targeted ("On-the-Spot") Therapy in Ovarian Cancer. Submitted to the journal: Carbohydrate Polymers. December 2020

3. An Inside Perspective on Artificial Intelligence and Future Ovarian Cancer Strategies: How Data Comes to the Rescue. Submitted to the journal: Artificial Intelligence in Medicine. November 2020

4. Synthesis and Evaluation of Chondroitin Sulphate-1,12 Diaminododecane Crosslinked Networks for Potential Utilization in Nanoarchetypes Targeting Ovarian Cancer. Awaiting submission.

5. Novel Anti-MUC 16 Functionalized Didodecyldimethyl Ammonium Bromide Cationic Nanoliposomes for Inhibition of Ovarian Cancer Activity In Vitro. Awaiting submission

6. Novel Anti-MUC 16 Functionalized 1,12 Diaminododecane Loaded Nanoliposomes for Targeted Ovarian Cancer Therapy. Awaiting submission

7. Anti-MUC 16 Functionalized DDAB and 1,12 Diaminododecane Nanoliposomes Arrest Chondroitin Sulphate-E Activity in 3D Ovarian Tumourospheres. Awaiting submission

ABSTRACT

Ovarian Cancer (OC) is ranked amongst the top virulent gynecological malignancies, implicated with high rates of disease relapse and failed drug therapies. The integration of innate biological macromolecules in cancerous environments facilitates complex inter-and intra-cellular cascades, which induce a formidable attack against healthy tissue leading to tumour cell dissemination. For decades, cancer cells, receptors and proteins were defined as key therapeutic drug targets for conventional molecules. However, a recent revolution in research has diversified the scope of niche molecular targets, such as the ones contained in the extra-tumoral spaces i.e., the extracellular matrix (ECM). The ECM contains over expressed glycosaminoglycans (GAGs) such as the anionic chondroitin sulphate-E (CS-E) carbohydrate polymer. CS-E aggressively stimulates OC cell migration, proliferation, adhesion, and catalyzes the up-regulation of a plethora of growth factors. Inherent with this research was a *world's-first* hypothesis which anchored the foundations of this project. Herein, an innovative mechanistic forecast to treat OC independently of drug therapy is described. Using two chemical techniques: 1) chemical crosslinking and 2) polyelectrolyte complexations, we aimed to irreversibly modify the structural architecture of CS-E polymer backbone to impede its functional role in OC metastasis. To validate the integrity of the hypothesis, didodecyldimethyl ammonium bromide (DDAB) and 1,12 diaminododecane were assessed as suitable CS-E modifying agents, with extensive characterization performed on the CS-DDAB and CS-1,12 diaminododecane archetypes in Chapters 4 and 5. Upon validation, advanced drug delivery platforms engineered in tandem with nanotechnological techniques that feature active targeting mechanisms drastically enhanced the site specific cytotoxicity of these molecules, detailed in Chapters 6 and 7. The ability of these nano-archetypes to alter the genetic integrity expressions of OC cells was a hallmark discovery that conclusively supported the CS-E mediated arresting induced by these systems, in addition to displaying toxic potentials on 3D tumourosphere models. Lastly, a clinically mimetic, stage-4 cancer model in athymic nude mice was established, where the Anti-MUC 16 functionalized cationic nanoliposomal implant restricted the growth, prolonged the survival times, and increased tumour inhibition rates with minimal off-target effects. To this end, the validation of this hypothesis and the therapeutic benefits was concluded.

RESEARCH ACCOLADES

1. Conference Awards

- Second prize for the best oral presentation in the category of nanotechnology at the South African Chemistry Institute (SACI), 43rth National Convention, 2018.

- Second prize for the best poster presentation at the Faculty of Health Science Research Day, 2018.

- Second prize for emerging researcher award at the Wits School of Therapeutic Science Research Day 2019.

2. International Travel

Selected to represent South Africa, as part of a BRICS Cancer Research Team, for a multilateral research project entitled “Development of the Dual Inhibitors Targeting *Wnt* signalling as Colorectal Cancer Therapeutics”. Invitation by Professor Ahmed Kamal, pro Vice Chancellor of Jamia Hamdard University India, New Delhi, to undertake research and testing of the novel anti-cancer dual inhibitors in 2019.

3. Postgraduate Research Scholarship Awards

- University of the Witwatersrand Postgraduate Academic Merit Award (PMA) 2019-2020.

- National Research Foundation (NRF) Freestanding, Innovation and Scarce Skills Development Fund Doctoral Scholarships 2019-2020.

ACKNOWLEDGEMENTS

I would like to deeply express these acknowledgments in chronological order and mention the names of the significant individuals who impacted my life. First and foremost, in the name of the Almighty, the most merciful and most powerful. I attribute this opportunity to him and every blessing that has touched my life. I thank the Almighty for showering me with the resilience, determination, and courage to perform such a ginormous task.

I would like to take this time to deeply thank my parents; Ashruf and Fameeda Hoosen. My parents are truly the primary anchor in my success story. There consistent guidance, infinite encouragement and earth-moving support has propelled me far in life. You have shown me the ropes and moulded me into all I am today. You gave me the confidence to face my fears, grounded me as an individual to overcome my doubts, taught me the patience to accept my circumstances and vigour to take on any challenge life has to offer. Your consistent efforts and sacrifices are the key roots in my foundation and development. I hope to always make you proud, my major goal in life.

I would also like to take this time to express my deepest appreciation to some of my high school teachers who played a key role in my early success and development. Thank you for believing in me and for transforming me from an underperforming student, to one that was accepted into university. Without your early support, my entrance into the world of academia would have never been impossible. There are a few names I would like to mention, Ms Kubeshni Naidoo, Mr Shaffat Yacoob, and Mr KB Pillay. A special thanks to you for simply never giving up on me and doing the extra to make sure I was performing at my best.

I would also like to take this time to give thanks to my Rhodes University lecturers who have remarkably become my closest colleagues to date. Dr L. Goosen, a special thanks goes to you. You inspired me to become the top achiever in my Bachelors of Pharmacy class and planted the seed of research in me. I would also like to take this time to thank Mr Michael. J. Naidoo, my 3rd and 4th year pharmacology lecturer, for your consistent encouragement and assistance in enrolling me into the WADDP research program.

To my Masters and PhD supervisors. With an extremely heavy heart, I would firstly like to pay a special tribute to Professor Viness Pillay. There are no words that could do justice for how saddened I am that you will not be here to see me through this time. I pray that the Almighty shower you with his mercy and make it easy for your family during this time. Thank you from the bottom of my heart for the opportunity to do research at WADDP. This has been a milestone turning point event in my life. You played a key role in my life as a mentor and granted me the platform to solidify my future place as a specialist pharmacist in the industry. Your world class guidance and bold persona will resonate in my heart forever. You have inspired me to be a happy and charismatic worker, with an ultimate work ethic that sees no limitations. You taught me how to be simple and kind in words, and aggressive in action. You have truly

touched my life and lined me up for a great career ahead. You have truly made my dreams a reality. You shaped me from being a misguided student, to a meticulous young scientist. Your level of care, empathy, encouragement, engagement, and involvement is absolutely unmatched. I still think of the times we laughed after meetings and truly wish I had the chance to look you in the eye, shake your hand and simply say 'Thank you Prof'. Because if it were not for your active supervision, I would not be here today.

I would also like to take this time to try and bring to light the depth of appreciation I have towards my co-supervisors. My words may not do the justice, but I am true in my intention. To my life mentor, my life couch and my key guiding light, GPS and mapping system throughout the Masters and PhD projects, Professor Pradeep Kumar. Thank you for navigating me through this. You pushed me out of my comfort zone and taught me how to swim in the deep end. You shaped me into a top achiever. You have played a crucial role in my intellectual development. I would like to thank you for your help with procuring my research funding, your door was never closed for any of my problems and concerns, be it research related, writing related or when I just needed someone to speak to on a personal level. In this study, you were my living Pharmacopeia of knowledge that aided me on tap when experiments were failing which promptly guided me back on track. Thank you for being patient with me and giving me so much of your time and effort. Thank you for the extreme effort you put in making sure I was progressing timeously. Thank you for the fun laughs and interesting chats in my times of stress. Thank you for caring for me. Thank you for being my teacher. Thank you for imparting your knowledge onto me. Thank you for granting me the opportunity to visit India. Thank you for your countless words of wisdom and inspiration. You are a monumentally special role model to me.

To Professor Lisa du Toit, I am extremely grateful for all your time and effort. I remember all the times in your office, under extreme pressure and stress. You had a brilliant way of telling me that it is going to be okay. Thank you for your pleasant smile and continuous support. To Dr Priyamvada Pradeep, my special thanks go to you. You laid the foundation for my research project. You sparked the desire in me to achieve the unknown. I thank you for your valuable knowledge that formed the foundation of my skill set. I thank you for the never-ending support and supervision. And lastly, thank you for making me feel like family thousands of kilometres away from home. To Dr Thashree Marimuthu, the patience and time you spent teaching me the basics of science is unmeasurable. Thank you for all you have done. To Professor Kondiah, your assistance and guidance during my PhD conversion was extremely significant. Thank you for the constant encouragement and assistance with administrative tasks. To Dr Penny, thank you for granting me the opportunity to work in your lab and meeting regularly with me to find out if I needed any assistance. Thank you for taking the time to be in the lab with me and aiding me in achieving the great fluorescent imagery seen in the study. Thank you for always being on tap for any of my lab related queries. To Dr Subramanian and Dr Kandhavelu, you have certainly shown me the ropes in cell biology. Words cannot describe how grateful I am for your help, guidance, and supervision in my study. The time and effort you spent in assisting me is unmeasurable. Thank you for your constant support in assisting me during the late nights and early weekend mornings we spent in the lab. Thank you for stopping at nothing to make sure my experiments were done to perfection.

To my principal supervisor, Professor Yahya Choonara. Your tenacity and persona will be ingrained in me throughout my life. I look up to you and gain motivation to keep moving forward. I look up to you and become inspired that anything in life is possible. Apart from being my life mentor and an astonishingly brilliant leader, I look up to you with a more role model like position. You have played the primary role in my critical thinking. You have changed my ability to perceive information. You have crafted me into thinking world class. You have optimised me as a human being. Your role as a teacher and leader is off the charts. Be it assisting me with publications or getting me ready for a big presentation that usually resulted in podium finishes, I owe most of my postgraduate and future success to you. I pray that the Almighty grants you a long career so that you may continue touching the hearts of future pharmacists the way you have done for me. You stop at nothing in making your students world class performers. I thank you for being my window into the world of greatness, for imparting your great wisdom onto me and for taking the time. My appreciation is infinite.

I would also like to give a special thanks to the Central Animal Services at the University of Witwatersrand. Ms Thembeka Kosa, Ms Lorraine Matjila, Mr Mduduzi Mashaba, Mr Patrick Selahle and Ms Amelia Rammekwa in assisting me in my animal studies, for teaching me the basics and for literally holding my hand and showing me how to handle the animals. Your support in my animal study is unmatched and your efforts will never be forgotten. To Dr Kimberely Jardine, your encouragement and support goes beyond expectation. As a general gratitude to the Central Animal Service at the University of Witwatersrand and all their staff members, my hat goes out to you. Thank you for making the most difficult objective of my PhD that much easier.

To Mr Sello Ramarumo, my appreciation to you cannot be confounded by these words. You make the theoretical experiments in our research group a reality. To Mr KB, Mr Bafana, Ms Pumzele and Ms Pride, again my appreciation for your work on the ground is beyond words. Your role as lab techniques played a key part in my lab success. Thank you for also keeping me safe during this experience and making sure I was never short of chemicals and consumables.

I would like to pay a special thanks to Dr Kuben Naidoo for his constant assistance and support. I would further like to mention Dr Ekene Nwele for his guidance and support.

To my teachers at the Wits Microscopy Unit, A special thanks to Dr Deran Reddy. You instilled a passion for microscopy in me. You inspired me in becoming meticulous about my work. I am grateful for every time you went your way to make sure my images were of world class quality. A further special gratitude goes to all members of the unit, who never failed to assist me in my times of need. A special thanks to Dr Aurelie Deroubiax for your guidance in confocal microscopy.

To all my colleagues and friends at WADPP, who taught me how to find my way around the lab. Thank you, none of my success would have ever been possible without our laughs, our planning, and our grieving together. As a group, we overcame adversity and helped each other tick away objectives. A special thanks to Ms Henna Cassimjee for your constant assistance as my co-worker during my animal study.

I would also like to acknowledge my beloved family members Mr Reza Timol and Dr Yasmin Mayet for the continuous encouragement, support, care and love shown to me. A special thanks to my aunt Mrs Nadia Timol and my uncle Mr Zaid Timol for their constant support and guidance.

Lastly, I would like to thank the National Research Foundation, The University of the Witwatersrand and the South African Medical Research Council for funding the research conducted in the study.

ANIMAL ETHICS DECLARATION

I, Yasar Hoosen confirm that the study entitled "*In vivo* Chemotherapeutic Potential of Novel Nanoliposomes on Athymic Nude Mice Cancer Models" received the approval from the Animal Ethics Committee of the University of the Witwatersrand with ethics clearance number: 2019/04/30/C (see Appendix).

TABLE OF CONTENTS

CHAPTER 1: 1

1.1. Introduction 1

1.1.1. The Ovarian Tumour Microenvironment 1

1.1.2. The Role of CS-E in Ovarian Cancer 2

1.1.3. Rationale and Motivation of the study (A *first-in-the* World Hypothesis) 3

1.2. Possible Applications of this Delivery System Include: 5

1.3. Novelty of the PhD Study 6

1.4. Aims and Objectives (With Expected Outcomes) 6

1.4.1. To Evaluate and Characterize the CS-E-Crosslinker (CS-E-CL) and CS-E-polyelectrolyte complexing agent (CS-E-PEC) Archetypes to Determine if the Crosslinking and Complexing Agents are Effective against CS-E. 7

1.4.2. To Formulate/Develop the anti-MUC 16 Nanoliposomes 7

1.4.3. To Characterize and Measure the Size and Morphology of the Nanoliposomes using Transmission Electron Microscopy 7

1.4.4. To perform Sensitivity Assays on Ovarian Cancer Cell Lines to Measure the Effectiveness of the Nanoliposomes to Inhibit OC Tumour Growth. 7

1.4.5. To Investigate CS-E-CL Mediated Inhibition of Proteoglycan Activity and Determine Cell Viability 7

1.4.6. To Investigate the GalNAc4S-6ST Gene Expression Analysis of Cancer Cells Induced by the Nanoliposomes 8

1.4.7. To determine the Nanoliposomal Mediated Cytotoxic Performance of the Nanoliposomes on 3D Cell Cultures. 8

1.4.8. To Evaluate the In Vivo Anticancer Performance of the Nanoliposomes on an Animal Model. 8

1.5. Overview of this Thesis 8

1.6 Concluding Remarks 10

1.6. References 11

CHAPTER 2: 14

2.1. Synopsis of this Chapter. 14

2.2. Introduction 15

2.3. Active Targeting in Ovarian Cancer 16

2.3.1. Antibody Based Targeting in OC 18

2.3.2. Aptamer Based Targeting and Detection in OC 20

2.3.3. Folate Receptor Targeting in OC 25

2.4. Is the Active Targeting Avenue Alone a Way Forward for Cancer Nanomedicines? 27

2.5. Nanocarrier Based Delivery in OC 27

2.5.1 Nanocarriers for the Delivery of siRNAs to OC 28

2.5.2. Nanocarrier for the Delivery of OC Drugs 33

2.6. What Happens to These Nanosystems Beyond the Realms of Research? 38

2.7. Glycosaminoglycans as a Potential Molecular Target to Stop the Progression of OC 39

2.7.1. Chondroitin Sulphate as a Molecular Target 40

2.7.2. The Role of CS in OC 40

2.7.3. Targeting Chondroitin Sulphate-E 42

2.7.4. Hyaluronan (HA) As a Potential Molecular Target 47

2.8. Conclusions and Outlook 51

2.9. References 52

Chapter 3 71

3.1. Introduction 71

3.2. Artificial Neural Networks as a tool to Super Optimize and Predict the Performance of Prototype Drug Delivery Systems 73

3.3. Artificial Intelligence as a Predictive Tool for Early Ovarian Cancer Diagnostics 74

3.3.1. Integrating Genetic Data and AI for Accurate OC Diagnosis 82

3.3.2. Integrating AI and Proteomics Data for OC Diagnosis 89

3.3.3. Other AI-Inspired Models as OC Diagnostic Platforms 92

3.4. Artificial Intelligence and Nanotherapeutics for Ovarian Cancer 96

3.4.1. Machine Learning of nanotherapeutics 96

3.4.2. Artificial Neural Networks for Nanotherapeutics Targeting Cancer 99

3.5. Pharmacokinetic Modelling Approaches for Nano-Therapeutics Against Ovarian Cancer 101

3.6. Conclusions 105

3.7. References 105

CHAPTER 4: 122

4.1. Synopsis of The Chapter 122

4.2. Introduction 122

4.3. Materials and Methods 127

4.3.1. Materials 127

4.3.2. Synthesis of the CS-DDAB PEC 127

4.3.2.2. Synthesis of the “On the Spot” CS-DDAB Nanoconjugates by PEC .. 128

4.3.3. Electrochemical Characterization of the CS-DDAB PEC 128

4.3.4. Macromolecular Characterisations Based on Size and Stability Analysis of CS-DDAB PEC 130

4.3.5. Cell Viability Sensitivity Assay on Human Derived Ovarian Carcinoma Cell lines 132

4.4. Results and Discussion 133

4.4.1. Evaluation of CS-DDAB PEC 133
4.4.2. Morphological, Size and Stability Analysis of CS-DDAB PEC 146
4.4.3. Anti-cancer activity of DDAB on SKOV3 Ovarian Carcinoma Cell Lines 149
4.5. Conclusions 151
4.6. References 152
CHAPTER 5 158
5.1. Synopsis of this Chapter 158
5.2. Introduction 159
5.3. Materials and Methods 161
5.3.1. Materials 161
5.3.2. Synthesis of CS-1,12 Diaminododecane Crosslinked Networks 162
5.3.3. Physico-Chemical and Thermal Analysis of the CS-1,12 Diaminododecane Crosslinked Network 162
5.3.4. Size, Zeta Potential, Polydispersity Index and Morphological Analysis of the CS-1,12 Diaminododecane Crosslinked Network 164
5.3.5. Degree of 1,12 Diaminododecane Crosslinking onto CS Backbones 165
5.4. Results and Discussion 166
5.4.1. Physico-Chemical Analysis of the CS-1,12 Diaminododecane Crosslinked Network 166
5.4.2. Morphological Characterization of the CS-1.12 Diaminododecane Crosslinked Network 171
5.4.3. Degree of 1,12 Diaminododecane Crosslinking on CS 173
5.5. Conclusion 175
5.6. References 176
CHAPTER 6 180
6.1. Synopsis of this Chapter 180

6.2. Introduction 180

6.3. Materials and Methods 183

6.3.1. Materials 183

6.3.2. Formulation of DDAB Cationic Nanoliposomes 184

6.3.3. Surface-Engineering of Anti-MUC 16 Antibody onto the Nanoliposomes 184

6.3.4. Optimization of the DDAB Cationic Nanoliposomes 184

6.3.5. Physicochemical Characterization of the Anti-MUC 16-Functionalized Nanoliposomes 186

6.3.6. Determination of Size and Zeta Potential of the Nanoliposomes 186

6.3.7. Assessment of Anti-MUC 16 Antibody Functionalization onto the Surface of the Nanoliposomes 186

6.3.8. Evaluation of the Surface Morphology and Architecture of the Nanoliposomes 187

6.3.9. Determination of the DDAB Content that was Fixated on the Surface of Nanoliposomes 187

6.3.10. Cytotoxic Performance of Nanoliposomes on SKOV3 Carcinoma and HEK293 Cell Lines (All three Assays were Performed on the MUSE^{TM} Cell Analyser) 187

6.3.11. Cellular Migration Assays using xCELLigence System 189

6.3.12. In vitro Uptake of FITC Labelled Anti-MUC 16 NLs 190

Statistical Analysis 190

6.4. Results and Discussion 190

6.4.1. Characterization and Determination of Particle Size and Zeta Potential of the Nanoliposomes 190

6.4.2. Determination of Anti-MUC 16 Functionalization onto the Nanoliposome Surface 194

6.4.3. Assessment of the N^+ fixation on the Surface of the Anti-MUC 16 Nanoliposomes by Zeta Potential Analysis. 195

6.4.3. Evaluation of the Surface Morphology and Architecture of the Anti-MUC 16 Nanoliposomes 197

6.3.4. Determination of the Residual DDAB Content on the Surface of Nanoliposomes 198

6.4.5 *In vitro* Cell Viability, Apoptosis and Proliferation Assays..... 198

6.4.6. Evaluation of Cell Migration Assays using xCELLigence System 203

6.4.7. Cellular Uptake Studies of FITC Tagged Anti-MUC 16 DDAB NLs on SKOV3 cells..... 204

6.5. Conclusions 206

6.6. References 206

CHAPTER 7 211

7.1. Synopsis of this Chapter 211

7.2. Introduction..... 211

7.3. Methods and Materials 213

7.3.1. Materials..... 213

7.3.2. Synthesis and Characterization of the Anti-MUC 16 1,12 Diaminododecane NLs..... 214

7.3.4. *In Vitro* Cytotoxic Performance of the Nanoliposomes on SKOV3 Carcinoma and HEK293 Cell Lines (All three Assays were Performed on the MUSE^{TM} Cell Analyser)..... 220

7.4. Results and Discussions 223

7.4.1. Synthesis and Characterization of the Anti-MUC 16 1,12 Diaminododecane NLs..... 223

7.4.2. Cytotoxic Evaluation of the Novel Anti-MUC 1,12 Diaminododecane Loaded Nanoliposomes 234

7.5. Conclusion 240

7.6. References 241

CHAPTER 8 246

8.1. Synopsis of this chapter 246

8.2. Introduction 247

8.3. Materials and Methods 249

8.3.1. Materials 249

8.3.2. Formulation of DDAB Cationic Nanoliposomes 250

8.3.3. Formulation of the 1,12 Diaminododecane Loaded Nanoliposomes. 251

8.3.4. Surface-Engineering of Anti-MUC 16 Antibody onto the Nanoliposomal Surfaces. 251

8.3.5. Oxidative Stress Assay. 252

8.3.6. Anti-VEGF Assessment of the Nanoliposomal Systems 252

8.3.7. Cytotoxic Evaluation of the Anti-MUC 16 Nanoliposomal Systems on 3D Tumourosphere Models 253

8.3.8. Assessment of CS-E Biosynthesis by Gene Expression Analysis 253

8.4. Results and Discussion 254

8.4.1. Reactive Oxygen Species (ROS) Determination of the Anti-MUC 16 DDAB Nanoliposomes on SKOV3 cells 254

8.4.2. Determination of the Anti-VEGF Capabilities of Anti-MUC 16 DDAB and 1,12 Diaminododecane Nanoliposomes by ELISA Testing 256

8.4.3. Cytotoxic Evaluation of the Anti-MUC 16 DDAB and 1,12 Diaminododecane Nanoliposomes on 3D Tumour Spheroid Models 259

8.4.4. GALNAc4S-6ST Gene Expression Analysis 262

8.5. Conclusions 264

8.6. References 264

CHAPTER 9 268

9.1. Synopsis of this Chapter 268

9.2. Introduction 269

9.3 Materials and Methods 271

9.3.1. Animal Husbandry and Athymic Nude Mice Specifications 271

9.3.2. *In Vivo* Experimental Design 272

9.3.4. Assessment of the Tumour Volume, Ultrasound Imagery and Mice Weight Transition Analysis 275

9.3.5. Chemotherapeutic activity of DDAB in Ovarian Carcinoma Athymic Mice Models 276

9.3.6. Histopathological Analysis of Tumours and Overall Dose Tolerability ... 277

9.4. Results and Discussion 277

9.4.1. Assessment of the Chemotherapy Efficacy and Dose Tolerability of DDAB in Separate Delivery Systems and Doses (Model 1) 277

9.4.2. Assessment of the Chemotherapeutic Potential of the Anti-MUC 16 DDAB NLs on Advanced Stage 4 OC Tumours (Model 2) 292

9.5. Conclusions 300

9.6. References 301

CHAPTER 10: 305

10.1. Conclusion 305

10.2. Recommendations 308

APPENDICES 309

11. 1. APPENDIX A 309

11.1.1. Review Publication 309

8.2. APPENDIX B 310

8.2.1. Abstracts of Research Outputs at Conference Proceedings 310

11.3. APPENDIX C 318

11.3.1. Award Certificate for SACI oral Presentation 318

11.3.2. Award for School of Therapeutic Science, Research Day 2019 319

11.4. APPENDIX D 320

11.4.1. Animal Ethics Approval 320

LIST OF FIGURES

Figure 1.1. Proposed schematic of the cationic nanoliposome coated with the OC targeting antibody and loaded with a crosslinker (Sercombe et al., 2015)**…….5**

Figure 2.1. A schematic depicting method employed for active targeting of nanoparticles. I. Antibody-based targeting, which involves the use of: (A) monoclonal antibodies such as anti-Her2/neu antibody directed towardHer2/neu receptors on the target cell membrane; and (B) antibody fragments: single-chain variable fragments (scFV) such as single-chain anti-epidermal growth factor receptor (EGFR) antibody directed toward EGFR, or antigen-binding fragment (Fab) such as anti-Her2/neu Fab. II. Aptamer-based targeting such as the A10 RNA aptamer directed toward prostate-specific membrane antigen (PSMA) on the surface of the target cells. III. Ligand-based targeting such as: (A) transferrin-based targeting of nanoparticles toward transferrin receptors where uptake of the nanoparticles takes place through receptor-mediated endocytosis through clathrin-coated pits; and (B) folate-based targeting using folic acid (FA) to target folate receptor alpha (FRα), which is up-regulated on the surface of neoplastic cells. (Reprinted from [Bazak et al., 2015] with permission from Cancer Research Clinical Oncology)**…….17**

Figure 2.2. Flow chart representing the two ovarian cancer targets with their respective antibodies (Chen et al., 2008.39). **…….20**

Figure 2.3. Schematic illustration of the fabrication processes of Ag2S QDs/aptamer/5-Fu hybrid-based near-infrared (NIR) photoluminescence (PL) turn-on probe of CA125. (Reprinted from (Jin et al., 2017) with permission from Biosensors and Bioelectronics).**…….23**

Figure 2.4. Schematic representation of NCP-1/siRNAs carrying cisplatin in the solid core and siRNAs in the lipid shell. Reprinted (adapted) with permission from (He at al., 2016). Copyright (2016) American Chemical Society**……..29**

Figure 2.5. Construction of cancer targeting lyophilisomes depicting conjugation between albumin based lyophilisomes and GD3G7 antibodies reactive with CS-E, by applying a two-step approach comprising sortase mediated ligation and click chemistry. (A) LPETG-His-VSV tagged single chain GD3G7 antibodies were modified for click chemistry by introducing amino-PEG4-DBCO through a reaction mediated by Sortase A. (B) Lyophilisomes were functionalized for click chemistry by conjugating PEG4-azide to the primary amine groups of lyophilisomes mediated by *N*hydroxysuccinimide (NHS). (C) Antibody-functionalized lyophilisomes were generated by a click reaction between azido-conjugated lyophilisomes and GD3G7-PEG4-DBCO antibodies.Abbreviations: CS-E, chondroitin sulphate E; DBCO, dibenzylcyclooctyne; VL, light chain variable domain; VH, heavy chain variable domain; SrtA, Sortase A. (Reprinted from (van de Steen et al., 2017) with permission from Elsevier)**……46**

Figure 3.1. An overview of how genetic, protein and drug delivery data sourced from ovarian cancer studies and clinical setups can be fed into AI technologies for reliable and important patient outcomes**……79**

Figure 3.2. Systematic flow diagram for how machine learning takes place**……80**

Figure 3.3. The architecture and illustration of DCNN for ovarian cancer images classification (with permission from Wu and co-workers**)……..94**

Figure 3.4. Highlighting the various steps for identification of ovarian mass (adapted fromPathak and co-workers)**……..95**

Figure 3.5. Schematic representation of artificial neural network –based method for prediction of nanoparticle size and shape. Pre-processed XANES spectrum for a nanoparticle is discretized and used to set the values of neural network (NN) nodes in the input layer. The input is then processed in the NN hidden layers. Each hidden node represents a function, which adds together the node inputs, weighted with $\theta\theta$, applies to the sum the activation function f, and returns the result as a real number a to be used by NN nodes in the subsequent layers. Hidden layers map the input to the

output – set of predicted average coordination numbers $\boldsymbol{C\ i}$. Average coordination numbers are then used to determine the size and shape of the nanoparticle (with permission from Timoshenko and co-workers)**……98**

Figure 3.6. A graphical summary of the main stages involved in the setting-up of the QSTR-perturbation model based on ANNs (With permission from Concu and co-workers)**……..100**

Figure 3.7. Fractional-order two-compartment pharmacokinetic model**……...104**

Figure 4.1. Depicting the potential electrostatic interactions with CS^- and $DDAB^+$. The N-acetylgalactosamine (A) D-glucuronic acid (U) and sulphate moieties of CS are in equimolar quantities for potential sulphation on A, with potential for any individual disaccharide unit to be 6-sulphated, 4-sulphated, 4,6-disulphated, or unsulphated**..126**

Figure 4.2. FT-IR spectrum displaying the characteristic surface modifications on the CS polymer backbone by DDAB to yield nanoconjugates**……139**

Figure 4.3. ^1H NMR spectrum of CS-DDAB PEC**……141**

Figure 4.4. Graphical representation of the inclusion polyelectrolyte complexation of CS during the micellization of DDAB with molecular docking of CS-DDAB showing highly stable nanoconjugates**……...141**

Figure 4.5. Thermal analysis utilizing DSC thermograms for the CS-DDAB PEC**…143**

Figure 4.6. TGA curves for a) CS = blue b) DDAB= red and c) CS-DDAB PEC = black**……..144**

Figure 4.7. XRD patterns for the determination of phase transitions on the CS backbone by DDAB**……145**

Figure 4.8. Graphical representation of the average particle size of CS-DDAB nanoconjugates**……..146**

Figure 4.9. ΔBS and Δ transmission spectrums for CS-DDAB "*on the spot"* PEC for stability analysis at 37°C for 24 h**…….148**

Figure 4.10. Graphical representation of a typical vesicle used for turbiscan analysis**…….148**

Figure 4.11. Typical SEM imaging and EDS elemental mapping of the of CS-DDAB nanoconjugates**……...149**

Figure 4.12. Quantitative expressions of cell viability of SKOV3 ovarian carcinoma cells against DDAB (0-200 µg/mL - IC_{50}=12.3 µg/mL). An unpaired, two-tailed student t test was conducted comparing the cell viability obtained from DDAB dosed at 200 µg/mL and the untreated control, which showed a significant difference after the 48 hour treatments (P=0.000625)**……..…150**

Figure 4.13. Light Microscopy images to assess changes in morphology of SKOV3 ovarian carcinoma cell lines after 48 h DDAB exposure**……150**

Figure 5.1. Showing the various sulphation positions of the CS molecule**……160**

Figure 5.2. Graphical representation of 1,12 diaminododecane crosslinking CS, forming an arrested CS-1,12 diaminododecane network**……..161**

Figure 5.3. FT-IR spectra for pristine CS, CL = 1,12 diaminododecane, and the various crosslinked networks represented on the graph by the total molar % of 1,12 diaminododecane used (30, 50 and 90 Molar percentage)…**……..167**

Figure 5.4. DSC thermograms for pristine CS, CL = 1,12 diaminododecane, and the various crosslinked networks represented on the graph by the total molar % of 1,12 diaminododecane used (30, 50 and 90 Molar percentage)**……...168**

Figure 5.5. XRD patterns for pristine CS, CL = 1,12 diaminododecane, and the various crosslinked networks represented on the graph by the total molar % of 1,12 diaminododecane used (30, 50 and 90 Molar percentage)**……..169**

Figure 5.6. Thermogravimetric curves for pristine CS, CL = 1,12 diaminododecane, and the various crosslinked networks represented on the graph by the total molar % of 1,12 diaminododecane used (30, 50 and 90 Molar percentage)**…….170**

Figure 5.7. Graphical illustration of the size trends of CS and the various sizes of structurally modified CS backbones with various concentrations of 1,12 diaminododecane forming crosslinked networks**……172**

Figure 5.8. Typical SEM imagery of the CS-1,12 diaminododecane crosslinked networks**……...173**

Figure 5.9. Graphical illustrations of the relative MB adsorption factor for the various molar % of the crosslinked CS networks where 40 molar = 46.67 ± 8.07, 50 Molar= 26,36 ± 2.28; 90 Molar= 18,63 ± 4,68)**……..175**

Figure 6.1. Graphical illustration of the Anti-MUC 16 DDAB NLs, which directly target the ovarian ECM. *In situ*, knockdown of the CS-E GAGs occurs as a consequence of PEC, resulting in a reduction of the ovarian tumour size (Pradeep et al., 2016)**…..182**

Figure 6.2. Depicting the size and zeta potentials of the various optimized nanoliposomal formulations**……...193**

Figure 6.3. Showing FT-IR spectrum of successful conjugation of Anti-MUC 16 antibody onto the surface of NLs, where A= unfunctionalized and B=functionalized**.195**

Figure 6.4. Graphical illustration of the cationic shielding contributed by the Anti-MUC 16 localized on the NLs periphery (adapted from Mitchell et al., 2013)**…….196**

Figure 6.5. Typical TEM micrographs of Anti-MUC 16 functionalized DDAB NLs**…197**

Figure 6.6. Cell viability profiles **s**howing IC_{50} values of **A)** DDAB-loaded NLs (1.905 µg/ml) and **B)** anti- MUC 16 functionalized NLs (0.5031 µg/ml)**…….....199**

Figure 6.7. Graphical representation of apoptosis profiles, where A and D are untreated, B and E are treated with DDAB-loaded NLs and C and F are treated with anti-MUC 16-DDAB-loaded NLs. A student T-test (unpaired) for the total apoptotic percentages of the anti-MUC 16 DDAB NLs and DDAB NLs against the untreated controls showed no significance for the HEK 293 cell line (P=0.23 and P=0.017 cells respectively), whilst for the SKOV3 cells, the anti-MUC 16 NLs displayed a significance of P=0.0007 and the unfunctionalized DDAB NLs displayed a significance of P=5.794 $X10^{-6}$**……..……201**

Figure 6.8. Graphical representation of proliferation profiles, where A and D are untreated, B and E are treated with DDAB-loaded NLs and C and F are treated with anti-MUC 16 DDAB-loaded NLs. A student T-test (unpaired) for the percentages of proliferating cells for the anti-MUC 16 DDAB NLs and DDAB NLs against the untreated controls in the HEK 293 cell lines showed no significance (P=0.50 and P=0.02 respectively), whilst for the SKOV3 cells, the systems displayed a significance of P=0.006 for the anti-MUC 16 NLs and P=1.28 x 10^{-5} for the DDAB NLs.**……..……202**

Figure 6.9. Graphical representation of the migration patterns for the various NLs formulations on SKOV3 cell lines. A student T-test (unpaired) for the cell index values representing the migratory patterns of the anti-MUC 16 DDAB NLs and DDAB NLs against the untreated controls displayed a significance of P=0.09 and P=0.05, respectively.**…..……..204**

Figure 6.10. Fluorescent images showing the cellular uptake of FITC labelled anti-MUC 16 DDAB-loaded NLs (B) and non-FITC tagged NLs on a) SKOV3 cell lines and c) FITC labelled anti-MUC 16 DDAB-NLs**……205**

Figure 7.1. Displaying the typical TEM micrographs of 1,12 diaminododecane NLs (A and B) and the Anti-MUC 16 functionalized 1,12 diaminododecane NLs (C and D)**..223**

Figure 7.2. Graphical Illustration of the size and ZP =Zeta potential distributions of the CL=1,12 diaminododecane NLs, and anti MUC 16 1,12 diaminododecane NLs**……224**

Figure 7.3. FT-IR spectrums showing the microstructural modifications of the anti-MUC 16 antibody on the nanoliposomal surface, where (A) Unfunctionalized 1,12 diaminododecane NLs and (B) Functionalized 1,12 diaminododecane NLs**……..225**

Figure 7.4. Graphical representation of the average 1,12 diaminododecane release from 3 NLs samples at pH 7.4 and 5.5. at 37°C**……228**

Figure 7.5. 1,12 diaminododecane kinetic profiles for the various mathematical models**……..230**

Figure 7.6. Describes the FTIR spectrum showing 1,12 diaminododecane nanoliposomal mediated crosslinking of CS *in vitro*. Left = 0.47 µg/mL right = 0.93 µg/mL**……232**

Figure 7.7. Cell viability profiles **s**howing IC_{50} values of **A)** 1,12 diaminododecane loaded NLs (2.036 µg/ml) and **B)** anti- MUC 16 functionalized 1,12 diaminododecane loaded NLs (0.4063 µg/ml)**……234**

Figure 7.8. Graphical representation of apoptosis profiles generated from the MUSE™ cell analyser, where A and D are untreated, B and F are treated with 1,12 diaminododecane-NLs and C and E are treated with anti-MUC 16-1,12 diaminododecane NLs. A student T-test (unpaired) for the total apoptotic percentages of the anti-MUC 1,12 diaminododecane NLs and 1,12 diaminododecane NLs against the untreated controls showed no significance for the HEK 293 cell lines (P=0.14 and P=0.40, respectively) and for the SKOV3 cells; the anti-MUC 16 1,12 diaminododecane NLs showed a significance of P=0.0007 and the 1.12 diaminododecane NLs showed a significance of P=0.0003……**……235**

Figure 7.9. Graphical representation of profiles, where A and D are untreated, B and E are treated with CL-NLs and C and F are treated with anti-MUC 16 CL-NLs. A student T-test (unpaired) for the percentages of proliferating cells for the anti-MUC 16 1.12 diaminododecane NLs and 1,12 diaminododecane NLs against the untreated controls in the HEK 293 cell lines showed no significance (P=0.04 and P=0.84, respectively) and for the SKOV3 cells; the anti-MUC 16 1,12 diaminododecane NLs showed a significance of P=0.0003 and the 1.12 diaminododecane NLs showed a significance of P=0.02**……..237**

Figure. 7.10. Graphical representation of ROS profiles, showing the various percentages of ROS + and ROS – cells treated. Where A and D are untreated, B and E are treated with 1,12 diaminododecane-NLs and C and F are treated with Anti-MUC 16 1,12 diaminododecane -NLs. A student t test (unpaired) for the percentages of ROS - cells for the anti-MUC 16 1,12 diaminododecane NLs and 1,12 diaminododecane NLs against the untreated controls in the HEK 293 cell lines showed a significance of P = 0.0019 and P= 0.07, respectively, and for the SKOV3 cells; the anti-MUC 16 1.12 diaminododecane NLs showed a significance of P = 0.003 and the 1,12 diaminododecane NLs showed a significance of P= 0.004**……..238**

Figure 8.1. Graphical representation of ROS profiles, showing the various percentages of ROS + and ROS – cells treated with the various nanoliposomal formulations. Where A and D are untreated, B and E are treated with DDAB NLs and C and F are treated with Anti-MUC 16 DDAB NLs. A student t test (unpaired) for the percentages of ROS - cells for the anti-MUC 16 DDAB NLs and DDAB NLs against the untreated controls of showed a significance of P = 0.002 and P= 0.00019 for the HEK 293 cell lines respectively, and for the SKOV3 cells; the anti-MUC 16 DDAB NLs displayed a significance P = 0.0001 and the DDAB NLs displayed a significance P= 1.66×10^{-6}**……254**

Figure 8.2. VEGF levels (ng/mL) of SKOV3 and HEK 293 cell treated with or without the various nanoliposomal formulations (where DDAB = DDAB NLs; F. DDAB = Anti-

MUC 16 DDAB NLs; CL= 1,12 diaminododecane NLs and F.CL = Anti-MUC 16 1,12 diaminododecane NLs)**……..256**

Figure 8.3.a. Graphical illustration SKOV3 Tumourospheres, where A) untreated spheroid, B) DDAB-NLs @ IC_{50} treated spheroid and C) anti-MUC 16 DDAB NLs @ ic50 was analysed for the effects of **spheroid formation** in the present of these systems and D) untreated spheroid, E) DDAB-NLs @ IC_{50} treated spheroid and F) anti-MUC 16 DDAB NLs @ IC_{50} was analysed for the effect of the following systems on **intact spheroid……258**

Figure 8.3.b. Graphical illustration SKOV3 Tumourospheres, where A) untreated spheroid, B) DDAB-NLs @ IC_{50} treated spheroid and C) anti-MUC 16 DDAB NLs @ ic50 was analysed for the effects of **spheroid formation** in the present of these systems and D) untreated spheroid, E) 1,12 diaminododecane NLs @ IC_{50} treated spheroid and F) anti-MUC 16 1,12 diaminododecane NLs @ IC_{50} was analysed for the effect of the following systems on **intact spheroids……259**

Figure 8.4. Graphical illustration of GalNAc4S-6ST expressions initiated by the various nanoliposomal formulations**……261**

Figure 9.1. Study outline/protocol for model 1**……..270**

Figure 9.2. Study outline/protocol for model 2**……271**

Figure 9.3. Graphical comparison of tumour volumes of mice that received 5 mg/kg DDAB within the various formulations**……..276**

Figure 9.4. Photographic imagery of mice that received 5 mg/kg of DDAB in different delivery systems. Where **A** represents the mouse that received the anti-MUC 16 NLs; (left image = day 1 of therapy, middle image = day 21 and right image = post-mortem image of tumour at day 21). **B)** represents the mouse that received the DDAB in unfunctionalized NLs; (left image = day 1 of therapy, middle image = day 21 and right image = post-mortem image of tumour at day 21). **C)** represents the mouse

that received DDAB in PBS; (left image = day 1 of therapy, middle image = day 21 and right image = post-mortem image of tumour at day 21)**……280**

Figure 9.5. Ultrasound imagery for the detection of the internal formation of tumour development between the mice that received the 5 mg/kg of DDAB in the various formulations following the 21-day treatment period. Where **A** represents the mouse that received the anti-MUC 16 NLs, **B** represents the mouse that received the DDAB in unfunctionalized NLs and **C** represents the mouse that received DDAB in PBS. The overlying subcutaneous fat demarcating the tumour appeared relatively hyperechoic on the sonogram (seen to outline the tumour). The tumour mass shows distinct signs of echogenicity changes represented by the letters annotated on the image. This image served to preliminary prove that the tumours were present internally before classification by means of histology**……281**

Figure 9.6. Histopathological images of the liver, kidney and tumour tissue of the mice that received the 5 mg/kg DDAB in separate delivery systems at 20x magnification. Where CT= untreated mouse**……286**

Figure 9.7. A) Photographic imagery of the mouse that received 5 mg/kg-DDAB unfunctionalized NLs which presented with a skin reaction and **B)** the mouse that received 10 mg/kg of DDAB/PBS that presented with a severe skin reaction**……..287**

Figure 9.8. Graphical comparison of tumour volumes of mice, where 1 and 3 are the IT inserts of the anti-MUC 16 DDAB NLs at 5 mg/kg and 2.5 mg/kg respectively; 2 and 5 are IV administered of the anti-MUC 16 DDAB NLs at 5 mg/kg and 2.5 mg/kg respectively and 4 is the untreated control sacrificed at day 1 of treatment**……292**

Figure 9.9. Photographical depictions of the increase in the tumours of the mice during the 21-day treatment period**……..293**

Figure 9.10. Representing the Kaplan-Meier Curve, where group A represents the mice that received both the IV doses and B represents the mice that received both the IT doses**……294**

Figure 9.11. Histopathological images of the liver, kidney and tumour tissue of mice utilized in model 2. Where CT = untreated control**……296**

LIST OF TABLES

Table 2.1. Presenting the various nanocarriers involved in siRNA delivery to target OC and the systems response**……30**

Table 2.2. Presenting various nanocarriers involved in drug delivery for OC and the systems response**……35**

Table 2.3. The correlation of CS-E to OC, summarising and supporting CS-E as an important biomarker**……..41**

Table 2.4. Various antibodies used to target their respective CS isomer**……43**

Table 2.5. The relationship of CD44 and HA to the ovarian cancer development**….49**

Table 3.1. lists several levels at which AI can be used as an effective strategy (detection, diagnosis, treatment, and management) for OC**……..76**

Table 3.2. Displaying the various ML software commonly used in cancer**……..81**

Table 3.3 Outlines ML technologies that have been applied to data generated from DNA microarrays to facilitate a deeper understanding of diagnostic cues in cancer**…83**

Table 3.4. Displaying the performance of the Wavelet features with PCA-SVM algorithm in comparison to other algorithms for analysis of proteomic data with different AI models. (Adapted from Alquda and co-workers, 2019)**……90**

Table 3.5. Comparison of the performance of different machine learning models (adapted from Bhattacharjee and co-workers, 2017)**……..91**

Table 4.1: Typical sulphation patterns of CS isoforms (Pradeep et al., 2016)**……124**

Table 4.2. Summarising the experimental outputs and calibration curve details used to quantify the number of reacting groups on the CS backbone. An unpaired t test, two-tailed P values for the total amount of MB vs MB with the addition of CS showed no significant difference (P=0.007)**……...135**

Table 4.3. Showing the various FT-IR peaks and their corresponding functional groups for pristine polymer and DDAB**…….137**

Table 4.4. Summary of average zeta potential and particle size of CS-DDAB nanoconjugates...**……147**

Table 5.1. Showing the various amounts of DCC and 1,12 diaminododecane used for chemical synthesis of CS networks**……..162**

Table 6.1. Typical formulation design template for producing the NLs with optimal size, potential and PDI and surface antibody peptide attachment**……185**

Table 6.2. Showing the various Sizes, Zeta potential, PDI and Conductance of the various nanoliposomal formulations**……192**

Table 6.3. Showing the average particle size and Zeta potential of the optimized NLs formulations**……193**

Table 6.4. Displaying the differences in size, ZP and PDI of the various nanoliposomal formulations 21 days after synthesis and storage at 4°C**……..195**

Table 6.5. Quantity of DDAB computed from the calibration curve and experimental parameters**……198**

Table 7.1. Varying amounts of lipids and hydration mediums used for the nanoliposomal formulation**……215**

Table 7.2. Showing the average particle size, PDI and zeta potential for the various nanoliposomal systems**……..224**

Table 7.3. Displaying the amount of 1,12 diaminododecane obtained from 3 NLs samples, with the experimental parameters**……226**

Table 7.4. Mathematical modelling for 1,12 diaminododecane release kinetics from the nanoliposomes**……..230**

Table 7.5. Summarising the degree of crosslinking based on the relative MB adsorption factor for the various doses at various time points**……232**

Table 7.6. Summarising the percentages of cell viability with the respective IC_{50} of CL-NLs (2.036 µg/mL) and Anti-MUC 16 functionalized CL-NLs (0.4063 µg/mL) on SKOV3 cell lines**……234**

Table 7.7. Showing the percentages of live cells, Early and late apoptotic cell, and the total apoptotic cells, in both SKOV3 and HEK293 cell lines, where Control = untreated, CL = 1,12 diaminododecane NLs and F CL=Anti-MUC 16 functionalized NLs**…….236**

Table 7.8. Showing the various percentages of proliferating and non-proliferating cells in both SKOV3 and HEK 293 cell lines, where Control =untreated, CL = 1,12 diaminododecane NLs and F CL = Anti-MUC 16 1,12 diaminododecane NLs**.....237**

Table. 7.9. Summarising the percentages of ROS negative and ROS positive cells in both SKOV3 and HEK 293 cell lines, where Control = untreated, CL = unfunctionalized 1,12diaminododecane NLs and F CL = Anti-MUC 16 1,12diaminododecane NLs**..239**

Table 8.1. Showing the various composition of the optimized nanoliposomal formulation**……..249**

Table 8.2. Amounts of lipids used and hydration fluids for each NLs formulation**..249**

Table 8.3. Experimental parameters utilized to quantify the expression of VEGF by OD ELISA measurements and VEGF expressions at T= 48 h, and showing a student unpaired T test for each formulation at time 48 h relative to the untreated control. (where DDAB = DDAB NLs; F.DDAB = Anti-MUC 16 DDAB NLs; CL= 1,12 diaminododecane NLs and F.CL = Anti-MUC 16 1,12 diaminododecane NLs)**……256**

Table 8.4.a Semi-Quantitative analysis of the percentage of dead regions(red) in the SKOV3 Tumourospheres, where DDAB= DDAB-NLs and F. DDAB= anti-MUC 16 DDAB NLs**……258**

Table 8.4.b Semi-Quantitative analysis of the percentage of dead regions(red) in the SKOV3 Tumourospheres, where CL= 1,12 diaminododecane NLs -NLs and F.CL= anti-MUC 1,12 diaminododecane NLs NLs**……259**

Table 9.1.a. Showing the various mice, dose and form and formulation types used in model 1**……269**

Table 9.1.b. Showing the various mice, DDAB dosages and routes of administrations used in model 2**……..269**

Table 9.2.a. Tumour volumes and physical assessment of the mice in response to the anti-MUC16 DDAB NLs therapy**……..…277**

Table 9.2.b. Tumour volumes and physical assessment of the mice in response to the unfunctionalized DDAB NLs therapy**……278**

Table 9.2.c. Tumour volumes and physical assessment of the mice in response to the DDAB in PBS therapy**……279**

Table 9.3. A summary of the various histological changes of the mice that received the 5 mg/kg of DDAB using separate systems**……282**

Table 9.4.A. Showing the various mice weights in the anti-MUC 16 DDAB NLs treatment group**……...288**

Table 9.4.B. Showing the various mice weights in the unfunctionalized DDAB NLs treatment group**…….,,288**

Table 9.4.C. Showing the various mice weight in the DDAB/PBS treatment group**..288**

Table. 9.5. Summarising the tumour inhibition rates for both routes of administration of the anti-MUC 16 NLs**……..293**

LIST OF EQUATIONS

Equation 3.1……**103**

Equation 3.2……**104**

Equation 4.1……**128**

Equation 5.1……**165**

Equation 5.2……**174**

Equation 5.3……**174**

Equation 7.1……**217**

Equation 7.2……**218**

Equation 7.3……**218**

Equation 7.4……**218**

Equation 7.5……**219**

Equation 7.6……**219**

Equation 7.7……**219**

Equation 7.8……**220**

Equation 9.1……**272**

Equation 9.2……**273**

LIST OF ABBREVIATIONS

DSPC 1,2-Distearoyl-sn-glycero-3-phosphocholine
CHOL Cholesterol
CL Crosslinking/Crosslinker
CT Control
CS Chondroitin sulphate
DDAB Didodecyldimethylammonium bromide
DDW Double distilled water
DSC Differential Scanning Calorimetry
ELISA enzyme-linked immunosorbent assay
FITC Fluorescein Isothiocyanate isomer 1
FRET Fluorescence resonance energy transfer
FTIR Fourier Transmission Infrared
GAGs Glycosaminoglycans
GalNAc4S-6ST N-acetyl galactosamine 4-sulphate 6-*O*-sulfotransferase
HA Hyaluronan
L-α PEDM L-α-Phosphatidylethanolamine distearoyl methoxypolyethylene glycol conjugate
MB Methylene blue
ML Machine learning
NLs Nanoliposomes
NPs Nanoparticles
OC Ovarian Cancer
PDI Polydispersity index
PEC Polyelectrolyte complex
qPCR quantitative polymerase chain reactions
ROS Reactive Oxygenated Species
SELEX Systematic Evolution of Ligands by Exponential enrichment
SEM Scanning electron microscopy
TEM Transmission Electron Microscopy
TGA Thermogravimetric analysis

VEGF	Vascular endothelial growth factor
XRD	X-ray diffraction

CHAPTER 1:
INTRODUCTION

1.1. Introduction

Ovarian cancer (OC) is notoriously known as the most lethal gynecologic malignancy, with over 151,000 fatalities occurring annually (Nami et al., 2019). Despite standard surgical interventions (Siegel et al., 2012) (cytoreductive surgery or debulking surgery (kanaani et al., 2017)) or the first-line chemotherapy (such as paclitaxel and platinum-based treatments [the breakthrough therapy] in OC treatment) (Lin et al., 2016), over 70% of patients will eventually die due to tumour recurrence and widespread metastasis (Xue et al., 2020). The complication arises as a majority of patients are diagnosed primarily in advanced stages, presenting with poor prognosis due to chemoresistance (Lin et al., 2016). Furthermore, OC has become the fifth leading cause of cancer associated fatalities in women in the U.S. and is estimated to contribute to 22,440 new diagnosis and 14,080 deaths in 2017 (Siegel et al., 2017), which rapidly escalates the demand for earlier diagnostic strategies coupled with aggressive treatment regimens. In aims to fight back, nano inspired medicines are frequently utilized as engineered drug delivery systems that add various advantages to conventional chemotherapy and diagnostics (Corradetti et al., 2019). In tandem with active targeting, (delivery of a corresponding therapeutic drug to a specific cellular and molecular tumour-related site; Xue et al., 2020)) these systems offer a great promise in detangling the complexity surrounding chemotherapy by reducing adverse effects, which enhance clinical outcomes and increase patient adherence.

1.1.1. The Ovarian Tumour Microenvironment

The extracellular matrix (ECM) is a vital component for cellular function, structure and stability maintenance (Davis et al., 2005). The ECM is able to specifically interact with cellular receptors and growth factors which are essential for balance and homeostasis (Afratis et al., 2012). In healthy individuals, proteoglycans (PGs) are present in the ECM (Pradeep et al., 2016). These PGs are vastly anionic macromolecules and are important to cells for their role in maintaining the cellular integrity, structure, and rigidity in order for normal cellular processes to occur (Athanasia et al., 2008). Core proteins and

unbranched polysaccharides covalently bind to form PGs; these polysaccharides are termed glycosaminoglycans (GAGs). Based on the particular monosaccharides and sulphation patterns, various groups of GAGs are derived, these include: Chondroitin sulphate (CS), Dermatan sulphate (DS), Heparin Sulphate, Keratin sulphate and Hyaluronic acid (Pradeep et al., 2016; Afratis et al., 2012).

CS is a negatively charged water soluble carbohydrate polymer consisting of repeated units of D- glucuronic acid and D-N acetyl galactosamine. This molecule can then be sulphated at various positions i.e., C-4 and/or C-6 OR C-2 of the N acetylgalactosamine and the glucuronic acid moiety respectively (Athanasia et al., 2008).

CS differentiates into five isoforms based on their specific sulphation patterns, this gives rise to molecules such as CS-A [GlcA-GalNAc-4-sulphate], CS-C [GlcA-Gal-NAc-6-O-sulphate], CS-D [GlcA(2-O-sulphate)–GalNAc(6-O-sulphate)], CS-E [GlcA-GalNAc-(4,6)-O-disulphate] and CS-B(DS) [IdoA (2-O-sulphate) – GalNAc(6-O-sulphate)]. Furthermore, these sulphation patterns dictate the specific interactions between various molecules such as growth factor including transforming growth factor (TGF) and vascular endothelial growth factor (VEGF), to name a few (Vallen et al., 2014), as well as cytokines, adhesion molecules and lipoproteins (Pradeep et al., 2016; Athanasia et al., 2008). In addition, CS forms bonds with proteins via its serine moiety using a tetrasaccharide linkage producing chondroitin sulphate proteoglycans (CSPGs) such as aggrecan and versican (Athanasia et al., 2008). These CSPGs located in the extra tumoural regions are essential in regulating key aspects associated with cellular behaviour and function (Prinz et al., 2014).

1.1.2. The Role of CS-E in Ovarian Cancer

The stromal component of the OC tumour ECM is responsible for the vicious tumour progression and metastasis (Vallen et al., 2014). This region has recently been associated with the up regulation of CS-E (Pradeep et al., 2016). CS-E plays a key regulatory role in OC dissemination due to its correlation with angiogenesis (ten Dam et al., 2007), tumour cell adhesiveness (Casey et al., 2003) and metastasis (Georges et al., 2012).

The accelerated biosynthesis of CS-E is due to an over expression of N-acetyl galactosamine 4-sulphate 6-O-sulfotransferase (GalNAc4S-6ST), which is the sole enzyme responsible for the CS-E biosynthesis (Li et al., 2008). This over-expression aids in tumour angiogenesis as CS-E serves as an imperative binding site for VEGF attachment. Furthermore, high CS-E levels correlate to high VEGF levels which is significant in tumour spheroid formation, this spheroid formation is associated with the extremely aggressive and invasive metastasis characteristics of OC (Vallen et al., 2014).

CS-E further aids the adhesion of tumours as it is responsible for increasing the adhesive properties of adhesion molecules namely N-cadherin and E- cadherin (Pradeep et al., 2016). In addition, integrins interact directly to CS-E chains, and play a direct role in enhanced cell adhesion (Vallen et al., 2014). Additionally, CS-E is further responsible for the invasion and migration of tumours. Metalloproteinases (MMPs) are a group of enzymes responsible for OC progression. The activation and regulation are strongly influenced by CS-E, Furthermore CS-E is able to interact with MPPs such as pro-MMP7, contributing to the activation and metastasis of tumour cells (Vallen et al., 2014). To this end, it is evident that CS-E plays a paramount role in OC tumour progression and is a promising molecular target to inhibit for OC intervention (Pradeep et al., 2016).

1.1.3. Rationale and Motivation of the Study (A *first-in-the* World Hypothesis)

Recently, our research group hypothesized in a published article entitled '*"On-The-Spot" Arresting of Chondroitin Sulphate Proteoglycans: Implications for Ovarian Adenocarcinoma Recognition and Intervention'* a highly innovative mechanistic forecast to target CS chains to treat OC independently of drug therapy.

The first approach is to counteract malignant tumour cells by forming a spontaneous (or "*On-The-Spot*") polyelectrolyte complex (PEC) on the anionic CS-E polymer backbone with a cationic substance. This electrostatic interaction will modify the structural architecture of CS, leading to less free available CS molecules. The second approach is to load nano-archetypes with various biocompatible but non-biodegradable crosslinkers. This phenomenon could be utilized in the targeted chemotherapy of OC. Nano-

archetypes of compounds known to crosslink with CS could be synthesized and then conjugated with an OC targeting antibody for site specific delivery. Once at the tumour site, the crosslinker would crosslink with CS-E to produce a hydrogel-based “biogel mass” that would become isolated from the tumorous vasculature and tumour growth could be terminated. In addition, If CS is crosslinked/complexed (or ‘arrested’), less CS will be freely available for its metastatic role in OC dissemination. In addition, due to its non-biodegradable nature and altered physicomechanical properties, the inherent *in vivo* rejection of the tumorous tissue may also be possible. Furthermore, the formation of such a complex hydrogel may interrupt the nutritional supply to the tumorous tissue, thereby preventing further tumour proliferation and growth (Pradeep et al., 2016).

In this study, cationic nanoliposomes (NLs) have been chosen as the suitable nano-archetype due to its favourable chemoresistance properties (Liu et al., 2014). The surface rich positively charged moiety will allow for the formation of an *on the spot* PEC formation between the anionic over-expressed CS-E located in the tumour stroma and cellular surfaces. NLs will further serve as delivery vehicles for the loading of a crosslinker that is CS specific (Figure 1.1). The crosslinker will act as ‘handcuffs’ to bind together the long polysaccharides chains of CS-E. By arresting the excess CS chains in a crosslinked network, will subsequently inhibit CS-E from interacting with the adhesion molecules, growth factors and MPPs that are responsible for tumour dissemination.

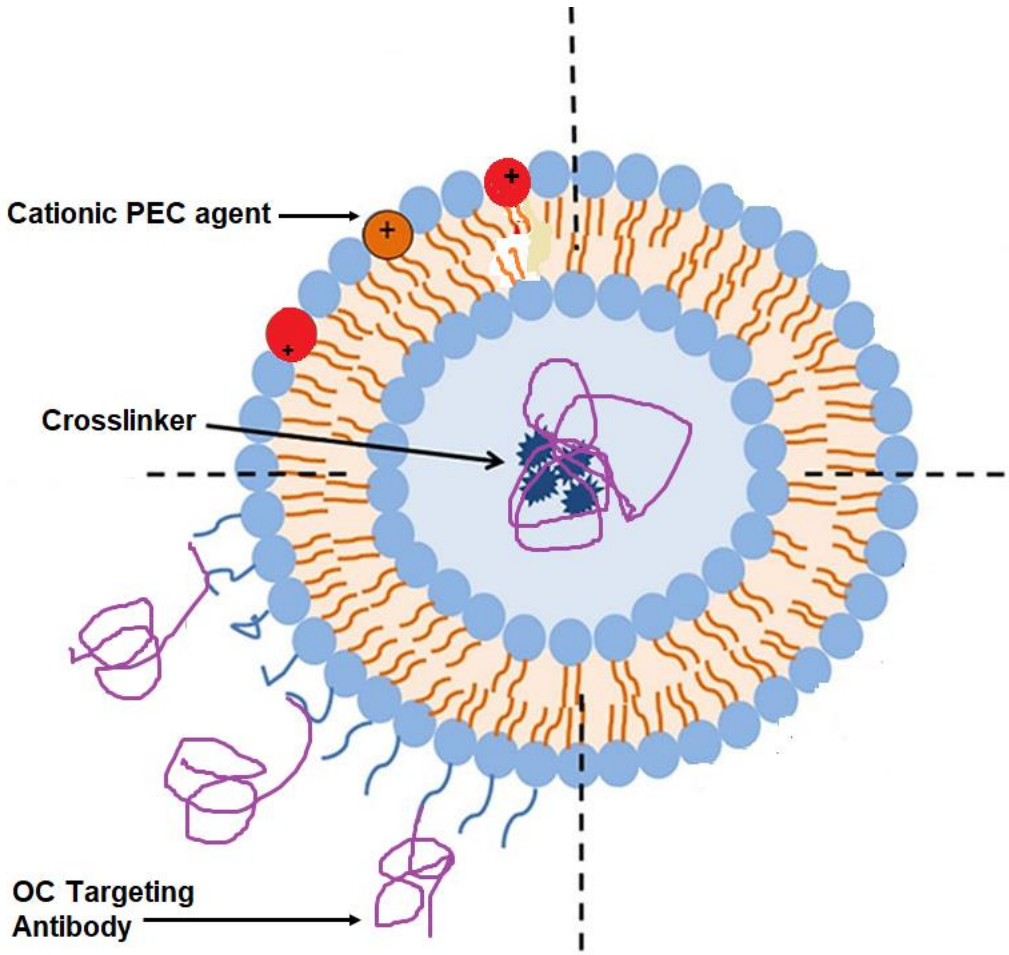

Figure 1.1. Proposed representation of the cationic nanoliposome engineered with the OC targeting antibody and loaded with a crosslinker (Sercombe et al., 2015).

1.2. Possible Applications of this Delivery System Include:

- These systems can serve as adjuvant OC therapy in aims of retarding the growth of tumours in order to prolong the survival times of a patient in order to assess and conduct the optimal surgical intervention.

- Because these systems target the ovarian stromal regions and OC cell surfaces, their co-delivery with drugs targeting OC cells will provide a more holistic range of molecular targeted synergistic therapy.

- The cationic rich NLs designed to target CS by PEC may act as a housing platform to deliver various drug molecules in the empty hydrophilic core, with specific antibodies to target multiple cancers where GAGs are implicated in tumour dissemination.

- Because of the site specific and active targeting features of the system, it could be used in the primary treatment of OC, particularly in patients that are responding adversely to conventional non-targeting chemotherapies.

1.3. Novelty of the PhD Study

- The mechanism of action of this system was published as a *first-in-the-world* hypothesis. Thus, the intended mode of OC inhibition has never been proposed nor tested previously.

- The system is independent of conventional drug molecules, however, utilizes crosslinking and PEC as means to structurally modify a relatively neglected OC causing polymer (i.e., CS) to slow the progression of OC.

- The crosslinking and PEC agents will be delivered by nanotechnological inspired systems such as NLs, with added features such as the surface engineering of antibodies for active targeting. These drug delivery platforms further enhance the already novel concept.

1.4. Aims and Objectives (With Expected Outcomes)

The aim of this study is to develop a nano-archetype that has the ability to polyelectrolyte complex and crosslink CS in order to slow down the progression of ovarian cancer. This will be achieved by the following objectives:

1.4.1. To Evaluate and Characterize the CS-E-Crosslinker (CS-E-CL) and CS-E-polyelectrolyte complexing agent (CS-E-PEC) Archetypes to Determine if the Crosslinking and Complexing Agents are Effective against CS-E.

In this preliminary stage of the study, we expect to identify a suitable crosslinker and polyelectrolyte complexing agent that can react irreversibly with CS in order to change the structural architecture and chemical integrity of the polymer backbone.

1.4.2. To Formulate/Develop the anti-MUC 16 Nanoliposomes

Here, we aim to use the previously identified suitable crosslinker and PEC agents and formulate a nanoliposomal system. We further aim to surface engineer an OC targeting antibody for site specific delivery of the described agents.

1.4.3. To Characterize and Measure the Size and Morphology of the Nanoliposomes using Transmission Electron Microscopy

In this phase, we expect to achieve nanosized characteristics; we aim to further visualize these systems as a proof of concept.

1.4.4. To perform Sensitivity Assays on Ovarian Cancer Cell Lines to Measure the Effectiveness of the Nanoliposomes to Inhibit OC Tumour Growth.

The identification of the IC_{50} value for the nanoliposomal system, acting against OC cell lines over-expressing CS-E.

1.4.5. To Investigate CS-E-CL Mediated Inhibition of Proteoglycan Activity and Determine Cell Viability

We expect to display anti-proliferation and migration effects on the CS-E over-expressed cell lines.

1.4.6. To Investigate the GalNAc4S-6ST Gene Expression Analysis of Cancer Cells Induced by the Nanoliposomes

Here we aim to assess the ability of the designed formulation to knockdown the GalNAc4S-6ST gene expression, which is involved in the rapid biosynthesis of CS-E (Vallen et al., 2014).

1.4.7. To determine the Nanoliposomal Mediated Cytotoxic Performance of the Nanoliposomes on 3D Cell Cultures.

The growing of cells in 3D architectures better mimics the *in vivo* microenvironment. Here we aim to validate the cytotoxic effects on 3D cells prior to testing in animals. Here we aim to see morphological changes in 3D spheroids, as a consequence of these nanoliposomal therapies; such morphological changes infer reduction in cell viability, proliferation, and induction of apoptosis.

1.4.8. To Evaluate the In Vivo Anticancer Performance of the Nanoliposomes on an Animal Model.

The *in vivo* studies will be performed to determine the effects of the system in animal models; the expected outcomes include a reduction in tumour size, relative to untreated control. This reduction in size will be compared to the conventional chemotherapeutics.

1.5. Overview of this Thesis

Chapter 1 Serves as an introductory trailer into the thesis. Here the background and rationale of the study is highlighted. The published hypothesis that described the mechanistic forecast which founded the project is described. The potential applications and novelty of the system formulated in the study is further discussed. Lastly, the aims and objectives of the studies are outlined in this chapter.

Chapter 2 Provides an in-depth literature review which focuses on highlighting the latest nano systems employed in OC drug delivery strategies. Here the various OC targeting

antibodies are also discussed. The second section of the chapter highlights the virulent contribution of GAGs (e.g. CS and HA) on OC cell dissemination, establishing GAGs as notorious molecular targets.

Chapter 3 Provides an in-depth literature review which focuses on highlighting the use of ultramodern technologies such artificial intelligence (AI) in tandem with genetic and protein data to better detect OC. Here the pertinence of earlier diagnostic strategies is discussed as a key asset in curbing the rapid metastases of the ovarian tumour. The review further displays a fairly new concept termed '*fractional pharmacokinetics'*, with non-linear differential mathematical equations for assisting the prediction of movement of drugs in tumorous and non-diffusional regions of the body.

Chapter 4 Provides a description of the synthesis and characterization of a suitable CS polyelectrolyte complexing agent. Here the cationic didodecyldimethylammonium bromide (DDAB) was tested for its ability to spontaneously interact with CS with no external interference. The interaction was predicted utilizing molecular docking studies. The CS-DDAB PEC was extensively physiochemically, structurally and morphologically characterized to ensure that structural architecture of the CS polymer backbone was modified. Lastly, the IC_{50} of DDAB on over-expressed CS-E cell lines was determined.

Chapter 5 Provides a description of the synthesis and characterization of the CS and 1,12 diaminododecane crosslinked network. Here we aimed to assess if 1,12 diaminododecane could act as a suitable candidate to interact with CS. The CS-1,12 diaminododecane crosslinked network was physicochemically, architecturally and thermally characterized to prove the successful crosslinking of CS. Lastly, the degree of 1,12 diaminododecane crosslinking to CS was verified.

Chapters 4 and 5 were aimed at validating the use of DDAB as a suitable CS PEC agent and 1,12 diaminododecane as a suitable CS crosslinking agent. Here studies were conducted to verify their successful and stable interaction with CS. Once proven, these two molecules will be incorporated into drug delivery systems for further specific OC testing.

Chapter 6 Provides a description of the formulation and characterization of the surface active, DDAB cationic nanoliposomes. Stability, size, and morphological investigations are conducted. The surface engineering of the anti-MUC 16 antibody and assessment of the attachment is verified. The systems are tested (using various biological assays) against SKOV3 ovarian carcinoma cells (rich in CS-E) to validate the anticancer performance and contrasted to that of healthy HEK 293 cells

Chapter 7 Provides insight into the formulation and characterization of the 1,12 diaminododecane loaded nanoliposomes. The nanoliposomes are tested for loading, release and release kinetic behaviours of 1,12 diaminododecane from the nanoliposome. The surface engineering of the anti-MUC 16 antibody and assessment of the attachment is verified. The systems are tested against SKOV3 ovarian carcinoma cells (rich in CS-E) to validate the anticancer performance.

Chapter 8 Provides a description into the advanced cellular biological experimentation such as the GalNAc4S-6ST gene expression analysis on SKOV3, HEK 293 and OVCAR-5 cells following the administration of the 1,12 diaminododecane and DDAB nanoliposomal independent systems. These independent systems were then tested for anticancer activity against a 3D spheroidal architecture of SKOV3 cells. Lastly, these systems were assessed to verify their anti-VEGF capabilities.

(all biological assays performed in the study relate to the pathogenic role of CS-E to OC dissemination)

Chapter 9 Provides the *in vivo* performance of the anti-MUC 16 DDAB nanoliposomes against athymic nude mice models on two separate models. Where we first assessed the optimal dose for chemotherapy, and secondly tested this dose in an advanced stage 4 mimetic OC model.

1.6 Concluding Remarks

The novel arresting mechanics of CS hypothesized by our research group provided a favourable ability to down regulate the process such as proliferation, migration and VEGF

production stimulated by the over expression of CS-E. This system displays a promising potential to slow the progression of advanced stage tumours by retarding tumour volumes and increasing the survival times of athymic nude mice. It is therefore envisaged as a future therapy approach against OC.

1.6. References

Afratis, N., Gialeli, C., 2012. Glycosaminoglycans: key players in cancer cell biology and treatment.FEBS journal. 279, 1177-1197.

Athanasia, P., Asimakopoulou., 2008.The biological role of chondroitin sulphate sulphate in cancer and chondroitin – based anti- cancer drugs. In Vivo. 22, 385 – 389.

Casey, R.C., Oegema, T.R., Skubitz, K.M., Pambuccian, S.E., Grindle, S.M., Skubitz, A.P., 2003. Cell membrane glycosylation mediates the adhesion, migration, and invasion of ovarian carcinoma cells. Clin Exp Metastasis. 20, 143–52.

Corradetti, B., Pisano, S., Conlan, R. S., & Ferrari, M., 2019. Nanotechnology and immunotherapy in ovarian cancer: tracing new landscapes. Journal of Pharmacology and Experimental Therapeutics. jpet.118.254979.

Davis, G., 2005. Endothelial Extracellular Matrix: biosynthesis, remodelling and functions During Vascular Morphogenesis and Neovessel Stabilization. Circulation research. 97, 1093-1107.

Georges, S., Heymann, D., Padrines, M., 2012. Modulatory effects of proteoglycans on proteinase activities. Methods Mol Biol. 836, 307–22.

Kanaani, L., Ebrahimi Far, M., Kazemi, S. M., Choupani, E., Mazloumi Tabrizi, M., Ebrahimi Shahmabadi, H., & Akbarzadeh Khiyavi, A., 2017. General Characteristics and Cytotoxic Effects of Nano-Poly (Butyl Cyanoacrylate) Containing Carboplatin on Ovarian Cancer Cells. Asian Pacific journal of cancer prevention : APJCP.18, 87–91.

Li, F., Ten Dam, G.B., Murugan, S., Yamada, S., Hashiguchi, T., Mizumoto, S., et al., 2008. Involvement of highly sulfated chondroitin sulfate in the metastasis of the Lewis lung carcinoma cells. J Biol Chem. 283, 34294–304.

Lin, C. K., Bai, M. Y., Hu, T. M., Wang, Y. C., Chao, T. K., Weng, S. J., Huang, R. L., Su, P. H., & Lai, H. C., 2016. Preclinical evaluation of a nanoformulated antihelminthic, niclosamide, in ovarian cancer. Oncotarget. 7, 8993–9006.

Liu, X., Peng, H., Wang, Q., 2014.Surface Engineering of Liposomal Formulations for Targeted Drug Delivery. Chem Eng Process Tech 2. 1024.

Nami, F., Saadati, A., Hassanpour, S., Hasanzadeh, M., & Hassanzadeh, A., 2019. Bioassay of ovarian cancer tumor protein CA 125 using novel nano-ink on the flexible paper substrate: A new platform for efficient diagnosis of cancer. International Journal of Biological Macromolecules.

Pradeep, P., Choonara, Y., Kumar, P., Pillay, V., 2016. “On the spot” Arresting of chondroitin sulphate proteoglycans: Implications for ovarian adenocarcinoma recognition and intervention. International Journal of molecular science. 17, 1136.

Prinz. R., Willis, C., van Kuppevelt, T., Kluppel, M., 2014. Biphasic role of chondroitin sulphate in cardiac differentiation of embryonic stem cells through inhibition of wnt/β-catenin signalling.PloS ONE. 9, e92381.

Sercombe, L., Veerati, T., Moheimani, F., Wu, S., Sood, A.,Hua, S., 2015. Advances and Challenges of Liposome Assisted Drug Delivery. Frontiers in Pharmacology, 6.

Siegel, R., Naishadham, D., Jemal, A., 2012. Cancer statistics. CA Cancer J Clin. 62, 10–29.

Siegel, R.L., Miller, K.D., Jemal, A., 2017. Cancer statistics. CA Cancer J Clin. 67, 7–30.

Vallen, M., Schmidt, S., Oosterhof, A., Bulten, J., Massuger, L., Kuppevelt, T., 2014. Primary Ovarian Carcinomas and Abdominal Metastasis Contain 4,6-Disulfated Chondroitin Sulfate Rich Regions, Which Provide Adhesive Properties to Tumour Cells. PLoS ONE. 9, e111806.

Vallen, MJ., van der Steen, S., van Tiborg, A., Massuger, L., van Kuppevelt, T., 2014.Sulfated sugars in the extracellular matrix orchestrate ovarian cancer development: 'when sugars turn sour'. Gynaecologic oncology.135, 371-381.

Xue, J., Li, R., Gao, D., Chen, F., & Xie, H., 2020. CXCL12/CXCR4 Axis-Targeted Dual-Functional Nano-Drug Delivery System Against Ovarian Cancer. International journal of nanomedicine. 15, 5701–5718.

CHAPTER 2:

Nanotechnology and Glycosaminoglycans: Paving the Way Forward for Ovarian Cancer Intervention; A Comprehensive review (Available online: doi:10.3390/ijms19030731)

2.1. Synopsis of this Chapter.

OC has gained a great deal of attention due to its aggressive proliferative capabilities, high death rates and poor treatment outcomes, rendering the disease the ultimate lethal gynaecological cancer. Nanotechnology provides a promising avenue to combat this malignancy by the niche fabrication of optimally structured nanomedicines that ensure potent delivery of chemotherapeutics to OC. These are achieved by employing nanocarriers to act as “intelligent” drug delivery vehicles, functionalized with active targeting approaches for precision delivery of chemotherapeutics to over-expressed biomarkers in cancer cells. Recently, much focus has been implemented to optimize these active targeting mechanisms for treatment/diagnostic purposes employing nanocarriers. This two-part article aims to review the latest advances in active target-based OC interventions, where the impact of the newest antibody, aptamer and folate functionalization on OC detection and treatment is discussed in contrast to the limitations of this targeting mechanism. Furthermore, we discuss the latest advances in nanocarrier based drug delivery in OC, highlighting their commercial/clinical viability of these systems beyond the realms of research. Lastly, in the second section of this review, we comprehensively discussed a focus shift in OC targeting from the well-studied OC cells to the vastly neglected extracellular matrix and motivate the potential for glycosaminoglycans (GAGs) as a more focused extracellular molecular target.

Keywords: Ovarian Cancer; Nanomedicine; Glycosaminoglycans; Antibodies; Chemotherapy.

2.2. Introduction

OC is a highly lethal disorder, responsible for more deaths than all other gynaecological cancers collectively with over 220,000 cases recorded worldwide annually (Jemal et al., 2011). The poor prognosis of OC is attributed to its vicious metastasising ability, resulting in approximately 75 % of patients being diagnosed in the advanced FIGO (Federation of Gynecology and Obstetrics) stages, in addition to high rates of relapse and inefficacious treatments (Burger et al., 2011; Yang et al., 2015; Liang et al., 2017). Despite the current gold standard treatments for OC (carboplatin and paclitaxel) and standard primary debulking surgery (PDS), only 20–25 % of cases are cured effectively (Menderes et al., 2017). Although the majority of women respond well to treatment initially, recurrence, unbearable side effects and drug resistant challenges the management and treatment of OC.

Nanotechnology is the synthesis of materials and devices that manipulate matter at an incredibly small scale—between 1 and 100 nm (Alvisatos et al., 1996; Sutherland et al., 2002). Nanotechnology holds great promise for revolutionizing the field of oncology by the development of new drug delivery systems such as several nanocarriers (Coccia et al., 2015) as well their use in diagnosis, imaging, synthetic vaccine development and miniature medicals (Shi et al., 2017).

Nanocarriers include organic and inorganic nanomaterials (gold, iron, silver, cerium, titanium dioxide, and silica), non-degradable and biodegradable polymers as well as lipids, e.g., liposomes, nanoemulsions and solid-lipid nanoparticles (NPs). Self-assembling amphiphilic molecules, dendrimers, metal inorganic semiconductor nanocrystals and carbon nanotubes are also employed as nanocarriers or medicinal and diagnostic purposes (Ganta et al., 2008; Nobile et al., 2017). Nanocarriers display favourable abilities to encapsulate drug molecules to enhance the delivery of poorly soluble drugs. Furthermore, their higher surface area to volume ratio offers enhanced half-life circulation time and pharmacokinetics, improved tissue distribution, decreased non-specific toxicities and reduced incidence of resistance (Bertrand et al., 2014; Ganta et al., 2015; Mishra et al., 2010). These systems can preferentially deliver drugs to targeted locations, in contrast to systemic administration of free drugs (Yang et al., 2015).

The combination of these nanocarriers with active targeting approaches for specific molecular targets provides precision delivery of chemotherapeutics.

This two-part review article aims to discuss the latest advances in molecular target specific nanocarriers employing active targeting strategies including aptamer, antibody and folate (FA) functionalization, as an update to our research group's previous publications (Rhoda et al., 2015; Wadee et al., 2011) for OC treatment and detection in Sections 1–3 of the article. Section 4 of the article critically evaluates the potential for glycosaminoglycans (GAGs) as a more focused OC molecular target, where we discuss their clinical roles in OC and the potential interventions to target them.

2.3. Active Targeting in Ovarian Cancer

Despite the current advances in chemotherapeutics, the common flaw i.e., the lack of biological specificity leads to failed treatment outcomes (Kwon et al., 2012; Raave et al., 2015), consequently resulting in uncontrolled bio distribution of chemotherapeutics to healthy tissues (Cunliffe et al., 2005). Over-expressed molecular targets are exploited, employing polyvalent engineered nanocarriers encompassing a targeting ligand for enhanced affinity, spatial localization and therapeutic efficacy of chemotherapeutics at the lowest possible dosages (Rhoda et a., 2015), following their uptake into the desired cell via receptor mediated endocytosis (Sudimack et al., 2000; Xu et al., 2015). Such active targeting moieties include antibody, aptamer and folate-based targeting, as summarized in Figure 2.1.

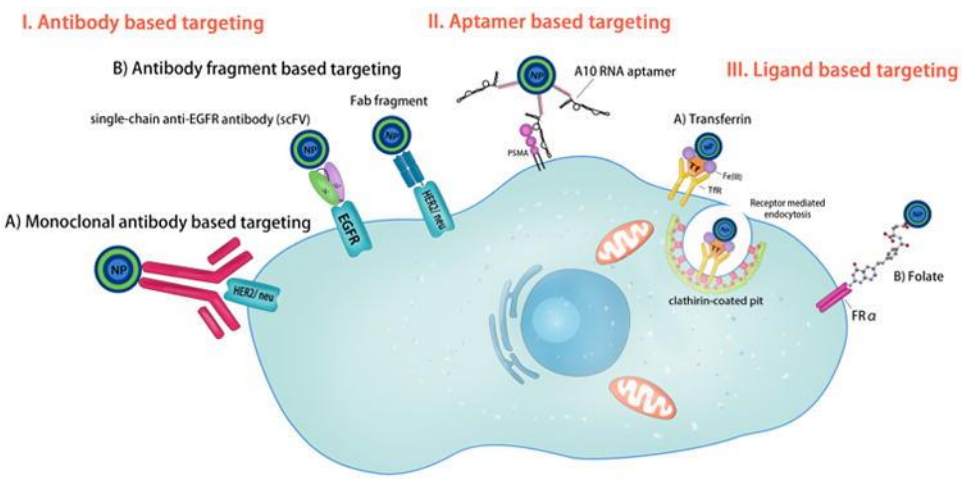

Figure 2.1. A schematic depicting method employed for active targeting of nanoparticles. I. Antibody-based targeting, which involves the use of: (A) monoclonal antibodies such as anti-Her2/neu antibody directed towardHer2/neu receptors on the target cell membrane; and (B) antibody fragments: single-chain variable fragments (scFV) such as single-chain anti-epidermal growth factor receptor (EGFR) antibody directed toward EGFR, or antigen-binding fragment (Fab) such as anti-Her2/neu Fab. II. Aptamer-based targeting such as the A10 RNA aptamer directed toward prostate-specific membrane antigen (PSMA) on the surface of the target cells. III. Ligand-based targeting such as: (A) transferrin-based targeting of nanoparticles toward transferrin receptors where uptake of the nanoparticles takes place through receptor-mediated endocytosis through clathrin-coated pits; and (B) folate-based targeting using folic acid (FA) to target folate receptor alpha (FRα), which is up-regulated on the surface of neoplastic cells. (Reprinted from [Bazak et al., 2015] with permission from Cancer Research Clinical Oncology).

Due to their favourable specificity and small particle size, peptides are the natural choice for targeting ligands (Lin et al., 2016; Kulhari et al., 2016). Targeting ability of the 4EBP peptide, which targets the eukaryotic translation initiation factor 4E (eIF4E), has been successfully exploited in OC *in vivo* (Ko et al., 2009), as has the OA02 peptide, which has been employed to deliver polymeric micellar NPs to 3 integrin receptors (Xiao et al., 2012). Despite this specificity, limitations such as enzymatic degradation leading to their metabolic instability hinder their use (Spencer et al., 2015). Efforts to circumvent these limitations through modification of the native proteins with the intention of increasing resistance to degradation have been conducted successfully by Dharap and co-workers

(Dharap et al., 2005). Briefly, researchers modified the native sequence of Luteinizing hormone releasing hormone (LHRH) peptide to provide a reactive amino group specifically on the side chain of a lysine residue to yield the super active, degradation-resistant Lys-6-des-Gly-10-Pro-9-ethylamide LHRH analog (Dharap et al., 2005). Apte and co-workers (Apte et al., 2014) successfully implemented a strategy to circumvent the degradation of the transactivator of transcription peptide (TATp). TATp is a cell penetrating peptide that aids in the cellular uptake and transportation of micellular and liposomal nanocarriers into cells. This protein is susceptible to proteolytic enzymatic degradation from the acidic tumour environment which reduces its targeting performance in vivo. Success was achieved by shielding the peptide using a polyethylene glycol–Hydrazine–phosphatatidylethanolamine (PEG-Hz-PE) conjugate, bound via a pH sensitive bond that remains stable under normal pHs, shielding the TATp, whilst degrading at acidic tumour pH facilitating polymer hydrolysis and exposure of the TATp for cellular internalization (Apte et al., 2014).

2.3.1. Antibody Based Targeting in Ovarian Cancer

Antibodies are one of the major moieties employed as targeting agents for nanocarrier based precision drug delivery systems (Bazak et al., 2015). Since their introduction, great developments have been made in this field. HER2 (also known as ERBB2 or NEU) is a transmembrane glycoprotein receptor that exhibits tyrosine kinase activity and extensive homology to the epidermal growth factor (Tuefferd et al., 2007; Peoples et al., 1995). It is ubiquitously expressed in tumours and known to be over-expressed in approximately 30–40% of all ovarian and breast cancers (Peoples et al., 1995), with considerable variation (Tuefferd et al., 2007). HER2 thus presents itself as a promising receptor to exploit for antibody mediated therapy (Menderes et al., 2017).

Trastuzumab, a monoclonal antibody (mAb) was the first HER2 targeting agent evaluated resulting in a poor 7.3% response rate in phase II clinical trials utilizing HER2 positive cancer patients. In 2006, the anti-HER2 antibody Pertuzumab underwent clinical evaluation in OC, therapeutically benefiting 14.5% of patients (Langdon et al., 2016). Since then, studies have been undertaken to maximize the effects of these mAbs. Palanca-Wessels and co-workers (Palanca-Wessels et al., 2016) obtained favourable

results for Trastuzumab employing Small interfering RNA (siRNAs) for gene suppression. A biotinylated polymeric nanocarrier conjugated with Trastuzumab served as a platform to deliver siRNA. Results indicate that siRNA successfully accumulated in tumours in excessive amounts with a 70% targeted gene suppression in mice bearing intraperitoneal (i.p.) human ovarian tumour xenografts. This system therefore displays improvements in the anticancer activity of Trastuzumab in contrast to sole treatment (Palanca-Wessels et al., 2016).

SYD985 is a novel HER2-targeting antibody drug conjugate (ADC), attached via a cleavable linker to duocarmycin. This novel antibody displays strong activity towards OC as well as moderate to low HER2 expressions. Menderes and co-workers (Menderes et al., 2017) compared the anti-tumour activity of SYD985 against Trastuzumab emtansine (T-DM1), an ADC (which possess superior clinical activity against Trastuzumab due to the HER2 targeting effects of Trastuzumab and the antimicrotubular affect the DM1 portion) in ten primary OC cell lines with HER2 expression. Results indicate that, in the presence of peripheral blood lymphocytes (PBL), both SYD985 and T-DM1 induce similar antibody-dependent cellular cytotoxicity (ADCC). In contrast, SYD985 were 3-42-fold more cytotoxic in the absence of PBL when compared to T-DM1. Unlike T-DM1, SYD985 were successful in effectively destroying HER2 tumour cells. Furthermore, *in vivo* studies proved that SYD985 is significantly more active than T-DM1 against HER2 positive epithelial ovarian cancer (EOC) xenografts with moderate to low heterogeneous HER2 expressions (Menderes et al., 2017). This study provides useful evidence suggesting SYD985 possesses superior potency over T-DM1.

The B7-H3 epitope is expressed on OC cells and cancer initiating cells (CICs) (Kasten et al., 2017). B7-H3 appears to be expressed in 93% of ovarian tumours after immunohistochemical experimentation demonstrated by Zang and co-workers (Zang et al., 2010). B7-H3 is a group of transmembrane proteins with 20–30% common amino acid sequences with other B7-family molecules. It retains 88% of the amino acid sequence with mouse B7-H3 (Fauci et al., 2012). Studies conducted by Fauci and co-workers (Fauci et al., 2012) revealed that, by decreasing the B7-H3 expression in tumours, it inhibits cell migration and invasion, thus making it a promising molecular target to investigate (Collins et al., 2005).

Recently, Kasten and co-workers (Kasten et al., 2017) exploited the B7-H3 epitope for OC intervention using the monoclonal antibody (mAb) 376.96, which recognizes the B7-H3 epitope for particle radioimmunotherapy (RIT) in pre-clinical models of human OC. Survival and biodistribution of the 212Pb-376.96 archetype were compared against an isotype of 212Pb-F3-C25, utilized as a non-targeting control. 212Pb-376.96 inhibited the clonogenic survival of OC cells 40 times more effectively than the control 212Pb-F3-C25. Furthermore, the 212Pb-376.9 system demonstrated high peritoneal retention and tumour tissue accumulation in contrast to healthy tissue (Kasten et al., 2017). Figure 2.2 provides a brief summary of the main antibodies that effectively targetHER-2 and B7-H3.

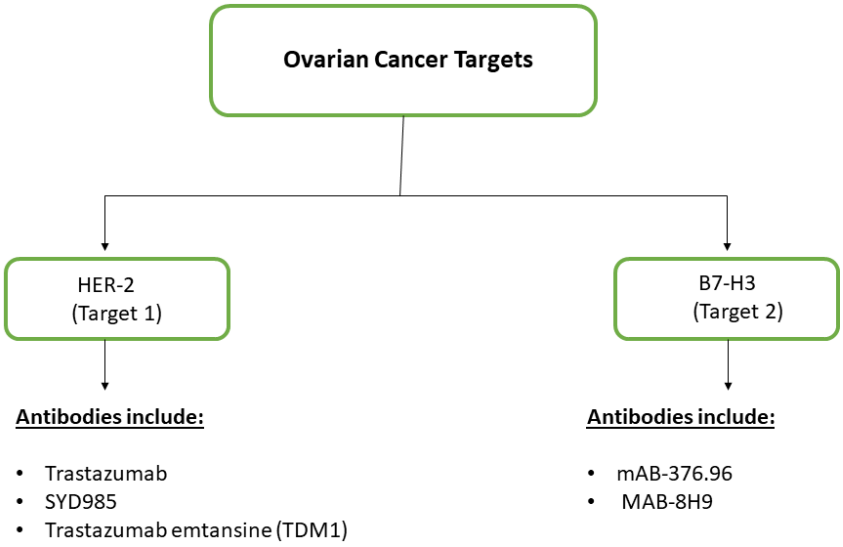

Figure 2.2. Flow chart representing the two OC targets with their respective antibodies (Chen et al., 2008).

2.3.2. Aptamer Based Targeting and Detection in Ovarian Cancer

Nucleic acid aptamers have recently gained much attention as an emerging class of active targeting moieties and serve as an impressive bioanalytical tool for the medical field (Lamberti et al., 2016). Aptamers are short single-stranded DNA or RNA oligonucleotides that are folded into secondary and tertiary three-dimensional (3D) structures allowing binding to particular molecular targets with high affinity, specificity, and precision. Aptamers commonly bind to proteins but may also bind to nucleic acids, small compounds, or entire cells. Although often protein based (Bazak et al., 2015;

Lamberti et al., 2016; Xiang et al., 2015; Shigdar et al., 2013; Gao et al., 2014), aptamers also comprise of metal ions, drugs and entire cells or viruses (Wu et al., 2015). In contrast to the animal derived antibodies, aptamer synthesis employs a Systematic Evolution of Ligands by Exponential enrichment (SELEX) technology (Lamberti et al., 2016) (which is an experimental procedure that involves the screening of a particular molecular target with the desired binding affinities from an initial random pool of oligonucleotides and oligomer [Huang et al., 2010]). Because of this chemical synthesis, aptamers offer improved stability when compared to the conventional antibodies and enzymes. Furthermore, the flexible nature of aptamers facilitates conformational changes within their structure upon binding to their targets, thus making their use in biorecognition of proteins, cancerous cells, toxins, drugs, and other molecules highly favourable (Jin et al., 2017).

Aptamers possess several advantageous traits over conventional antibodies (Wu et al., 2015), which were previously regarded as the gold standard approach for detection of proteins (Brody et al., 2000). Aptamers achieve high batch to batch uniformity for any given target, whilst excluding the need of biological models for their production (Wu et al., 2015, Zhang et al., 2012). Aptamers can also be selected against toxic or non-immunogenic targets. Aptamers can also be selected against toxic or non-immunogenic targets with the further benefit of ease of characterization over conventional antibodies. In addition, aptamers are not immunogenic and due to their small size, generate greater tissue penetration. Different from antibodies, they are sufficiently stable, resistant to harsh environments (pH and temperatures) and can be simply modified to further enhance their stability, bioavailability, and pharmacokinetics (Xi et al., 2014). Thus, aptamers are a promising targeting moiety for precision drug delivery. This section of the article will review the latest advances in aptamer targeting approaches for diagnostic and treatment in OC.

2.3.2.1. Aptamers in Ovarian Cancer Diagnostics

Early identification of neoplastic diseases is vital for the prompt initiation of therapy, particularly for rapidly metastasizing OC (Lamberti et al., 2016). CA125 is a repeated peptide epitope of mucin, and is implicated in the proliferation of cancer cells, currently

becoming the best and most commonly employed serum-based biomarker for OC. Previous methods employed to detect CA125 include a variety of immunological and biochemical methods such as radioimmunoassay, enzyme-linked immunosorbent assay (ELISA) electrochemiluminescent immunoassay, chemiluminescence, electrochemical, piezoelectric immunosensors and field effect transistors. These methods are flawed by high cost, long analysis time, sophisticated instrumentation, and low levels of sensitivity to detect tumours at an early stage, thus making aptamers a promising candidate for CA 125 detection (Hamd-Ghadreh et al., 2017).

Lambertia and co-workers recently developed two nuclease resistant RNA aptamers (CA125.1 and CA125.11) using protein-SELEX strategy. Binding characteristics were studied using real time (RT) PCR and Surface Plasmon Resonance (SPR) towards CA125, with the intention of developing a new aptamer based SPR biosensor for CA125 detection. Results by reverse transcription polymerase chain reaction (RT-PCR) suggest that CA125.1 displays stronger binding affinities compared to CA125.11. This was further confirmed using SPR binding experiments. SPR results further highlight that the aptamer/CA125 complex can be easily overturned with different binding conditions such as flow action during the SPR measurements. Consequently, additional efforts on aptamer based SPR bioassays is required to achieve a more stable and reproducible immobilization of the aptamer on the SPR chip (Lamberti et al., 2016). Despite the current limitations, this aptamer provides a useful discovery for future study and development.

More recently, Hamd-Ghadareh and co-workers developed a complex ultrasensitive antibody-ssDNA aptamer sandwich-type fluorescence immunosensor for CA125 detection in OC. The system is based on a novel signal amplification strategy where carbon dots (CDs) were functionalized with the aptamer. Polyamidoamine (PAMAM)-dendrimers/gold nanoparticles (AuNP) were covalently attached to the CA125 antibody to complete the sandwich assay method. The AuNPs possesses high fluorescence resonance energy transfer (FRET) quenching efficiency and utilized as a FRET reagent, whilst the PAMAM-dendrimers served as a platform to immobilize the CA125 antibody, allowing increased sensitivity and accuracy of the immunosensors. Results indicate the immunosensor can detect an extremely low calculated limit of CA125 when compared to other biosensors, exhibiting extremely high selectivity toward CA125. Furthermore, the

immunosensor successfully achieved selective imaging of these cells (Hamd-Ghadreh et al., 2017).

Progressing with the use of aptamers in diagnosis for OC, Jin and co-workers developed Ag2S quantum dots (QDs) for near-infrared emitting photoluminescence (NIR PL) combined with the aptamer/5-fluorouracil (5-Fu) to produce Ag2S QDs/aptamer/5-Fu (Figure 2.3).

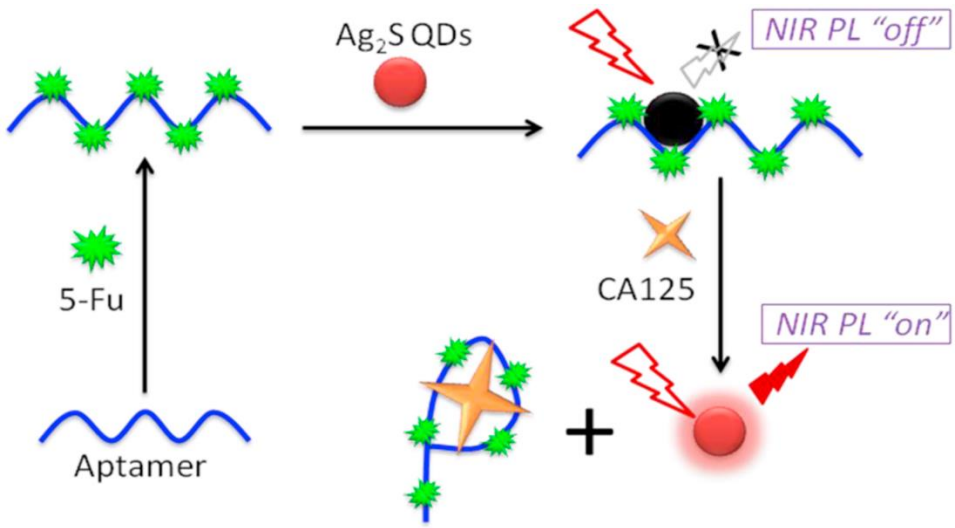

Figure 2.3. Schematic illustration of the fabrication processes of Ag2S QDs/aptamer/5-Fu hybrid-based near-infrared (NIR) photoluminescence (PL) turn-on probe of CA125. (Reprinted from (Jin et al., 2017) with permission from Biosensors and Bioelectronics)

Results display sensitive NIR PL responses of the probe to the CA125 antigen. Furthermore, the system exhibits high performance in human body fluids including human serum, urine, and gastric juice, in addition to high detection recoveries (Jin et al., 2017).

An alternative avenue for OC targeting is the heat shock protein 10 (HSP10). This protein is over-expressed in tissues surrounding the ovaries. HSP10 is implicated in tumour formation due to its role in suppressing T cell activation, allowing the tumour to escape immune surveillance. In addition, HSP10 suppresses apoptosis of malignant cells, thus gaining much recent interest as potential biomarker for early OC detection and clinical

diagnosis (Akoyl et al., 2006; Chen et al., 2016). Chen and co-workers aimed to detect this protein by developing a new protocol for the silane-based surface modification of quartz substrates for the immobilization of hexa-histidine-tagged HSP10, to determine the interaction between the HSP10 protein and a novel DNA aptamer, MND-38, selected through SELEX using electromagnetic piezoelectric acoustic sensor (EMPAS). In this paper, researchers conducted proof of concept work, to show that this method can successfully detect HSP10. This study made use of an electromagnetic piezoelectric acoustic sensor (EMPAS), which was able to achieve extremely high sensitivity. The EMPAS is designed to detect the resonance frequency generated from an electrode-less quartz disc. Researchers in this study were aware of the specificity of the aptamer used, i.e., the MND-38 aptamer via the selection process through SELEX, which was confirmed through DNA–Native PAGE analyses when HSP10 was introduced to the aptamer solution. With properly modified quartz surfaces, aptamer was injected over the surface using the EMPAS. The measurements highlighted that there was a specific interaction between the protein and aptamer when the protein was on the surface. The investigators concluded that the EMPAS is not a gravimetric device but encompasses a myriad of surface interactions and phenomena that may be questionable for solely quantitative measurements of the protein, and thus may be valuable for qualitative tests to initially confirm when complex interactions are occurring. Furthermore, researchers highlighted the need to investigate the nonspecific binding of the aptamer and the necessity to further optimize the system before testing in clinical samples. It was shown the applicability of this surface in acoustic wave sensors for detecting aptamer binding and allows for future applications towards other His-tagged proteins and corresponding binding partners (Chen et al., 2016). This study highlights the significant role aptamers play in HSP10 detection, as antibodies are difficult to produce against this protein, it also highlights the complexity of early OC diagnosis interventions, with potential for greater developments in the field.

2.3.2.2. Aptamers in Ovarian Cancer Treatment

Pi and co-workers (Pi et al., 2017) recently developed a novel a nucleic acid-based NP to deliver doxorubicin (DOX) to the over-expressed Annexin A2 protein by incorporating an Annexin A2 A phosphorothioate-modified DNA aptamer, Endo28. The system utilizes a highly robust and thermostable phi 29 pRNA three-way junction (3WJ) as a platform to

develop the new therapeutic NPs (Pi et al., 2017; Kanlikilicer et al., 2017; Binzel et al., 2014; Shu et al., 2011). Result demonstrate that the Endo28-3WJ possesses stronger binding affinity to IGROV-1 (71.2 %) than to SKOV3 (51.7 %) (Annexin A2 positive control), with exceptionally low affinity for HEK29T (17.3%) (Annexin A2 negative control). These results correlate to the level of Annexin A2 expressions found within the cells (Somasundram et al., 2010; Lokman et al., 2013). *In vivo* biodistribution studies show accumulation of the NPs in tumours, in contrast to healthy tissue. This comprehensive study highlights the promising targeting capabilities of this aptamer for future OC research and treatment.

The receptor tyrosine kinase AXL proves to be a promising molecular target to investigate due to its role in cancer cell survival, invasion, and metastasis. AXL is over-expressed in ovarian tumours in contrast to healthy ovarian epithelium. Kanlikilicer and co-workers investigated the potential for the AXL aptamer to therapeutically inhibit tumour formation *in vitro* and *in vivo*. The AXL aptamer proved to be highly stable, exhibiting good resistance to nucleases and high affinity for AXL with no aptamer localization in non-AXL expressing cells. Therapeutically, the aptamer inhibits AXL activity and reduces OC cell proliferation, further impairing migration, and invasion of OC cells, resulting in inhibition of tumour growth and I.p metastatic nodules.

Despite the above reviewed studies, the recent use of aptamers for treatment purposes has been limited since 2016 (Pi et al., 2017; Kanlikilicer et al., 2017), as compared to the use of aptamers in pancreatic cancer (PC). Recently, much work on aptamers in PC treatment has shown promising advances (Yoon et al., 2017; Yoon et al., 2016; Yoon et al., 2017). Is it therefore possible to apply the techniques employed for the aptamer mediated treatment in PC to OC? This is an important question to consider for the future developments of aptamers in OC treatment (Sharma et al., 2017).

2.3.3. Folate Receptor Targeting in Ovaria Cancer

Folic acid (FA) has become increasingly significant as a targeting moiety for the localized delivery of chemotherapeutics to specific cancer tissues and sites of inflammation (Low et al., 2008). FA is an atypical cell-targeting agent which possesses high affinity for its

corresponding over-expressed folate receptor (FR) (Feng et al.m 2013). A study conducted by Garin-Chesa and co-workers (Garin-Chesa at el., 1993) to determine the frequency of FR over-expression in various tumours revealed that 52 out of 56 OC cases presented with FR over-expression (Sudimack et al., 2000). Extensive studies on the FR (Lv et al., 2017) enabled researchers to conjugate antineoplastic drugs, antisense oligonucleotides, protein, toxins, and imaging agents with FA for targeting purposes (Quintana et al., 2002).

Recently, Lv and co-workers (Lv et al., 2017) developed a Capsaicin (CAP)-loaded FA-conjugated lipid NP for OC intervention. Results confirmed a higher cellular uptake was obtained in the FA targeting system when compared to the non-targeting system, in addition to higher toxic effects and cellular apoptosis. FA conjugation was further employed for the precision delivery of DOX and docetaxel (DTX)-conjugated poly (lactic acid)-poly (ethylene glycol)-folate (PLA-PEG-FOL) based polymeric micelles for controlled release OC combination therapy, as a strategy to reduce resistance. *In vitro* cellular uptake studies of the polymeric micelles revealed that DOX, FA-conjugated DOX and non-targeting PLA-PEG micelles were 52%, 32.8% and 16.8%, respectively. Cytotoxicity results revealed that both DTX and DOX targeted polymeric micelles exhibit greater cytotoxic effects in contrast to the non-targeting micelles. These two polymeric micelles display promising outcomes in targeting the over-expressed FR and desirable drug release in acidic environments, to produce an improved *in vitro* cytotoxic performance to circumvent resistance (Hami et al., 2017).

Alberti and co-workers demonstrated a novel theranostic polylactic and polyglycolic acid (PLGA) NP to deliver boron (B)-curcumin complex (RbCur) and gadolinium (Gd) complex into tumour cells for B and Gd neutron capture therapy (NCT), whilst Gd allowed for magnetic resonance imaging (MRI). Results confirmed that the FA-targeted NPs displayed stronger affinities for the FR, with negligible cell binding for the non-targeted NPs (Alberti et al., 2017). Furthermore, cells treated with PLGA-NP-FA irradiated with neutrons (Gd-BNCT-group) show lower percentage of viable cells in contrast to the cells treated with the currently clinical investigated BNCT drug l-para-boronophenylalanine (BPA) (BNCT group). This indicates that the presence of Gd in conjunction with FA conjugation produces successful anticancer outcomes when compared to sole BNCT. In

addition, curcumin benefited the system by decreasing cell proliferation. The system effectively measured Gd and B concentrations indirectly by MRI, opening new perspectives for neutron capture applications (Alberti et al., 2017).

2.4. Is the Active Targeting Avenue Alone a Way Forward for Cancer Nanomedicines?

The active targeting avenue presents recent success in cancer therapies but faces several crucial limitations. Challenges, such as heterogeneous blood flow, large intervascular distances, long interstitial path lengths, slow transportation rates and differences between tumour structure and composition of various cancers, hinder their direct tumour targeting abilities. In addition, upon exit from blood vessels, these targeting systems usually bind to cells they first interact with on the periphery, possibly healthy cells, hence the need for targeting systems to not solely target over-expressed receptors but rather receptors that are in cancerous tissue specifically (Chauhan et al., 2013). The ultimate cancer nanomedicine should be formulated such that targeting, distribution and anti-cancer performance is independent of the inherent bodily processes. To achieve this, a complete understanding of tumour microenvironment and vasculature in addition to the route the nanosystem must travel is necessary. To this end, sole active targeting approaches may require additional aid of passive targeting interventions as a combination strategy for cancer drug delivery.

2.5. Nanocarrier Based Delivery in OC

Nanocarriers are extensively employed in the pharmaceutical industry for their biomedical applications including imaging, diagnosis, and delivery of chemotherapeutic (Torchilin et al., Sivakumar et al., 2009; Wang et al., Sharma et al., 2015; Goethals et al., 2013; Campbell et al., 2011; Shukla et al., 2012). Their versatility ensures an optimal drug release, maximizing therapeutic efficacy. Various carriers used for drug delivery include polymers, quantum dots, nanospheres, nanogels, liposomes, micelles, and the more recent magnetic NPs (Saad et al., 2008; Haiba et al., 2016). Nanocarriers create an avenue to overcome various limitations, e.g., increasing the bio distribution of potent drugs at the target site whilst minimizing system exposure (Smetsers et al., 2004).

Furthermore, these carriers provide rate-controlled drug delivery, allowing predictable concentrations and clearances (Jia et al., 2013). In cancer, NPs are exploited, as they ensure increased penetration of blood capillaries in cancerous tissue by enhanced permeation and retention (EPR) resulting in increased drug concentrations, in addition to providing an ideal platform for active and passive targeting interventions (Saraswathy et al., 2013; Safari et al., 2014; Ramasamy et al., 2014; Nicolas et al., 2013).

Many reviews have previously highlighted the nanocarriers employed in OC (Rhoda et al., 2015; Arora et al., 2016). In this updated review, we will focus specifically on the most recent and novel nanocarrier based systems targeting OC.

2.5.1 Nanocarriers for the Delivery of siRNAs to OC

siRNAs play a key role in drug resistant OC due to their ability to disrupt cellular multiple drug resistant (MDR) pathways by silencing the expression of relevant genes including MDR genes and over-expressed receptors (He at al., 2016). Their discovery has revolutionized the field of gene-based therapies, providing greater opportunities for successful cancer treatments (Guo et al., 2011). The effective delivery of siRNAs relies heavily on the appropriate nanocarrier system as native siRNAs following systemic administration fail to exhibit features required for movement through cellular membranes. Native siRNAs are also susceptible to degradation by serum nucleases and rapid renal clearance (Ozpolat et al., 2010). Despite previous success of nanosystems to increase the therapeutic potential of siRNAs, the optimal delivery of siRNAs requires a more “tailor made” approach to overcome these limitations (Yang et al., 2015; He at al., 2016; Huang et al., 2016). He and co-workers (He at al., 2016) produced a novel core-shell nanoscale coordination polymer (NCP) NP for the combination delivery of cisplatin and cisplatin plus gemcitabine (in the core), whilst siRNA resided in the lipid layer (Figure 2.4). This system is intended to down regulate the MDR gene expression in drug resistant OC.

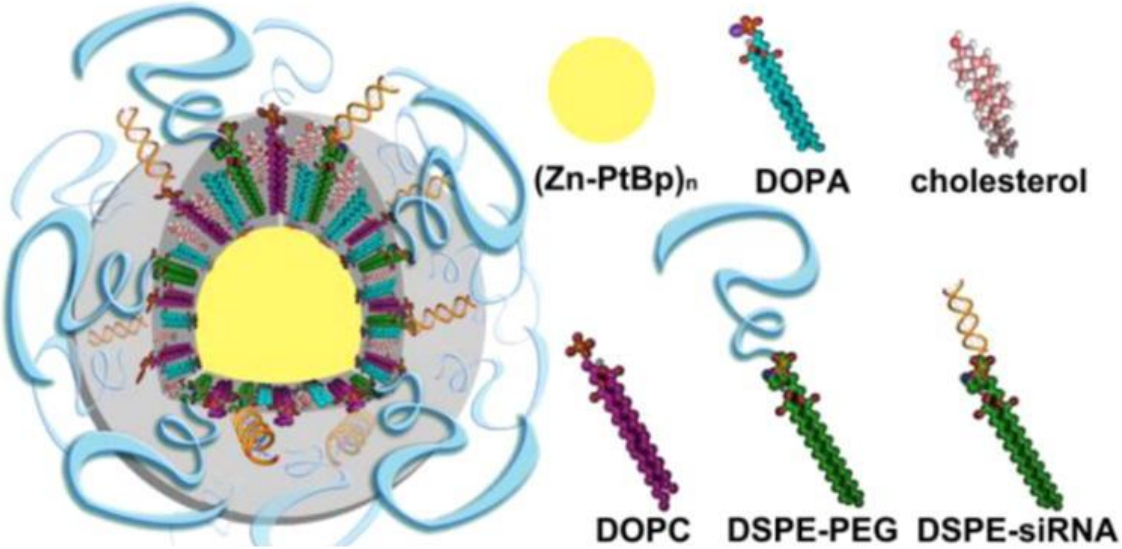

Figure 2.4. Schematic representation of NCP-1/siRNAs carrying cisplatin in the solid core and siRNAs in the lipid shell. Reprinted (adapted) with permission from (He at al., 2016). Copyright (2016) American Chemical Society.

The smart release of the siRNAs exploited the addition of cisplatin, in contrast to the conventional cationic excipients that are generally required for the effective endosomal escape of siRNA. It was hypothesized in the study that the carbon dioxide (CO2) obtained from cisplatin will disrupt the membranes facilitating siRNA release. This was confirmed by research using confocal laser scanning microscopy (CLSM). The system further displayed enhanced blood circulation of siRNA to provide long lasting tumour eradication in addition to increased tumour uptake. Overall, effective therapy was obtained in mouse models with cisplatin resistance OC (He at al., 2016). Thus, this system offers a promising direction for the delivery of siRNAs to cancer.

HuR is a ubiquitous protein that is highly expressed in OC and correlates to poor prognosis (Huang et al., 2014). Huang and co-workers (Huang et al., 2014) employed a novel derivatized DNA dendrimer (3DNA) as a nanocarrier for the effective delivery of siHuR (combination of siRNAs against HuR) to target the HuR in nude mice. Targeting was achieved via the use of FA conjugation to produce the FA-3DNA-siHuR system. The conjugation of siHuR to 3DNA retained its ability to suppress HuR expression, following the *in vitro* transfection of A2780 cells. Therapeutic efficacy was studied in OC mouse

models indicating suppression of tumour growth, although not significant, and an increase in survival times for mice. In addition, the FA targeting system improved both efficacy and life span outcomes in contrast to the non-targeting system. It was concluded from the study that the system employed systemically administered siHuR to inhibit HuR expression to achieve desirable therapeutic outcomes (Huang et al., 2016). Table 2.1 provides a summary of the siRNAs employed in OC intervention.

Table 2.1. Presenting the various nanocarriers involved in siRNA delivery to target OC and the systems response.

Drug	Targeting moiety	Nanocarrier	Response	Reference
Cisplatin, GEM and siRNA	NA	Lipid based nanocarrier, with a self - assembled core-shell NCP	- NCP-siRNAs NPs efficiently down regulated the Bcl-2 gene expression in SKOV-3 and A2780/CDDP cells by >70%. - NCP-siRNAs NPs successfully eradicated tumours causing 100% survival in mouse models for > 90 days. - 92 days after tumour inoculation, NCP-1/siRNAs treated mice were sacrificed with no evidence of tumours.	(Huang et al., 2016)
siRNA	FA to target HuR Over-expression	Derivatized DNA dendrimer	- When Mice were injected twice weekly with FA-3DNA-siHuR for 4 weeks, the median survival of FA-3DNA-siHuR– treated mice were approximately 1.5	(Huang et al., 2016)

			times longer than the controls.	
Co-delivery of cisplatin and siRNAs	NA	NMOFs	- The cisplatin IC_{50} values of free cisplatin, UiO-Cis, pooled siRNAs/UiO-Cis, free cisplatin plus free pooled siRNAs, and free cisplatin plus pooled siRNAs/UiO were 53.9 ± 4.7, 53.2 ± 4.4, 4.7 ± 1.8, 45.1 ± 7.0, and 6.6 ± 0.3 μM, respectively. - Co-delivering of pooled siRNAs and cisplatin employing NMOFs decreased the IC_{50} value > 11- fold, in contrast to free cisplatin and UiO-Cis.	(He at al., 2014)
PTX and siRNA	LHRH peptide	Nanoscale PPI dendrimer	- LHRH-PPI-siRNA and LHRH-PPI-PTX combination enhanced the cytotoxicity of the conjugate. - The viability of ascitic cells were decreased almost 10-fold in comparison to the control cells, more than 5-fold when compared with free PTX and more than 2-fold when compared with non-	(Shah et al., 2013)

			targeted PPI-PTX-siRNA complex. - The combination caused almost complete tumour shrinkage within 28-days.	
siRNA	HA-NP system targeting CD44 receptors	HA based self-assembling NPs	- Tumour volume of mice treated with HA-PEG/MDR1 siRNAs targeted NPs was approximately 3-fold lower than in mice treated with native PTX.	(Yang et al., 2015)
			- MSNP with siRNAs caused increased cellular accumulation of DOX.	
DOX and siRNA	NA	MSNP	- The IC_{50} value of the siRNA delivering MSNP was approximately 2.5 times lower than the IC_{50} of free Dox or other Dox loaded particles.	(Meng et al., 2010)
			- The highest apoptosis of 77.5% were observed in cells incubated with FA-DOX-Bcl2 siRNA-NPs leading to potent synergistic effects inducing cell apoptosis.	
Blc2-siRNA and DOX	FA-targeting over-expressed FR	copolymer self-assembled cationic micelles		(Zou et al., 2012)
siID4	tandem tumour-penetrating and membrane-translocating peptide to target ID4	TPN	- The tumour burden in mice that received TPN/ siID4 remained low compared to controls, 80% of these recipients survived > 60 days,	(Ren et al., 2012)

			despite treatments stopping at day 50. - No visible tumour lesions in 4 out of 5 TPN/siID4–treated mice occurred indicating tumour regression. - Histological analysis revealed significant reduction in ID4 levels and increased apoptosis in the tumour parenchyma of mice treated with TPN/siID4.

Abbreviations in the table are defined as follows: NMOFs, nanoscale metal-organic frameworks; GEM, gemcitabine; LHRH, luteinizing hormone-releasing hormone peptide; PPI, polypropylenimine; PTX, paclitaxel; CD44, Cluster of differentiation 44; HA-NP, Hyaluronan Nanoparticle; DOX, Doxorubicin; MSNP, mesoporous silica nanoparticles; siID4, ID4-specific siRNA; TPN, tumour penetrating nanocomplex.

2.5.2. Nanocarrier for the Delivery of OC Drugs

Hydrophobic chemotherapeutics have been incorporated into advanced self-assembling amphiphilic NPs. The hydrophobic region acts as a reservoir to house the poorly soluble drug, whilst the hydrophilic region offers protection against the removal by the reticuloendothelial system. Employing a pH stimuli responsive linker to the drug enables release at specific conditions and predetermined rates, a factor necessary for control release purposes (Fleige et al., 2012; Torchilin et al., 2009). Theranostic approaches provide the perfect combination for treatment and detection and recent work conducted by Lin and co-workers (Lin et al., 2016) intended to produce such a system (Xie et al., 2010).

Hyaluronic acid (HA) NPs were employed as self-assembling nanocarriers for the targeted delivery of DOX coupled with a NIR dye for theranostic application in OC. LHRH

served as targeting peptide to actively target the over-expressed corresponding LHRH receptor (Engels et al., 2012; Choi et al., 2012). Controlled drug release was achieved via a stimuli responsive spacer, using cis aconityl linkage and a disulphide bond that possess pH sensitive and redox properties, respectively. The cis aconityl linkage allowed cleavage of DOX in acidic environments (pH 7.5–5.5) and the disulphide linkage enhanced its stability at low extracellular glutathione concentrations whilst at high glutathione concentrations facilitated drug release (Lin et al., 2016). Cytotoxicity studies revealed that high uptake and therapeutic activity was obtained in cell lines over-expressing the LHRH receptors, with lower toxic effects in non-receptor expressing cell lines. Furthermore, the LHRH-conjugated NPs possess desirable tumour imaging capabilities and an excellent anticancer effect, such that almost 30% of original tumour size was reduced in 20 days (Lin et al., 2016). This “Environmentally sensitive” system exhibits excellent performance in orthotropic ovarian tumour models possessing greater efficacy over conventional drug delivery systems due to its stimuli responsive nature (Liu et al., 2014).

Kulhari and co-workers successfully improved the delivery of Gemcitabine hydrochloride (GEM) towards OC. GEM is a water soluble, clinically approved anticancer drug that encompasses limitations including short plasma half-life, degradation in body fluids and severe haematological side effects, rendering the drug unsuitable for intravenous injection. To achieve enhanced delivery, a polymeric drug delivery system synthesized using PLGA NPs was developed. Cyclic RGDfK (cRGDfK), a five-amino acid peptide, was selected as an active targeting ligand, due to its favourable characteristics including high stability and specificity for the over-expressed αvβ3 integrin receptors observed in OC (Danhier et al., 2012; Landen et al., 2008; Lossner et al., 2008). Following synthesis and characterization, results demonstrate a narrow size distribution, high encapsulation efficiency, sustained drug release, increased biocompatibility, and efficient uptake of the nanoconjugates were obtained. Furthermore, the anti-proliferative activity of GEM was enhanced via intracellular processes including reduction of mitochondrial membrane potential, increased intracellular reactive oxygen species levels and promotion of apoptosis. Following blood compatibility studies, encapsulated GEM was able to overcome the haemolysis effect to a considerable extent over native GEM as direct contact to RBCs was reduced, a highly successful outcome for the future safe clinical use

of GEM (Kulhari et al., 2016). Table 2.2 summarizes the Nanocarriers involved in delivery of cancer therapeutics to OC.

Table 2.2. Presenting various nanocarriers involved in drug delivery for OC and the systems response.

Drug	Targeting moiety	Nanocarrier	Response	Ref
DOX	FA to target FR	pH-sensitive micelles	- The micelle formulation effectively decreased the growth of existing MDR tumours in mice for at least 50 days by three *i.v.* injections at a 3-day interval at a dose of 10 mg DOX/kg. - Tumour growth rate of the micelle group was delayed when compared with the free DOX group.	(Kim et al., 2009)
PTX	OA02 peptide	Micellar NPs formed using PEG-block-dendritic CA copolymers (PTX-OA02-NPs)	- PTX-OA02-NPs displayed superior tumour growth inhibition than Taxol®, at equivalent PTX dose of 10 mg/kg. - The median survival time of mice in the group of PBS control, Taxol®,	(Xiao et al., 2012)

			PTX-NPs (10, 30 mg/kg), and PTX-OA02-NPs (10, 30 mg/kg) were 20, 27, 29, 69, 32, and 95 days, respectively.	
PTX and CDDP	NA	Biodegradable, biocompatible polypeptide-based polymeric micelles	- MTT assays on A2780 cells revealed IC_{50} values Free CDDP is 1.5 in contrast to (CDDP + PTX)/cl-micelles of 0.14 exhibiting superior killing properties.	(Desale et al., 2013)
DOX	TATp	PEG-Hz-PE conjugated immunoliposomes	- *In vitro* cytotoxicity revealed the lowest cell viability was obtained Lipodox-TATp in both SKOV-3 sensitive and SKOV-3 resistant cells yielding IC_{50} values of 0.36 and 3.12 respectively in contrast to lipodox yielding IC_{50} values of 6.25 and 100.00 respectively.	(Apte et al., 2014)
Co-delivery of PTX and curcumin	TF to target resistant OC spheroids and *in vivo* tumours	PEG-PE based polymeric micelles	- The TF-targeted PTX system displayed and enhanced micelle penetration into spheroids reducing cell viability	(Sarisozen et al., 2014)

			to 35.3±2.7% at 6.9µM of micellar PTX concentrations when compared to free PTX at 80±22% at 6.9µM dosage.	
GEM	cRGDfK peptide targeting αvβ3 integrin receptors	PLGA based NPs	- The IC_{50} values after 48 hours of incubation in SKOV3 cells for GEM, GEM-NPs and GEM-RGDfK-NPs were 0.572 ± 0.013 µg/ml, 0.148 ± 0.01 µg/mL and 0.034 ± 0.004 µg/mL respectively. - The improved anticancer efficacy may be attributed to the targeting properties of the peptide.	(Kulhari et al., 2016)
DOX coupled with a NIR dye for therano stic applicat ion	LHRH	self-assembling HA NPs,	- Results demonstrate that LHRH-conjugated NPs possess a desirable tumour imaging capability and an excellent anticancer effect, such that almost 30% of the original tumour size was reduced in 20 days.	(Lin et al., 2016)

Abbreviations in the table are defined as follows: PTX, paclitaxel; i.v., intravenous; PEG, polyethylene glycol; CA, cholic acid; CDDP, cis-dichlorodiamminoplatinum; TATp,

transactivator of transcription peptide; PEG-Hz-PE, Polyethylene glycol– Hydrazine–phosphatidylethanolamine; TF, Transferrin; PEG-PE, polyethylene glycol phosphatidylethanolamine; GEM, Gemcitabine hydrochloride, PLGA, poly (D,L-lactic-co-glycolic) acid.

2.6. What Happens to These Nanosystems Beyond the Realms of Research?

Despite the recent advances in nanocarriers mentioned in this review, the goal of anticancer nanomedicines research should ultimately intend to produce a product that can be clinically beneficial. How big or small is the gap between the latest and cutting-edge research and final delivery to patients? A comprehensive review recently written by Lisa Bregoli and co-authors highlighted the nanocarriers, e.g., liposomes, micellular and polymeric drug delivery systems, that have made it to clinical approval as well as the nanosystems undergoing clinical trials. Unfortunately, the majority of the research rarely makes it to clinical approval. In addition, the movement of nanosystems to clinical use is much lower compared to native small molecule drugs.

The paper highlights the major scientific aspects that hinders the movement of nanomedicines to commercialization, such aspects can be summarized as follows: (1) the complexity of the cancer microenvironment makes understanding of the *in vivo* distribution of NPs difficult, which is a problem associated with both active and passive targeting; (2) safety and toxicity concerns, and the need to establish better models to determine safety that will best mimic human like behaviour; (3) the lack of physicochemical characterization of NPs and its surface ligation, which is of paramount importance for correlating biological toxicological consequences and biological responses; (4) large scale manufacturing with high batch to batch uniformity to maintain high product quality is necessary, with concerns related to the lack of appropriate methods to test impurities, contamination and aggregation; and (5) the quantification of the API encapsulated within this nanosystems to ascertain dosage requirements (Bregoli et al., 2016). To this end, the translating of well working nanomedicines from the literature, to meeting all requirements necessary for commercialization encompasses a great deal of complexity.

Cheng and co-workers (Cheng et al., 2016) highlighted that aspects such as safety, environmental and regulatory aspects are still key issues hindering the forward movement of recent literature to market. Further describing how regulatory requirements, environmental sustainability across product lifecycle, scientific information, safety of manufacturing materials, scientific uncertainties and scientific risks collectively hinder the movement of these research interventions to market. In conclusion, the majority of the systems developed in the literature rarely make it to market as the gap between current therapy developments and hospital treatment remains evident. The development cycle of nanomedicines should ideally cover novel, innovative and cutting-edge technological advances whilst not neglecting its potential fate in hospital use, employing pre-formulation approaches that ensure its future clinical use. Nevertheless, it is highly appreciated that producing novel research is a challenging task with further complexity involved for commercialization.

2.7. Glycosaminoglycans as a Potential Molecular Target to Stop the Progression of OC

In the past, most OC targeting initiatives focused primarily towards the sensitive and highly specific biomarkers on the tumour cells, including the currently exploited CA125 glycoprotein (Pothacharoen et al., 2006). Most OC initiatives address components such as the cell surface (glycol), proteins and over-expressed receptors, neglecting the potential of the tumour cell surroundings (extracellular matrix). This especially applies for the information-dense class of glycosaminoglycans (GAGs) (Afratis et al., 2012).

The ECM forms a vital component of cells and vascular biology. It is responsible for structure and stability (Davis et al., 2005). The ECM is a critical environmental determinant of tumour cell behaviour. The matrix serves as a scaffold for the tumour cells to adhere, migrate and proliferate and allows interactions with cellular receptors, growth factors as well as cytokines (Afratis et al., 2012; Engels et al., 2012).

In healthy individuals, proteoglycans (PGs) are present within ECM. PGs are vastly anionic macromolecules that are particularly important in cells as they are responsible for maintaining cellular integrity and function (Asimakopoulou et al., 2008). Core proteins and

unbranched polysaccharides covalently bind to form PGs; these polysaccharides are termed GAGs (Valcarcel et al., 2017). Based on the monosaccharides and their sulphation patterns, various groups of GAGs occur, including chondroitin sulphate (CS), dermatan sulphate (DS), heparin Sulphate (HS), keratin sulphate and HA (Afratis et al., 2012; Pradeep et al., 2016). Furthermore, these GAGs are implicated in the process of carcinogenesis, including tumour growth, migration, invasion, metastasis, and pathological angiogenesis, making them an attractive class of sugars to target (Afratis et al., 2012).

2.7.1. Chondroitin Sulphate as a Molecular Target

CS is a negatively charged water soluble polysaccharide consisting of repeated units of D-glucuronic acid and D-N acetyl galactosamine. CS can be sulphated at various positions, i.e., C-4 and/or C-6 or C-2 of the N-acetylgalactosamine and the glucuronic acid moiety, respectively [Asimakkopoulou et l., 2008]. CS differentiates into five isoforms based on the specific sulphation pattern, giving rise to molecules such as CS-A (GlcA-GalNAc-4-sulphate), CS-C (GlcA-Gal-NAc-6-O-sulphate), CS-D [GlcA(2-O-sulphate)–GalNAc(6-O-sulphate)], CS-E (GlcA-GalNAc-(4,6)-O-disulphate) and CS-B (DS) [(IdoA (2-O-sulphate)–GalNAc(6-O-sulphate)]. These sulphation patterns dictate specific interactions with various growth factor including Fibroblast growth factor (FGF), hepatocyte growth factor (HGF), Transforming growth factor (TGF) and vascular endothelial growth factor (VEGF) (Vallen et al., 2014). In healthy cells chondroitin sulphate proteoglycans (CSPGs) have been identified to control aspects of cellular behaviour and function (Prinz et al., 2014). As early as 2003, it was well recognized that these PGs and their carbohydrate residues mediate many tumour cell functions; however, their exact roles in cancer metastasis was poorly established. Since then, recent discoveries and advances reduce this knowledge gap and widen our understanding of GAGs and its contribution to OC.

2.7.2. The Role of CS in OC

The implication of CS-E to OC has been highlighted in a paper that was previously published from our group (Pradeep et al., 2016) and is summarized in Table 2.3. This

section of the article aims to further motivate the potential of CS-E as a potent molecular target. Many studies have reported the elevation of CSPGs levels in tumours, compared to non-malignant tissue. Some relationships have been proposed between tumour GAGs and tumour-cell properties (Adany et al., 1990; Isogai et al., 1996). Elevated CS-E levels have been reported in the ECM of OC, particularly in the stromal region, and correlate to the aggressiveness of tumours (Pradeep et al., 2016; Van Der Steen et al., 2016). This stromal component is responsible for the vicious tumour progression and metastasis of OC (Vallen et al., 2014).

Table 2.3. The correlation of CS-E to OC, summarising and supporting CS-E as an important biomarker for OC diagnosis as well as a powerful molecular target for OC treatment.

Implication in OC	References
CS-E displays strong up regulation in primary ovarian carcinomas which is responsible for the poor prognostic parameters, including high tumour grade and advanced FIGO stages.	(Pradeep et al., 2016; Vallen et al., 2012)
CS-E can strongly bind to VEGF which is the most important pro- angiogenic stimulator. Furthermore, high CS-E levels correlate to high VEGF, causing further neo-vascularization development in the tumour stroma causing ovarian spheroid formation. This spheroid formation is associated with the highly aggressive and invasive characteristics of OC.	(Pradeep et al., 2016; Vallen et al., 2014; Luis et al., 2017)
The elevated CS-E aids the adhesion of tumours as it is responsible for increasing the adhesive properties of adhesion molecules N-cadherin and E- cadherin. In addition, integrins also play a role in adhesion as they have the ability to interact directly with CS chains, blocking of integrin receptors result in inhibition of OC cell adhesion.	(Pradeep et al., 2016; Vallen et al., 2014)
The over-expression of CS-E improves the adhesive properties of tumour cells.	(Pradeep et al., 2016)
CS-E is responsible for the invasion and migration of tumours. MMPs is a group of enzymes responsible for OC progression.	(Vallen et al., 2014)

The activation and regulation are strongly influenced by CS, Furthermore CS-E can interact with MPPs such as pro-MMP7, contributing to the activation and metastasis of tumour cells.	
CS-E expression is predominantly seen in the stromal compartment of both primary ovarian carcinomas and metastasis.	(Vallen et al., 2014)
The expression of mRNA for GalNAc4S-6ST, an enzyme which is responsible for the biosynthesis of CS-E, is up-regulated in OC.	(Pradeep et al., 2016; ten Dam et al., 2007)
CHST15, the only sulfotransferase responsible for biosynthesis of CS-E presents an altered transcription pattern in OC, furthermore increased CHST15 levels lead to increased CS-E levels.	(Vallen et al., 2014; ten Dam et al., 2007)
CS has shown to be involved tumour cell proliferation, growth, angiogenesis, adhesion, migration, invasion, and survival of OC tumours.	(Vallen et al., 2014)

Abbreviations in the table are defined as follows: VEGF, Vascular endothelial growth factor; MMPs, Metalloproteinases; GalNAc4S-6ST, Gal-NAc-4-sulphate-6-O-sulfotransferase. Based on the above evidence, CS-E proves to be a major culprit in OC development and displays promising potentials for targeting. By inhibiting CS-E activity employing drug therapy, offers a new perspective for clinical treatment and diagnosis.

2.7.3. Targeting Chondroitin Sulphate-E

Despite previous targeting of cancer cells, the positive impact of tumour-cell targeting vs. non-targeting mechanisms proves unsatisfactory (Raave et al., 2015; Lammers et l., 2012). Most of these studies overlook the cancer ECM as a promising alternative for drug targeting. The largely neglected ECM provides several potential molecular targets for precision therapy of chemotherapeutics (van der Steen et al., 2017). Recent studies demonstrate that the delivery of anti-cancer drugs to the tumour stroma significantly eliminates cells and their micro-environment *in vivo* (Liang et al., 2015; Yasunaga et al., 2011). Furthermore, cellular target expressions may change over time resulting in resistance, posing additional challenges (van der Steen et al., 2017. Therefore, more

focus on targeting the ECM may be an important breakthrough for OC (van der Steen et al., 2017). Recently, CS-E was established to be over-expressed in OC ECM and made novel molecular targets for anti-cancer therapy (Pradeep et al., 2016; Watanabe et al., 2015).

In the past, Yamagata and co-workers (Yamataga et al.,1987), Smetsers and co-workers (Smetsers et al., 2004) and ten Dam and co-workers (ten Dam et al., 2007) established the ability of the MO-225, IO3D9 and GD3G7 antibodies to recognize CS-E respectively (Table 2.4). Problems associated with these antibodies were recognized. Despite the ability of the GD3G7 antibody to bind to CS-E, the antibody also displays specificity to CS-A and CS-H abundant H-units [IdoA-1-3GalNAc (4S, 6S)] after analysis using phage display technology directed against rat embryo (ten Dam et al., 2007). IO3D9 possesses weak binding affinities for CS-A or CS-C. Thus, in the past, no antibodies recognize CS-E specifically, increasing the demand for a CS-E specific antibody. Table 2.4 summarizes the various antibodies that target CS.

Table 2.4. Various antibodies used to target their respective CS isomers.

Antibody	Specificity	Target selectivity of CS isomer	Ref
GD3G7 antibody		antibody GD3G7 reacted strongly with CS-E, rich in GalNAc4S6S disaccharide units. - minor reactivity with CS-A. - no reactivity was observed with DS, CS-C, CS-D, and HS.	(ten Dam et al., 2007)
The mAb 473HD	DSD	- recognizes the characteristic CS structure named the DSD-1 epitope that contains the D-unit.	(ten Dam et al., 2007)
mAb CS-56		- reacts with CS-A and CS-C, - also reacts preferentially with CS-D - reacts weakly with CS-C, no reactivity with any other CS variants	(ten Dam et al., 2007)

mAb MO-225		- reacts strongly with CS-D, - moderately with CS-C and CS-E, - weakly with CS-A	(Yamatag a et al.,1987)
473HD	CS-D	- reacted with the hexa- and larger oligosaccharide fractions derived from CS-D	(Yamatag a et al.,1987)
IO3D9		- reacts with CS-C and weakly with CS-A - strong reactivity with CSE compared to CSA or CSC	(Smetsers et al., 2004)
IO3H10		- reacts with CSC - reacts with CSA	(Smetsers et al., 2004)
IO3H12		- reacts with CSC - reacts with CSA	(Smetsers et al., 2004)
12C and E-18H	CS-E specific	- no reactivity with any other CS isomer	(Watanab e et al., 2015)
GD3A11	CS-E specific	- no reactivity is observed with other immobilized GAGs such CS-A, CS-B, CS-C, CS-D, HS, and heparin	(Van Der Steen et al., 2016)

In 2015, Watanabe and co-workers discovered two novel CS-E specific monoclonal antibodies,E-12C and E-18H. These antibodies were obtained by digesting CS-E fractions rich in the E subunits with hyaluronidase, susceptible reacting with low sulphation moieties of the CS molecule. To rule out cross reactivity between 6-O-sulphated CS-A and DS that possessed 60% of GalNAc (4S, 6S) moieties in their structures, surface plasmon resonance assay with CS-E and CS-A were conducted, suggesting a strong correlation with the molecular weight of CS-E and the E-unit content of 6S-CS-A and providing evidence that these antibodies recognized CS-E specifically. To further verify this, E-12C and E-18H antibodies were reacted with an artificial CSH from DS possessing [IdoA_1-3GalNAc (4S)] resulting in no reacting ability of either antibody, concluding that these antibodies strictly recognize the E-unit [GlcA_1-3GalNAc (4S, 6S)]. Hence, these antibodies can distinguish the structural difference between GlcA

and IdoA in the GAG molecules (Watanabe et al., 2015). An important breakthrough for the future of targeted therapy considerations.

Van der Steen and co-workers recently formulated GD3G7 functionalized lyophilisomes to precisely deliver DOX to the tumour stroma of OC. This was achieved via a two-step approach involving sortase-mediated ligation and bioorthogonal click chemistry (Figure 2.5) (Van Der Steen et al., 2016). *In vitro*, the lyophilisome released a substantial amount of DOX leading to cell death. The lyophilisomes also showed superior cell viability reducing properties and entrapment in contrast to liposomal DOX. Furthermore, the GD3G7-lyophilisomes displayed strong reactivity in CS-E producing cells, in contrast to the non-targeting control. Specificity studies on the GD3G7-lyophilisomes suggest that high affinity for CS-E is obtained, with background signals for other immobilized GAGs. This study highlights the advantage of targeting the ECM, in addition to the niche design of suitable nanocarriers for enhanced anticancer performance (Van Der Steen et al., 2016).

The GD3A11 antibody selected through phage display technology by van der Steen and co-workers were used to investigate the potential of highly sulphated CS (CS-E) and the CSPG versican, as a biomarker in OC. Results revealed that the GD3A11 epitope was minimally expressed in normal organs. Intense expressions were noted in the ECM of different OC subtypes, relative to benign ovarian tumours. The expressions were independent of tumour grade and FIGO stage. Furthermore, no mutational change in methylation status was observed for the CHST15 gene. The GD3A11 antibody showed strong reactivity for CS-E subtype rich in GalNAc4S6S disaccharides (Van Der Steen et al., 2016).

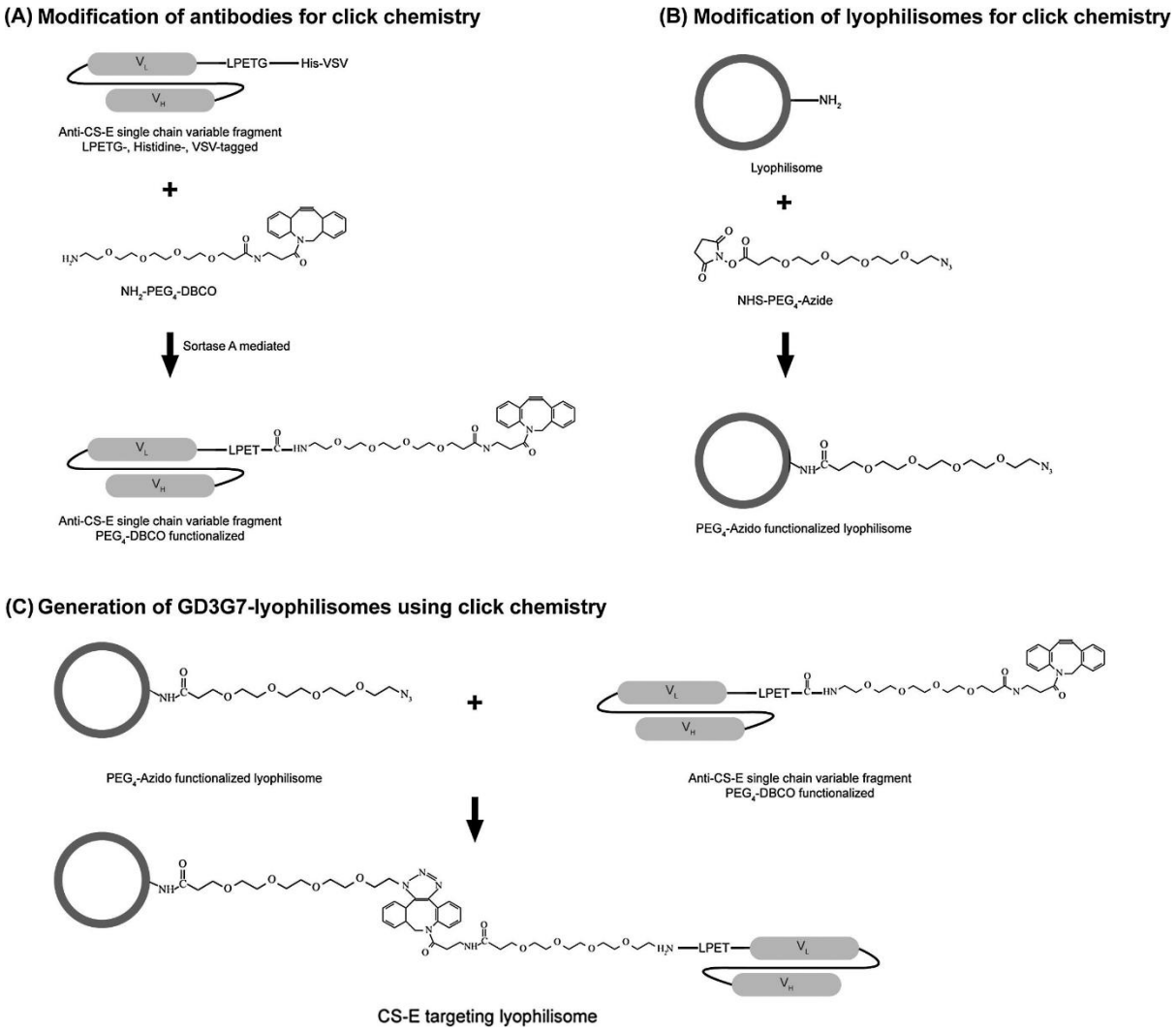

Figure 2.5. Construction of cancer targeting lyophilisomes depicting conjugation between albumin based lyophilisomes and GD3G7 antibodies reactive with CS-E, by applying a two-step approach comprising sortase mediated ligation and click chemistry. (A) LPETG-His-VSV tagged single chain GD3G7 antibodies were modified for click chemistry by introducing amino-PEG4-DBCO through a reaction mediated by Sortase A. (B) Lyophilisomes were functionalized for click chemistry by conjugating PEG4-azide to the primary amine groups of lyophilisomes mediated by *N*hydroxysuccinimide (NHS). (C) Antibody-functionalized lyophilisomes were generated by a click reaction between azido-conjugated lyophilisomes and GD3G7-PEG4-DBCO antibodies.Abbreviations: CS-E, chondroitin sulphate E; DBCO, dibenzylcyclooctyne; VL, light chain variable domain; VH, heavy chain variable domain; SrtA, Sortase A. (Reprinted from (van de Steen et al., 2017) with permission from Elsevier)

2.7.4. Hyaluronan (HA) As a Potential Molecular Target

Similar to other GAGs, HA is an extracellular anionic polysaccharide (Weigel et al., 2007; Delpech et al., 1997). HA is nonsulphated and consists of repeated units of d-glucuronic and *N*-acetylglucosamine (Weigel et al., 2007). HA is ubiquitously expressed in the ECM of various tissues including connective, neural, epithelial, and rapidly growing foetal tissues, in contrast to mature adult tissues (Delpech et al., 1997; Anttila et al., 2000; Yeo et al., 1996). The biosynthesis of HA is facilitated by the plasma membrane protein; HA synthase (HAS), which have several isoenzymes i.e., HAS1, HAS2 and HAS3, with active sites present on the intracellular surface of the membrane (Weigel et al., 2007). HA degradation is induced by a family of six hyaluronidases (Hyal), consisting of Hyal1, Hyal2, Hyal3, Hyal4, PH-20/PSAM1 and the pseudogene HyalP1 (Csoka et al., 2011). HA is responsible for regulating cellular activities such as proliferation, migration, and infiltration (Delpech et al., 1997).

2.7.4.1. The Role of Hyaluronan, CD44, Hyaluronidase and Hyaluronan Synthase in OC

Cluster of differentiation 44 (CD44) is a group of multifunctional trans-membrane acidic glycoproteins. It is particularly important to OC progression as it serves as a surface receptor for HA binding at the N terminus of the extracellular domain (Yang et al., 2015). HA is the primary ligand for CD44 which is over-expressed in OC, causing cell adhesion, migration, invasion, proliferation, and angiogenesis (Yang et al., 2015; Montagner et al., 2015). Furthermore, this binding initiates the direct cross-signalling between different signalling pathways including HER2, Src kinase and ERK. CD44 is proposed to be involved in increasing the motility of cancer cells and differentiation of cancer stem cells (Shah et al., 2013; Bourguignon et al., 2008). Co-over-expression of CD44 and MDR1 and MDR2 proteins correlate to OC progression (Ween et al., 2011). In addition, it has been proposed that CD44 positive OC patients show a remarkably lower survival when compared to negative CD44 tumours (Yang et al., 2015).

Metastatic tumours, including breast tumours are frequently enriched with HA (Herrera-Gayol et al., 2001). HA mediates the action of physical linkage between CD44s and

Her2/ErbB2 tyrosine kinase, which results in the rapid stimulation of ovarian carcinoma cell growth (Bourguignon et al., 1997). When CD44-siRNAs are delivered to ovarian tumours it down regulates CD44 resulting in prevention of HRG-mediated ovarian tumour cell growth and decreased migration (Bourguignon et al., 2007).

Hiltunen and co-workers analysed the HA concentration and Hyal activity in OC. Quantitative HA assays indicate a statistically significant increase in HA levels occurs in malignancies in contrast to normal tissues, functional cysts, borderline and benign tumours. This elevated HA concentration provides an additional growth advantage for primary ovarian tumours. Hyal levels were found higher in borderline and benign epithelial ovarian tumours, as compared with functional cysts but remained low in the malignant epithelial tumours. Despite the large pool of information, unclear results question the defining roles of HA-synthesizing and HA degrading enzymes in OC. With respect to Hyal, it was found that high activity was reported in malignant ovarian tumours compared to endometrial and cervical tumours (Tamakoshi et al., 1997), but reported to be lower in another study when compared to benign and borderline tumours of the ovary (Hiltunen et al., 2002).

Weiss and co-workers performed a study that intended on establishing the expression and clinical role of the various HAS and Hyal enzymes and their splice variants in serous OC effusions. HAS1 mRNA were over-expressed in effusions, in contrast to primary carcinomas and solid metastases, whilst HAS2 mRNA was over-expressed in solid metastases and primary carcinomas compared to effusions and HAS3 mRNA was over-expressed in all subtypes. Similarly, the Hyal family also displayed varying degrees of expression with respect to tumour subtype, however HYAL1 was uniformly absent. The latter finding agrees with the data obtained by Nykopp and co-workers (Nykopp et al., 2009). Furthermore, HAS1 mRNA was over-expressed in pre- compared to post-chemotherapy effusions, with opposite findings for HYAL2-var1 and HYAL3-WT. These data suggest that both enzymes, excluding Hyal1, are present in fluctuating concentrations with respect to tumour type, with HAS1 being associated with the more aggressive subtypes. These results highlight the complexity of these enzymes and their roles in OC (Weiss et al., 2012). The implications of HA and CD44 to OC is further summarized in Table 2.5.

Table 2.5. The relationship of CD44 and HA to OC development.

Implication in OC	References
CD44 is proposed to be involved in increased motility of cancer cells as well as differentiation of cancer stem cells	(Shah et al., 2013)
Co-over-expression of CD44 and multiple drug resistance proteins such as MDR1 and MDR2 correlate to OC progression.	(Ween et al., 2011)
RHAMM and CD44 are vital components for tumour progression.	(Herrera-Gayol et al., 2001)
When HA synthase and HA are down regulated directly using siRNAs it causes impaired cytoskeletal activation and decreased migration of tumours.	(Bourguignon et al., 2007)
HA mediates the physical linkage between CD44s and Her2/ErbB2 tyrosine kinase, which results in the rapid stimulation of ovarian carcinoma cell growth.	(Bourguignon et al., 1997)
Elevated CD44 expression is observed in OC in contrast to benign and borderline tumours.	(Ween et al., 2011)
Elevated HA concentration provides an additional growth advantage of primary ovarian tumours due to the cells ability to produce a HA rich stroma environment.	(Hiltunen et al., 2002)
The high stromal HA levels are significantly associated with poor differentiation, serous histological type, advanced stage, and large primary residual tumour in epithelial OC.	(Anttila et al., 2000)
CD44 expressions correlate with the expression of the drug efflux pump Pgp causing resistance and progression of metastases.	(Shah et al., 2013)
CD44 inhibition following treatment of the CD44 monoclonal antibody inhibits OC cell motility no significant impact on invasion	(Yang et al., 2015)
Anti-CD44 antibody has been shown to decrease the number of total peritoneal OC metastases in mice.	(Yang et al., 2015)

2.7.4.2. Targeting Hyaluronan

HA conjugated to chemotherapeutics, e.g., paclitaxel (PTX), has been introduced previously to enhance the targeting of therapies (Ween et al., 2011; Weiss et al., 2012). Hyaluronic acid (HA) provides favourable traits for the prodrug approach where the drug-HA conjugate becomes active upon release. Several of these conjugates are observed due to HA possessing several functional groups facilitating drug conjugation. In addition, HA has been ligand onto drug loaded NPs for enhanced targeted delivery (Choi et al., 2009). Furthermore, HA offers physiological and biological advantages such as biocompatibility, biodegradability, and non-immunogenicity characteristics. Currently, HA has been employed in various drug delivery systems including nanocomplexes in addition to NPs and drug conjugates as targeting agents (Choi et al., 2012).

Previous *in vivo* anti-tumour activity of HA-based drug delivery systems have been reported. However, recent advances show promising results for HA in OC targeting (Auzenne et al., 2007). Yang and co-workers designed a self-assembling HA-PEI/HA-PEG NP targeting CD44 receptors to deliver MDR1 siRNAs to circumvent MDR OC. Results support the ability of the system to actively target and effectively deliver MDR1 siRNA to MDR OC *in vitro* and *in vivo*. Furthermore HA-PEI/HA-PEG NPs down-regulate the expression of MDR1 and increase MDR cellular sensitivity of PTX. Cellular uptake and encapsulation efficacy of siRNA were also favourable (Yang et al., 2015). This study provides a highly promising perspective for future HA targeting in OC treatment. Montagner and co-workers developed a bioconjugate composed of HA and SN-38, an active metabolite of the FDA approved anticancer drug irinotecan, to target the CD44 receptor in OC. Positive interaction of the bioconjugate and CD44 receptors were obtained in addition to improved therapeutic efficacy compared to native irinotecan. The SN-38 conjugation to HA enhanced the *in vivo* tolerability and broadened the therapeutic application of irinotecan (Montagner et al., 2015). To conclude, this approach offers a promising approach for the loco-regional treatment of OC.

2.8. Conclusions and Outlook

This article intends to highlight the recent advances in OC treatment and diagnosis, introducing the novel and innovative technologies currently developed. The majority of studies exploited various active targeting mechanisms to provide potent, site specific delivery of chemotherapeutics to specific over-expressed molecular targets. Coupling this with a suitable vehicle provides a platform to notably: (1) reduce the toxicity of native drugs towards healthy cells; (2) enhance circulation of native drugs; (3) increase efficacy of treatment; (4) improve cellular uptake of native drugs; and (5) increase spatial localization of drugs at target sites, thus rendering effective clinical responses less reliant on the pharmacological activity of conventional chemotherapeutics. This means of formulation development creates avenues to detour previous limitations of native drug treatment, e.g., insolubility, whilst providing potent therapeutic effects. Studies reviewed in this paper highlighted a collective movement in OC initiatives, with further room for optimization before their application in clinical treatment. The discovery of novel biomarkers and targeting ligands becoming increasingly studied aid the formulation development process, particularly for targeted delivery, that has displayed some success thus far.

The second half of this paper reviewed GAGs as potential molecular targets, with the intention of providing comprehensive evidence that encourages more research and treatment strategies aimed towards CS-E and GAGs. Employing NPs loaded with drug molecules that specifically target GAGs creates the potential for the development of a novel class of cancer therapy termed “GAG inhibitors”. Although these advances provide useful treatment/diagnostic platforms, OC is still a highly complex disease with the need for further research interventions to ensure safe, efficacious and cost-effective future medicines.

2.9. References

Adany, R., Heimer, R., Caterson, B., Sorrell, J. M., Iozzo, R. V., 1990. Altered expression of chondroitin sulfate proteoglycan in the stroma of human colon carcinoma. Hypomethylation of PG-40 gene correlates with increased PG-40 content and mRNA levels. J. Biol. Chem. 265, 11389–11396.

Afratis, N., Gialeli, C., Nikitovic, D., Tsegenidis, T., Karousou, E., Theocharis, A. D., Pavão, M. S., Tzanakakis, G. N., Karamanos, N. K., 2012. Glycosaminoglycans: Key players in cancer cell biology and treatment. FEBS J. 279, 1177–1197.

Akyol, S., Gercel-Taylor, C., Reynolds, L.C., Taylor, D.D., 2006. HSP-10 in ovarian cancer: Expression and suppression of T-cell signaling. Gynecol. Oncol. 101.

Alberti, D., Protti, N., Franck, M., Stefania, R., Bortolussi, S., Altieri, S., Deagostino, A., Aime, S., Geninatti Crich, S., 2017. Theranostic Nanoparticles Loaded with Imaging Probes and Rubrocurcumin for Combined Cancer Therapy by Folate Receptor Targeting. ChemMedChem. 12, 502–509.

Alivisatos, A.P., 1996. Perspectives on the Physical Chemistry of Semiconductor Nanocrystals. J. Phys. Chem. 100, 13226-13239.

Anttila, M. A., Tammi, R. H., Tammi, M. I., Syrjänen, K. J., Saarikoski, S. V., Kosma, V. M., 2000. High levels of stromal hyaluronan predict poor disease outcome in epithelial ovarian cancer. Cancer Res 2000.

Apte, A., Koren, E., Koshkaryev, A., Torchilin, V.P., 2014. Doxorubicin in TAT peptide-modified multifunctional immunoliposomes demonstrates increased activity against both drug-sensitive and drug-resistant ovarian cancer models. Cancer Biol. Ther .15, 69-80.

Arora, D., Jaglan, S., 2016. Nanocarriers based delivery of nutraceuticals for cancer prevention and treatment: A review of recent research developments. Trends Food Sci. Technol. 54, 114–126.

Asimakopoulou, A. P., Theocharis, A. D., Tzanakakis, G. N., Karamanos, N. K., 2008. The biological role of chondroitin sulfate in cancer and chondroitin-based anticancer agents. In Vivo (Brooklyn). 22, 385–390.

Auzenne, E., Ghosh, S. C., Khodadadian, M., Rivera, B., Farquhar, D., Price, R. E., Ravoori, M., Kundra, V., Freedman, R. S., Klostergaard, J., 2007. Hyaluronic acid-paclitaxel: antitumor efficacy against CD44(+) human ovarian carcinoma xenografts. Neoplasia. 9, 479–486.

Bazak, R., Houri, M., El Achy, S., Kamel, S., Refaat, T., 2015. Cancer active targeting by nanoparticles: a comprehensive review of literature. J. Cancer Res. Clin. Oncol. 141, 769-784.

Bertrand, N., Wu, J., Xu X., Kamaly, N., Farokhzad, O.C., 2014. Cancer nanotechnology: The impact of passive and active targeting in the era of modern cancer biology. Adv. Drug Deliv. Rev 66, 2-25.

Binzel, D.W., Khisamutdinov, E.F., Guo, P., 2014. Entropy-driven one-step formation of phi29 pRNA 3WJ from three RNA fragments. Biochemistry. 53, 2221-2231.

Bourguignon, L. Y. W., Gilad, E., Peyrollier, K., 2007. Heregulin-mediated ErbB2-ERK signaling activates hyaluronan synthases leading to CD44-dependent ovarian tumor cell growth and migration. J. Biol. Chem. 282, 19426–19441.

Bourguignon, L. Y. W., Peyrollier, K., Xia, W., Gilad, E., 2008. Hyaluronan-CD44 interaction activates stem cell marker Nanog, Stat-3-mediated MDR1 gene expression, and ankyrin-regulated multidrug efflux in breast and ovarian tumor cells. J. Biol. Chem. 283, 17635–17651.

Bourguignon, L. Y. W., Zhu, H., Chu, A., Iida, N., Zhang, L., Hung, M. C.,1997. Interaction between the adhesion receptor, CD44, and the oncogene product, p185(HER2), promotes human ovarian tumor cell activation. J. Biol. Chem. 272, 27913–27918.

Bregoli, L., Movia, D., Gavigan-Imedio, J. D., Lysaght, J., Reynolds, J., Prina-Mello, A., 2016. Nanomedicine applied to translational oncology: A future perspective on cancer treatment. Nanomedicine Nanotechnology, Biol. Med.12, 81–103.

Brody, E.N., Gold, L., 2000. Aptamers as therapeutic and diagnostic agents. J. Biotechnol.74, 5-13.

Burger, R.A., Brady, M.F., Bookman, M.A., Fleming G.F., Monk, B.J., Huang, H., Mannel, R.S., Homesley, H.D., Fowler, J., Greer, B.E., Boente, M., Birrer, M.J., Liang, S.X., 2011. Incorporation of bevacizumab in the primary treatment of ovarian cancer. N. Engl. J. Med. 365, 2473-83.

Campbell, J. L., Arora, J., Cowell, S. F., Garg, A., Eu, P., Bhargava, S. K., Bansal, V., 2011. Quasi-cubic magnetite/silica core-shell nanoparticles as enhanced mri contrast agents for cancer imaging. PLoS One. 6.

Chauhan, V. P., Jain, R. K., 2013. Strategies for advancing cancer nanomedicine. Nat. Mater. 12, 958–62.

Chen, J.B., Neves, M.A.D., Thompson, M., 2016. Biosensor surface attachment of the ovarian cancer biomarker HSP10 via His-tag modification. Sens. Bio-Sensing Res. 11, 107-112.

Chen, Y.-W., Tekle, C., Fodstad, O., 2008. The immunoregulatory protein human B7H3 is a tumor-associated antigen that regulates tumor cell migration and invasion. Cancer Drug Targets. 8, 404-413.

Cheng, H. N., Doemeny, L. J., Geraci, C. L., Schmidt, D. G., 2016. Nanotechnology Overview: Opportunities and Challenges. In ACS Symposium Series. 1220, 1–12.

Choi, K. Y., Min, K. H., Na, J. H., Choi, K., Kim, K., Park, J. H., Kwon, I. C.; Jeong, S. Y., 2009. Self-assembled hyaluronic acid nanoparticles as a potential drug carrier for cancer therapy: synthesis, characterization, and in vivo biodistribution. J. Mater. Chem. 19, 4102.

Choi, K. Y., Saravanakumar, G., Park, J. H., Park, K., 2012. Hyaluronic acid-based nanocarriers for intracellular targeting: Interfacial interactions with proteins in cancer. Colloids Surfaces B Biointerfaces. 99, 82–94.

Coccia, M., Wang, L., 2015. Path-breaking directions of nanotechnology-based chemotherapy and molecular cancer therapy. Technol. Forecast. Soc. Change. 94, 155-169.

Collins, M., Ling, V., Carreno, B.M., 2005. The B7 family of immune-regulatory ligands. Genome Biol. 6, 223.

Csoka, A. B., Frost, G. I., Stern, R., 2001. The six hyaluronidase-like genes in the human and mouse genomes. Matrix Biol. 20, 499–508.

Cunliffe, D., Kirby, A., Alexander, C., 2005. Molecularly imprinted drug delivery systems. Adv. Drug Deliv. Rev. 57, 1836-1853.

Danhier, F., Breton, A. Le, Préat, V., 2012. RGD-based strategies to target alpha(v) beta (3) integrin in cancer therapy and diagnosis. Mol. Pharm. 9, 2961–2973.

Davis, G. E., Senger, D. R., 2005. Endothelial extracellular matrix: Biosynthesis, remodeling, and functions during vascular morphogenesis and neovessel stabilization. Circ. Res. 97,1093–1107.

Delpech, B., Girard, N., Bertrand, P., Courel, M. N., Chauzy, C., Delpech, A., 1997. Hyaluronan: fundamental principles and applications in cancer. J. Intern. Med. 242, 41–48.

Desale, S. S., Cohen, S. M., Zhao, Y., Kabanov, A. V., Bronich, T. K., 2013. Biodegradable hybrid polymer micelles for combination drug therapy in ovarian cancer. J. Control. Release. 171, 339–348.

Dharap, S. S., Wang, Y., Chandna, P., Khandare, J. J., Qiu, B., Gunaseelan, S., Sinko, P.J., Stein, S., Farmanfarmaian, A., Minko, T., 2005. Tumor-specific targeting of an anticancer drug delivery system by LHRH peptide. Proc. Natl. Acad. Sci. U. S. A. 102, 12962-7.

Engel, J., Emons, G., Pinski, J., Schally, A. V., 2012. AEZS-108 : a targeted cytotoxic analog of LHRH for the treatment of cancers positive for LHRH receptors. Expert Opin. Investig. Drugs. 21, 891–9.

Engels, B., Rowley, D. A., Schreiber, H., 2012. Targeting stroma to treat cancers. Semin. Cancer Biol. 22, 41–49.

Fauci, J.M., Straughn, J.M., Ferrone, S., Buchsbaum, D.J., 2012. A review of B7-H3 and B7-H4 immune molecules and their role in ovarian cancer. Gynecol. Oncol. 127, 420-5.

Feng, D., Song, Y., Shi, W., Li, X., Ma, H., 2013. Distinguishing folate-receptor-positive cells from folate-receptor-negative cells using a fluorescence off-on nanoprobe. Anal. Chem. 85, 6530–6535.

Fleige, E., Quadir, M. A., Haag, R., 2012. Stimuli-responsive polymeric nanocarriers for the controlled transport of active compounds: Concepts and applications. Adv. Drug Deliv. Rev. 64, 866–884.

Ganta, S., Devalapally, H., Shahiwala, A., Amiji, M., 2008. A review of stimuli-responsive nanocarriers for drug and gene delivery. J. Control. Release. 126, 187-204.

Ganta, S., Singh, A., Kulkarni, P., Keeler, A. W., Piroyan, A., Sawant, R. R., Patel, N. R., Davis, B., Ferris, C., O'Neal, S., Zamboni, W., Amiji, M. M., Coleman, T.P., 2015. EGFR targeted theranostic Nanoemulsion for image-guided ovarian cancer therapy. Pharm. Res. 32, 2753-2763.

Gao, Y., Xie, J., Chen, H., Gu, S., Zhao, R., Shao, J., Jia, L., 2014. Nanotechnology-based intelligent drug design for cancer metastasis treatment. Biotechnol. Adv. 32, 761-77.

Garin-Chesa, P., Campbell, I., Saigo, P. E., Lewis, J. L., Old, L. J., Rettig, W. J., 1993. Trophoblast and ovarian cancer antigen LK26. Sensitivity and specificity in immunopathology and molecular identification as a folate-binding protein. Am. J. Pathol. 142, 557–67.

Goethals, E. C., Shukla, R., Mistry, V., Bhargava, S. K., Bansal, V., 2013. Role of the templating approach in influencing the suitability of polymeric nanocapsules for drug delivery: LbL vs SC/MS. Langmuir. 29, 12212–12219.

Guo, J., Bourre, L., Soden, D .M., O'Sullivan, G. C., O'Driscoll, C., 2011. Can non-viral technologies knockdown the barriers to siRNA delivery and achieve the next generation of cancer therapeutics? Biotechnol. Adv. 29, 402-17.

Hajba, L., Guttman, A., 2016. The use of magnetic nanoparticles in cancer theranostics: Toward handheld diagnostic devices. Biotechnol. Adv. 34, 354–361.

Hamd-Ghadareh, S., Salimi, A., Fathi, F., Bahrami, S., 2017. An amplified comparative fluorescence resonance energy transfer immunosensing of CA125 tumor marker and ovarian cancer cells using green and economic carbon dots for bio-applications in labeling, imaging and sensing. Biosens. Bioelectron. Biosens. Bioelectron. 96, 308-316.

Hami, Z., Rezayat, S. M., Gilani, K., Amini, M., Ghazi-Khansari, M., 2017. In-vitro cytotoxicity and combination effects of the docetaxel-conjugated and doxorubicin-conjugated poly (lactic acid)-poly(ethylene glycol)-folate-based polymeric micelles in human ovarian cancer cells. Journal of pharmacy and pharmacology. 69, 151-160.

He, C., Lu, K., Liu, D., Lin, W., 2014. Nanoscale metal-organic frameworks for the co-delivery of cisplatin and pooled siRNAs to enhance therapeutic efficacy in drug-resistant ovarian cancer cells. J. Am. Chem. Soc. 136, 5181-5184.

He, C., Poon, C., Chan, C., Yamada, S.D., Lin, W., 2016. Nanoscale coordination polymers codeliver chemotherapeutics and sirnas to eradicate tumors of cisplatin-resistant ovarian cancer. J. Am. Chem. Soc. 138, 6010–6019.

Herrera-Gayol, a., Jothy, S.,2001. Effects of hyaluronan on the invasive properties of human breast cancer cells in vitro. Int. J. Exp. Pathol. 82, 193–200.

Hiltunen, E. L. J., Anttila, M., Kultti, A., Ropponen, K., Penttinen, J., Yliskoski, M., Kuronen, A. T., Juhola, M., Tammi, R., Tammi, M., Kosma, V. M., 2002. Elevated hyaluronan concentration without hyaluronidase activation in malignant epithelial ovarian tumors. Cancer Res. 62, 6410–6413.

Huang, C.J., Lin, H.I., Shiesh, S.C., Lee, G.B., 2010. Integrated microfluidic system for rapid screening of CRP aptamers utilizing systematic evolution of ligands by exponential enrichment (SELEX), Biosensors and Bioelectronics. 25, 1761-1766.

Huang, Y.H., Peng, W., Furuuchi, N., Gerhart, J., Rhodes, K., Mukherjee N., 2016. Delivery of therapeutics targeting the mRNA-binding protein HuR using 3DNA nanocarriers suppresses ovarian tumor growth. Cancer Res. 76, 1549-59.

Isogai, Z., Shinomura, T., Yamakawa, N., Takeuchi, J., Tsuji, T., Heinegård, D., Kimata, K., 1996. 2B1 antigen characteristically expressed on extracellular matrices of human malignant tumors is a large chondroitin sulfate proteoglycan, PG- M/versican. Cancer Res. 56, 3902–3908.

Jemal, A., Bray, F., Center, M., Ferlay, J.; Ward, E., Forman, D., 2011. Global cancer statistics. CA Cancer J Clin. 61, 69-90.

Jia, F., Liu, X., Li, L., Mallapragada, S., Narasimhan, B., Wang, Q., 2013. Multifunctional nanoparticles for targeted delivery of immune activating and cancer therapeutic agents. J. Control. Release. 172, 1020-34.

Jin, H., Gui, R., Gong, J., Huang, W., 2017. Aptamer and 5-fluorouracil dual-loading Ag2S quantum dots used as a sensitive label-free probe for near-infrared photoluminescence turn-on detection of CA125 antigen. Biosens. Bioelectron. 92, 378-384.

Kanlikilicer, P., Ozpolat, B., Aslan, B., Bayraktar, R., Gurbuz, N., & Rodriguez-Aguayo, C., 2017. Therapeutic Targeting of AXL Receptor Tyrosine Kinase Inhibits Tumor Growth and Intraperitoneal Metastasis in Ovarian Cancer Models. Molecular Therapy - Nucleic Acids. 9, 251-262.

Kasten, B. B., Arend, R.C., Katre, A. A., Kim, H., Fan, J., Ferrone, S., Zinn, K. R., Buchsbaum, D. J., 2017. B7-H3-targeted 212Pb radioimmunotherapy of ovarian cancer in preclinical models. Nucl. Med. Biol. 47, 23-30.

Kim, D., Zhong, G. G., Eun, S. L., You, H. B., 2009. In vivo evaluation of doxorubicin-loaded polymeric micelles targeting folate receptors and early endosomal pH in drug-resistant ovarian cancer. Molecular Pharmaceutics. 6, 1353–1362.

Ko, S. Y., Guo, H., Barengo, N., Naora, H., 2009. Inhibition of ovarian cancer growth by a tumor-targeting peptide that binds eukaryotic translation initiation factor 4E. Clin. Cancer Res. 15, 4336-47.

Kulhari, H., Pooja, D., Kota, R., Reddy, T. S., Tabor, R. F., Shukla, R., Adams, D. J., Sistla, R., Bansal, V., 2016. Cyclic RGDfK Peptide Functionalized Polymeric Nanocarriers for Targeting Gemcitabine to Ovarian Cancer Cells. Mol. Pharm. 13, 1491-1500.

Kwon, I. K., Lee, S. C., Han, B., Park, K., 2012. Analysis on the current status of targeted drug delivery to tumors. J. Control. Release. 164, 108-114.

Lamberti, I., Scarano, S., Esposito, C. L., Antoccia, A., Antonini, G., Tanzarella, C., De Franciscis, V., Minunni, M., 2016. In vitro selection of RNA aptamers against CA125 tumor marker in ovarian cancer and its study by optical biosensing. Methods. 97, 58-68.

Lammers, T., Kiessling, F., Hennink, W. E., Storm, G., 2012. Drug targeting to tumors: Principles, pitfalls and (pre-) clinical progress. J. Control. Release.161, 175–187.

Landen, C. N., Kim, T.-J., Lin, Y. G., Merritt, W. M., Kamat, A. A., Han, L. Y., Spannuth, W. A., Nick, A. M., Jennnings, N. B., Kinch, M. S., Tice, D., Sood, A. K., 2008. Tumor-selective response to antibody-mediated targeting of alphavbeta3 integrin in ovarian cancer. Neoplasia. 10, 1259–67.

Langdon, S. P., Andrew, H. S., 2016. HER2-Targeted Antibody Treatment for Ovarian Cancer – Future Opportunities. J Mol Pharm Org Process Res. 4, e125.

Liang, H., Li, X., Chen, B., Wang, B., Zhao, Y., Zhuang, Y., Shen, H., Zhang, Z., Dai, J., 2015. A collagen-binding EGFR single-chain Fv antibody fragment for the targeted cancer therapy. J. Control. Release. 209, 101–109.

Liang, S.B., Fu, L.W., 2017. Application of single-cell technology in cancer research. Biotechnol. Adv. 35, 443-449.

Lin, C. J., Kuan, C. H., Wang, L. W., Wu, H. C., Chen, Y., Chang, C.W., Huang, R. Y., Wang, T. W., 2016. Integrated self-assembling drug delivery system possessing dual responsive and active targeting for orthotopic ovarian cancer theranostics. Biomaterials. 90, 12-26.

Liu, J., Huang, Y., Kumar, A., Tan, A., Jin, S., Mozhi, A., Liang, X. J., 2014. PH-Sensitive nano-systems for drug delivery in cancer therapy. Biotechnol. Adv. 32, 693–710.

Lokman, N. A., Elder, A. S. F., Ween, M.P., Pyragius, C. E., Hoffmann, P., Oehler, M. K., Ricciardelli, C., 2013. Annexin A2 is regulated by ovarian cancer-peritoneal cell interactions and promotes metastasis. Oncotarget. 4, 1199-211.

Lössner, D., Abou-Ajram, C., Benge, A., Reuning, U., 2008. Integrin alphavbeta3 mediates up-regulation of epidermal growth-factor receptor expression and activity in human ovarian cancer cells. Int. J. Biochem Cell Biol. 40, 2746–61.

Low, P. S., Henne, W. A., Doorneweerd, D .D., 2008. Discovery and development of folic-acid-based receptor targeting for imaging and therapy of cancer and inflammatory diseases. Acc. Chem. Res. 41,120-129.

Luís A. Rocha.L.A., David A. Learmonth, D.A., Rui A. Sousa, R.A., Salgado, A.J., 2017 (In press). αvβ3 and α5β1 integrin-specific ligands: From tumor angiogenesis inhibitors to vascularization promoters in regenerative medicine?. Biotechnol. Adv.

Lv, L., Zhuang, Y. X., Zhang, H. W., Tian, N. N., Dang, W. Z., Wu, S. Y., 2017. Capsaicin-loaded folic acid-conjugated lipid nanoparticles for enhanced therapeutic efficacy in ovarian cancers. Biomed. Pharmacother. 91, 999–1005.

Menderes, G., Bonazzoli, E., Bellone, S., Black, J., Altwerger, G., Masserdotti, A., Pettinella, F., Zammataro, L., Buza, N., Hui, P., Wong, S., Litkouhi, B., Ratner, E., Silasi, D.A., Huang, G.S., Azodi, M., Schwartz, P. E.; Santin, A. D., 2017. SYD985, a novel duocarmycin-based HER2-targeting antibody-drug conjugate, shows promising antitumor activity in epithelial ovarian carcinoma with HER2/Neu expression. Gynecol Oncol. 146, 179-186.

Meng, H., Liong, M., Xia, T., Li, Z., Ji, Z., Zink, J. I., Nel, A. E., 2010. Engineered design of mesoporous silica nanoparticles to deliver doxorubicin and p-glycoprotein siRNA to overcome drug resistance in a cancer cell line. ACS Nano. 4, 4539–4550.

Mishra, B., Patel, B. B., Tiwari, S., 2010. Colloidal nanocarriers: a review on formulation technology, types and applications toward targeted drug delivery. Nanomedicine Nanotechnology, Biol. Med. 6, 9-24.

Montagner, I. M., Merlo, A., Carpanese, D., Zuccolotto, G., Renier, D., Campisi, M., Pasut, G., Zanovello, P., Rosato, A., 2015. Drug conjugation to hyaluronan widens therapeutic indications for ovarian cancer. Oncoscience. 2, 373–381.

Nicolas, J., Mura, S., Brammbilla, D., Mackiewicz, N., Couvreur, P., 2013. Design, functionalization strategies and biomedical applications of targeted biodegradable/biocompatible polymer-based nanocarriers for drug delivery. Chem. Soc. Rev. 42(43), 1147-235.

Nobile, S., Nobile, L., 2017. Nanotechnology for biomedical applications: Recent advances in neurosciences and bone tissue engineering. Polym. Eng. Sci. 57, 644-650.

Nykopp, T. K., Rilla, K., Sironen, R., Tammi, M. I., Tammi, R. H., Hämäläinen, K., Heikkinen, A.-M., Komulainen, M.; Kosma, V.-M., Anttila, M., 2009. Expression of hyaluronan synthases (HAS1-3) and hyaluronidases (HYAL1-2) in serous ovarian carcinomas: inverse correlation between HYAL1 and hyaluronan content. BMC Cancer. 9, 143.

Ozpolat, B., Sood, A. K., Lopez-Berestein, G., 2010. Nanomedicine based approaches for the delivery of siRNA in cancer. Journal of Internal Medicine. 267, 44–53.

Palanca-Wessels, M. C., Booth, G. C., Convertine, A. J., Lundy, B. B., Berguig, G. Y., Press, M. F., Stayton, P. S., Press, O. W., 2016. Antibody targeting facilitates effective intratumoral siRNA nanoparticle delivery to HER2- xpressing cancer cells. Oncotarget. 7, 9561-9575.

Peoples, G., Goedegebuure, P., Smith, R., Linehan, D., Yoshino, I., & Eberlein, T., 1995. Breast and ovarian cancer-specific cytotoxic T lymphocytes recognize the same HER2/neu-derived peptide. Proceedings of The National Academy of Sciences. 92, 432-436.

Pi, F., Zhang, H., Li, H., Thiviyanathan, V., Gorenstein, D.G., Sood, A.K., Guo, P., 2017. RNA nanoparticles harboring annexin A2 aptamer can target ovarian cancer for tumor-specific doxorubicin delivery. Nanomedicine Nanotechnology, Biol. Med. 13, 1183-1193.

Pothacharoen, P., Siriaunkgul, S., Ong-Chai, S., Supabandhu, J., Kumja, P., Wanaphirak, C., Sugahara, K., Hardingham, T., Kongtawelert, P., 2006. Raised serum chondroitin sulfate epitope level in ovarian epithelial cancer. J. Biochem. 140, 517–524.

Pradeep, P., Choonara, Y. E., Kumar, P., Pillay, V., 2016. “On-the-spot” arresting of chondroitin sulphate proteoglycans: Implications for ovarian adenocarcinoma recognition and intervention. Int. J. Mol. Sci.17.

Prinz. R., Willis, C., van Kuppevelt, T., Kluppel, M., 2014. Biphasic role of chondroitin sulphate in cardiac differentiation of embryonic stem cells through inhibition of wnt/β-catenin signalling.PloS ONE. 9, e92381.

Quintana, A., Raczka, E., Piehler, L., Lee, I., Myc, A., Majoros, I., Patri, A. K., Thomas, T., Mulé, J., Baker, J. R., 2002. Design and function of a dendrimer-based therapeutic nanodevice targeted to tumor cells through the folate receptor. Pharm. Res. 19, 1310–1316.

Raavé, R., de Vries, R. B. M., Massuger, L. F., van Kuppevelt, T. H., Daamen, W.F., 2015. Drug delivery systems for ovarian cancer treatment: a systematic review and meta-analysis of animal studies. PeerJ. 3, e1489.

Ramasamy, T., Kim, J., Choi, J., Tran, T., Choi, H., Yong, C., Kim, J., 2014. pH sensitive polyelectrolyte complex micelles for highly effective combination chemotherapy. Journal Of Materials Chemistry B. 2, 6324-6333.

Ren, Y., Cheung, H. W., von Maltzhan, G., Agrawal, A., Cowley, G. S., Weir, B. A., Boehm, J. S., Tamayo, P., Karst, A. M., Liu, J. F., Hirsch, M. S., Mesirov, J. P., Drapkin, R., Root, D. E., Lo, J., Fogal, V., Ruoslahti, E., Hahn, W. C., Bhatia, S. N., 2012. Targeted

Tumor-Penetrating siRNA Nanocomplexes for Credentialing the Ovarian Cancer Oncogene ID4. Sci. Transl. Med. 4, 147ra112-147ra112.

Rhoda, K., Choonara, Y .E., Kumar, P., Bijukumar, D., Du Toit, L. C., Pillay, V., 2015. Potential nanotechnologies and molecular targets in the quest for efficient chemotherapy in ovarian cancer. Expert Opin. Drug Deliv. 12, 613-634.

Saad, M., Garbuzenko, O. B., Ber, E., Chandna, P., Khandare, J. J., Pozharov, V. P., Minko, T., 2008. Receptor targeted polymers, dendrimers, liposomes: Which nanocarrier is the most efficient for tumor-specific treatment and imaging? J. Control. Release. 130, 107–114.

Safari, J., Zarnegar, Z., 2014. Advanced drug delivery systems: Nanotechnology of health design A review. J. Saudi Chem. Soc. 18, 85–99.

Saraswathy, M., Gong, S., 2013. Different strategies to overcome multidrug resistance in cancer. Biotechnol. Adv. 31, 1397–1407.

Sarisozen, C., Abouzeid, A., & Torchilin, V., 2014. The effect of co-delivery of paclitaxel and curcumin by transferrin-targeted PEG-PE-based mixed micelles on resistant ovarian cancer in 3-D spheroids and in vivo tumors. Eur. J. Pharm. Biopharm. 88, 539-550.

Shah, V., Taratula, O., Garbuzenko, O. B., Taratula, O. R., Rodriguez-Rodriguez, L., Minko, T., 2013. Targeted nanomedicine for suppression of CD44 and simultaneous cell death induction in ovarian cancer: An optimal delivery of siRNA and anticancer drug. Clin. Cancer Res.19, 6193–6204.

Sharma, T. K., Bruno, J. G., Dhiman, A., 2017. ABCs of DNA aptamer and related assay development. Biotechnol. Adv. 35, 275–301.

Sharma, T. K., Ramanathan, R., Rakwal, R., Agrawal, G. K., Bansal, V., 2015. Moving forward in plant food safety and security through NanoBioSensors: Adopt or adapt biomedical technologies? Proteomics. 15, 1680-92.

Shi, J., Kantoff, P.W., Wooster, R., Farokhzad, O.C., 2017. Cancer nanomedicine: progress, challenges and opportunities. Nat. Rev. Cancer. 17, 20-37.

Shigdar, S., Qian, C., Lv, L., Pu, C., Li, Y., Li, L., Marappan, M., Lin, J., Wang, L., Duan, W., 2013. The Use of Sensitive Chemical Antibodies for Diagnosis: Detection of Low Levels of Epcam in Breast Cancer. PLoS One. 8, e57613.

Shu, D., Shu, Y., Haque, F., Abdelmawla, S., Guo, P., 2011. Thermodynamically stable RNA three-way junction for constructing multifunctional nanoparticles for delivery of therapeutics. Nat. Nanotechnol. 6, 658-667.

Shukla, R., Chanda, N., Zambre, a., Upendran, a., Katti, K. V., Kulkarni, R. R., Nune, S.K., Casteel, S. W., Smith, C. J., Vimal, J., Boote, E., Robertson, J.D., Kan, P., Engelbrecht, H., Watkinson, L.D., Carmack, T. L., Lever, J. R., Cutler, C. S., Caldwell, C., Kannan, R., Katti, K. V.,2012. Laminin receptor specific therapeutic gold nanoparticles (198AuNP-EGCg) show efficacy in treating prostate cancer. Proc. Natl. Acad. Sci. 109, 12426-12431.

Sivakumar, S., Bansal, V., Cortez, C., Chong, S. F., Zelikin, A. N., Caruso, F., 2009. Degradable, surfactant-free, monodisperse polymer-encapsulated emulsions as anticancer drug carriers. Adv. Mater. 21, 1820–1824.

Smetsers, T. F. C. M., Van De Westerlo, E. M. A., Ten Dam, G. B., Overes, I. M., Schalkwijk, J., Van Muijen, G. N. P., Van Kuppevelt, T. H., 2004. Human single-chain antibodies reactive with native chondroitin sulfate detect chondroitin sulfate alterations in melanoma and psoriasis. J. Invest. Dermatol.122, 707–716.

Somasunderam, A., Thiviyanathan, V., Tanaka, T., Li, X., Neerathilingam, M., Lokesh, G.L.R., Mann, A., Peng, Y., Ferrari, M., Klostergaard, J., Gorenstein, D.G., 2010. Combinatorial selection of DNA thioaptamers targeted to the HA binding domain of human CD44. Biochemistry. 49, 9106-9112.

Spencer, D. S., Puranik, A. S., Peppas, N. A., 2015. Intelligent nanoparticles for advanced drug delivery in cancer treatment. Curr. Opin. Chem. Eng. 7, 84-92.

Sudimack, J., Lee, R.J., 2000. Targeted drug delivery via the folate receptor. Adv. Drug Deliv. Rev. 41, 147-162.

Sutherland, A.J., 2002. Quantum dots as luminescent probes in biological systems. Curr. Opin. Solid State Mater. Sci. 6, 365-370.

Tamakoshi, K., Kikkawa, F., Maeda, O., Suganuma, N., Yamagata, S., Yamagata, T., Tomoda, Y., 1997. Hyaluronidase activity in gynaecological cancer tissues with different metastatic forms. Br. J. Cancer. 75, 1807–11.

ten Dam, G. B., van de Westerlo, E. M. A., Purushothaman, A., Stan, R. V, Bulten, J., Sweep, F. C. G. J., Massuger, L. F., Sugahara, K., van Kuppevelt, T. H., 2007. Antibody GD3G7 selected against embryonic glycosaminoglycans defines chondroitin sulfate-E domains highly up-regulated in ovarian cancer and involved in vascular endothelial growth factor binding. Am. J. Pathol. 171, 1324–1333.

Torchilin, V. P. Multifunctional nanocarriers. Adv. Drug Deliv. Rev. 64, 302–315.

Torchilin, V., 2009. Multifunctional and stimuli-sensitive pharmaceutical nanocarriers. Eur. J. Pharm. Biopharm. 71, 431–444.

Tuefferd, M., Couturier, J., Penault-Llorca, F., Vincent-Salomon, A., Broët, P., Guastalla, J.P., Allouache, D., Combe, M., Weber, B., Pujade-Lauraine, E., Camilleri-Broët, S., 2007. HER2 status in ovarian carcinomas: A multicenter GINECO study of 320 patients. PLoS One. 2, e1138.

Valcarcel, J., Novoa-Carballal, R., Pérez-Martín, R. I., Reis, R. L., Vázquez, J. A., 2017. Glycosaminoglycans from marine sources as therapeutic agents. Biotechnol. Adv. 35, 711-725.

Vallen, M. J. E., Massuger, L. F. A. G., Ten Dam, G. B., Bulten, J., Van Kuppevelt, T. H., 2012. Highly sulfated chondroitin sulfates, a novel class of prognostic biomarkers in ovarian cancer tissue. Gynecol. Oncol. 127, 202–209.

Vallen, M. J. E., Schmidt, S., Oosterhof, A., Bulten, J., Massuger, L. F. A. G., Van Kuppevelt, T. H., 2014. Primary ovarian carcinomas and abdominal metastasis contain 4,6-disulfated chondroitin sulfate rich regions, which provide adhesive properties to tumour cells. PLoS One. 9, e111806.

Vallen, M. J. E., Van Der Steen, S. C. H. A., Van Tilborg, A. A. G., Massuger, L. F. A. G., Van Kuppevelt, T. H., 2014. Sulfated sugars in the extracellular matrix orchestrate ovarian cancer development: “When sweet turns sour.” Gynecol. Oncol. 135, 371–381.

Van Der Steen, S. C. H. A., Van Tilborg, A. A. G., Vallen, M. J. E., Bulten, J., Van Kuppevelt, T. H., Massuger, L. F. A. G., 2016. Prognostic significance of highly sulfated chondroitin sulfates in ovarian cancer defined by the single chain antibody GD3A11. Gynecol. Oncol. 140, 527–536.

van der Steen, S. C. H. A., Raave, R., Langerak, S., van Houdt, L., van Duijnhoven, S. M. J., van Lith, S. A. M., Massuger, L. F. A. G., Daamen, W. F., Leenders, W. P., van Kuppevelt, T. H., 2017. Targeting the extracellular matrix of ovarian cancer using functionalized, drug loaded lyophilisomes. Eur. J. Pharm. Biopharm. 113, 229–239.

Wadee, A., Pillay, V., Choonara, Y. E., du Toit, L. C., Penny, C., Ndesendo, V. M. K., Kumar, P., Murphy, C. S., 2011. Recent advances in the design of drug-loaded polymeric implants for the treatment of solid tumors. Expert Opin. Drug Deliv. 8, 1323-40.

Wang, Y., Bansal, V., Zelikin, A. N., Caruso, F., Templated synthesis of single-component polymer capsules and their application in drug delivery. Nano Lett. 8, 1741-1745.

Watanabe, I., Hikita, T., Mizuno, H., Sekita, R., Minami, A., Ishii, A., Minamisawa, Y., Suzuki, K., Maeda, H., Hidari, K. I. P. J., Suzuki, T., 2015. Isolation and characterization of monoclonal antibodies specific for chondroitin sulfate e. Glycobiology. 25, 953–962.

Ween, M. P., Oehler, M. K., Ricciardelli, C., 2011. Role of versican, hyaluronan and CD44 in ovarian cancer metastasis. Int. J. Mol. Sci. 12, 1009–1029.

Weigel, P. H., DeAngelis, P.L., 2007. Hyaluronan synthases: A decade-plus of novel glycosyltransferases. J. Biol. Chem. 282, 36777-81.

Weiss, I., Trope, C. G., Reich, R., Davidson, B., 2012. Hyaluronan synthase and hyaluronidase expression in serous ovarian carcinoma is related to anatomic site and chemotherapy exposure. Int. J. Mol. Sci.13, 12925–12938.

Wu, X., Chen, J., Wu, M., Zhao, J.X., 2015. Aptamers: Active targeting ligands for cancer diagnosis and therapy. Theranostics. 5, 322-344.

Xi, Z., Huang, R., Deng, Y., He, N., 2014. Progress in selection and biomedical applications of aptamers. J. Biomed. Nanotechnol. 10, 3043-62.

Xiang, D., Shigdar, S., Qiao, G., Wang, T., Kouzani, A.Z., Zhou, S.F., Kong, L., Li, Y., Pu, C., Duan, W., 2015. Nucleic acid aptamer-guided cancer therapeutics and diagnostics: The next generation of cancer medicine. Theranostics. 5, 23-42.

Xiao, K., Li, Y., Lee, J.S., Gonik, A.M., Dong, T., Fung, G., Sanchez, E., Xing, L., Cheng, H.R., Luo, J., Lam, K.S., 2012. “OA02” peptide facilitates the precise targeting of paclitaxel-loaded micellar nanoparticles to ovarian cancer In Vivo. Cancer Res. 72, 2100-2110.

Xie, J., Lee, S., Chen, X., 2010. Nanoparticle-based theranostic agents. Adv. Drug Deliv. Rev. 62, 1064–1079.

Xu, X., Ho, W., Zhang, X., Bertrand, N., Farokhzad, O., 2015. Cancer nanomedicine: From targeted delivery to combination therapy. Trends Mol. Med. 21, 223-32.

Yamagata, M., Kimata, K., Oike, Y., Tani, K., Maeda, N., Yoshida, K., Shimomura, Y., Yoneda, M., Suzuki, S., 1987. A monoclonal antibody that specifically recognizes a glucuronic acid 2-sulfate-containing determinant in intact chondroitin sulfate chain. J. Biol. Chem. 262, 4146–4152.

Yang, G., Wang, J., Wang, Y., Li, L., Guo, X., Zhou, S., 2015. An implantable active-targeting micelle-in-nanofiber device for efficient and safe cancer therapy. ACS Nano. 9, 1161-1174.

Yang, X., Iyer, A. K., Singh, A., Choy, E., Hornicek, F.J., Amiji, M. M., Duan, Z., 2015. MDR1 siRNA loaded hyaluronic acid-based CD44 targeted nanoparticle systems circumvent paclitaxel resistance in ovarian cancer. Sci Rep. 5, 8509.

Yasunaga, M., Manabe, S., Tarin, D., Matsumura, Y., 2011. Cancer-stroma targeting therapy by cytotoxic immunoconjugate bound to the collagen 4 network in the tumor tissue. Bioconjug. Chem. 22, 1776–1783.

Yeo, T. K., Nagy, J. A., Yeo, K. T., Dvorak, H. F., Toole, B. P., 1996. Increased hyaluronan at sites of attachment to mesentery by CD44-positive mouse ovarian and breast tumor cells. Am. J. Pathol.148, 1733–1740.

Yoon, S., & Rossi, J., 2017. Treatment of Pancreatic Cancer by Aptamer Conjugated C/EBPα-saRNA. RNA Activation. 983, 173-188.

Yoon, S., Huang, K., Reebye, V.; Mintz, P., Tien, Y., & Lai, H., 2016. Targeted Delivery of C/EBPα -saRNA by Pancreatic Ductal Adenocarcinoma-specific RNA Aptamers Inhibits Tumor Growth in Vivo. Molecular Therapy. 24, 1106-1116.

Yoon, S., Huang, K.W., Reebye, V., Spalding, D., Przytycka, T.M., Wang, Y., Swiderski, P., Li, L., Armstrong, B., Reccia, I., Zacharoulis, D., Dimas, K., Kusano, T., Shively, J., Habib, N., Rossi, J.J., 2017. Aptamer-Drug Conjugates of Active Metabolites of Nucleoside Analogs and Cytotoxic Agents Inhibit Pancreatic Tumor Cell Growth. Mol. Ther. - Nucleic Acids. 6, 80-88.

Zang, X., Sullivan, P. S., Soslow, R. A., Waitz, R., Reuter, V. E., Wilton, A., Thaler, H. T., Arul, M., Slovin, S. F., Wei, J., Spriggs, D. R., Dupont, J., Allison, J.P., 2010., 2010. Tumor associated endothelial expression of B7-H3 predicts survival in ovarian carcinomas. Mod. Pathol. 23, 1104-12.

Zhang, Y., Hong, H., Cai, W., 2012. Tumor-targeted drug delivery with aptamers. Curr. Med. Chem. 18, 4185-94.

Zou, S., Cao, N., Cheng, D., Zheng, R., Wang, J., Zhu, K., Shuai, X., 2012. Enhanced apoptosis of ovarian cancer cells via nanocarrier-mediated codelivery of siRNA and doxorubicin. Int. J. Nanomedicine. 7, 3823–3835.

Chapter 3: An Inside Perspective on Artificial Intelligence and Future Ovarian Cancer Strategies: How Data Comes to the Rescue

3.1. Synopsis of This Chapter: In this review, the pertinence of AI Technologies in light of combating dynamic issues revolving OC are previewed. The need for diagnostic platforms that function at optimal are paramount in detangling the complexity surrounding the ideal management of OC regimens. Computer Aided Systems and Machine Learning (ML) approaches absorb knowledge superiorly to human intelligence and are equipped to exhaust the roots of historically accumulating data libraries, from various generations of patients with OC. This enables challenging decision making based on a consortium of robust genetic, protein and image data on tap. We further discuss the significance of ML and Artificial Neural Networks (ANNs) technologies to synergistically aid nanotherapeutic efficacy, and how matters relating to the design of drug delivery systems are overcome. On the topic of data, we added a complex section of fractional pharmacokinetics, and how this kinetic data of drugs, integrated with non-integer-differential algorithms can support many un-answerable questions regarding the movement and distribution of nano-chemotherapeutics in ovarian tumours.

Key words: Diagnostics; Proteomics; Artificial Neural Networks; Pharmacokinetic Modelling.

3.2. Introduction

Cancer is one of the leading causes of death worldwide and confounded by a poor prognosis, debilitating side-effects of chemotherapies and the emergence of drug resistance (Chen et al., 2019). OC is the most lethal malignancy in women with 230,000 new cases and 152,000 OC mortalities recorded annually (Jafari et al., 2019). To add to the complexity, OC goes largely undetected as it presents with vague symptoms and quite indistinctive on mammograms and scans (Hoosen et al., 2018) with significant relapse even after surgical intervention. Furthermore, accurate predictions (with high certainty) of OC prognosis are extremely rare. Therefore, the research and development of advanced

computer-aided predictive tools using multi-variate lab and clinical data in tandem with high-resolution diagnostic technologies in cancer research is paramount for making an early (and accurate) diagnosis of OC an initiating prompt personalized treatment (Huang et al., 2020).

The advances made in AI provide a foundation for integrating medical research and innovation in order to pave the way forward for earlier and more accurate diagnosis of OC leading to improved chemotherapy. Despite the lack of a single collective definition for AI (Wang et al., 2019), Nils J. Nilsson defined AI usefully as; “Artificial intelligence is that activity devoted to making machines intelligent, and intelligence is that quality that enables an entity to function appropriately and with foresight in its environment” (Nilsson et al, 2010, Stone et al., 2016). Utilizing computers, AI can perform advanced modelling and the execution of tasks in a manner that showcase intelligent behaviour from a consortium of inputs (for instance, the understanding, identifying, and probing of biomarkers distinctive to OC, to make an informed diagnosis) that is achieved with minimal human intervention (Dande et al., 2018). AI encompasses a branch of engineering and information technology that implements innovative concepts and algorithms to crack complex challenges in order to make accurate predictions, trends, and forecasts of anything attached to a history of data (Coccia et al., 2019).

Since 1968 there has been an exponential growth in the number of research outputs relating to the application of AI tools that are linked to the detection, diagnosis, and monitoring of cancer (Mangasarian et al., 1990). Several of these studies focused on overcoming the challenges with the methods of diagnosis using a library of existing data for superior early detection of cancer. In the 1990s, AI was further established by various researchers to train deep neural networks with partially assigned weights that discriminated between malignant and healthy tissue with great success (Mangasarian et al., 1990). The term “deep” – as opposed to “shallow” – neural networks, refers to the use of several layers in the architecture of neural networks; this way, deep networks can extract features automatically from raw data and are particularly suitable for applications where the feature space can be of very high dimension (e.g., images).

This review provides a concise incursion on the recent advances in AI-inspired systems to rapidly diagnose OC and the application of AI in mining genetic and proteomic data for early OC detection. In addition, an assimilation is provided of AI technologies implemented as a strategy to optimize and design nanomedicines and other drug delivery platforms for targeted chemotherapeutics. Lastly, fractional pharmacokinetics is described, and the integration of pharmacokinetic drug data with non-integer-order differential equations for studying the optimal dosage requirement of chemotherapeutics and their toxicities are highlighted.

3.3. Artificial Neural Networks as a tool to Super Optimize and Predict the Performance of Prototype Drug Delivery Systems

Artificial Neural Networks (ANNs) simulate neuron function mimicking that of a human brain (Tehrani et al., 2017) (Kondiah et al., 2020). ANNs comprise connecting neurons between inputs and outputs. Between the neurons, nodes mimic the synapses between biological neurons. The number of connecting neurons in a specific network dictates the power of neural computations. Each neuron in ANNs delivers the data to the following neuron through a transfer function, and once the data is processed through the designed number of neurons, the network produces an output (result). This theoretical output is then compared with the actual output. The difference between the actual vs theoretical is calculated as an error. This error facilitates network learning through a predetermined learning rule, by adjusting the weights of the connecting neurons and then reprocessing the data. This learning process of the network in the form of iterations, which is called “network training”, is continued until the lowest value of error is obtained (Agatonovic-Kustrin et al., 2000). The main advantage of ANN is that they can depict functions without the need of rule-based or well-structured experimental designs. ANNs can further recognize both linear and non-linear patterns using imprecise or incomplete input data (Davoudizadeh et al., 2018).

“Quality-by-Design (QbD)” adapted from ICH Q8, involves statistical tools and mathematical models to express the relationship between operational parameters (inputs) and critical quality attributes (outputs) in which, the role of data-mining software(s) is highlighted for pharmaceutical research and development (Nguyen et al., 2019). Other

conventional design models including full-face and Box–Behnken are flawed by the need for too many runs with high number of resources or laborious experimental constraints due to the fact that several factor settings are not feasible or are be impossible to run (Ho et al., 2015, Esnaashari et al., 2018, Turkoglu et al., 1999). Making ANNs a better suitable tool in the pre-formulation of advanced drug delivery systems (Nguyen et al., 2019).

Computer-aided design software was employed by Kondiah and co-workers (2020) for development of other advanced drug delivery platforms including 3D bioprinted scaffolds for bone tissue engineering. Optimization of the scaffold was undertaken using MATLAB® software and artificial neural networks (ANN). The ANN-optimized 3D bioprinted scaffold displayed significant properties as a controlled release platform, in addition, the scaffold further displayed formation as a pseudo-bone matrix and mimicked the hardness and matrix resilience similar to that of the clavicle bone (Kondiah et al., 2020).

ANNs were further utilized by Ndesendo and co-workers (2012) to determine the optimal synergistic polymer composite for achieving a desirable molecular bioadhesive and matrix erosion properties for a bioactive-loaded Intravaginal Bioadhesive Polymeric Device (IBPD). The use of ANNs enabled strategic polymer selection for developing an IBPD with an optimally prolonged matrix erosion and superior molecular bioadhesivity compared to controls. Thus, highlighting the utility and usefulness of this approach in the pre-formulation stages of advanced drug delivery systems (William et al., 2018).

3.4. Artificial Intelligence as a Predictive Tool for Early Ovarian Cancer Diagnostics

The prognosis of OC depends on the stage at which a diagnosis is made (Hoskins et al., 1995). At Stage 1 the cure rate approaches 90% with cyto-reductive surgery and combination chemotherapy (Hoskins et al., 1995, Sethi et al., 2013). Identifying biomarkers for OC facilitates early detection, surveillance of tumour progression and the discovery of novel targeted therapies (Budman et al., 2013, Hirasawa et al., 2018, Compton et al., 2003, Tomasetti et al., 2010).

Conventional approaches to biomarker screening involve specific antibodies that efficiently recognize the corresponding cancerous antigen (Jermal et al., 2003). Despite this approach being limited by high costs and laborious processing, it has led to the discovery and identification of an approved biomarker for OC detection i.e. CA125 (Bast et al., 1983). Recently, using Machine Learning (ML) and Deep Learning (DL) algorithms, remarkable progress has been made in circumventing key limitations in productively identifying new biomarkers from existing data (such as clinical data from CT-images of thousands of patients) (Wang et al., 2019) (Figure 3.1). To this end, there are several levels at which AI implementation can benefit clinic strategies against OC
(Table 3.1).

Table 3.1. lists several levels at which AI can be used as an effective strategy (detection diagnosis, treatment, and management) for OC

Description of the strategy	Input	Output	Ref
AI as a prognostic and predictive tool for OC (Predicting survival and outcome of surgery).	The authors created a database comprising 668 cases of EOC during a 10-year period and collected data routinely available in a clinical environment. They also collected survival data for all the patients.	The model was used to predict overall survival and demonstrated that an artificial neural network (ANN) algorithm was capable of predicting survival with high accuracy (93 %) and an area under the curve (AUC) of 0.74 and that this outperformed logistic regression.	Enshaei et al., 2015.
AI as a classification tool for accurately determining the presence of OC from protein serum samples	Test set of 116 serum samples with a particular expression of proteins indicative of OC	All 50 OC were correctly classified, including all 18 stage I cancers. 63 of 66 unaffected or benign cases were classified as non-cancer, which gives a 100% sensitivity and 95% specificity.	Petricoin et al., 2002.
AI as a tool to detect early-stage EOC in asymptomatic high-	Data was gathered from participants that underwent comprehensive gynaecologic	All cancers were detected in asymptomatic women who had normal ultrasound and physical examinations 12 and 6 months	David et al., 2005.

risk women from sonography data	and ultrasound examinations every 6 months.	before the cancer diagnosis, highlighting the benefit of ultrasound with AI for the detection of early-stage EOC in asymptomatic women who have a predisposition to OC.	
AI used to tell between benign ovarian tumours and OC	Human epididymis protein 4 (HE4) and carcinoembryonic antigen (CEA) using a training set of 235 patients and a test set of 114 individuals. The study identifies eight predictive features	A statistical decision tree was constructed using both HE4 and CEA as biomarkers. The decision tree outputs the risk of ovarian malignancy and exhibits high specificity (95.5%) and sensitivity (82.2%).	Lu et al., 2020
From genomic profiles to individualization and customization of OC treatment using SVM.	Gene expression profiles of cancer cells	The proposed Support vector machine-based method predicts the individual response of patients to gemcitabine or 5-fluorouracil therapy; the method was used to predict the sensitivity of 273 patients with OC to the same therapies.	Huang et al., 2018
Automatic annotation of tomography images	657 quantitative mathematical descriptors from the	The proposed Radiomic Prognostic Vector machine-based method was able to identify the 5% of patients with median	Lu et al., 2019

	preoperative CT images of 364 EOC patients.	overall survival less than 2 years and significantly improved prognostic methods	
Diagnosis of OC using a Bayesian network approach	The proposed Bayesian model allows to take into account genetic information (e.g., family members with OC), age and more, together with serum tumour markers to diagnose whether a tumour is benign or malignant.	The proposed methodology leads to Bayesian networks that predict whether a tumour is malignant or benign (binary classification) with a ROC of 95.2%, a sensitivity of 94.7% and a specificity of 83.4%.	Antal et al., 2000

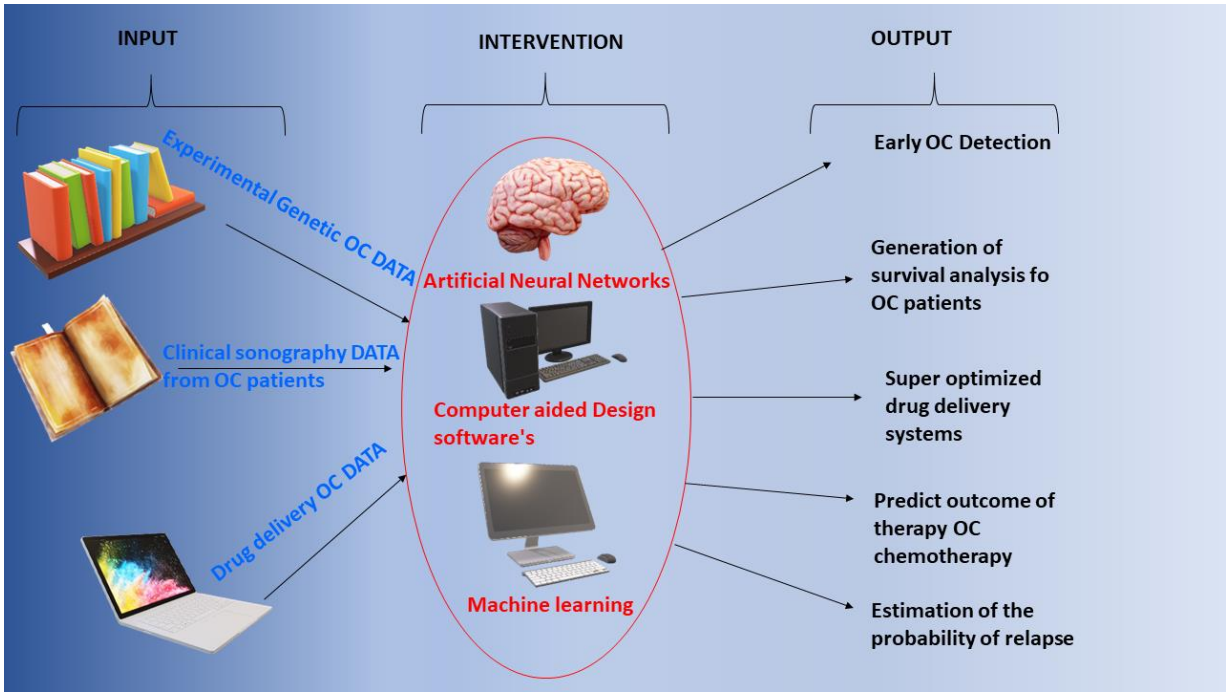

Figure 3.1. An overview of how genetic, protein and drug delivery data sourced from OC studies and clinical setups can be fed into AI technologies for reliable and important patient outcomes.

Similarly, such AI techniques have made invaluable contributions to the screening of pathological images, diagnosis in radiation oncology, skin cancer classification and diabetic retinopathy (Horie et al., 2019). DL models have also been shown to outperform other ML methods in identifying more complex features from data for better diagnosis, thus a potential avenue to exploit for OC detection (Mnih et al., 2015).

Historically, ML technologies have been successfully implemented to computer-aided diagnosis (CAD) systems (Zhou et al., 2002, Hothorn et al., 2003, Sharkey et al., 1998). ML software can discover behavioural trends within a particular cancer, based on a vast library of previously diagnosed cases and translate this to accurately predict future cases (Table 3.2) (Li et al., 2007). ML algorithms are mathematical model mapping methods that can preferentially learn trends rooted in a dataset using groups of computational algorithms that can perform pattern recognition, classification, and prediction of data by understanding existing data (the training set) (Figure 3.2). The most common ML approaches in biology (the study of genes and proteins) are Support Vector Machines

(SVM) (Mingyao et al., 2020) and Artificial Neural Networks (ANNs) (Kavitha et al., 2020). ANN modelling is particularly beneficial in cancer data mining due to the deep neuron layers that can predict sequences of DNA- and RNA-binding proteins, noncoding variants, alternative splicing, and quantitative structure-activity relationships (QSAR) of drugs to predict the success of various cancer therapeutics (Palanichamy et al., 2019). ANNs are typically preferred to SVM models when processing large datasets, as they are more parsimonious and can be trained easier; in fact, the size of an SVM model grows with the size of the training dataset.

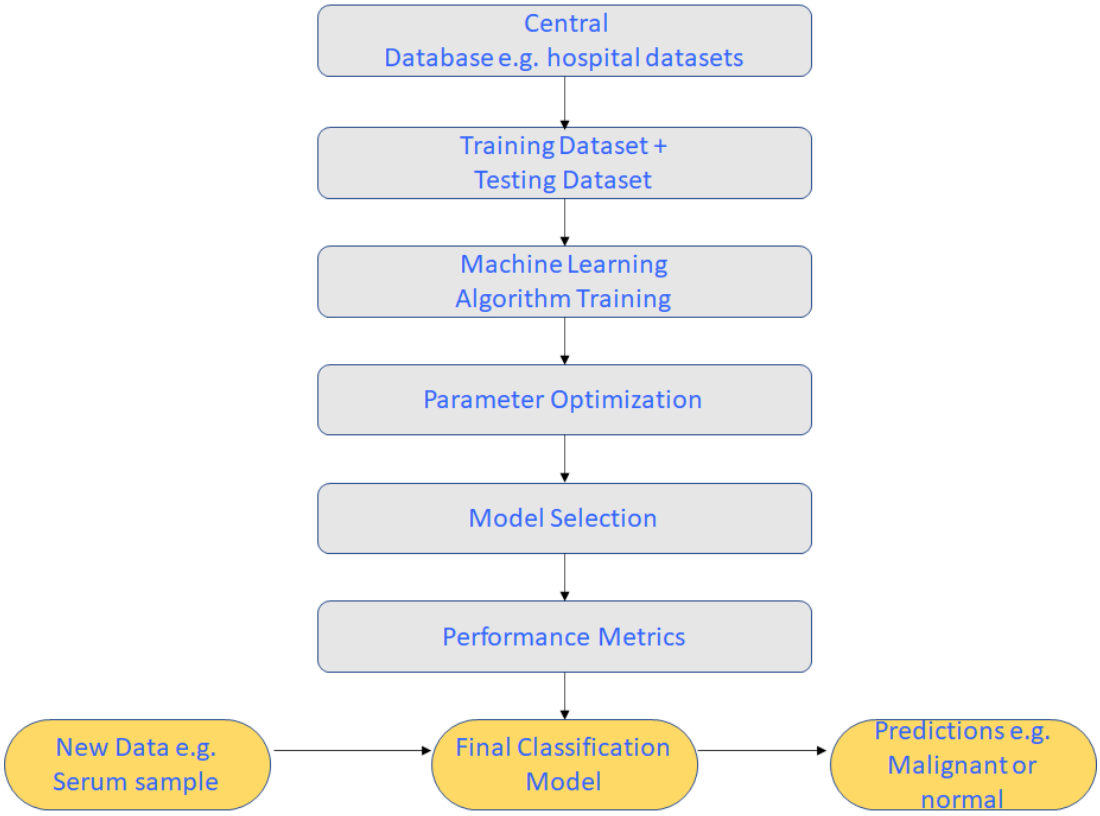

Figure 3.2. Systematic flow diagram for how machine learning takes place (adapted with permission from Bhattacharjee et al., 2017).

DL algorithms (a class of ML algorithms) has gained increasing attention, with several studies highlighting their use and performance in medical imaging, particularly in the detection of features from images relating to OC pathologies (Wang et al., 2019, Rajpurkar et al., 2018, Fu et al., 2020). In addition, through a hierarchical neural network structure and convolutional operation, DL can extract the most intrinsic characteristics of tumours that show a promising prognostic value (Chaudhary et al., 2018), which aid in

treatment selection in clinical set ups. DL algorithms differ from traditional ML algorithms in the ability to organize data. ML algorithms involve the training of classifiers produced from natural features mined from raw signals using signal processing (Martin et al., 2019). On the contrary, in DL algorithms the feature extractor is trained on data simultaneously as the classifier (i.e. end-to-end trainable models). This facilitates the construction of linear and non-linear features from mined data and builds an adapted internal representation. Technically, one or more layers of the model are dedicated to the extraction of statistical features from raw data and then suppress the signal-processing step. Thus, DL models (after being trained) can offer new possibilities in a mobility context and/or real time and offer an invaluable approach for early OC detection (Martin et al., 2019). Notably, deep convolutional neural networks have been successfully used to assess the effect of the exposure of planktonic crustaceans of the species Daphnia Magna to nanomaterials leading to models of high sensitivity and specificity that can detect nanomaterial-induced malformations (Karatzas et al., 2020).

Table 3.2. Displaying the various ML software commonly used in cancer.

Cancer Type	Software's	Uses	Ref
Cervical Cancer	CHAMP digital image software	Image analysis and ML for the automated diagnosis and classification of cervical cancer from pap-smear images	William et al., 2018
Leukaemia	WEKA software	Classifications of cancer based on microarray data	Wang et al., 2005
Breast Cancer	MetaboAnalyst and Ingenuity® Pathway Analysis (IPA®) software	To elucidate biomarkers and corresponding genes for the classification of the various stages of breast cancer	Kouznetsova et al., 2019
Breast cancer	R (open source) statistical software	For the detecting and visualising significant prognostic indicators of breast cancer survival rates	Ganggayah et al., 2019

	program and Python3		
Head-and-neck (H&N) cancer	WEKA and R software	To predict sensorineural hearing loss following chemoradiotherapy treatment	Abdollahi et al., 2018

3.4.1. Integrating Genetic Data and AI for Accurate OC Diagnosis

DNA microarray technology has been in the spotlight for several years as a tool for advanced cancer diagnosis. These tools generate and analyse big data on gene expression profiles to better understand how specific genes behave in cancerous states (Sarkar et al., 2002). After genomic sequencing, DNA microarrays have become the primary source of genome-scale data in biotechnology. Microarrays produce unprecedented quantities of gene expressions and other functional genomic data that provide key insights into gene function and interactions within and across metabolic pathways (Tan et al., 2003). Furthermore, DNA microarrays facilitate the screening of numerous genes simultaneously and determine whether any genes are active, hyperactive or silent in normal or cancerous tissue (Guyon et al., 2002). However, it is monotonous to interpret gene expression data directly. To this end, several ML technologies/classifiers have been used to accurately classify whether cancer tissues have distinctive signatures of gene expression over normal tissues in a more simplified manner (Hong et al., 2006). It Is thus paramount to select machine classifiers that can define the most probable overly expressed gene markers to explain the biological pathological contributions to OC. Especially for selecting markers according to statistics or ML algorithms (Lee et al., 2008). These technologies include but are not limited to; ANNs, Bayesian approaches, SVM, Decision Trees, and k nearest neighbours (kNN) (Hong et al., 2006). Table 3.3. outlines the latest ML technologies that have been applied to data generated from DNA microarrays to facilitate a deeper understanding of diagnostic cues in cancer and demonstrates the performance of different ML algorithms and classifiers for optimal OC detection or identification.

Table 3.3. Outlines ML technologies that have been applied to data generated from DNA microarrays to facilitate a deeper understanding of diagnostic cues in cancer.

Machine Classifier	Application	Salient Features	Model outputs	References
CLFNN-DNA Microarray	Classification of cancerous or noncancerous states	The CLFNN generated positive and negative rules capable of producing a relatively superior classification performance due to the lateral inhibition feature existing between the positive and negative fuzzy rule-bases.	Their design involved a positive sample (malignant case) that concurrently activated the positive rules and inhibited the negative rules reducing inference process and produced relatively superior classification performance. In addition, improvements in comprehensibility (when compared to other non-fuzzy methods) and a reasoning process that closely mimics the performance of humans was achieved.	Tan et al., 2008

GA, PSO, SVM, and ANOVA were hybridized to select gene markers from target genes, utilizing a fuzzy model to classify cancerous tissues	Gene selection and classification of OC from microarray data. To identify significant genes, molecular targets or biomarkers that specifically contribute to the reliable classification of OC and to discard irrelevant genes (as many as possible)	In simulation, 200 target genes were obtained after regression analysis and six gene markers which were selected from the hybrid process of GA, PCO, SVM and ANOVA.	The selected gene markers can successively classify invaluable data such as the subtype of ovarian tumours in addition to differentiating between tumour stages.	(Lee et al., 2008; Shah et al., 2004)
A comparison of SVM (with Linear, Polynomial and RBF	The classification of *BRCA1, BRCA2* and Sporadic founder mutation for OC. The *BRCA1* and *BRCA2* are the	This study was made unique by the odd comparison between mutation classification results using GRNN and SVM which are	The study indicates that amongst GRNN, PNN and SVM, the novel GRNN classifier model exhibited maximum accuracies of 100%, 81% and 75% for the pairs *BRCA1-BRCA2,BRCA1*-Sporadic and	Amin et al., 2020; Ghezelayagh et al., 2020; Sehgal et al., 2004.

kernels), GRNN and PNN for the classification of susceptibility genes in OC.	most frequently mutated susceptibility genes in OC. These genes are vital for their correlations to hereditary epithelial OC and is an established predictive biomarker for potential benefit to chemotherapies (such as poly ADP ribose polymerase [PARP] inhibitors), thus routine testing for these gene markers are on the rise . Carriers of the *BRCA1 and BRCA2* genes are	rarely reported in literature as GRNN is primarily used for regression glitches, yet these researchers used GRNN as a classifier. Briefly, an "*AllPairs technique" utilized* 3 pairs viz Pair 1: *BRCA1* and *BRCA2,* Pair 2: *BRCA1* and Sporadic and Pair 3: *BRCA2* and Sporadic	*BRCA2*-Sporadic respectively. These researchers demonstrated additional applications for the GRNN classifier for satisfactory classifications of *BRCA1* and *BRCA2* in OC

	recommended to undergo risk-reducing \salpingo-oophorectomy (RRSO) between the ages of 35–40 and 40–45 years respectively, leading to an improvement in overall mortality.			
ANNs to Predict survival time in OC patients using public microarray and clinical data	Survival analysis is routinely applied for analysing microarray gene expressions to assess cancer outcomes by the time to an event of interest e.g. death. By uncovering the	A total of 15-30 genes (correlation coefficient>0.4) were selected as ANNs input variables to train the software	It was demonstrated that these ANNs can predict survival times from microarray gene expression data with good measurements.	Zhang et al., 2013; Chen et al., 2009

	relationship between gene expression profiles and time of death, allows for the construction of comprehensive survival models which achieve accurate prognosis or diagnosis, and in addition, in identifying suspect genes that are relevant to or predictive of death			
Bayesian network model that was based on The	For the selection of important genetic and epigenetic features related to OC that correlate	Four important data types in the analysis from the TCGA OC data was considered	The constructed Bayesian network successfully identified four gene clusters of distinct cellular functions, 13 driver genes and novel biological	Zhang et al., 2016

Cancer Genome Atlas (TGCA) data library	with the cancer phenotype, leading to discoveries of pathways underlying the molecular mechanism of cancers	pathways which may provide a new insight into OC

Abbreviations: Complementary Learning Fuzzy Neural Network (CLFNN); Genetic algorithm (GA); particle swarm optimization (PSO); analysis of variance (ANOVA); Generalized regression neural network (GRNN); Probabilistic neural network (PNN).

In summary, the niche utilization of untapped clinical data from genetic sources, coupled with AI technologies provides information to better diagnose, detect, manage, and treat a particular patient case with a more profound knowledge and insight. These technologies display further abilities to save predisposed women from contracting the virulent stages of the disease, improving survival and overall health.

3.4.2. Integrating AI and Proteomics Data for OC Diagnosis

Proteomics encompasses the study of expressed proteins, including identification and elucidation of the structure-activity relationships under healthy and diseased conditions, such as in cancer (Celis et al., 2000; Srinivas et al., 2001). In particular, proteomics provides the possibility of identifying disease-associated protein markers to assist in diagnosis or prognosis and to select potential targets for targeted drug delivery (Chambers et al., 2000; Li et al., 2004).

Proteins are frequently the functional molecules and are most likely to reflect differences in gene expression. Genes may be present or mutated, but they are not necessarily transcribed into their final fully functional protein moieties. Some messengers are transcribed but not translated, and the number of mRNA copies does not necessarily correlate to the number of functional protein molecules (Anderson et al., 1997). The latter is a limitation of the cDNA microarray approach, as a result of key transcriptional differences in the tumour that does not accurately reflect the protein observed peripherally, because many protein–protein interactions and post-translational modifications may change the protein patterns found in blood (Wu et al., 2006). To this end, proteomics can provide deeper insight into the detection and diagnosis of OC.

A recent study performed by Alquda and co-workers utilized a wavelet-based statistical features extraction from MS proteomic profiles to compare and contrast the optimal performance between the four most commonly used ML algorithms (ANN, SVM, KNN and ELM) with GA and Principal Components Analysis (PCA) serving as a two-feature selection algorithm. The ML algorithms were applied on low-resolution surface-enhanced laser desorption/ionization–time-of-flight (SELDI-TOF) datasets for OC diagnosis. Based

on the results, the majority of the combined classifier-feature selections systems succeeded with high rates for OC classification based on wavelet features from MS protomeric profiles. The most successful operating algorithm was PCA-SVM, which revealed the best performance (accuracy, sensitivity, and precision), whereas the least performing was PCA-ELM. The researchers concluded that the proposed methods exhibited higher rates of sensitivity, accuracy and precision compared with other reported systems (Table 3.4) (Alqudah et al., 2019).

Table 3.4. Displaying the performance of the Wavelet features with PCA-SVM algorithm in comparison to other algorithms for analysis of proteomic data with different AI models. (Adapted from Alquda and co-workers, 2019).

Method	Accuracy %	Sensitivity %	Specificity %	Reference
Wavelet and linear discernments analysis	98.65	100	97.15	55
Wavelet and quadratic discriminant analysis	98.65	100	97.15	55
Wavelet and ANN	98.65	100	97.15	55
Genetic algorithm, self-organizing cluster analysis, and pattern	97.4	100	95.0	56
SVMGA	95.4	96.0	94.8	57
Spectra with decision tree	81.5	-	-	58
Wavelet features with PCA-SVM	99.0	99.45	100	Proposed

Based on similar principles to test performance of the machine learning classifier in OC detection (accuracy, sensitivity, and specificity), Bhattacharjee and co-workers demonstrated that ANN-based Multi-Layered Perceptrons (MLP) was the most promising compared with SVM, Decision Tree, KNN and Ensemble Classifiers (EN) using MS data from proteomic studies for the diagnosis of OC (Table 3.5). Thus, demonstrating the performance of different algorithms and classifiers for optimal OC detection (Bhattacharjee et al., 2017).

Table 3.5. Comparison of the performance of different machine learning models (adapted from Bhattacharjee and co-workers, 2017).

Name of Classifier	Accuracy (%)	Sensitivity (%)	Specificity (%)
Neural Network	99.1	100	97.9
Decision Tree: Simple Tree	89.8	93	86
Decision Tree:Medium Tree	86	87.6	84
Decision Tree: Complex Tree	86	87.6	84
DA: Linear Discriminant	87	91.1	81.7
DA: Quadratic Discriminant	90.2	95.4	84.8
SVM: Linear SVM	94	94.9	91.7
SVM: Quadratic SVM	94.4	94.1	89.7
SVM: Cubic SVM	93	92.7	93.4
SVM:Fine Gaussian SVM	86.5	81.9	95.8
SVM: Medium Gaussian SVM	93	95.7	89.9
SVM: Coarse Gaussian SVM	90.7	93.2	82
NNC: Fine KNN	90.7	89.8	92
NNC: Medium KNN	91.6	93.3	89.6
NNC:Coarse KNN	87.9	93.6	82.1
NNC: Cosine KNN	92.1	98.1	86
NNC: Cubic KNN	92.6	94	90.6
NNC: Weighted KNN	93.5	93.5	93.5
EN Classifiers: Boosted Trees	56.3	56.3	0
EN Classifiers: Bagged Trees	91.6	93.3	89.6
EN Classifiers: Subspace Discriminant	93	95.7	89.9
EN Classifiers: Subspace KNN	91.6	91.9	91.3
EN Classifiers: RUSBoosted trees	91.2	92.5	89.5

Alzubaidi and co-workers proposed an intelligent system able to effectively locate predictors and patterns of proteins in serum, derived from proteomic data for the detection of OC. The study assessed the suitability of a hybrid framework that utilized a GA with a

novel extraction Mutual-Information and Linear Discriminant Analysis (MI-LDA) approach to select the most suitable features for identifying the presence of OC. Briefly, experiments were performed using an OC dataset obtained from the FDA-NCI Clinical Proteomics Program Databank. The performance of the hybrid feature selection approach was evaluated using the SVM and the LDA classifier. A comparison of the results revealed that the proposed (MI-LDA)-LDA model (that combines a hybrid extraction-based global optimization algorithm for feature selection and then a LDA for risk prediction) outperformed the (MI-LDA)-SVM model on selecting the maximum discriminative feature subset and achieved the highest predictive accuracy. Despite the success, further work is needed to explore the ability of other ML approaches such as ANN, Naïve Bayes, EN and Decision Trees to identify the best combination for optimal OC detection from serum samples (Alzubaidi et al., 2016).

Wu and co-workers used a clinical data set for the early detection of OC. The data set consists of 216 SELDI-TOF-MS samples. An MS analysis method based on Probabilistic Principal Components Analysis (PPCA) and SVM was proposed and applied to the OC early classification in the dataset. Additionally, a traditional PCA-SVM model was established as a control. Experimentation involved 10 times (10-fold?) training and testing approach to ensure the validity of the OC detection models in comparing the performance between the models. The PCA-SVM model showed 83.34%, 82.70%, and 83.88% accuracy, specificity, and sensitivity, respectively. In contrast, those of the PPCA-SVM model were 90.80%, 92.98%, and 88.97%, respectively. In conclusion the PPCA-SVM model with the SELDI-TOF-MS technology was declared as a prospect for early clinical detection and diagnosis of OC (Wu et al., 2016).

3.4.3. Other AI-Inspired Models as OC Diagnostic Platforms

The five major histo-type classifications for epithelial OC (EOC) include high-grade serous carcinoma (HGSC), endometrioid carcinoma, clear cell carcinoma, mucinous carcinoma, and low-grade serous carcinoma (LGSC). These classes have distinct features in their surface morphology, etiology and biological activities (Kurman et al., 2014). The need in clinical practice is to mitigate concerns relating to the lack of histotype-specific and/or

stage-tailored treatment options as the majority of EOC patients are treated with a conventional "*one-size fits all*" approach (Grunewald et al., 2017).

To this end, Kawakami and co-workers highlighted diverse systemic biomarkers suitable to construct a predictive framework for clinical stage, histo-type, residual tumour burden, and prognosis using ML methods for advanced OC diagnosis. A total of 334 patients with EOC and 101 patients with benign OC tumours were randomly assigned to "training" and "test" cohorts. In addition, 7 supervised ML classifiers, including Gradient Boosting Machine (GBM), SVM, Random Forest (RF), Conditional RF (CRF), Naïve Bayes, Neural Network, and Elastic Net were used to derive diagnostic and prognostic data from 32 parameters (mined from pre-treatment peripheral blood tests). Ensemble methods combining weak Decision Trees such as GBM, RF and CRF showed the best performance in EOC predictions (Kawakami et al., 2019).

Wu and co-workers also utilized CADs from Deep Convolutional Neural Networks (DCNN) to detect OC histo-types based on cytological images. The DCNN constituted 5 convolutional layers, 3 max pooling layers, and 2 full reconnect layers (Figure 3.3). The testing results were obtained by the proposed method of 10-fold cross-validation, displaying the accuracy of classification models was improved from 72.76 to 78.20% by using augmented images (opposed to the original images) as the training data, highlighting the usefulness of this data augmentation in the prediction OC histo-type (Wu et al., 2018).

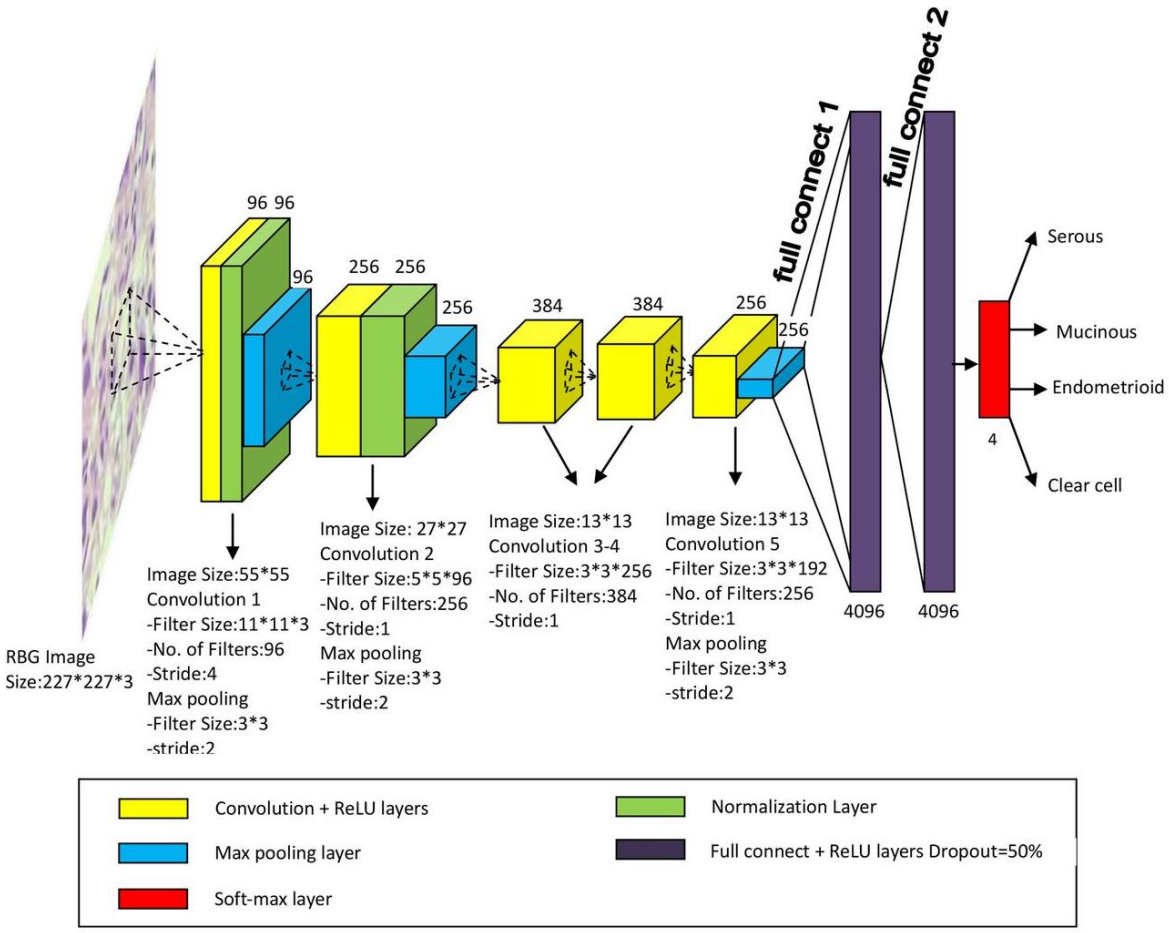

Figure 3.3. The architecture and illustration of DCNN for OC images classification (with permission from Wu et al., 2018).

Despite the advances in both OC diagnosis and therapy, the majority of OC patients still relapsed (Colombo et al., 2017). To build on this foundation, Bogani and co-workers (2018) used data supporting that complete cytoreduction (CC) at the time of secondary cytoreductive surgery (SCS) improved the survival in patients affected by recurrent OC (ROC). Using ANN, disease-free intervals were discovered to be the most important factor predicting OC. However, further studies on this project are necessary to estimate the clinical utility of AI in providing aid in decision making processes (Bogani et al., 2018).

ML algorithms have also been used to accurately classify benign and malignant tumours in OC from ultrasound imaging data (Chu et al., 1990). This technique denoised images using wavelet transform and grey level texture features extracted using a Grey Level Co-

occurrence algorithm (GLCM). Extracted features and selected non-redundant features (selected through Relief-F) underwent training through SVM systems as shown in (Figure 3.4).

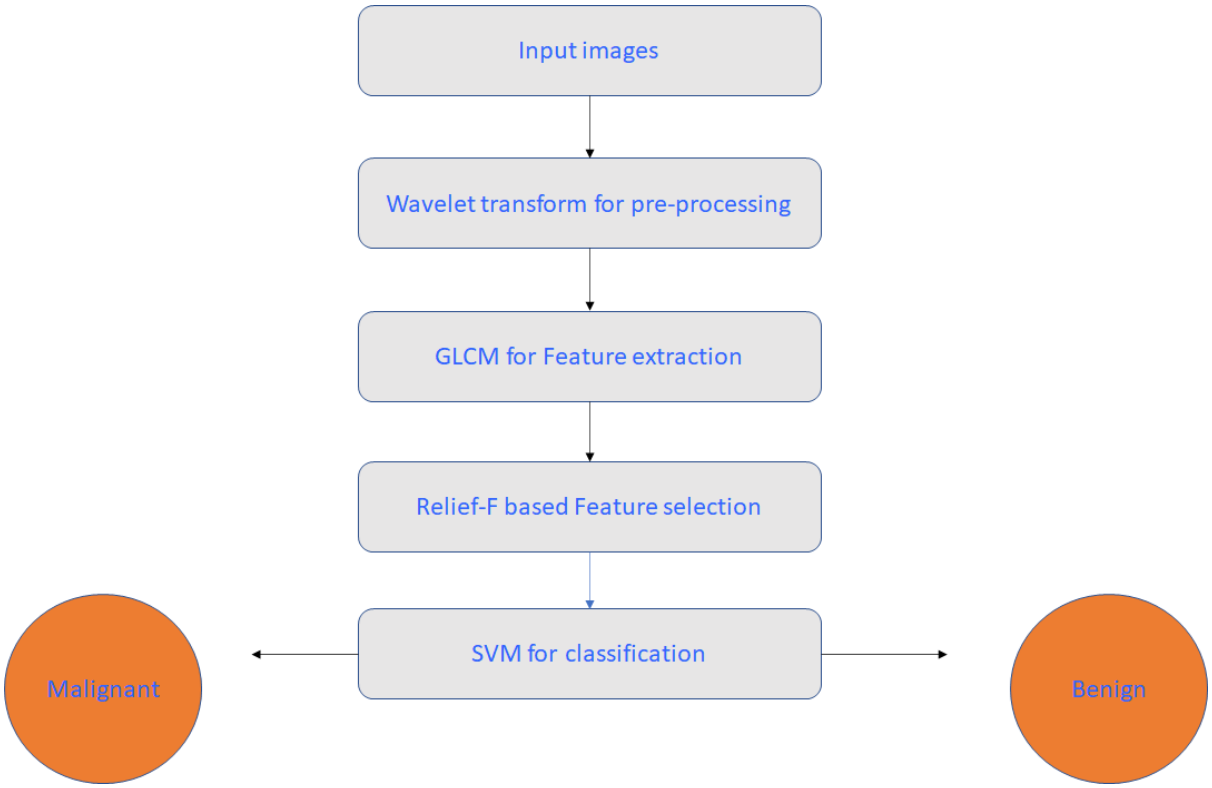

Figure 3.4. Highlighting the various steps for identification of ovarian mass (adapted with permission from Pathak et al., 2015).

This proposed technique was validated on 60 malignant and 60 benign images of patients. On evaluating the classifier for 14-texture descriptors this gave rise to 74% and relief-F produced an accuracy of 82%. The selection of 6 features from the list of 14 features demonstrated an accuracy value of 86% and relief-F generated 92% accuracy, highlighting the all-round effectiveness of this approach (Pathak et al., 2015).

Apart from ultrasound and cytological imaging, other imaging techniques such as confocal microscopy are routinely used to create ultra-high-quality optical images of cancerous cells and tissues (Dickensheets et al., 1996, Webb et al., 1995). A major advantage in confocal microscopy is that large segments of the ovary can be imaged and aids in diagnosis (Zheng et al., 1997).

Srivastava and co-workers introduced a real-time CAD model to facilitate detection of OC using confocal microscopy. The cellular structure in ex vivo confocal images is modelled as texture and features were extracted based on first-order statistics, spatial gray-level-dependence matrices and spatial-frequency content (Srivastava et al., 2008). Selection of the features was performed using stepwise discriminant analysis, forward sequential search, a non-parametric method, PCA and a heuristic technique that holistically combined the outputs of these methods. The selected features were used for classification, and the performance of various machine classifiers was compared by analysing areas under their receiver operating characteristic curves. The machine classifiers studied included LDA, quadratic discriminant analysis, and the *k*-nearest-neighbour algorithm. The results suggest it is possible to automatically identify pathology based on textural features extracted from confocal images and that the machine performance is superior to that of a human observer (Srivastava et al., 2008).

3.5. Artificial Intelligence and Nanotherapeutics for Ovarian Cancer

Advanced nano-enabled drug delivery systems (nanotherapeutics) and active targeting approaches to combat OC have been reported previously (Hoosen et al., 2018). However, the integration of nanotherapeutics with AI provides a new paradigm for modern nanomedicine. A review published by Hassanzadeh and co-workers (2019) highlighted the key features and superior characteristics of AI inspired drug delivery systems and how various ML algorithms utilize drug delivery data such as drug concentrations and particle size to overcome concerns relating to drug release (Hassanzadeh et al., 2019)(Rafienia et al., 2010). However, there are limited studies highlighting the use of AI specifically in targeting cancers such as OC.

3.5.1. Machine Learning of nanotherapeutics

Numerous investigations have linked cell distribution profiles of anticancer drugs to controlled drug entrapment in nanoparticles (NPs). The rationale behind this approach is to increase antitumor efficacy, while reducing systemic side-effects (Brigger et al., 2012). Cancer nanotherapeutics are rapidly progressing and are being implemented to solve several limitations of conventional drug molecules including non-specific biodistribution

and targeting, lack of water solubility, poor oral bioavailability, low therapeutic indices, and sub-optimal bioavailability. For instance, NPs have been designed for optimal size and surface characteristics to increase circulation time in the bloodstream, leading to successful prognosis (Cho et al., 2008). However, nanoscale biophysical and biochemical interaction characteristics containing nanomaterials behave distinctly, with some added complexity in contrast to conventional molecules used in drug delivery (de la Iglesia et al., 2014). Engineering and predicting the collective behaviour of various NPs interacting in complex tumour environments is unpredictable, even for a straightforward nanosystem. Using a systems approach, researchers have explored NP designs using crowdsourcing and ML, document the resulting collective behaviours in simulation and directly test the top candidates experimentally through fast prototyping of both the NPs and their target tumour ecosystem (Hauert et al., 2014).

The use of ML is gaining much momentum in nanomedicine applications for rational based formulation design (Santana et al., 2019), particularly in using untapped data, rapidly analysing it, and producing new results (Hathout et al., 2016). Yamankurt and co-workers described a novel approach for synthesizing a library of spherical nucleic acids (SNAs) NPs that are qualitatively similar but structurally different. AMS-based screening protocol that quantitatively determines SNA-NPs-Toll-likereceptor-9 (TLR9) interaction was utilized. ML led to the advanced analysis of the data library with the non-intuitive and nonlinear particulars of the structural variations of SNA-NPs on TLR9 activation. Identification of these relationships/interactions were achieved due to the parallel examinations of multiple variables. Collectively, the results provide key insights in the intelligent design of SNA-based nanotherapeutics. Since this methodology can be diversified to a variety of nanotherapeutics, the work points towards a new manner of designing and optimizing SNAs for a wide variety of applications (Yamankurt et al., 2019).

Supervised ML combined with X-ray absorption near-edge structure (XANES) spectroscopy also served as the tool to design a 3D geometry of crystals for textbook metallic NPs. *Ab initio* XANES simulation training techniques allowed Timoshenko and co-workers to solve the structure of a metal catalyst from its experimental XANES (Figure 3.5). This was demonstrated by reconstructing the average size, shape, and morphology

of well-defined platinum NPs. This method is widely applicable as it can be generalized to other nanoscale systems (Timoshenko, et al., 2017).

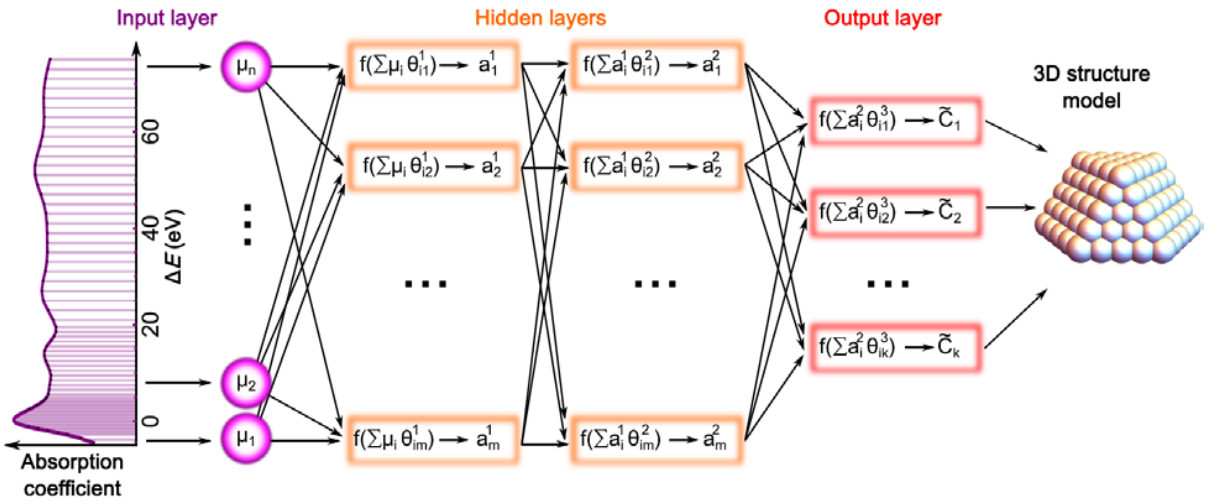

Figure 3.5. Schematic representation of artificial neural network –based method for prediction of nanoparticle size and shape. Pre-processed XANES spectrum for a nanoparticle is discretized and used to set the values of neural network (NN) nodes in the input layer.The input is then processed in the NN hidden layers. Each hidden node represents a function, which adds together the node inputs, weighted with $\theta\theta$, applies to the sum the activation function f, and returns the result as a real number a to be used by NN nodes in the subsequent layers. Hidden layers map the input to the output – set of predicted average coordination numbers $\boldsymbol{C_i}$. Average coordination numbers are then used to determine the size and shape of the nanoparticle (with permission from Timoshenko, et al., 2017)

Although defining the size, sharp and other physical/morphological characterizations of NPs is paramount, in silico simulations of complementary interaction of the NPs to their target receptor is a vital initial step in pre-formulation, dictating the fate of the NP for enhanced endocytosis and selectivity (Oh et al., 2014). Sparse ML methods are used to computationally model surface chemistry-uptake relationships, to make quantitative predictions of uptake for new NPs surface chemistries, and to elucidate molecular aspects of the interactions (Le et al., 2015). These understandings are extremely important considerations in the tailor making process for targeted NPs. The combination of combinatorial surface chemistry modification and ML models facilitate the rapid development of targeted theragnostic, as described by Le and co-workers as ML was

used to optimize the uptake of gold NPs to target four common cancer cell lines (three having high levels of folate receptors expression). The researchers generated models with high predictivity for cancer cell uptake, providing an important proof of concept for computational approaches based on sparse ML methods (Le et al., 2015).

In light of NPs for cancer co-therapy with vitamins which show potential advantageous adjuvant effects on chemotherapy. Santana and co-workers proposed a combined Perturbation Theory Principles (PTP) and ML to develop a perturbation-theory machine learning (PTML) model for rational selection of the components of cancer co-therapy drug–vitamin release nano-systems (DVRNs). A LDA algorithm was used to seek the PTML model. Using two data sets, the researchers produced a PTML model that displayed high specificity, sensitivity, and accuracy. Yielding one-of-the-first general purpose model for the rational design of DVRNs for cancer co-therapy (Santana et al., 2019).

3.5.2. Artificial Neural Networks for Nanotherapeutics Targeting Cancer

ANN can be used as an alternative statistical approach for design and simulations of advanced drug delivery nanosystems (Sun et al., 2003). For instance, a major concern for most researchers in the field of nanotechnology is the uncertain effects of nanoparticles on safety and accumulation in organs over prolonged exposure has been an uncertain debate. Several preliminary studies have highlighted several toxic effects of nano-scale particles. For instance, carbon nanomaterials (nanotubes and fullerene), titanium, quantum dots, ultrafine polystyrene and ultrafine particulate pollutants can interrupt cell function, causing cell membrane and DNA damage mainly through oxidative stress and lipid peroxidation (Lin et al., 2006). Concu and co-workers developed a quantitative structure–toxicity relationships (QSTR)-perturbation model based on ANNs, where predicting the general toxicity profiles of NPs under diverse experimental conditions was undertaken (Figure 3.6). The model was derived from 54,371 NP-NP pair cases generated by applying the perturbation theory to a set of 260 unique NPs. An accuracy of >97% in both training and validation sets was achieved. To validate the application of the QSTR-perturbation model for other nano-scale particles, the toxic effects of several NPs not included in the original dataset was predicted. The theoretical

results obtained for this independent set are strongly consistent with the experimental evidence found in the literature, suggesting that the present QSTR-perturbation model can be viewed as a promising and reliable computational tool for probing the toxicity of NPs (Concu et al., 2017).

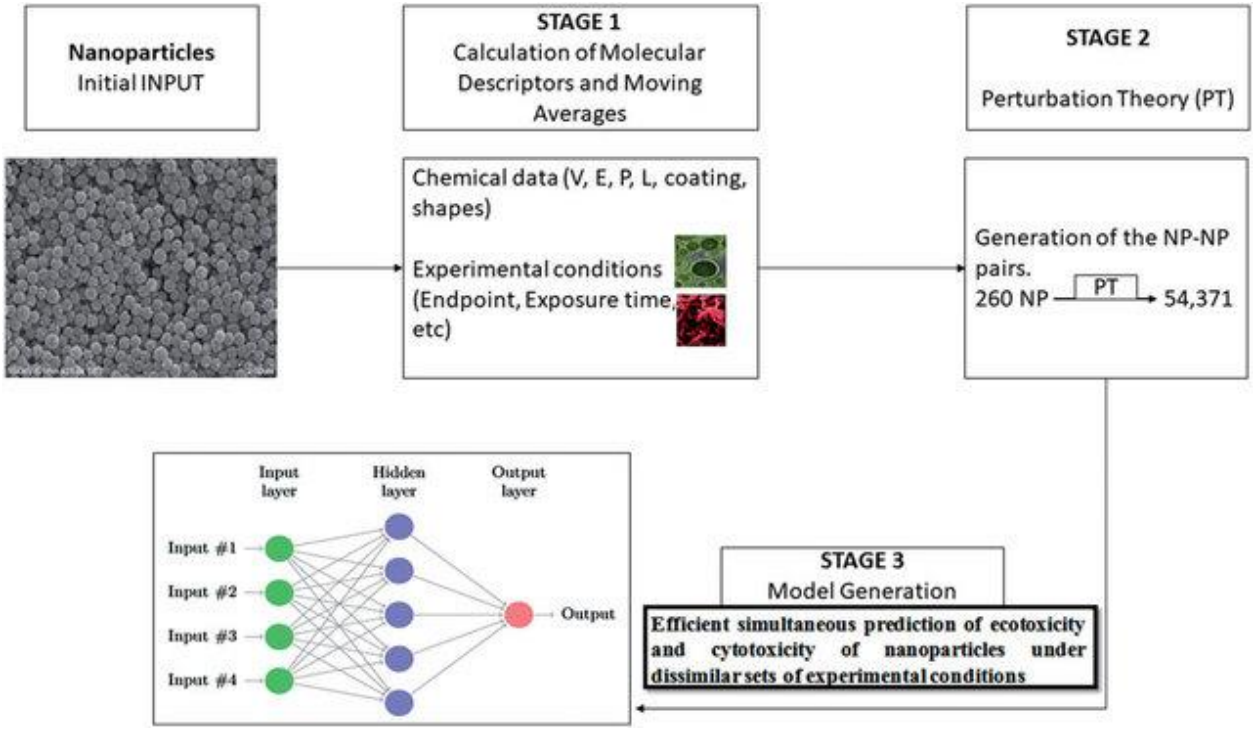

Figure 3.6. A graphical summary of the main stages involved in the setting-up of the QSTR-perturbation model based on ANNs (With permission from Concu et al., 2017).

ANNs were constructed and tested for their ability to predict particle size and entrapment efficiency for di- and tri- block copolymers based on polyethylene glycol and polylactide NPs loaded with noscapine. Molecular weight of the polymer, ratio of polymer to drug, and number of blocks that make up the polymer served as drug delivery factors utilized to train the network. Using ANNs, it was discovered that polymer molecular weight has the greatest effect on particle size. In addition, polymer to drug ratio was found to be the most critical factor on drug entrapment efficiency. This study demonstrated the ability of ANNs to predict not only the particle size of the formed NPs but also the drug entrapment efficiency, which has major implications on therapeutic efficacy (Shalaby, et al., 2014).

Paclitaxel (PTX) was loaded into poly-lactic-co-glycolic acid (PLGA) NPs. The optimal coating process of chitosan (CS) onto PLGA NPs was investigated by a QbD approach

(employing ANNs). Inputs to train the software included CS/PLGA ratios, temperature, and pH, whilst particle size, zeta potential, polydispersity index (PDI), encapsulation efficiency, and loading capacity served as the selected outputs. Data analysis was performed using Modde 8.0 concurrently with ANNs such as INform 3.1 and FormRules 2.0. Furthermore, enhancement of cytotoxicity, cellular uptake, and apoptosis by CS coating was also determined. The results confirmed the influence of inputs on output ($R^2 > 90\%$). The optimized formulation showed particle size of 161.53 ± 0.97 nm, PDI of 0.270 ± 0.007, Zeta potential of 41.87 ± 1.42 mV, and entrapment efficiency of $98.59 \pm 0.22\%$; the results were close to the predicted calculations. The optimal formulation: CS-PLGA NPs, showed higher cytotoxicity than PLGA NPs in Hela and SK-LU-1 cell-lines (cell viability assay). Furthermore, apoptosis and intracellular uptake studies confirmed enhancement of the CS layer. Thus, displaying the potential benefits of ANNs to superior performing anti-cancer therapeutics (Nguyen et al., 2019).

Baharifar and co-workers developed an albumin-loaded chitosan NP. These researchers demonstrated the effects of four independent variables (i.e., chitosan and albumin concentrations, pH, and reaction time) on three dependent variables (i.e., particle size, loading efficiency, and cytotoxicity) by using ANNs. Results demonstrated that the most influential factors that affect the dependent variables are the polymer and drug concentrations. For instance, a drop in the concentrations decreases the size directly, but they simultaneously decrease loading efficiency and increase cytotoxicity. Therefore, optimizations of the independent variables are mandatory in the pre-formulation stages to achieve well performing nano-scale formulation (Baharifar et al., 2017).

3.6. Pharmacokinetic Modelling Approaches for Nano-Therapeutics Against Ovarian Cancer

A considerable body of research on the pharmacokinetics and pharmacodynamics of chemical compounds for the treatment of OC including, but not limited to, niraparib (Longoria et al., 2018), paclitaxel (Ansaloni et al., 2015) and carboplatin (Joerger et al., 2007) and others.

Nanomaterials are highly promising, not only because of their therapeutic properties *per se*, in terms of having a desired effect on cancer cells, but can also have a higher specificity and affinity to target cancer cells, higher permeability leading to higher bioavailability and favourable intra-tumoural delivery propertie (Gupta et al,. 2019).

Several drug delivery nano-carriers have also been proposed to deliver conventional chemotherapeutics(Yao et al., 2018; Engelberth et al., 2014) In other cases, nanomaterials can serve as primary and active therapeutic agents: for example Pradeep and co-workers propose the administration of nano-systems to bind to highly anionic CS-E to form a polyelectrolyte complex so as to inhibit the formation of ovarian tumour spheroids responsible for mesothelial clearance and OC progression (Pradeep et al., 2016).

The availability of pharmacokinetic and pharmacodynamic models is essential so that we can design appropriate dosing regimens that achieve the therapeutic objectives (such as, retention of the concentration of the drug in a certain tissue within a “therapeutic window” of concentrations for a certain period of time) without exceeding certain safety limits in other tissues and avoiding over-accumulation (Sopasakis et al., 2014; Sopasakis et al., 2012).

Nevertheless, most studies are empirical and do not provide insights into the mechanisms of absorption, distribution and excretion, while there is a dearth of mathematical models that describe the pharmacokinetics of such drugs. Joerger and co-workers**,** are among the few exceptions in the pertinent literature where there have been attempts at identifying a pharmacokinetic model for paclitaxel and carboplatin (Joerger et al., 2007).

At the same time, the profusion of combinations of (nano) drugs, nano-carriers and administration routes make it difficult to establish a common pharmacokinetic/ pharmacodynamic modelling framework. Nanomaterials have received great attention as it is becoming evident that their favourable ADME properties may fall short in light of their complicated accumulation patterns and toxic effects in certain tissues (Yuan et al., 2019; Riviere et al., 2009; Marcato et al., 2014; Li et al., 2008; Kang et al., 2015). We can identify two large classes of pharmacokinetic models that are used for nanomaterials: simple

compartmental models (Malfatti et al., 2012) and physiologically based pharmacokinetic (PBPK) models (e.g., Yuan et al., 2019). PBPK models for nanodrugs (Dogra et al., 2020; Dogra et al., 2019), offer a holistic modelling framework, but require highly intrusive sampling from across the whole body to be identified which justifies why they are scarcer in the literature.

The presence of non-exponential accumulation patterns that is observed in a number of drugs such as amiodarone, diclofenac, propofol, valproic acid and bumetanide has revealed certain anomalous diffusion mechanisms at play, which manifest themselves by a polynomial-rate (sub-exponential) clearance Sopasakis et al., 2014; Weiss 1999). It turns out that such non-standard pharmacokinetic behaviour can be accurately and elegantly modelled in terms of non-integer-order derivatives ushering in what is now known as “fractional pharmacokinetics” (Sopasakis et al., 2018).

Non-integer-order (also known as “fractional-order”) derivatives, unlike integer-order derivatives, are non-local operators in the sense that the knowledge of the drug concentration in a small window of time is not sufficient to determine their value. This way, they can model drug distribution patterns with long-memory effects. There is no unique definition of a fractional-order derivative; instead, several definitions are used in the literature, the most common being the Riemann-Liouville, Caputo and Grünwald-Letnikov definitions. The Riemann-Liouville fractional-order derivative hinges on the definition of the namesake fractional-order integral of order $a > 0$ which is given by the following integral:

Eq. 3.1. $$(0RLI_t^a f)(t) = \frac{1}{\Gamma(a)} \int_0^t \quad (t-\tau)^{a-1} f(\tau) d\tau.$$

In other words, the Riemann-Liouville integral of order a is a scaled convolution of f with t^{a-1}. Then, the Riemann-Liouville derivative of order a is defined as $0RLD_t^a = D \circ 0RLI_t^a$, where D is the standard first-order derivative. The Caputo definition, $0CD_t^a = 0RLI_t^a \circ D$, is one where we swap the order of differentiation and integration. The practical implication is that Caputo-derivative-based fractional-order initial value problems are well posed. It can be seen from the definition that non-integer-order derivatives are not local operators, i.e., they cannot be described by mere knowledge of f in a neighbourhood of a time

instant t. For that reason, they can be used to describe dynamical systems with infinite memory.

The structure of a simple two-compartment fractional-order PK model is shown below where we see that the diffusion from Compartment 2 to the central compartment (Compartment 1) is governed by a fractional-order kinetics (Figure 3.7).

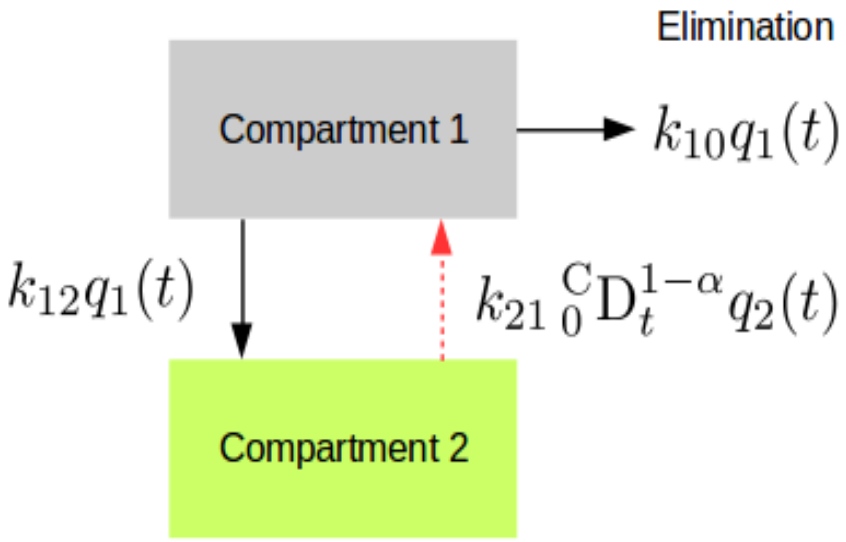

Figure 3.7. Fractional-order two-compartment pharmacokinetic model.

Note that the above fractional-order dynamical model is reminiscent of classical compartmental pharmacokinetic models; this allows one to make use of intuitive concepts of classical pharmacokinetics, however the ‘‘fractionalisation’’ does not consist in merely replacing all derivatives by fractional ones. For example, the accumulation of the compound in Compartment 1 is described by:

Eq. 3.2. $$\dot{q}_1 = -k_{10}q_1 - k_{12}q_1 + k_{21}\,{}_0CD_t^{1-a}q_2,$$

for a fractional order $a \in (0,1)$: the accumulation is described by the term $\dot{q}_1$, while $k_{21}\,{}_0CD_t^{1-a}q_2$ corresponds to the diffusion, or otherwise transfer of drug from Compartment 2 to Compartment 1. The pharmacokinetic meaning of the value of a can be sought in anomalous diffusion phenomena – that is, diffusion that does not follow Fick’s

standard model – although other effects such as deep tissue trapping, and processes governed by reactions. Given that the distribution of nanodrugs and nanostructures used in drug delivery is often driven by its diffusion dynamics (Son et al., 2017; Siepmann et al., 2001), this new fractional-order modelling approach can play an important role both in understanding their pharmacokinetics and design of safe and optimal administration regimens (Sopasakis et al., 2016).

3.7. Conclusions

The exploitation of vastly untapped data libraries to draw further insight in the detection, diagnosis and treatment of disease is gaining momentum with ML central to obtaining breakthroughs. AI-inspired detection platforms in OC certainly add significant value in learning patient data, the exploration of personalized medicine, optimized therapies and drug delivery systems, timeous surgical procedures that reduce recurrence, multi targeted formulations and optimal cocktails of existing chemotherapies can be designed and selected. This system-based approach provides a strategic approach to minimize blindside treatments and *one size fits all* therapies. AI-inspired systems provide insights beyond the realms of human intelligence.

3.8. References

Abdollahi, H., Mostafaei, S., Cheraghi, S., Shiri,I., Mahdavi, S.R., Kazemnejad, A., 2018. Cochlea CT radiomics predicts chemoradiotherapy induced sensorineural hearing loss in head and neck cancer patients: A machine learning and multi-variable modelling study, Physica Medica.45, 192-197.

Agatonovic-Kustrin, S., Beresford, R., 2000. Basic concepts of artificial neural network (ANN) modeling and its application in pharmaceutical research. J Pharm Biomed Anal. 22, 717–727.

Alqudah, A.M., 2019. Ovarian Cancer Classification Using Serum Proteomic Profiling and Wavelet Features A Comparison of Machine Learning and Features Selection Algorithms. Journal of Clinical Engineering. 44, 165-173.

Alzubaidi, A., Cosma, G., Brown, D., & Pockley, A. G., 2016. A new hybrid global optimization approach for selecting clinical and biological features that are relevant to the effective diagnosis of ovarian cancer. IEEE Symposium Series on Computational Intelligence (SSCI). Proceedings. Piscataway, NJ: Institute of Electrical and Electronic Engineers. ISBN 9781509042401.

Amin, N., Chaabouni, N., George,A ., 2020. Genetic testing for epithelial ovarian cancer. Best Practice & Research Clinical Obstetrics & Gynaecology. 65, 125-138.

Anderson, L., Seilhamer J. A., 1997. comparison of selected mRNA and protein abundances in human liver. Electrophoresis. 18, 533-537.

Ansaloni, L., Coccolini, F., Morosi, L. et al., 2015. Pharmacokinetics of concomitant cisplatin and paclitaxel administered by hyperthermic intraperitoneal chemotherapy to patients with peritoneal carcinomatosis from epithelial ovarian cancer. Br J Cancer. 112, 306–312.

Antal, P., Verrelst, H., Timmerman, D., Moreau, Y., Huffel, S.V., B. Moor, B.D., Vergote, I., 2000. “Bayesian networks in ovarian cancer diagnosis: potentials and limitations,” Proceedings of the 13th IEEE Symposium on Computer-Based Medical Systems. Houston, TX, USA. 103-108.

Baharifar, H., Amani, A., 2017. Size, Loading Efficiency, and Cytotoxicity of Albumin-Loaded Chitosan Nanoparticles: An Artificial Neural Networks study. Journal of Pharmaceutical Sciences.106, 411-417.

Bast, R. C., Klug, T. L., John, E. S., Jenison, E., Niloff, J. M., Lazarus, H., Berkowitz, R. S., Leavitt, T., Griffiths, C. T., Parker, L., Zurawski, V. R., & Knapp, R. C., 1983. A Radioimmunoassay Using a Monoclonal Antibody to Monitor the Course of Epithelial Ovarian Cancer. New England Journal of Medicine. 309, 883-887.

Bhattacharjee, S., Singh, Y. J., & Ray, D., 2017. Comparative performance analysis of machine learning classifiers on ovarian cancer dataset. Third International Conference on Research in Computational Intelligence and Communication Networks (ICRCICN). Kolkata. 213-218,

Bogani, G., Rossetti, D., Ditto, A., Martinelli, F., Chiappa, V., Mosca, L., Leone Roberti Maggiore, U., Ferla, S., Lorusso, D., & Raspagliesi, F., 2018. Artificial intelligence weights the importance of factors predicting complete cytoreduction at secondary cytoreductive surgery for recurrent ovarian cancer. Journal of gynecologic oncology. 29, e66.

Brigger, I., Dubernet, C., Couvreur, P., 2012. Nanoparticles in cancer therapy and diagnosis. Advanced Drug Delivery Reviews. 64, 24-36.

Budman, L.I., Kassouf, W., Steinberg, J.R., 2013. Biomarkers for detection and surveillance of bladder cancer. Canadian Urological Association Journal. 2, 212.

Celis, J. E., Kruhøffer, M., Gromova, I., Frederiksen, C., Østergaard, M., Thykjaer, T., Gromov, P., Yu, J., Pálsdóttir, H., Magnusson, N., & Ørntoft, T. F., 2000. Gene expression profiling: Monitoring transcription and translation products using DNA microarrays and proteomics. In FEBS Letters. 480, 2-16.

Chambers, G., Lawrie, L., Cash, P., & Murray, G. I., 2000. Proteomics: A new approach to the study of disease. In Journal of Pathology. 192, 280-8.

Chaudhary, K., Poirion, O.B., Lu, L., Garmire, L.X., 2018. Deep Learning-Based Multi-Omics Integration Robustly Predicts Survival in Liver Cancer. Clin Cancer Res. 24, 1248-1259.

Chen, W., Wang, X., Zhao, B., Zhang, R., Xie, Z., He, Y., Chen, A., Xie, X., Yao, K., Zhong, M., & Yuan, M., 2019. CuS-MnS2 nano-flowers for magnetic resonance imaging guided photothermal/photodynamic therapy of ovarian cancer through necroptosis. Nanoscale. 11, 12983-12989.

Chen, Y. C., Yang, W. W., & Chiu, H. W., 2009. Artificial neural network prediction for cancer survival time by gene expression data. 3rd International Conference on Bioinformatics and Biomedical Engineering, Beijing, 1-4.

Cho, K., Wang, X., Nie, S., Chen Z.G., Shin, D.M., 2008. Therapeutic Nanoparticles for Drug Delivery in Cancer. 14, 1310-1316.

Chu,A ., Greenleaf, J.F., Sehgal, C.M., 1990. Use of Gray Value Distribution of Run Lengths for Texture Analysis. Pattern Recognition Letter. 11, pp. 415-420.

Coccia, M., 2019. Artificial intelligence technology in cancer imaging: Clinical challenges for detection of lung and breast cancer. In Journal of Social and Administrative Sciences. 6, 82-89.

Colombo, N., Lorusso, D., Scollo, P., 2017. Impact of recurrence of ovarian cancer on quality of life and outlook for the future. International Journal of Gynecological Cancer. 27, 1134–1140.

Compton, C., 2003. Colorectal Carcinoma: Diagnostic, Prognostic, and Molecular Features. Mod Pathol.c. 16, 376–388.

Concu, R., Kleandrova, V. V., Speck-Planche, A., & Cordeiro, M. N. D. S., 2017. Probing the toxicity of nanoparticles: a unified in silico machine learning model based on perturbation theory. Nanotoxicology. 11, 891–906.

Dande, P and Samant, P., 2018. Acquaintance to Artificial Neural Networks and use of artificial intelligence as a diagnostic tool for tuberculosis: A review. Tuberculosis. 108, 1-9.

Fishman, D.A., Cohen, L., Blank, S.V., Shulman, L., Singh, D., et al., 2005. The role of ultrasound evaluation in the detection of early-stage epithelial ovarian cancer. American Journal of Obstetrics and Gynecology. 192, 1214-1221.

Davoudizadeh, T., Sajjadi, S.M. & Ma'mani, L., 2018. Exhaustive investigation of drug delivery systems to achieve optimal condition of drug release using non-linear generalized artificial neural network method: feedback from the loading step of drug. J IRAN CHEM SOC. 15, 1999–2006.

de la Iglesia, D., García-Remesal, M., Anguita, A., Muñoz-Mármol, M., Kulikowski, C., & Maojo, V., 2014. A machine learning approach to identify clinical trials involving nanodrugs and nanodevices from ClinicalTrials.gov. PloS one. 9, e110331.

Dickensheets, D.L., Kino, G.S., 1996. Micromachined scanning confocal optical microscope," Opt. Lett. 21, 764-766.

Dogra, P., Butner, J. D., Chuang, Y., Caserta, S., Goel, S., Brinker, C. J., Wang, Z., 2019. Mathematical modeling in cancer nanomedicine: a review. Biomedical Microdevices, 21. 40.

Dogra, P., Butner, J. D., Ruiz Ramírez, J., Chuang, Y., Noureddine, A., Jeffrey Brinker, C., Wang, Z., 2020. A mathematical model to predict nanomedicine pharmacokinetics and tumor delivery. Computational and Structural Biotechnology Journal. 18, 518–531.

Engelberth, S. A., Hempel, N., & Bergkvist, M., 2014. Development of nanoscale approaches for ovarian cancer therapeutics and diagnostics. Critical reviews in oncogenesis.19, 281–315.

Enshaei, A., Robson, C.N. & Edmondson, R.J., 2015. Artificial Intelligence Systems as Prognostic and Predictive Tools in Ovarian Cancer. Ann Surg Oncol. 22, 3970–3975.

Esnaashari, S.S., Amani, A., 2018. Optimization of Noscapine-Loaded mPEG-PLGA Nanoparticles and Release Study: a Response Surface Methodology Approach. J Pharm Innov. 13, 237–246.

Fu, Y., Patel, B.K., Wu, T., Li, J., Gao F., 2020. Advanced Medical Imaging Analytics in Breast Cancer Diagnosis. In: Smith A. (eds) Women in Industrial and Systems Engineering. Women in Engineering and Science. 301-319.

Ganggayah, M.D., Taib, N.A., Har, Y.C. et al., 2019. Predicting factors for survival of breast cancer patients using machine learning techniques. BMC Med Inform Decis Mak. 19, 48.

Ghezelayagh, T., Stewart, L., Yu, V., Agnew, K. J., Norquist, B. M., Pennington, K., & Swisher, E. M., 2020. Perceptions of risk and reward in BRCA1 and BRCA2 mutation carriers choosing salpingectomy for ovarian cancer prevention. Gynecologic Oncology. 19, 143-151.

Grunewald, T., Ledermann, J.A., 2017. Targeted therapies for ovarian cancer. Best Pract Res Clin Obstet Gynaecol. 41,139–52.

Gupta, S., Pathak, Y., Gupta, M. K., & Vyas, S. P., 2019. Nanoscale drug delivery strategies for therapy of ovarian cancer: conventional vs targeted. Artificial Cells, Nanomedicine, and Biotechnology. 47, 4066–4088.

Guyon, I., Weston, J., Barnhill, S., 2002. Gene Selection for Cancer Classification using Support Vector Machines. Machine Learning. 46, 389–422.

Hassanzadeh, P., Atyabi, F., Dinarvand, R., 2019. The significance of artificial intelligence in drug delivery system design. Advanced Drug Delivery Reviews. 151–152, 169-190.

Hathout, R.M., Metwally, A.A., 2016. Towards better modelling of drug-loading in solid lipid nanoparticles: Molecular dynamics, docking experiments and Gaussian Processes machine learning. European Journal of Pharmaceutics and Biopharmaceutics. 108, 262-268.

Hauert, S., Bhatia, S. N., 2014. Mechanisms of cooperation in cancer nanomedicine: towards systems nanotechnology. Trends in Biotechnology. 32, 448–455.

Hirasawa, T., Aoyama, K., Tanimoto, T., Ishihara, S., Shichijo, S., Ozawa, T., Ohnishi, T., Fujishiro, M., Matsuo, K., Fujisaki, J., & Tada, T., 2018. Application of artificial intelligence using a convolutional neural network for detecting gastric cancer in endoscopic images. Gastric Cancer. 21, 653-660.

Ho, H.N., Tran, T.H., Tran, T.B., Yong, C.S., Nguyen, C.N., 2015. Optimization and characterization of artesunate-loaded chitosan-decorated poly (D, L-lactide-co-glycolide) acid nanoparticles. J Nanomater. 2015, 1–12.

Hong, J. H., & Cho, S. B., 2006. The classification of cancer based on DNA microarray data that uses diverse ensemble genetic programming. Artificial Intelligence in Medicine. 36, 43-58.

Hoosen, Y., Pradeep, P., Kumar, P., du Toit, L.C., Choonara, Y.E., Pillay, V., 2018. Nanotechnology and Glycosaminoglycans: Paving the Way Forward for Ovarian Cancer Intervention. Int. J. Mol. Sci. 19, 731.

Horie, Y., Yoshio, T., Aoyama, K., Yoshimizu, S., Horiuchi, Y., Ishiyama, A., Hirasawa, T., Tsuchida, T., Ozawa, T., Ishihara, S., Kumagai, Y., Fujishiro, M., Maetani, I., Fujisaki, J., & Tada, T., 2019. Diagnostic outcomes of esophageal cancer by artificial intelligence using convolutional neural networks. Gastrointestinal Endoscopy. 89, 25-32.

Hoskins, W. J., 1995. Prospective on ovarian cancer: Why prevent? Journal of Cellular Biochemistry. 59, 189-199.

Hothorn, T., & Lausen, B., 2003. Bagging tree classifiers for laser scanning images: a data- and simulation-based strategy. Artificial Intelligence in Medicine. 27, 65–79.

Huang, C., Clayton, E.A., Matyunina, L.V., et al., 2018. Machine learning predicts individual cancer patient responses to therapeutic drugs with high accuracy. Sci Rep. 8, 16444.

Huang, S., Yang, J., Fong, S., & Zhao, Q., 2020. Artificial intelligence in cancer diagnosis and prognosis: Opportunities and challenges. In Cancer Letters. 471, 61-71.

Jafari, M., Hasanzadeh, M., Solhi, E., Hassanpour, S., Shadjou, N., Mokhtarzadeh, A., Jouyban, A., & Mahboob, S., 2019. Ultrasensitive bioassay of epitope of Mucin-16 protein (CA 125) in human plasma samples using a novel immunoassay based on silver conductive nano-ink: A new platform in early stage diagnosis of ovarian cancer and efficient management. International Journal of Biological Macromolecules. 126, 1255-1265.

Jermal, A., Murray, T., Samuels. A., Ghafoor, A., Ward, E., Thun, M.J, 2003. Cancer statistic, 2003. CA: Cancer Journal for Clinician.13, 5-26.

Joerger, M., Huitema, A. D. R., Richel, D. J., Dittrich, C., Pavlidis, N., Briasoulis, E., Schellens, J. H. M., 2007. Population Pharmacokinetics and Pharmacodynamics of Paclitaxel and Carboplatin in Ovarian Cancer Patients: A Study by the European Organization for Research and Treatment of Cancer-Pharmacology and Molecular Mechanisms Group and New Drug Development Group. Clinical Cancer Research. 13, 6410–6418.

Kang, H., Mintri, S., Menon, A. V., Lee, H. Y., Choi, H. S., & Kim, J., 2015. Pharmacokinetics, pharmacodynamics and toxicology of theranostic nanoparticles. Nanoscale. 7, 18848–18862.

Karatzas, P., Melagraki, G., Ellis, L.J.A., Lynch, I., Varsou, D.D., Afantitis, A., Tsoumanis, A., Doganis, P., Sarimveis, H., 2020. Development of Deep Learning Models for Predicting the Effects of Exposure to Engineered Nanomaterials on Daphnia magna.Nano Micro Small. 16, 2001080.

Kavitha, M.S., Shanthini,J., Bhavadharini, R.M., 2020. ECIDS-Enhanced Cancer Image Diagnosis and Segmentation Using Artificial Neural Networks and Active Contour Modelling. Journal of Medical Imaging and Health Informatics. 10, 428-434.

Kawakami, E., Tabata, J., Yanaihara, N., Ishikawa, T., Koseki, K., Iiya, Y., Saito, M et al., 2019. Application of artificial intelligence for preoperative diagnostic and prognostic prediction in epithelial ovarian cancer based on blood biomarkers. Clinical Cancer Research. 25, 3006-3015.

Kondiah, P.J., Kondiah, P.P.D., Choonara, Y.E., Marimuthu, T., Pillay, V. A., 2020. 3D Bioprinted Pseudo-Bone Drug Delivery Scaffold for Bone Tissue Engineering. Pharmaceutics. 12, 166.

Kordy, H.M, Miranbaygi, M., Moradi, M., 2006. Ovarian cancer diagnosis using discrete wavelet transform based feature extraction from serum proteomic patterns. Cairo Int Biomed Eng Conf. 1, 139–142.

Kouznetsova, V.L., Kim, E., Romm, E.L., et al., 2019. Recognition of early and late stages of bladder cancer using metabolites and machine learning. Metabolomics. 15, 94.

Kurman, R.J., Carcangiu, M.L., Herrington, C.S., 2014. World Health Organisation Classification of Tumours of the Female Reproductive Organs. 4th Revised edn, International Agency for Research on Cancer.

Le, T. C., Yan, B., & Winkler, D. A., 2015. Robust Prediction of Personalized Cell Recognition from a Cancer Population by a Dual Targeting Nanoparticle Library. Advanced Functional Materials. 25, 6927–6935.

Lee, Z. J. 2008. An integrated algorithm for gene selection and classification applied to microarray data of ovarian cancer. Artificial Intelligence in Medicine. 42, 81-93.

Li, L, Tang, H, Wu, Z, et al., 2004. Data mining techniques for cancer detection using serum proteomic profiling. Artif Intell Med. 32, 71–83.

Li, L., Tang, H., Wu, Z., Gong, J., Gruidl, M., Zou, J., Tockman, M., & Clark, R. A., 2004. Data mining techniques for cancer detection using serum proteomic profiling. Artificial Intelligence in Medicine. 32, 71-83.

Li, M., & Zhou, Z.H., 2007. Improve Computer-Aided Diagnosis With Machine Learning Techniques Using Undiagnosed Samples. IEEE Transactions on Systems, Man, and Cybernetics - Part A: Systems and Humans. 37, 1088–1098.

Li, S.D., & Huang, L., 2008. Pharmacokinetics and Biodistribution of Nanoparticles. Molecular Pharmaceutics. 5, 496–504.

Lin, W., Huang, Y., Zhou, X.-D., & Ma, Y., 2006. Toxicity of Cerium Oxide Nanoparticles in Human Lung Cancer Cells. International Journal of Toxicology. 25, 451-457.

Longoria, T.C., Tewari, K.S., 2018. Pharmacokinetic drug evaluation of niraparib for the treatment of ovarian cancer. Expert Opin Drug Metab Toxicol. 14, 543-550.

Lu, H., Arshad, M., Thornton, A. et al., 2019. A mathematical-descriptor of tumor-mesoscopic-structure from computed-tomography images annotates prognostic- and molecular-phenotypes of epithelial ovarian cancer. Nat Commun.10, 764.

Lu, M., Fan, Z., Xu, B., Chen,L., Zheng, X., Li, J., Znati, T., Qi Mi, Q., Jiang, J., 2020. Using machine learning to predict ovarian cancer. International Journal of Medical Informatics. 141, 104195.

Malfatti, M. A., Palko, H. A., Kuhn, E. A., & Turteltaub, K. W., 2012. Determining the Pharmacokinetics and Long-Term Biodistribution of SiO2 Nanoparticles In Vivo Using Accelerator Mass Spectrometry. Nano Letters. 12, 5532–5538.

Mangasarian, O.L., Wolberg, W.H., 1990. Cancer diagnosis via linear programming. Center for parallel optermization.

Marcato, P. D., 2014. Pharmacokinetics and Pharmacodynamics of Nanomaterials. Nanomedicine and Nanotoxicology, 97–110.

Martin, N., Diverrez, J.M., Em, S., Pallamin, N., & Ragot, M., 2019. How to Recognize Emotions Without Signal Processing. Neuroergonomics. 191–194.

Mingyao, L., Changyuan, H., Fadia, F., 2020. Skin Cancer Diagnosis Based on Support Vector Machine and a New Optimization Algorithm. Journal of Medical Imaging and Health Informatics. 10, 356-363.

Mnih. V., Kavukcuoglu, k., Silver, D., Rusu, A., Veness, J., et al., 2015. Human-level control through deep reinforcement learning. Nature. 518, 529-533.

Ndesendo, V. M., Pillay, V., Choonara, Y. E., du Toit, L. C., Kumar, P., Buchmann, E., Meyer, L. C., & Khan, R. A., 2012. Optimization of a polymer composite employing molecular mechanic simulations and artificial neural networks for a novel intravaginal bioadhesive drug delivery device. Pharmaceutical development and technology. 17, 407–420.

Nguyen, C.N., Tran, B.N., Do, T.T., et al., 2019. D-Optimal Optimization and Data-Analysis Comparison Between a DoE Software and Artificial Neural Networks of a Chitosan Coating Process onto PLGA Nanoparticles for Lung and Cervical Cancer Treatment. J Pharm Innov. 14, 206-220.

Nilsson, N J., 2010. The Quest for Artificial Intelligence: A History of Ideas and Achievements (Cambridge, UK: Cambridge University Press, 2010).

Oh, N., & Park, J. H., 2014. Endocytosis and exocytosis of nanoparticles in mammalian cells. International journal of nanomedicine. 9, 51–63.

Palanichamy, K., 2019. Integrative Omic Analysis of Neuroblastoma. Computational Epigenetics and Diseases. 9, 311–326.

Pathak, H., Kulkarni, V., 2015. Identification of ovarian mass through ultrasound images using machine learning techniques. IEEE International Conference on Research in Computational Intelligence and Communication Networks (ICRCICN). 137-140.

Petricoin, E. F., Mills, G. B., Kohn, E. C., & Liotta, L. A., 2002. Proteomic patterns in serum and identification of ovarian cancer. The Lancet. 360, 170–171.

Petricoin, E.F., Ardekani A.M., Hitt B.A., et al., 2002. Use of proteomic patterns in serum to identify ovarian cancer. Lancet. 359, 572-577.

Pradeep, P., Choonara, Y. E., Kumar, P., Pillay, V., 2016. “On-the-spot” arresting of chondroitin sulphate proteoglycans: Implications for ovarian adenocarcinoma recognition and intervention. Int. J. Mol. Sci.17.

Rafienia, M., Amiri, M., Janmaleki, M., Sadeghian., 2010. APPLICATION OF ARTIFICIAL NEURAL NETWORKS IN CONTROLLED DRUG DELIVERY SYSTEMS. Applied Artificial Intelligence. 24, 807-820.

Rajpurkar, P., Irvin, J., Ball, R.L., Zhu, K., Yang, B., Mehta, H., Duan, T., Ding, D., Bagul, A., Langlotz, C.P., Patel, B.N., Yeom, K.W., Shpanskaya, K., et al., 2018. Deep learning for chest radiograph diagnosis: A retrospective comparison of the CheXNeXt algorithm to practicing radiologists. PLoS Med. 15, e1002686.

Riviere, J. E., 2008. Pharmacokinetics of nanomaterials: an overview of carbon nanotubes, fullerenes and quantum dots. Wiley Interdisciplinary Reviews: Nanomedicine and Nanobiotechnology. 1, 26–34.

Santana, R., Zuluaga, R., Gañan, P., Arrasate, S., Onieva, E., Gonzalez-Diaz, H., 2019. Designing Nanoparticle Release Systems for Drug-Vitamin Cancer Co-Therapy with Multiplicative Perturbation-Theory Machine Learning (PTML) Models. Nanoscale. 11, 21811-21823.

Sarkar, I. N., Planet, P. J., Bael, T. E., Stanley, S. E., Siddall, M., DeSalle, R., & Figurski, D. H., 2002. Characteristic attributes in cancer microarrays. Journal of Biomedical Informatics. 35, 111-122.

Sehgal, M. S. B., Gondal, I., & Dooley, L., 2004. Statistical neural networks and support vector machines for the classification of genetic mutations in ovarian cancer. 2004 Symposium on Computational Intelligence in Bioinformatics and Computational Biology, La Jolla, CA, USA. 140-146.

Sethi, S., Ali, S., Philip, P.A., Sarkar, F.H., 2013. Clinical Advances in Molecular Biomarkers for Cancer Diagnosis and Therapy. Int. J. Mol. Sci.14, 14771–14784.

Shah, S.C., Kusiak, A., 2004. Data mining and genetic algorithm based gene/SNP selection. Artificial Intelligence in Medicine. 31, 183-196.

Shalaby, K. S., Soliman, M. E., Casettari, L., Bonacucina, G., Cespi, M., Palmieri, G. F., Sammour, O. A., & El Shamy, A. A., 2014. Determination of factors controlling the particle size and entrapment efficiency of noscapine in PEG/PLA nanoparticles using artificial neural networks. International journal of nanomedicine. 9, 4953–4964.

Sharkey, N.E and S. Cross, S., 1998. Adapting an ensemble approach for the diagnosis of breast cancer. In Proc.6th Int.Conf.Artif. Neural Netw. 98, 281–286.

Siepmann J., & Göpferich, A., 2001. Mathematical modeling of bioerodible, polymeric drug delivery systems. Advanced Drug Delivery Reviews. 48, 229-247.

Son, G.H., Lee, B.J., 2017. Mechanisms of drug release from advanced drug formulations such as polymeric-based drug-delivery systems and lipid nanoparticles. J. Pharmaceut. Invest. 47, 287–296.

Sopasakis, P., & Sarimveis, H., 2012. An integer programming approach for optimal drug dose computation. Computer Methods and Programs in Biomedicine. 108, 1022–1035.

Sopasakis, P., & Sarimveis, H., 2016. Stabilising model predictive control for discrete-time fractional-order systems. Automatica. 75, 24–31.

Sopasakis, P., and Sarimveis, H., 2014. Controlled Drug Administration by a Fractional PID, 19th IFAC World Congress, Cape Town, South Africa.

Sopasakis, P., Patrinos, P., & Sarimveis, H., 2014. Robust model predictive control for optimal continuous drug administration. Computer Methods and Programs in Biomedicine. 116, 193–204.

Sopasakis, P., Sarimveis, H., Macheras, P., & Dokoumetzidis, A., 2018. Fractional calculus in pharmacokinetics. Journal of Pharmacokinetics and Pharmacodynamics. 45, 107–125.

Srinivas, P. R., Srivastava, S., Hanash, S., & Wright, J., 2001. Proteomics in early detection of cancer. Clinical Chemistry. 47, 1901–1911.

Srivastava,S., Rodríguez, J.J., Rouse, A.R., Brewer, M.A., Gmitro, A.F., 2008. Computer-aided identification of ovarian cancer in confocal microendoscope images. J. Biomed. Opt. 13, 024021.

Stone, P., Brooks, R., Brynjolfsson, E., Calo, R., Etzioni, O., Hager, G., Hirschberg, J., Kalyanakrishnan, S.; et al., 2016. Artificial Intelligence and Life in 2030. One Hundred Year Study on Artificial Intelligence. Stanford University, Stanford, CA.

Sun, Y., Peng, Y., Chen, Y., & Shukla, A. J., 2003. Application of artificial neural networks in the design of controlled release drug delivery systems. Advanced Drug Delivery Reviews. 55, 1201-1215.

Tan, A. C., & Gilbert, D., 2003. Ensemble machine learning on gene expression data for cancer classification. Applied bioinformatics. 2, 75-83.

Tan, T. Z., Quek, C., Ng, G. S., & Razvi, K., 2008. Ovarian cancer diagnosis with complementary learning fuzzy neural network. Artificial Intelligence in Medicine. 43, 207-222.

Tehrani, A., Karbasi,H., 2017. A novel integration of hyper-spectral imaging and neural networks to process waste electrical and electronic plastics. IEEE Conference on Technologies for Sustainability (SusTech). 1-5.

Timoshenko, J., Lu, D., Lin, Y., & Frenkel, A. I., 2017. Supervised Machine-Learning-Based Determination of Three-Dimensional Structure of Metallic Nanoparticles. The Journal of Physical Chemistry Letters. 8, 5091–5098.

Tomasetti, M., Santarelli, L., 2010. Biomarkers for Early Detection of Malignant Mesothelioma: Diagnostic and Therapeutic Application. Cancers. 2, 523-548.

Turkoglu, M., Aydin, I., Murray, M., Sakr, A., 1999. Modeling of a roller-compaction process using neural networks and genetic algorithms. Eur J Pharm Biopharm. 48, 239–45.

Vlahou, A., Schorge, J.O., Gregory, B.W., Coleman, R., 2003. Diagnosis of ovarian cancer using decision tree classification of mass spectral data. Biomed Res Int. 2003, 308–314.

Wang, P., 2019. On Defining Artificial Intelligence, Journal of Artificial General Intelligence. 10, 1-37.

Wang, S., Liu, Z., Rong, Y., Zhou, B., et al., 2019. Deep learning provides a new computed tomography-based prognostic biomarker for recurrence prediction in high-grade serous ovarian cancer. Radiotherapy and Oncology. 132, 171-177.

Wang, Y., Tetko, I. V., Hall, M. A., Frank, E., Facius, A., Mayer, K. F. X., & Mewes, H. W., 2005. Gene selection from microarray data for cancer classification—a machine learning approach. Computational Biology and Chemistry. 29, 37–46.

Webb, R.H., Rogomentich, F.J., 1995. Microlaser microscope using self-detection for confocality," Opt. Lett. 20, 533-535.

Weiss M., 1999. The anomalous pharmacokinetics of amiodarone explained by nonexponential tissue trapping. Journal of pharmacokinetics and biopharmaceutics. 27, 383–396.

William,W., Ware, A., Basaza-Ejiri, A.H., Obungoloch,J., 2018.A review of image analysis and machine learning techniques for automated cervical cancer screening from pap-smear images,Computer Methods and Programs in Biomedicine. 164, 15-22.

Wu, J., Ji, Y., Zhao, L., Ji, Mengying., Ye, Z.,Li, S., 2016. A Mass Spectrometric Analysis Method Based on PPCA and SVM for Early Detection of Ovarian Cancer. Computational and Mathematical Methods in Medicine. 2016, 6169249.

Wu, M., Yan, C., Liu,H ., Liu, Q., 2018. Automatic classification of ovarian cancer types from cytological images using deep convolutional neural networks. Biosci. 38, BSR20180289.

Wu, S. P., Lin, Y. W., Lai, H. C., Chu, T. Y., Kuo, Y. L., & Liu, H. S., 2006. SELDI-TOF MS profiling of plasma proteins in ovarian cancer. Taiwanese Journal of Obstetrics and Gynecology. 45, 26-32.

Yamankurt, G., Berns, E.J., Xue, A., et al., 2019. Exploration of the nanomedicine-design space with high-throughput screening and machine learning. Nat Biomed Eng. 3, 318–327.

Yao, S., Li, L., Su, X., Wang, K., Lu, Z., Yuan, C., Song, K., 2018. Development and evaluation of novel tumor-targeting paclitaxel-loaded nano-carriers for ovarian cancer treatment: in vitro and in vivo. Journal of Experimental & Clinical Cancer Research. 37.

Yuan, D., He, H., Wu, Y., Fan, J., & Cao, Y., 2019. Physiologically-based pharmacokinetic modeling of nanoparticles. Journal of Pharmaceutical Sciences. 108, 58-72.

Zhang, W., Ota, T., Shridhar, V., Chien, J., Wu, B., & Kuang, R., 2013. Network-based Survival Analysis Reveals Subnetwork Signatures for Predicting Outcomes of Ovarian Cancer Treatment. PLoS Computational Biology. 9, e1002975.

Zheng,Y ., Greenleaf J.F., Gisvold, J.J., 1997. Reduction of breast biopsies with a modified self-organizing map. IEEE Trans. Neural Netw. 8, 1386-1396.

Zhou, Z.H., Jiang, Y., Yang, Y.B., Chen, S.F., 2002. Lung cancer cell identification based on artificial neural network ensembles. Artificial Intelligence in Medicine. 24, 25–36.

CHAPTER 4:

Synthesis and Evaluation of Chondroitin Sulphate-Didodecyldimethyl Ammonium Bromide Nanoconjugates for Potentially Targeted ("On-the-Spot") Therapy in Ovarian Cancer

4.1. Synopsis of The Chapter

This study introduces a novel approach to target OC. The ovarian tumour extracellular matrix (ECM) contains an over-expression of anionic carbohydrate polymers including chondroitin sulphate (CS), which aggressively stimulates OC metastasis. Structurally modified CS was hypothesized to reduce tumour growth, by changing the chemical integrity of the pristine polymer. Inherent with this research was the establishment and characterization of a structurally modified CS backbone with cationic didodecyldimethyl ammonium bromide (DDAB), forming spontaneous polyelectrolyte complexes (PEC or "*arrested CS*"; based on spontaneous [or "*on the spot"*] electrostatic interactions). The PEC (synthesized in physiological pH) was physicochemically (FT-IR, ^{1}H NMR, TGA, DSC), architecturally (SEM, size, zeta potential and EDX) and cytotoxically characterized against CS over-expressed cell lines (SKOV3). In conclusion, DDAB served as a suitable candidate to arrest CS, in addition to being highly cytotoxic against CS-rich SKOV3, with a potential for future use in advanced drug delivery systems targeting CS in OC.

Keywords: Ovarian Cancer; Glycosaminoglycans; Chondroitin sulphate; Polyelectrolyte complex.

4.2. Introduction

To date, the frequency of cancer diagnosis has rapidly escalated, widening the gap between the available therapeutic interventions and the disease occurrence. Despite the success of the recent OC drug delivery systems in literature (Frank et al., 2019;

Alizadeh et al., 2019; Song et al., 2019), OC still remains incurable (Banerjee et al., 2013). The major challenges with the current chemotherapies are issues relating to multiple drug resistance (MDR). A plethora of molecular mechanisms and complex cellular interactions mediate an individual MDR phenotype. Despite the application of new high throughput “omics” technologies which identify multiple new gene/protein expression signatures or factors associated with drug resistance, these findings fail to translate to the development of updated chemotherapeutics (Lage et al., 2008).

Burdened by the aforementioned drawbacks associated with conventional drug molecules, an innovative mechanism introducing non-drug associated therapy was hypothesized to pave the way forward for OC intervention (Pradeep et al., 2016; Hoosen et al., 2018). This mechanistic forecast exploits the OC tumour microenvironment (extracellular matrix (ECM)) region, which houses a rich network of glycosaminoglycans (GAGs), a promising class of molecular targets that contribute directly to the rapid OC dissemination (Vallen et al., 2014). Based on the particular monosaccharides and sulphation patterns, various forms of GAGs are derived, which include: Chondroitin sulphate (CS), Dermatan sulphate (DS), Heparin Sulphate, Keratin sulphate and Hyaluronic acid (Pradeep et al., 2016; Afratis et al., 2012).

CS is a polyanionic water soluble heteropolysaccharide comprising of repeated units of D-glucuronic acid and D-N acetyl galactosamine, with potential for various sulphated positions (C-4 and/or C-6 or C-2 of the N Acetylgalactosamine and the Glucuronic acid moiety respectively) (Athanasia et al., 2008). These give rise to molecules such as CS-A [GlcA-GalNAc-4-sulphate]; CS-C [GlcA-Gal-NAc-6-O-sulphate]; CS-D [GlcA (2-O-sulphate)–GalNAc (6-Osulphate)]; CS-E [GlcA-GalNAc-(4,6)-O-disulfate] or CS-B (IdoA (2-O-sulphate) – GalNAc (6-O-sulphate) (Table 4.1). These sulphation patterns dictate specific interactions with various molecules such as growth factors including vascular endothelial growth factor (VEGF) (Vallen et al., 2014), cytokines, adhesion molecules and lipoproteins (Pradeep et al., 2016; Athanasia et al., 2008).

Table 4.1: Typical sulphation patterns of CS isoforms (Pradeep et al., 2016).

CS Type	Disaccharide Unit	Substituents
CS-A	U = [β1-4]-d-glucuronic acid A = [β1-3]-*N*-acetyl-d-galactosamine	R^2 =H R^4 =  R^6 = H
CS-B/DS	U = [β1-4]-l-iduronic acid A = [α1-3]-*N*-acetyl-d-galactosamine	R^2 =H R^4 =  R^6 = H
CS-C	U = [β1-4]-d-glucuronic acid A = [β1-3]-*N*-acetyl-d-galactosamine	R^2 =H R^4 =H R^6 = 
CS-D	U = [β1-4]-d-glucuronic acid A = [β1-3]-*N*-acetyl-d-galactosamine	R^2 =  R^4 =H R^6 = 
CS-E	U = [β1-4]-d-glucuronic acid A = [β1-3]-*N*-acetyl-d-galactosamine	R^2 =H R^4 =  R^6 = 

Chondroitin sulphate- E (CS-E), is an over-expressed anionic GAG which is implicated in the rapid proliferation and migration of OC cells (van de Steen et al., 2017). CS-E is over-expressed in the tumour stroma and neoplastic cell surfaces (Pradeep et al., 2016). This stromal component is responsible for the vicious tumour progression and metastasis of OC (Vallen et al., 2014). The accelerated biosynthesis of CS-E is due to an over expression of N-acetyl galactosamine 4-sulphate 6-O-sulfotransferase, which is the enzyme responsible for the biosynthesis of CS-E. In OC, elevated CS-E levels correlate to high VEGF levels which is important in tumour spheroid formation and angiogenesis, which is associated with the overly aggressive and invasive characteristics of OC (Vallen et al., 2014). CS-E further aids the adhesion of tumours as it is responsible for increasing the adhesive properties of adhesion molecules N-adherin and E-cadherin. (Pradeep et al., 2016). In addition, integrins also play a role in the enhanced adhesion of cells as they have the ability to interact directly with CS

chains (Vallen et al., 2014). CS-E is responsible for the invasion and migration of tumours. Metalloproteinases (MMPs) is a group of enzymes responsible for OC progression. The activation and regulation are strongly influenced by CS. Furthermore, CS-E is able to interact with MPPs such as pro-MMP7, contributing to the activation and metastasis of tumour cells (Vallen et al., 2014).

To this end, an innovative, non-drug associated hypothesis to target CS was hypothesized. Briefly, the mentioned hypothesis described that targeted nano-archetypes conjugated with various cationic complexing agents will act against OC in a two-way manner. The complexing agent will specifically and locally polyelectrolyte complex (or *"arrest"*) CS-E and will subsequently impede CS-E mediated enhanced OC cell proliferation, migration, and adhesion. In this manner, tumour growth can be retarded. Arrested CS (by PEC) further inhibits CS interactions with various growth factors such as VEGF, with further potential to stop tumour dissemination (Pradeep et al., 2016).

In this study, the spontaneous (or "*on the spot*") process of polyelectrolyte complexation was assessed as a novel mechanism of action for OC inhibition, where didodecyldimethyl ammonium bromide (DDAB), a quaternary ammonium compound, was investigated for its potential to act as a suitable CS integral complexing agent, forming a primary CS-DDAB PEC based on its stable cationic surface charge (Figure 4.1.) (Gossmann et al., 2015). Previously, DDAB has been shown to form a PEC with polysaccharides including xanthan and GAGs (such as hyaluronate [HA] (Papagiannopoulos et al., 2018) and heparin (Ye et al., 2015)). However, a DDAB lipid to CS polymer PEC has not yet been reported in literature. The *"on the spot"* PEC between CS-DDAB, forming spontaneous nanoconjugates was validated. Utilizing FT-IR, DSC, XRD, TGA and SEM, certification of the PEC formation was achieved based on electrostatic interactions between negative charge densities on CS and the stable cationic surfaces on DDAB. Assessment of the physical stability of the PEC at 37 °C utilizing Turbiscan and Zeta Potential analysis was conducted. Lastly, the potential of DDAB to inhibit the growth of CS-E over-expressed (ten Dam et al., 2007) cells were evaluated, yielding a considerably low IC_{50}.

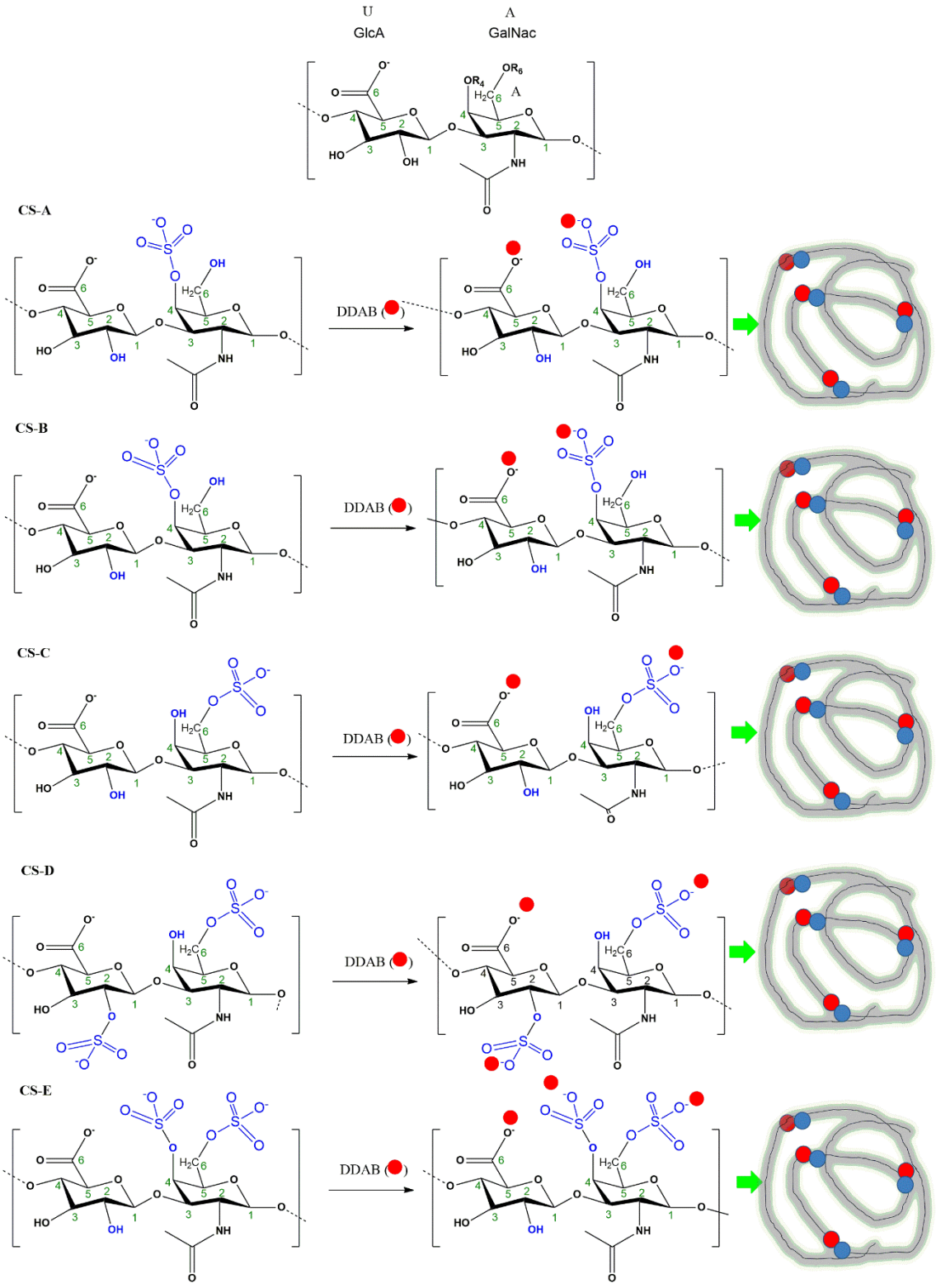

Figure 4.1. Depicting the potential electrostatic interactions of CS^- with $DDAB^+$. The CS utilized in the study have N-acetylgalactosamine (A) and D-glucuronic acid (U) moieties that are in equimolar quantities, with the potential for any individual

disaccharide unit to be sulphated (i.e., 6-sulphated, 4-sulphated, 4,6-disulphated, or unsulphated, Sigma Aldrich product)

4.3. Materials and Methods

4.3.1. Materials

CS sodium salt from shark cartilage, with an anionic content (determined via spectrophotometric mapping analysis) of 0.746 mmoL/g, and didodecyldimethyl ammonium bromide (DDAB) (≥98%; Mw= 462.63) were purchased from Sigma Aldrich (St. Louis, Missouri, United States). Methylene blue (MB) was purchased from BDH chemicals (Ltd, England). Cancer cell lines including SKOV3 were purchased from Fox Chase Cancer Centre, (Philadelphia, USA) and served as a positive control, over-expressing CS-E (ten Dam et al., 2007). Muse assay reagents such as the Count & Viability Kit (cat.no MCH 100102) were purchased from Merck (Kenilworth, New Jersey, United States). All cells were cultured in RPMI, supplemented with 10 % fetal bovine serum and penicillin/streptomycin, which were purchased from Sigma Aldrich (St. Louis, Missouri, United States).

4.3.2. Synthesis of the CS-DDAB PEC

4.3.2.1. Spectrophotometric Mapping of Anionic Moieties on CS

The amount of carboxylic acid and sulphate groups on CS (SO_4^{2-} and COO^-) was determined via selective adsorption in the presence of MB as reported by Fras and co-workers (Fras et al., 2004). To a solution of 25 mL of MB chloride (150 mg/L), CS (250 mg) was dissolved, and the solution was buffered to a pH 8.5 with borate buffer (25 mL). The resulting solution was left to react for 1 hour at room temperature in a 100 mL Erlenmeyer flask. The MB content was determined spectrophotometrically at 668 nm from the generated calibration curve (0 and 100 mg/L) (Table 1) All samples were analysed in triplicate on the Carry 50 Conc UV-Vis spectrophotometer (Varian (PTY) LTD, Australia). The total amount of moles reacting groups were calculated according to Equation 1 below:

Eq. 4.1. $$\mathrm{COO-\ and\ SO4\ 2-}\ \left[\frac{\mathrm{mmol}}{\mathrm{g}}\right] = \frac{(3.430 - A)\times 463.36 \times 10^{-3}}{E}$$

Where A is the total amount of free MB (mg) and E is the weight of the sample (g). For linear assay calibration, a stock solution of MB was prepared in water followed by preparation of several working solutions. All samples are the mean of 3 parallel measurements.

4.3.2.2. Synthesis of the "On the Spot" CS-DDAB Nanoconjugates by PEC

Briefly, 25 mg of CS was dissolved in 2 mL of deionized water. Approximately 16,67 mg of DDAB was dissolved in methanol (2 mL), the DDAB solution was then added to the CS solution to yield a murky white dispersion with precipitate. The mixture was then air dried for 24 hours and reconstituted with 5 mL of water, before freeze drying. Approximately 28 mg of solid PEC was dispersed in 40 mL of deionized water and placed in a bath sonicator for 5 minutes at room temperature, followed by centrifugation for 30 min at 3000 rpms to remove the unreacted DDAB and CS in the supernatant. The sample was then subjected to a second freeze drying process to yield a solid CS-DDAB PEC before further characterization.

4.3.3. Electrochemical Characterization of the CS-DDAB PEC

4.3.3.1. Chemical Integrity Characterization of CS-DDAB PEC

Fourier Transmission Infrared (FT-IR) spectrophotometry was performed in order to characterize the chemical structure of the CS-DDAB PEC. Analysis was undertaken at high resolution with wavenumbers ranging from 650-4000 cm^{-1} on a FT-IR Spectrophotometer using PerkinElmer® spectrum quant software (Perkin Elmer Inc. MA, USA).

4.3.3.2. Establishment of the CS-DDAB PEC Molecular Orientation

^{1}H NMR spectra of CS, DDAB and CS-DDAB PEC was recorded in $^{D}H_2O$, ^{D}methanol and ^{D}DMSO respectively utilizing the 500 MHz spectrometer (Bruker Avance III) to understand the structural compositions of the CS-DDAB PEC. The typical parameters used during the NMR run were number of scans, 20; relaxation delay, 1 s; pulse degree, 297.9 K. The chemical shifts were presented in terms of parts per million (ppm).

4.3.3.3. Analysis of Thermodynamic Behavior of CS-DDAB PEC

Differential Scanning Calorimetry (DSC) (Mettler Toledo DSC1 STARe System, Switzerland) analysis of the PEC was undertaken in order to determine the changes in heat flow between pristine DDAB, CS, a physical blend of DDAB and CS and CS-DDAB PEC. Indium was used to calibrate the instrument and samples were weighed in standard DSC aluminium pans and analysed within a temperature gradient of 25-300 °C under an 8 kPa nitrogen atmosphere. A bare pan served as a reference for all DSC scans.

4.3.3.4. Thermogravimetric Analysis for Thermal Stability Evaluation of CS-DDAB PEC

Thermogravimetric analysis (TGA) of the native CS, DDAB and CS-DDAB PEC was carried out using the TGA software (PerkinElmer STA 6000, Beaconsfield, United Kingdom) in order to elucidate the chemical reactions and/or weight changes relating to thermal stability. The following parameters were employed for the analysis: heat from 35-900 °C at a rate of 10 °C/min and nitrogen gas (N_2). The percentage mass loss was calculated using Delta Y Software against maximum decomposition temperature-initial decomposition temperature.

4.3.3.5. Assessment of Phase Transitions of CS-DDAB PEC Utilizing X-Ray Diffraction Analysis

XRD was used to validate the changes in phase (crystalline or amorphous) of CS upon complexation with DDAB. Briefly, both CS-DDAB PEC and CS-DDAB physical blends were produced and analysed to ensure complexation was achieved as opposed to the pristine polymers existing in a blend. XRD was performed utilising a variable and fixed slit system. This characterisation technique was performed on the Rigaku MiniFlex 600 Benchtop X-ray Diffractometer (Rigaku Corporation, Tokyo, Japan). A powdered sample secured on a sample holder and was scanned at a rate of 15° per minute with a diffraction angle range of 03-90° 2θ with a degree step of 0.02, a voltage of 40 kV and a current of 15 mA.

4.3.4. Macromolecular Characterisations Based on Size and Stability Analysis of CS-DDAB PEC

4.3.4.1. Optical Characterization and Stability of the CS-DDAB Nanoconjugate Suspension

The stability of the CS-DDAB nanoconjugates was investigated by means of optical interactions utilizing the Turbiscan™ LAB (Formulaction, L'Union, France). Briefly, a total of 10 mL of spontaneous (or "*on the spot*") CS-DDAB PEC was synthesized in solution phase and was introduced into the specialized sample holders. Analysis occurred at predetermined intervals over a 24-hour period (1 scan every hour) 37 (± 0.5) °C. The instrument was fixed with a pulsed near infrared light source moving vertically along the sample collecting data at 40 µm intervals. A 180°-positioned transmission detector detected transmitted light whereas a backscattering detector, positioned at 45°, detected rebounded light in response to the light-scattering effect by the suspended PEC particulates. The changes in backscatter (ΔBS) measurements were used to assess PEC stability.

4.3.4.2 Evaluation of Average Particle Size of CS-DDAB Nanoconjugates

Determination of the average particle size and polydispersity index (PDI) of the CS-DDAB nanoconjugates were analysed using a Zetasizer NanoZS instrument (Malvern Instruments (PTY) LTD, Worcestershire, UK) at 25 °C. Approximately 2 mg of solid lyophilized PEC was dispersed in 2 mL of deionized water, following sonication before being transferred to a plastic cuvette. Each test was performed in triplicate and the average value in each case was reported accordingly.

4.3.4.3. Evaluation of PEC Stability of the CS-DDAB Nanoconjugates by Zeta Potential Analysis

In order to verify the stability of the CS-DDAB PEC at 37 °C, zeta potential readings were recorded at various time points (0, 24, 48 and 72 h) to ensure no dissociation of the PEC using Zetasizer NanoZS instrument (Malvern Instruments (PTY) LTD, Worcestershire, UK). CS (25 mg/ 2 mL), DDAB (16.67 mg/ 2 mL) and CS-DDAB PEC were utilized for the experimentation. Each test was performed in triplicate and the average value in each case was reported accordingly.

4.3.4.4. Evaluation of the Surface Morphology and Energy Dispersive X-Ray Spectroscopy for the Elemental Mapping of CS-DDAB Nanoconjugates

Scanning electron microscopy- Energy Dispersive X-Ray Spectroscopy (SEM-EDS) (FEI Nova Nanolab 600 FIB, Oregon USA) was undertaken to establish the surface morphology of the newly formed DDAB-CS PEC, in addition to analysing the elemental content. A total 1 mg/ mL PEC was diluted and secured on a metallic sample stub and allowed to air dry, following sputter-coating with a layer of carbon and gold palladium. The sample was viewed under varying magnifications at an accelerating voltage of 20 kV.

4.3.5. Cell Viability Sensitivity Assay on Human Derived Ovarian Carcinoma Cell lines

Samples were analysed by Muse Cell Analyzer flow cytometry (EMD Millipore, Billerica, MA, USA) and by MUSE 1.4 Analysis software (EMD Millipore). Prior to analysis, the MUSE® cell analyser underwent a complete clean. In addition, after every replicate for each working sample, the quick clean function was used to ensure no contamination between samples occurred. The System Check procedure was undertaken prior to each experiment to verify the performance of the Muse® System by assessing counting accuracy and fluorescence detection.

4.3.5.1. Cytotoxicity Determination of DDAB on SKOV-3 Ovarian Carcinoma Cell Lines

Cell viability assays were performed in order to determine the cytotoxic potential of the anti-MUC 16 cationic NLs on SKOV3 OC cells. According to the American Type Culture Collection (ATCC), the SKOV3 cancer cells are resistant to tumour necrosis factor and to several cytotoxic drugs including diphtheria toxin, cis-platinum, and Adriamycin, in addition to over-expressing CS-E, and was thus selected as a robust model for anti-cancer screening.

The kit provides consistent staining and quantification of cell viability when the cell concentrations lie between the ranges of 1 x 10^5 to 1 x 10^7 cells/ mL. T-25 culture flasks were seeded with approximately viable 6 x 10^4 cells and were allowed to reach 70-80% confluency. At confluence, cells were serum starved overnight (to ensure all cells are in the same phase of the growth cycle) and subsequently treated with various concentrations (200, 150, 100 and 50 µg/mL) of a) DDAB cationic NLs; b) anti-MUC 16 Cationic NLs; and c) media only. The cells were then incubated for 48 hours before analysis on the Muse™ utilizing the Count & Viability Kit (Millipore, USA cat.no MCH 100102) as per manufacturer's protocol. The final concentration of cells obtained after treatment was approximately 3 x 10^6 on average. A total of 20 µL of cell suspension at various DDAB concentrations were mixed with 380 µL of cell count and viability reagent (<5 x 10^5 cells/ mL cell concentration) and incubated for 5 minutes before

analysis. The IC_{50} values were then computed using GraphPad Prism (Version 8) Software for each nanoliposomal formulation and administered in further studies below.

Statistical Analysis

All samples were performed in 3 biological replicates and their mean and standard deviations were recorded as computed. An unpaired student T-test, two-tailed was performed for the statistical significance of the spectrophotometric mapping study, where the MB-CS tests were compared against the free MB controls and the cell viabilities of the 200 µg/mL tests were compared against the untreated controls. Values that had a significance of $P < 0.05$ selected for analysis. All statistics and calibration curves were analysed on Microsoft Excel. All graphs were plotted using OriginPro 8.5 Software and/or GraphPad Prism 8 Software.

4.4. Results and Discussion

This work demonstrated the application of polyelectrolyte complexation to structurally modify polymers in order to change their chemical integrity, which is hypothesized to reduce the growth of ovarian carcinomas. Anionic chondroitin sulphate (implicated in tumour dissemination) was polyelectrolyte complexed with DDAB and further investigated. The studies herein are aimed to prove the successful interactions between the two moieties at physiological pH ranges (therefore in their partially ionized states) and conditions, which differ from the conventional experimental conditions to facilitate complete polyelectrolyte complexation (Meka et al., 2017). The physiological reaction conditions (such as pH) were set to simulate their potential interactions *in vivo*. This was done to ensure DDAB is a suitable candidate for its use as a CS-arresting agent, before its incorporation in advanced drug delivery systems targeting CS-E.

4.4.1. Evaluation of CS-DDAB PEC

The formation of stable PECs is dictated by various influential factors (Meka et al., 2017). Degree of ionization of each of the oppositely charged polyelectrolytes is

crucial, in addition to the charge distribution and position of ionic groups within the polymer chains, the concentration of each pristine polyelectrolyte, mixing ratios, polymer backbone flexibility, temperature, ionic strength and pH of the reaction conditions all dictate PEC formations (Schatz et al., 2004). These complexation reactions should ideally occur at pH ranges that lie between the two components pK_a values. For CS, the pK_a was estimated between 4.4–4.5 by pH titration experimentations or 3.84 on the basis of glucuronic residue content (Chen at al., 2005).

The degree of dissociation of the carboxylic groups is pH dependent (Chen at al., 2005). However, this low pH does not feature in physiological environments (pH 7.4) nor within the ovarian tumour microenvironment (lowest of pH 5,5) (Fathi et al., 2020). Therefore, this present PEC (CS-DDAB) serves as the most natural form as the majority of the crucial experimental parameters which facilitate polyelectrolyte complex formation was omitted in order to simulate the most physiological environments, then assessing these resultant interactions.

The formation of the PEC was thus achieved at relatively high acidic pH values (6.8) which was provided by the methanol solvent. It was seen in the case of low molecular weight heparin, that DDW was the medium for complexation with DDAB, which provided the necessary environment for sufficient interactions (Ye et al., 2015).

Once CS was reacted with DDAB *in situ*, CS molecules immediately precipitated as a consequence of insolubility, as PEC are historically known for their insoluble nature (Michaels, 1965). There are four major steps associated with the solubility of PECs: Step 1- PECs that dissolve in water can adopt an extended conformation. Step 2- Divalent counter ions will cause ion-bridging between two ionic sites on the polymer chain and the PECs remains soluble. Step 3- High volume of charge screening causes precipitation of PECs from solution with increased concentrations of salt (Na from CS, Br from DDAB); and Stage 4- A further increase in the concentration of salt will redissolve the PECs in solution as a result of high-charge screening (Solis et al., 2000).

An increase in the initial temperature of the solutions from 25 °C to 34 °C was further observed immediately after complex formation, the release of heat, supporting the exothermic interactions corresponds to an electrostatic interaction between CS and DDAB (Kawahara et al., 2018). Thus, these key solubility and heat features were observed, indicative of the successful interactions between CS polymer and DDAB at relatively unfavourable polyelectrolyte complexation conditions, which motivated further characterizations.

4.4.1.1. Spectrophotometric Mapping of Anionic Moieties in CS

The polysaccharide chains of CS were mapped to identify potential anionic groups for PEC formation with DDAB. COO^- and $-OSO3^{2-}$ are known anionic moieties on the CS backbone. In this mapping experiment the anionic CS moieties reacted with cationic methylene blue (MB). Therefore, the decrease in UV adsorption at 668 nm by adding a concentration of CS relative to free MB was indicative of the total number of anionic moieties available. The results obtained were used to confirm the presence of sufficient anionic reacting groups on the CS polysaccharide chains to form a PEC with cationic DDAB at the OC tumour micro-environment. The amount of CS reacting groups was computed to be 0.746 ± 0.100 mmol (N=3) (Table 4.2) of reacting groups per 1 g of CS using Equation 1. This led to developing a Molar Ratio for a complexation reaction between CS and DDAB. Based on the quantification of anionic CS-reacting groups (COO^- and $-OSO_4^{2-}$; 0.746 mmoL/ g), the equivalent quantity of DDAB to react with these groups was computed to establish effective CS-DDAB complexation. Results revealed that a total of 16,67 mg of DDAB was needed to complex with 25 mg of CS (a 2:1 Molar Ratio of CS: DDAB). We thus concluded that CS contains sufficient anionic reacting groups for DDAB PEC formation.

Table 4.2. Summarising the experimental outputs and calibration curve details. An unpaired T-test, two-tailed for the total amount of MB vs MB with the addition of CS showed a significant difference (P=0.007).

Experimental Parameters	Outputs
Correlation coefficient (r^2)	0.9988
Slope	0.0071
Number of samples (n)	3
Weight of CS (mg) (E)	250.33 ± 0.15
Amount of Free MB (A)	3.02 ± 0.06
Amount of CS anionic reacting groups/ g	0.746 ± 0.100 mmol

4.4.1.2. Chemical Integrity Characterization of CS-DDAB PEC

Fourier Transmission Infrared (FT-IR) spectrophotometry was used to assess chemical changes in the structure of CS when PEC with DDAB. The FT-IR spectra also provided an indication of the electrostatic interaction that existed within the PEC network. The FT-IR spectra of CS, DDAB and CS–DDAB PEC are represented in Figure 4.2. Table 4.3 summarises the peaks assigned to pristine CS and DDAB. In the FT-IR spectra of CS–DDAB PEC, an additional peak at 1657 cm^{-1} was detected confirming the presence of intermolecular electrostatic association between the $-N^+$ of DDAB and $-COO^-$ of CS, causing a shift and splitting of the glucuronic acid peaks (Farquhar et al., 1962). This finding was supported by the disappearance of the 1411 cm^{-1} peak in the CS-DDAB PEC suggesting a reduction in available free carboxylic acid groups, additional peaks at 2923 and 2854 cm^{-1} were also recorded in the PEC and corresponds to the symmetric and asymmetric stretching vibrations of methylene (seen in DDAB). Furthermore, a shift in the peak at 1219 cm^{-1} of CS ($-OSO3^{2-}$) to 1222 cm^{-1} confirmed the presence of CS in the PEC network, in addition to its interaction with positively charged DDAB.

Table 4.3. Showing the various FT-IR peaks and their corresponding functional groups for pristine polymer and DDAB.

CS			DDAB		
Wavenumber	**Functional group**	**Description**	**Wavenumber**	**Functional group**	**Description**
3321 cm^{-1}	Free hydroxyl group Amide group	-OH and -NH stretching vibration (Amrutkar et al., 2009)	2854 and 2921 cm^{-1}	Methyl & methylene	-CH stretching of methyl or methylene group (Amrutkar et al., 2009)
2886 cm^{-1}	Methyl & methylene	-CH stretching of methyl or methylene group (Amrutkar et al., 2009)	1488 cm^{-1}	Amine	characteristic -CN asymmetric stretching band from the ammonium group (Generosi et al., 2007)
1612 cm^{-} and 1026 cm^{-1}	Carbonyl group -CO	-CO vibrational stretching of amide II (Mohtashamian; Amrutkar et al., 2009)			
1410 and 1375 cm^{-1}	CO vibrational stretch	-CO stretch vibration and C-OH variable-angle vibration suggesting the			

		existence of free carboxyl groups
1219 cm^{-1}	Sulphate group	S=O bond of N-acetyl-d-galactosamine (-$OSO3^{2-}$) (Amrutkar et al., 2009)

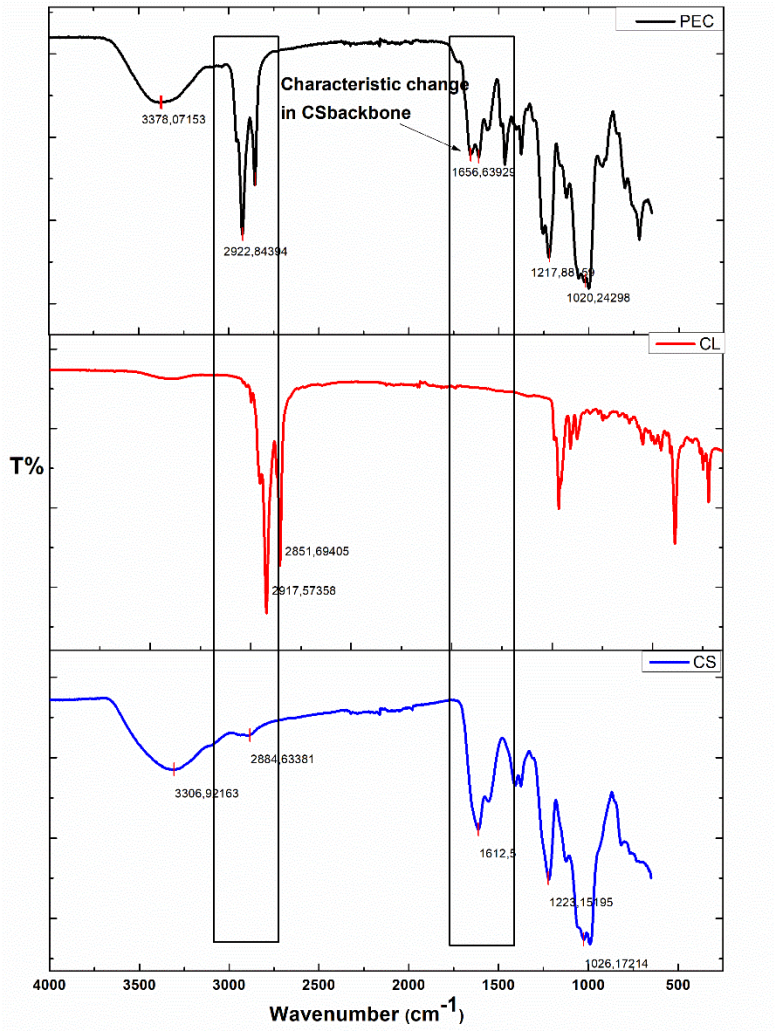

Figure 4.2. FT-IR spectrum displaying the characteristic surface modifications on the CS polymer backbone by DDAB to yield nanoconjugates.

4.4.1.3. ^{1}H NMR Analysis for the Molecular Orientation Determination of CS-DDAB PEC

The establishment of the CS-DDAB "*on the spot*" PEC was further verified by ^{1}H NMR analysis, which provides insight on the environment of individual atom nuclei by the chemical shifts of different proton signals (Aihua et al., 2017) (Figure 4.3). For CS, the acetylated moieties seen at 2 ppm of the spectrum is the characteristic signal for the proton units corresponding to the GalNAc (CH_3CO) (Chen et al., 2011). Since the N-acetyl side chain possesses the most flexible functional group of CS, C-H protons of the

carbohydrate rings are detected between 3.3 and 4.0 ppm (Servaty et al., 1998). Due to the complexity of CS, the more robust approach was to confirm PEC by assessing the proton signals of DDAB relative to the PEC. The assigning of peaks corresponding to carbon 2.3 of DDAB (chemically equivalent) integral at 6 (total number of protons; area under the peak) seen in the DDAB spectrum, in the PEC an up-field shift is observed due to electrostatic interactions. Equivalent carbons 16.4 of DDAB chemically shifted down-field (seen at 3.34 ppm: 5 protons) to 3.23 ppm in the PEC with 4.7 protons. The 5 protons observed in DDAB differ from the expected 4 protons as a consequence of the CO_2 from the methanol overlap, which is reduced to 4.7 in the complex (less methanol overlap).

^{1}H NMR further provides insight for the characterizations of inclusion PECs, by observing the location of CS included into the cavity of DDAB via microstructural characterizations (Chen et al., 2006). Figure 4.3 further displays significant differences between the three spectra, the equivalent protons of DDAB at 2.3; 4.16; and 5.17 are all present in the PEC, with slight downfield or up-field shifts corresponding to the electrostatic interactions. However, the peak region of CS at 4.87-3.57 ppm, relating to the protons on the carbohydrate rings are missing in the PEC motivating the presence of an inclusion PEC formation (Aihua et al., 2017; Chen et al., 2006). This inclusion PEC is highly favourable *in vivo*, for complete encapsulation of the over-expressed CS-E that is present in the tumour microenvironment. The inclusion PEC formation was further supported by molecular docking studies (Figure 4.4).

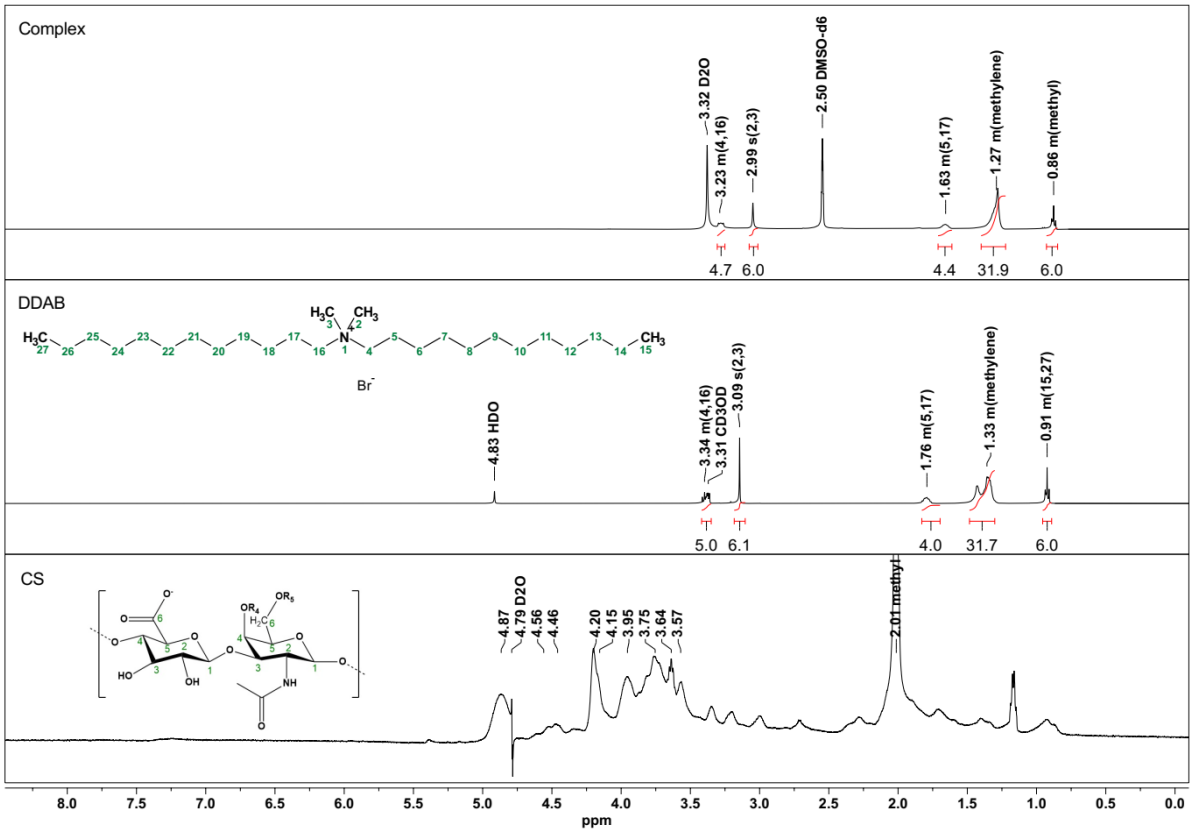

Figure 4.3. ^{1}H NMR spectrum of CS-DDAB PEC.

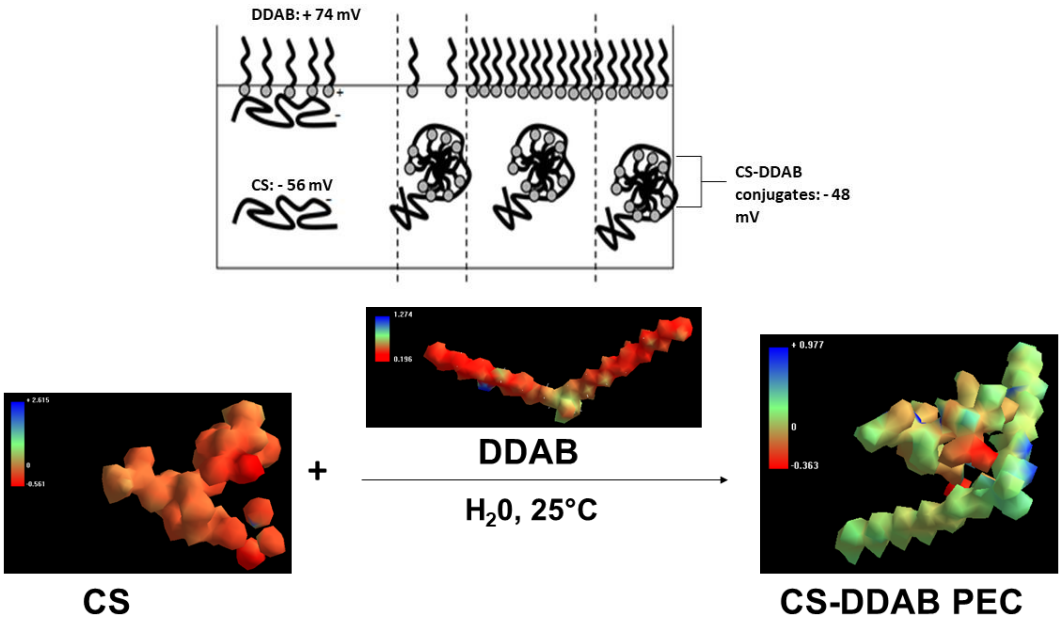

Figure 4.4. Visual representation of the inclusion polyelectrolyte complexation of CS during the micellization of DDAB with molecular docking of CS-DDAB showing highly stable nanoconjugates.

4.4.1.4. Thermal Behavior Analysis of the CS-DDAB PEC

Differential Scanning Calorimetry (DSC) was used to characterize the thermal behaviour of the CS-DDAB PEC in order to differentiate the heat flow properties of the PEC from a physical blend (Figure 4.5). The DSC thermogram of CS revealed a single endotherm at 116.96°C related to H_2O molecules bonded to the CS chains (Serra Moreno et al., 2008) and one exotherm at 244.05°C (Amrutkar et al., 2009) attributed to the degradation of CS (Farjado et al., 2012). Pristine DDAB revealed a total of four endothermic peaks at 59.65; 87.55; 140.86 and 197.21 °C. The peak at 59.65 °C was associated with the main phase transition melting temperature of DDAB. At the transition melting temperature, the double hydrocarbon chains of DDAB from the gel phase are transformed into a liquid crystalline phase. The peak at 87.55 °C correlates to the thermal transition of the headgroups of DDAB. The peak at 140.86 °C was associated with the melting temperature of pristine DDAB, and the fading of the electrostatic interactions among headgroups of DDAB (Zhang et al., 2006). For the physical blend, a combination of endothermic and exothermic peaks derived from the pristine CS and DDAB was observed. However, for the CS-DDAB PEC a disappearance in the endotherms at 65.1°C and 59.65 °C from the physical blend and DDAB was seen, respectively (including a new exotherm at 178.23 °C), which was associated with the release of heat due to the electrostatic reactions in the PEC network. This confirmed PEC formation between CS and DDAB and the absence of a simple physical blend.

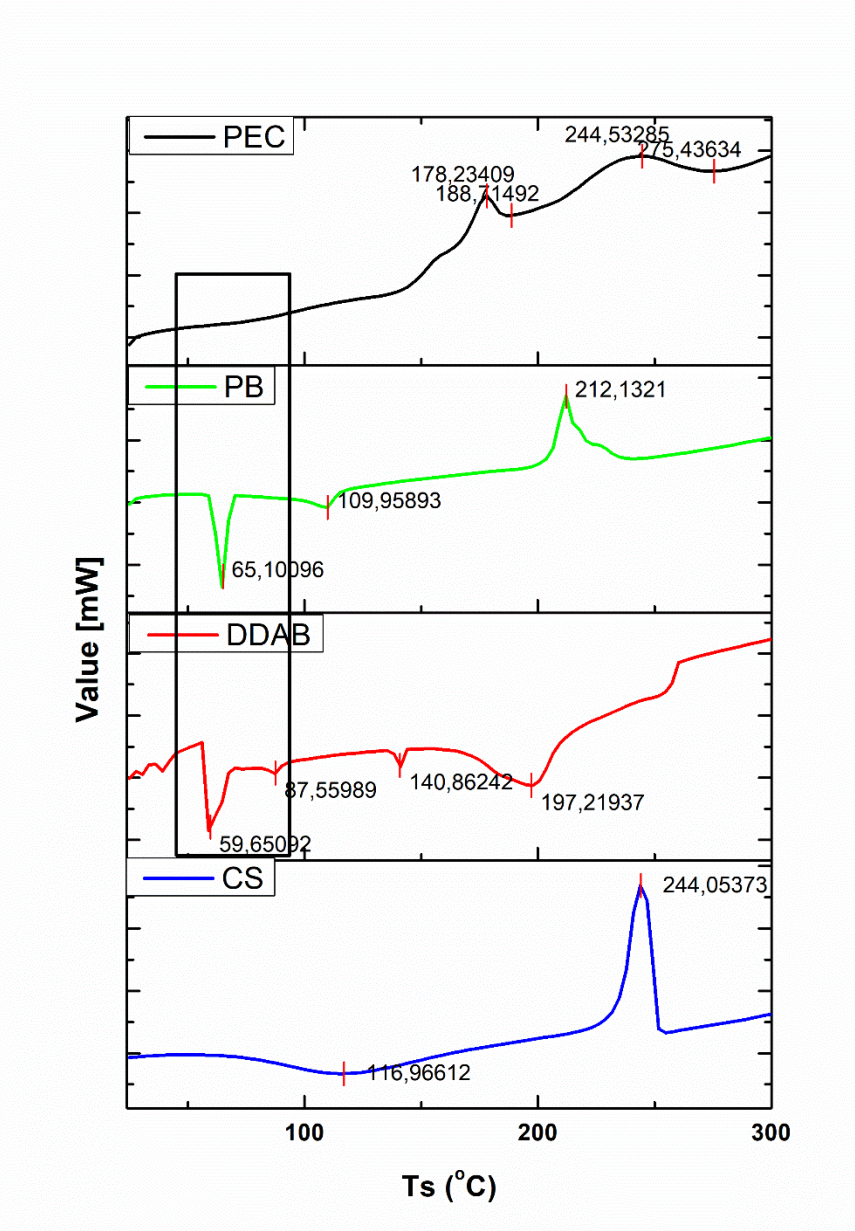

Figure 4.5. DSC thermograms for the CS-DDAB PEC.

4.4.1.5. Thermogravimetric Analysis for Thermal Stability of the CS-DDAB PEC

In order to determine the thermal stability of the complex; thermogravimetric analysis (TGA) was utilized. Weight loss vs. temperature curves for CS, DDAB and CS-DDAB PEC are presented in Figure 4.6. From the plot, a two-stage weight loss for pristine CS is observed. The first stage (200–250 °C) is attributed to the loss of water and other volatile compounds. The TGA curve of CS shows that this first stage occurs at a higher temperature (~245 °C) range for CS in comparison to the CS-DDAB PEC (~204 °C). This

suggests that the amount of moisture in the CS structure is greater than the amount present in CS-DDAB PEC.

In addition, the degradation occurs at a lower temperature range in the PEC compared to CS, suggesting a lower degree of stability. The functionalization of CS by the electrostatic association with N^+ of DDAB to form regions of COO^-/N^+ in the PEC yield a lower thermal stability, possibly because the hydrogen bonds between the COO^-/N^+ of the PEC are weaker than the hydrogen bonds between the carboxylic groups present on the pristine CS (Fajardo et al., 2012).

Minimal weight loss occurs between 30-195 °C in the PEC in contrast to CS, suggesting that the PEC exhibits a higher stability profile at this temperature range. This temperature range is of paramount importance for the *in vivo* (37 °C) PEC of the overly expressed CS-E molecules, thus the CS-DDAB PEC proves stable at bodily temperature.

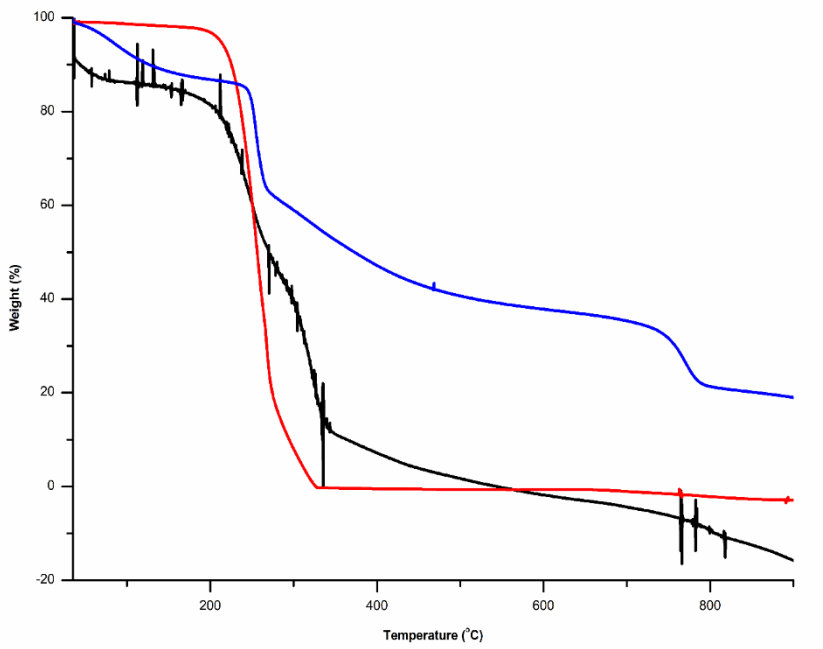

Figure 4.6. TGA curves for a) CS = blue b) DDAB= red and c) CS-DDAB PEC = black.

4.4.1.6. X ray Diffraction (XRD) studies on CS-DDAB PEC

XRD was used to assess transitions in the amorphous-crystalline nature of CS after complexing with DDAB. This provided further insight on the inter- and intra- molecular interactions of the PEC (Figure 4.7). The characteristic peak of CS was observed at a 2θ=21° attributed to the H-bonds and confirmed that CS was in a semi-crystalline phase (Hu et al., 2017). DDAB exhibited highly ordered liquid crystalline structures (Godlewska et al., 1997). Comparing the physical blend to the PEC; the interactions between the charged functional groups from $-N^{+}$ (DDAB) and $-OSO3^{2-}$ (CS) altered the diffraction peak patterns. For instance, the sharp peak at 10.7° of the physical blend disappeared, whilst new peaks at 2θ = 30.3° and 43° appeared for the PEC and were not present in the other XRD spectra. These new peaks (2θ = 30.3° and 43°) are associated with the electrostatic interaction between the $-N^{+}$ and $-OSO3^{2-}$ in the PEC network that formed the novel crystalline regions on the XRD patterns (Zhang et al., 2006). Therefore, this confirmed that the XRD patterns correlated with the FT-IR spectra for PEC formation between the $-N^{+}$ and $-OSO3^{2-}/COO^{-}$ groups of DDAB and CS, respectively.

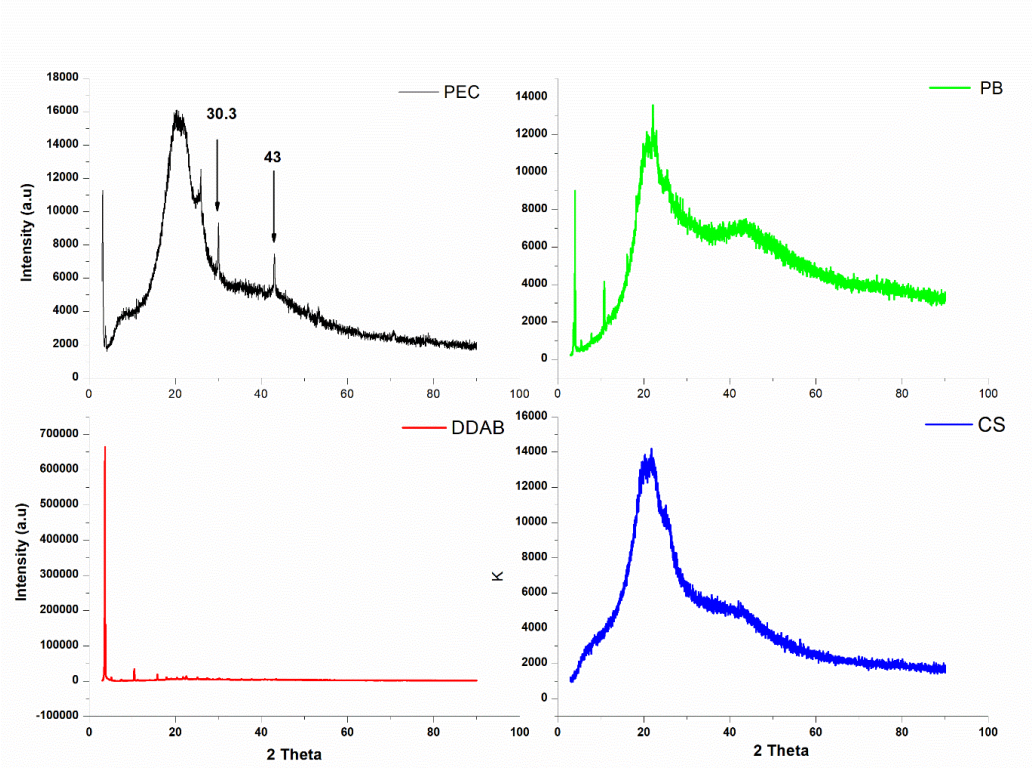

Figure 4.7. XRD patterns for the determination of phase transitions on the CS backbone by DDAB.

4.4.2. Morphological, Size and Stability Analysis of CS-DDAB PEC

4.4.2.1. Evaluation of the Average Particle Size and Stability of CS-DDAB Nanoconjugates by Means of Zeta Potential Analysis

Physicochemical characterization including the average particle size, zeta potential and polydispersity index (PDI) were measured using dynamic light scattering (DLS). The nanosize diameter of the conjugates was verified (286,76 nm (±7.85) (Figure 4.8) with a PDI of 0.232 (±0.007)). Zeta potential analysis of particles represent the overall charge the nanovesicle acquires in a particular environment (Danaei et al., 2018), an important parameter required to evaluate the surface charge of the CS-DABB nanoconjugates (Safari et al., 2013). Zeta potential analysis was conducted at various time points over 72 h (Table 4.4) to assess the stability of the PEC at 37 °C. The reduction in zeta potential is well in agreement with the reduction in physical stability. A minimum zeta potential of greater than −60 mV is required for excellent stability, or greater than −30 mV for good physical stability (Riddick et al., 1968). The high positive zeta potential of pristine DDAB (75,86 mV) was masked upon complexation with CS due to the cationic-anionic interaction, utilizing the stable N^+ charge of DDAB and the anionic carboxylic acid groups on CS to produce a stable negatively charged PEC immediately after synthesis (- 48.23 mV). Negligible changes to the zeta potential over the 3-day period was observed, with a slight decrease in -2 mV on day 3, inferring negligible dissociation of the PEC at 37 °C (Souza et al., 2015).

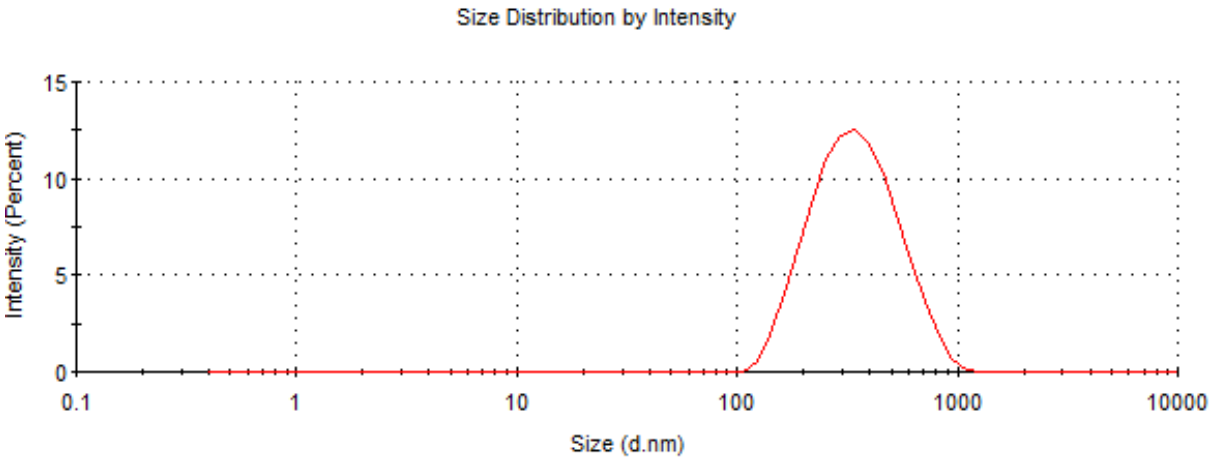

Figure 4.8. Graphical representation of the average particle size of CS-DDAB nanoconjugates.

Table 4.4. Summary of average zeta potential and particle size of CS-DDAB nanoconjugates.

Sample	Zeta potential (mV)	Average particle size (nm)	PDI
Pristine CS	-56.4 (±0.8)	-	-
Pristine DDAB	+ 75.86 (±1.10)	-	-
CS-DDAB PEC (T=0)	- 48.23 (±2.47)	286.76 (±7.85)	0.232 (±0.007)
CS-DDAB PEC (T= 24 h)	-48.03 (±2.7)	-	-
CS-DDAB PEC (T= 48 h)	-48.97 (±2.4)	-	-
CS-DDAB PEC (T= 72 h)	-50.1 (±2.78)	-	-

4.4.2.2. Optical Characterization and Stability of the DDAB-CS Nanoconjugates in Suspension

Stability studies were conducted on CS-DDAB nanoconjugates at 37 °C in order to assess the ability of this reaction to yield stable PECs in solution. In addition, the *"on the spot"* development of these conjugates was also determined. Turbidity measurements were recorded to determine the stability of the nanoconjugates, the principle is based on multiple light scattering, where photons are scattered by particles before being detected by the backscattering detector. This backscattering depends on particle size (flocculation, coalescence) and the kinetics of the particle such as migration, sedimentation and creaming, from which stability of the system can be concluded. The spectrum (Figure 4.9) below can be analysed as low, medium, and high regions of the vesicle (Figure 4.10) in which the particles spontaneously formed.

For ΔBS, at low regions (0 mm-20 mm) an increase in the peak is observed, suggesting the flocculation of bigger particles upon complexation. This is also motivated by the increase in particle size, which is seen by an increase in the ΔBS at the middle region of

the vesicle, suggesting immediate complexation, and formation of nanoconjugates when DDAB solution is introduced to CS solution.

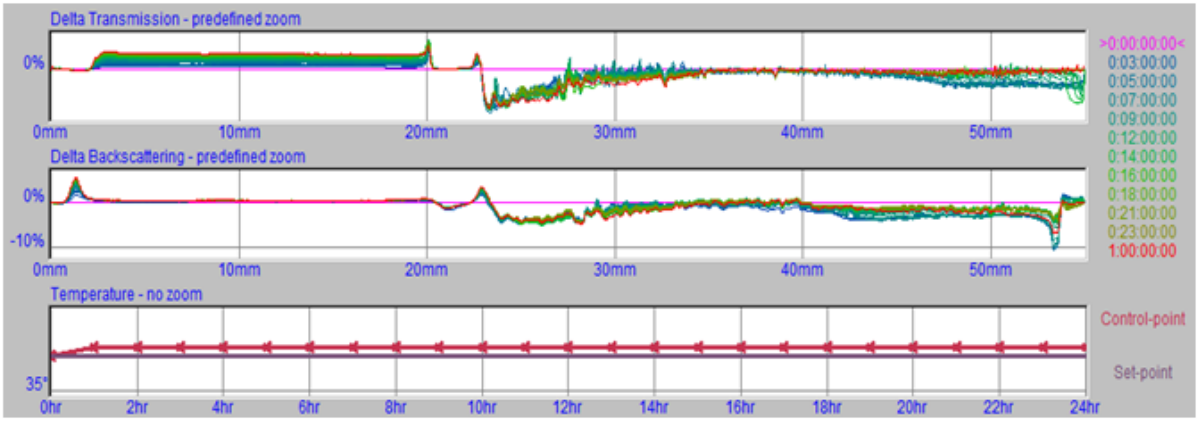

Figure 4.9. ΔBS and Δ transmission spectrums for CS-DDAB "*on the spot*" PEC for stability analysis at 37 °C for 24 h.

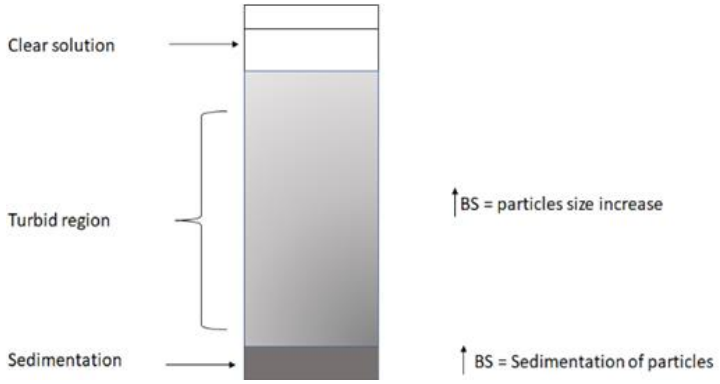

Figure 4.10. Representing a typical vesicle used for Turbiscan analysis.

4.4.2.3. Evaluation of the surface morphology of CS-DDAB PEC

Scanning Electron Microscopy (SEM) was used to reveal the surface morphology of the PEC (Figure 4.11). From the imagery obtained, spherical to oblong vesicle-like colloids appeared in aggregates. This was attributed to the ability of DDAB to form micelle-like conjugates in the presence of water (Mehta et al., 2008). A similar trend was observed previously when sodium dodecyl sulphate (SDS) was complexed with bovine serum albumin, to form a PEC that behaved identically to the SDS micelle (Mehta et al., 2008). Energy Dispersive X-Ray Spectroscopy (EDX) was further employed for the elemental mapping of sulphur and nitrogen atoms of the CS-DDAB nanoconjugates, from the

spectrum below (Figure 4.11), these elements of the pristine polymers were undetected, further motivating their utilization in the chemical reactions forming nanoconjugates (Ma et al., 2010; Esfahani et al., 2020).

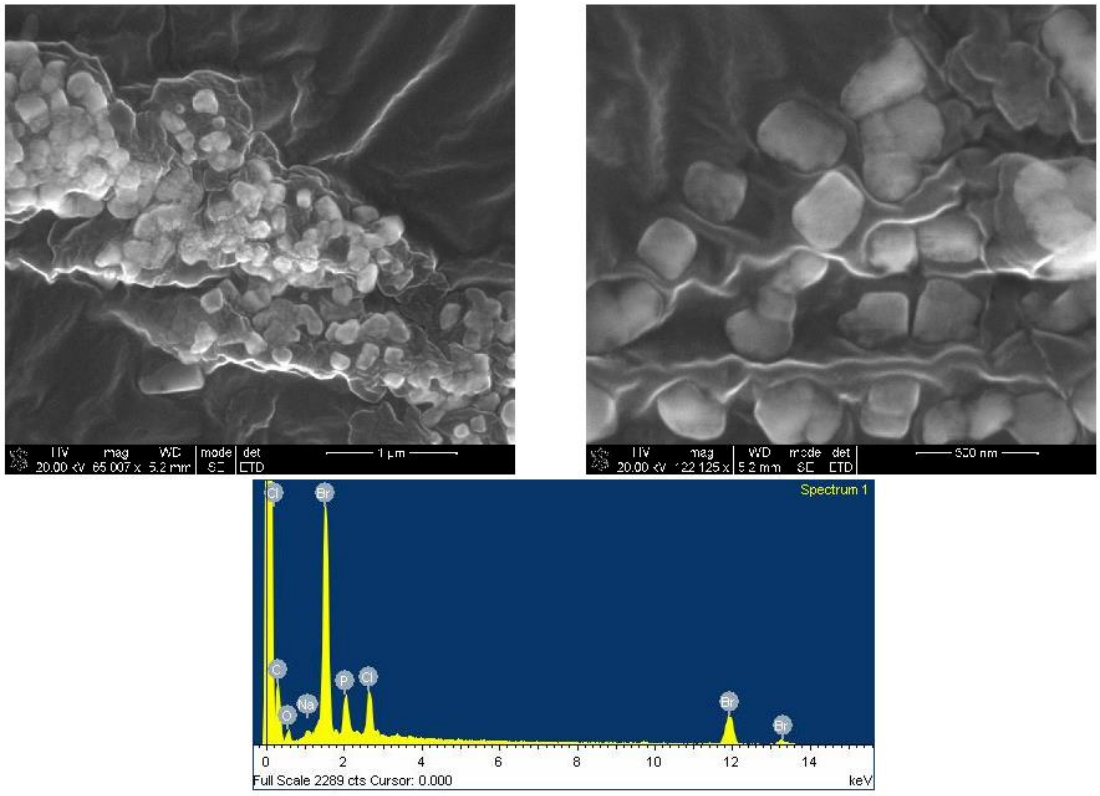

Figure 4.11. Typical SEM imaging and EDX elemental mapping spectrum of the CS-DDAB nanoconjugates.

4.4.3. Anti-cancer activity of DDAB on SKOV3 Ovarian Carcinoma Cell Lines

Throughout this paper, DDAB was added to CS directly *in vitro*, yielding stable PEC (or arrested CS modified structures). This section of the manuscript, aimed to simulate this in ovarian carcinoma cell lines that over-express CS (Vallen et al., 2014, ten Dam et al., 2007). We thus screened the potential of DDAB to contribute to a loss of viability against CS-E over-expressed SKOV3 cell lines with varying doses. It was determined experimentally that DDAB exhibits a dose dependent anti-cancer effect against SKOV3 cells due to the positively charged surface of the nanomicelle. This feature allows for enhanced cell internalization in contrast to both neutral and negatively charged particles (Alkilany et al., 2009), leading to sufficient receptor mediated endocytosis (Wu et al., 2012). Studies conducted by Bexiga and co-workers demonstrated that cells exposed to

cationic NPs displayed an increase in cell membrane permeability, suggesting an onset of an apoptotic followed by a secondary necrotic response. In addition, the activation of caspases 3/7 and 9 and cleavage of poly (ADP-ribose) polymerase (PARP)-1 was also detected (Bexiga et al., 2011). Interestingly, cytotoxicity results on DDAB-NPs on Caco-2, HepG2, MCF-7, SV-80 and Y-79 displayed a relatively high IC_{50s} (ranging from 500-1000 µg/mL) (Silva et al., 2019) in contrast to the low IC_{50} (12.3 µg/mL) results obtained in this study. Potential explanations for the lower IC_{50} obtained on SKOV3 cell lines could be related to the over expression of CS-E, and the arresting of CS-E leading to a lower IC_{50} (due to reduction in VEGF and cell proliferation) (Pradeep et al, 2016), however further studies are required to support these claims. This potential finding promotes the utility of DDAB in advanced drug delivery systems targeted CS-E. The results herein favour the preliminary cytotoxic nature of DDAB for utilization in further studies (Figure 4.12). In addition, a noteworthy change in cell morphology and detachment of cells from the surface of the plates was achieved, which requires further investigation (Figure 4.13).

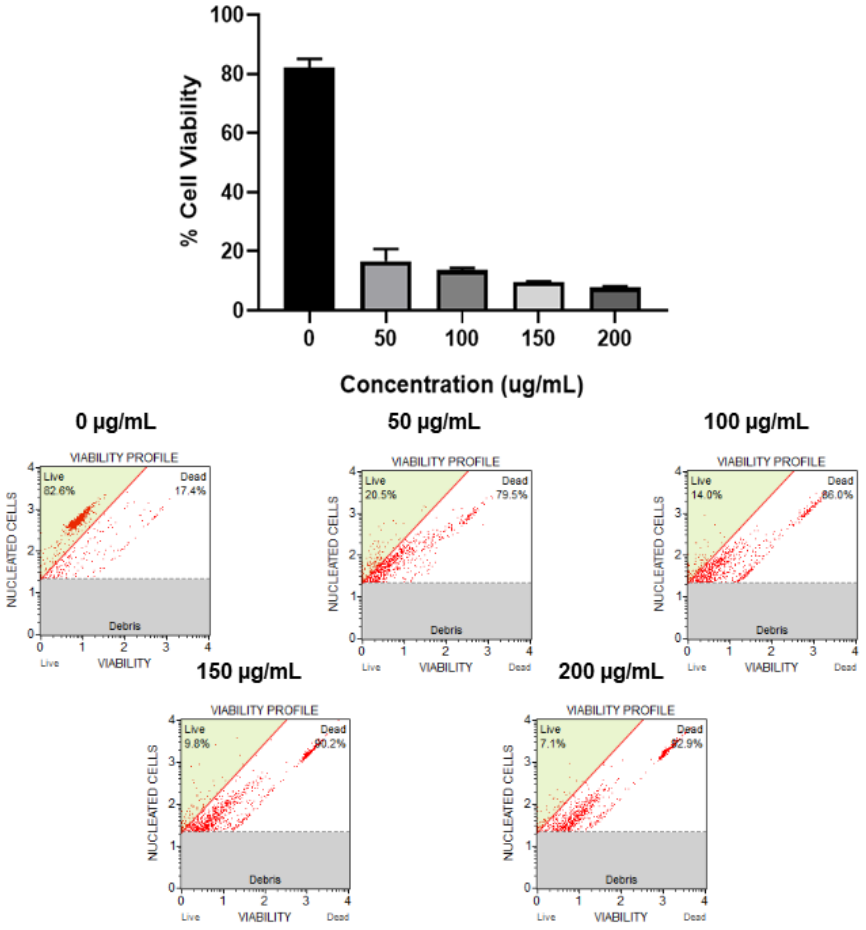

Figure 4.12. Quantitative expressions of cell viability of SKOV3 ovarian carcinoma cells against DDAB (0-200 µg/mL - IC_{50}=12.3 µg/mL). An unpaired, two-tailed student T-test

was conducted comparing the cell viability obtained from DDAB dosed at 200 µg/ mL and the untreated control, which showed statistical significance after the 48 hours treatment (P=0,0006).

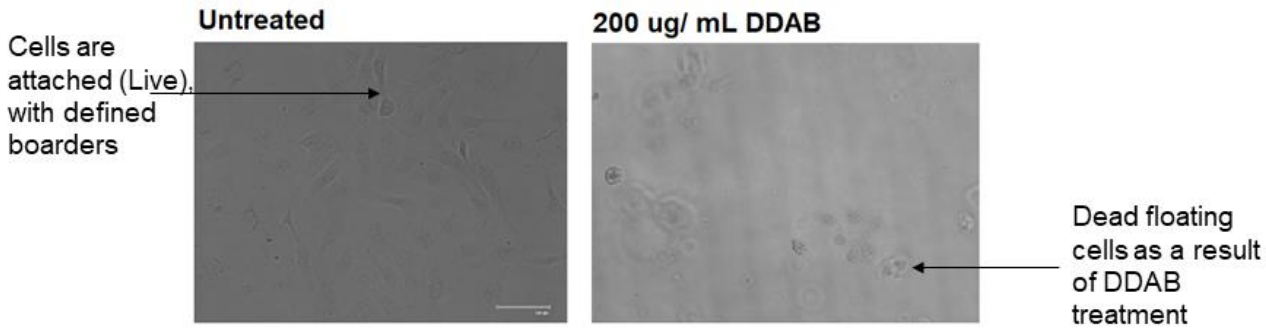

Figure 4.13. Light Microscopy images to assess changes in morphology of SKOV3 ovarian carcinoma cell lines after 48 h DDAB exposure.

4.5. Conclusions

In the present study, PEC was presented as an innovative mechanism of action to PEC (*or arrest*) the over-expressed CS in the OC tumour microenvironment (as defined by the hypothesis mentioned previously). Results of the study confirmed the suitability of DDAB to act as a promising CS complexing agent, forming highly stable CS-DDAB PEC nanoconjugates. The great discovery of an inclusion PEC was made, and confirmed via spectral, thermal, X-ray diffraction and ^{1}NMR studies. Additionally, the spherical micelle-like structure of the PEC was also discovered (SEM), correlating to the size (zeta sizer) and the structural elucidations predicted from the ^{1}NMR and FT-IR. The stability of the nanoconjugates was further confirmed by turbidity measurements and zeta potential analysis at 37°C, confirming the enhanced stability of the CS-DDAB PEC. Lastly, significant reduction in SKOV3 (over-expressing CS) cell viability upon DDAB treatment was achieved, concluding the suitability of the DDAB complexing agent and preliminary rationalizing the hypothesis. This study establishes the use of DDAB for future research in advanced drug delivery systems specifically targeting GAG activity in OC.

4.6. References

Afratis, N., Gialeli, C., Nikitovic, D., Tsegenidis, T., Karousou, E., Theocharis, A. D., Pavão, M. S., Tzanakakis, G. N., Karamanos, N. K., 2012. Glycosaminoglycans: Key players in cancer cell biology and treatment. FEBS J. 279, 1177–1197.

Aihua, Z., Xiaotong, Z., Handge, U.A., Garamus, V.M., Willumeit-Römer, R., Peihao, Y., 2017. Folate receptor targeted bufalin/β-cyclodextrin supramolecular inclusion complex for enhanced solubility and anti-tumor efficiency of bufalin. Materials Science and Engineering C. 78, 609–618.

Alizadeh, L., Zarebkohan, A., Salehi, R., Ajjoolabady, A., Rahmati-Yamchi, M., 2019. Chitosan-based nanotherapeutics for ovarian cancer treatment. J. Drug Target. 27, 839-852.

Alkilany, A.M., Nagaria, P.K., Hexel, C.R., Shaw, T.J., Murphy, C.J., Wyatt, M.D., 2009. Cellular uptake and cytotoxicity of gold nanorods: molecular origin of cytotoxicity and surface effects. Small Weinh. Bergstr. Ger. 5, 701–708.

Amrutkar, J.R., Gattani, S.G., 2009. Chitosan–Chondroitin Sulfate Based Matrix Tablets for Colon Specific Delivery of Indomethacin. AAPS PharmSciTech. 10, 670–677.

Athanasia, P., Asimakopoulou., 2008. The biological role of chondroitin sulphate sulphate in cancer and chondroitin – based anti- cancer drugs. In Vivo. 22, 385 – 389.

Banerjee, S., Kaye, S.B., 2013. New strategies in the treatment of ovarian cancer: Current clinical perspectives and future potential. Clin. Cancer Res. 19, 961–968.

Chen, M., Diao, G., Zhang, E., 2006. Study of inclusion complex of β-cyclodextrin and nitrobenzene. Chemosphere. 63, 522–529.

Chen,S., Xue, C.,Yin, L., Tang, Q., Yu, G., Chai,W., 2011. Comparison of structures and anticoagulant activities of fucosylated chondroitin sulfates from different sea cucumbers. Carbohydrate Polymers. 83, 688-696.

Chen, W.B., Wang, L.F., Chen, J.S. and Fan, S.Y., 2005. Characterization of polyelectrolyte complexes between chondroitin sulfate and chitosan in the solid state. J. Biomed. Mater. Res. 75, 128-137.

Danaei, M., Kalantari, M., Raji, M., Samareh Fekri, H., Saber, R., Asnani, G. P., … Taheriazam, A., 2018. Probing nanoliposomes using single particle analytical techniques: effect of excipients, solvents, phase transition and zeta potential. Heliyon. 4, e01088.

Esfahani, A. R., Zhang, Z., Sip, Y. Y. L., Zhai, L., & Sadmani, A. H. M. A.., 2020. Removal of heavy metals from water using electrospun polyelectrolyte complex fiber mats. Journal of Water Process Engineering. 37, 101438.

Fajardo, A.R., Lopes, L.C., Pereira, A.G.B., Rubira, A.F., Muniz, E.C., 2012. Polyelectrolyte complexes based on pectin-NH 2 and chondroitin sulfate. Carbohydr. Polym. 87, 1950–1955.

Fajardo, A.R., Piai, J.F., Rubira, A.F., Muniz, E.C., 2010. Time- and pH-dependent self-rearrangement of a swollen polymer network based on polyelectrolytes complexes of chitosan/chondroitin sulphate. Carbohydr. Polym. 80, 934-943.

Farquhar, E.L., 1962. The infrared spectra of primary aromatic amides, Retrospective Theses and Dissertations 2292. http://lib.dr.iastate.edu/rtd/2292.

Fathi, M., Barar, J., Erfan-Niya, H., Omidi,Y., 2020. Methotrexate-conjugated chitosan-grafted pH- and thermo-responsive magnetic nanoparticles for targeted therapy of ovarian cancer, International Journal of Biological Macromolecules. 154, 1175-1184.

Frank, D., Indermun,S., Govender,M., Kumar, P., Choonara, Y.E., du Toit, L.C., V. Pillay, V., 2019. Antineoplastic nano-lipobubbles for passively targeted ovarian cancer therapy. Colloids Surfaces B Biointerfaces. 177, 160–168.

Fras, L., Stana-Kleinschek, K.,Ribitsch, V., Sfiligoj-Smole, M., Kreze, T., 2004. Quantitative Determination of Carboxyl Groups In Cellulose Polymers Utilizing Their Ion Exchange Capacity And Using A Complexometric Titration. Mater. Res. Innov. 8, 145–146.

Generosi, J., Piccinini, M., Marcelli, A., Belardinelli, S., Pozzi, D., Castellano, A.C., 2007. Characterization of solid supported lipoplexes by FTIR microspectroscopy. Infrared Phys. Technol. 50, 14–20.

Godlewska, M., Wróbel, S., Borzęcka-Prokop, B., Michalec, M., Dynarowicz, P., 1997. Phase behavior of didodecyldimethylammonium bromide. Mol. Cryst. Liq. Cryst. Sci. Technol. Sect. A Mol. Cryst. Liq. Cryst. 300, 113–126.

Gossmann, R., Langer, K., Mulac, D., 2015. New perspective in the formulation and characterization of didodecyldimethylammonium bromide (DMAB) stabilized poly (lactic-co-glycolic acid) (PLGA) nanoparticles. PLoS One. 10, e0127532.

Hoosen, Y., Pradeep, P., Kumar, P., du Toit, L.C., Choonara, Y.E., Pillay, V., 2018. Nanotechnology and glycosaminoglycans: Paving the way forward for ovarian cancer intervention. Int. J. Mol. Sci. 19, 253.

Hu, Y., Chen, J., Fan, T., Zhang, Y., Zhao, Y., Shi, X., Zhang, Q., 2017. Biomimetic mineralized hierarchical hybrid scaffolds based on in situ synthesis of nano-hydroxyapatite/chitosan/chondroitin sulfate/hyaluronic acid for bone tissue engineering. Colloids and Surfaces B: Biointerfaces. 157, 93-100.

Kawahara T, Akiba I, Sakou M, Sakaguchi T, Taniguchi H., 2018. Inactivation of human and avian influenza viruses by potassium oleate of natural soap component through exothermic interaction. PLoS ONE. 13, e0204908.

Lage, H., 2008. An overview of cancer multidrug resistance: A still unsolved problem. Cell. Mol. Life Sci. 65, 3145–3167.

Ma, X.H., Xu, Z.L., Ji, C.Q., Wei, Y.M., & Yang, H., 2010. Characterization, separation performance, and model analysis of STPP-chitosan/PAN polyelectrolyte complex membranes. Journal of Applied Polymer Science. 120, 1017–1026.

Mehta, S.K., Bhawna, Bhasin, K.K., Kumar, A., 2008. An insight into the micellization of dodecyldimethylethylammonium bromide (DDAB) in the presence of bovine serum albumin (BSA). J. Colloid Interface Sci. 323, 426–434.

Meka, V. S., Sing, M. K. G., Pichika, M. R., Nali, S. R., Kolapalli, V. R. M., & Kesharwani, P., 2017. A comprehensive review on polyelectrolyte complexes. Drug Discovery Today. 22, 1697–1706.

Michaels, A.S., 1965. Polyelectrolyte complexes. Ind. Eng. Chem. 57, 32–40.

Mohtashamian, S., Boddohi, S., Hosseinkhani, S., 2018. Preparation and optimization of self-assembled chondroitin sulfate-nisin nanogel based on quality by design concept. Int. J. Biol. Macromol. 107, 2730–2739.

Papagiannopoulos, A., 2018. Bovine serum albumin interactions with cationic surfactant vesicles decorated by a low-molar-mass polysaccharide. Colloids Surfaces A Physicochem. Eng. Asp. 537, 495–501.

Pradeep, P., Choonara, Y.E., Kumar, P., Pillay, V., 2016. “On-the-spot” arresting of chondroitin sulphate proteoglycans: Implications for ovarian adenocarcinoma recognition and intervention. Int. J. Mol. Sci. 17, 1136.

Riddick, T.M., 1968. Control of Colloid Stability through Zeta Potential. Wynnewood, Pa., Livingston.

Safari, M.G., Hosseinkhani, S., 2013. Lipid composition of cationic nanoliposomes implicate on transfection efficiency. J. Liposome Res. 23, 174–186.

Schatz, C. et al., 2004. Formation and properties of positively charged colloids based on polyelectrolyte complexes of biopolymers. Langmuir. 20, 7766–7778.

Serra Moreno, J., Panero, S., Artico, M., Filippini, P., 2008. Synthesis and characterization of new electroactive polypyrrole-chondroitin sulphate A substrates. Bioelectrochemistry. 72, 3–9.

Servaty, R., Schiller, J., Binder, H., Kohlstrunk, B., Arnold,K., 1998. IR and NMR Studies on the Action of Hypochlorous Acid on Chondroitin Sulfate and Taurine. Bioorganic Chemistry. 26, 33-43.

Solis, F.J. and De la Cruz, M.O., 2000. Collapse of flexible polyelectrolytes in multivalent salt solutions. J. Chem. Phys. 112, 2030–2035.

Song, H., Quan, F., Yu, Z., Zheng, M., Ma, Y., Xiao, H., Ding, F., 2019. Carboplatin prodrug conjugated Fe 3 O 4 nanoparticles for magnetically targeted drug delivery in ovarian cancer cells. J. Mater. Chem. B. 7, 433–442.

Souza, C.J.F., Garcia-Rojas, E.E., 2015. Effects of salt and protein concentrations on the association and dissociation of ovalbumin-pectin complexes. Food Hydrocoll. 47, 124–129.

ten Dam, G. B., van de Westerlo, E. M. A., Purushothaman, A., Stan, R. V, Bulten, J., Sweep, F. C. G. J., Massuger, L. F., Sugahara, K., van Kuppevelt, T. H., 2007. Antibody GD3G7 selected against embryonic glycosaminoglycans defines chondroitin sulfate-E domains highly up-regulated in ovarian cancer and involved in vascular endothelial growth factor binding. Am. J. Pathol. 171, 1324–1333.

Topel, Ö., Çakir, B.A., Budama, L., Hoda, N., 2013. Determination of critical micelle concentration of polybutadiene-block- poly(ethyleneoxide) diblock copolymer by fluorescence spectroscopy and dynamic light scattering. J. Mol. Liq. 177, 40–43.

Vallen, M., Schmidt, S., Oosterhof, A., Bulten, J., Massuger, L., Kuppevelt, T., 2014. Primary Ovarian Carcinomas and Abdominal Metastasis Contain 4,6-Disulfated Chondroitin Sulfate Rich Regions, Which Provide Adhesive Properties to Tumour Cells. PLoS ONE. 9, e111806.

Vallen, M.J.E., Van Der Steen, S.C.H.A., Van Tilborg, A.A.G., Massuger, L.F.A.G., Van Kuppevelt, T.H., 2014. Sulfated sugars in the extracellular matrix orchestrate ovarian cancer development: “When sweet turns sour”. Gynecol. Oncol. 135, 371–381.

van der Steen, S.C.H.A., Raavé, R., Langerak, S., van Houdt, L., van Duijnhoven, S.M.J., van Lith, S.A.M., Massuger, L.F.A.G., Daamen, W.F., Leenders, W.P., van Kuppevelt, T.H., 2017. Targeting the extracellular matrix of ovarian cancer using functionalized, drug loaded lyophilisomes. Eur. J. Pharm. Biopharm. 113, 229–239.

Wu, W., Zheng, Y., Wang, R., Huang, W., Liu, L., Hu, X., et al., 2012. Antitumor activity of folate-targeted, paclitaxelloaded polymeric micelles on a human esophageal EC9706 cancer cell line. Int. J. Nanomed. 7, 3487–3502.

Ye, T., Jiang, X., Li, J., Yang, R., Mao, Y., Li, K., Li, L., Chen, F., Yao, J., Wu, Y., Yang, X., Wang, S., Pan, W., 2015. Low molecular weight heparin mediating targeting of lymph node metastasis based on nanoliposome and enzyme-substrate interaction, Carbohydr. Polym. 122, 26–38.

Zhang, L., Sun, X., Song, Y., Jiang, X., Dong, S., Wang, E., 2006. Didodecyldimethylammonium Bromide Lipid Bilayer-Protected Gold Nanoparticles: Synthesis, Characterization, and Self-Assembly. Langmuir. 22, 2838-2843.

CHAPTER 5:

Synthesis and Evaluation of Chondroitin Sulphate-1,12 Diaminododecane Crosslinked Networks for Potential Utilization in Nanoarchetypes Targeting Ovarian Cancer

5.1. Synopsis of this Chapter

OC is notoriously known as the most lethal gynecologic malignancy, with associated mortalities on the rise due to aggressive rates of relapse and inefficacious chemotherapies. Conventional chemotherapeutics suffer a myriad of flaws including drug related adverse effects and resistance, which drastically complicate the management and treatment regimens of OC. Inherent with this chapter is the introduction and establishment of 1,12 diaminododecane (CL), a chemical crosslinker, as novel *"arrester"* of Chondroitin sulphate (CS; an over-expressed glycosaminoglycan (GAG) implicated in the progression of OC. Extensive proof of concept groundwork was conducted to ascertain the successful crosslinking *(or "arresting")* of 1,12 diaminododecane to CS, yielding stable CS-1,12 diaminododecane crosslinked networks at 37 ^{o}C. The proposed CS-1,12 diaminododecane crosslinked network was synthesized and characterized (FT-IR, DSC, TGA and XRD), confirming amide formation between the carboxylic acid moieties of the glucuronic acid units of CS and the primary amine groups of 1,12 diaminododecane. Varying the concentration of 1,12 diaminododecane caused marked changes to the size and zeta potential of the crosslinked network. As the concentration of 1,12 diaminododecane increased, a steady decline in the size and zeta potential of the network was observed, relative to the pristine CS polymer. The morphology of the CS-1,12 diaminododecane crosslinked network was observed under SEM to reveal spherical nanoparticle like structures. Methylene blue (MB) probe technology was employed to quantitatively assess the degree of 1,12 diaminododecane arresting to CS, revealing a steady decrease in the amount of MB adsorbing to the crosslinked networks as the crosslinker concentration increased. To this end, the successful crosslinking interactions between 1,12 diaminododecane and CS was concluded.

Key words: Crosslinking; Physicochemical Characterizations; Chondroitin Sulphate.

5.2. Introduction

OC possesses advanced capabilities to rapidly metastasize and evade early detection, securing its status as the world's leading mortality-associated cancer (Pradeep et al., 2016). Currently, limitations adversely associated with conventional therapies include disease relapse (Xiao et al., 2012), sub-optimal bioavailability (Kulhari et al., 2016), resistance and adverse effects (Bai et al., 2017), which correlates to poor survival rates and prognosis. The tumour microenvironment is a dynamic functioning entity, with several regions of interest (Qiao et al., 2018). The extracellular matrix (ECM) of OC, located in the stromal compartment of the tumour houses a dense network of proteoglycans that have been reported to contribute directly to OC progression (van de Steen et al., 2017). This particularly applies to Glycosaminoglycans (GAGs). GAGs are naturally occurring, anionic hetero-polysaccharides, consisting of repeated disaccharide units (N-acetylated hexosamine and uronic acid) that are either sulphated or non-sulphated monosaccharides. Based on their particular disaccharide composition and sulphation patterns, GAGs are subdivided into broad categories including hyaluronan (HA), chondroitin sulphate (CS) dermatan sulphate (DS), heparin and heparan sulphate (HS) and keratan sulphate (KS). These GAGs are implicated in regulating cellular properties and function (Afratis et al., 2012). The highly variable sulphation patterns of GAGs including their C-5 epimerization dictate their specific biological properties. Through targeting selected growth factors or regulating (cancer-associated) cell adhesion, proliferation, migration, and angiogenesis (Afratis et al., 2012; Vallen et al., 2014; Wegrowski et al., 2004). For instance, previous studies demonstrate that elevated expressions of GAGs such as HA was discovered exclusively in OC states, which aid OC metastasis (Anttila et al., 2000; Hiltunen et al., 2002) and rapidly stimulate ovarian carcinoma cell growth (Bourguignon et al., 1997).

CS (a highly virulent cancer associated GAG) is an anionic polysaccharide consists of a sugar backbone with repetitive disaccharide units composed of d-glucuronic acid (GlcA; U) and N-acetyl galactosamine (GalNAc; A) residues, which are variably

modified by O-sulphation (2- *O*, 4- *O*, and 6- *O*) (Asimakopoulou et al., 2008) (Figure 5.1).

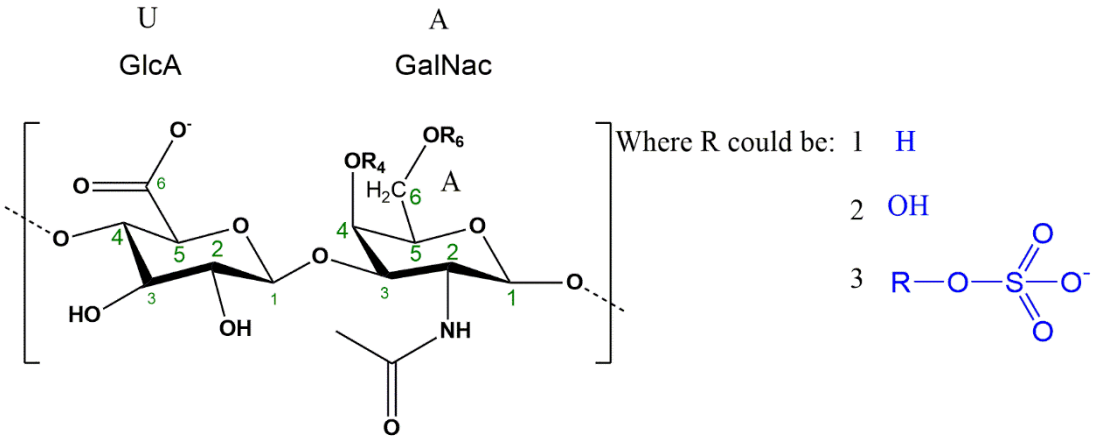

Figure 5.1. Showing the various sulphation positions of the CS molecule.

Up-to-date information has correlated the expression of the E sulphated form (CS-E) to OC. High levels of CS-E are expressed in tumour stroma and the surface of neoplastic cells (Pradeep et al., 2016), responsible for the accelerated tumour progression and metastasis. CS-E has been implicated with OC by binding to vascular endothelial growth factor (VEGF), responsible for niche tumour angiogenesis. In addition, High CS-E levels correlate with high VEGF levels which is crucial in tumour spheroid formation, which is associated with the highly aggressive and invasive characteristics of OC. CS-E further contributes to the advanced adhesive properties of tumours, stimulating the adhesive properties of adhesion molecules (N-cadherin and E- cadherin) (Vallen et al., 2014). To this end, the over-expressed CS structures in the ECM represents as a promising molecular target for research and development of OC drug delivery systems and diagnostics (van de Steen et al., 2017; Vallen et al., 2014; Vallen et al., 2014; Vallen et al., 2012; van de Steen et al., 2016).

In this proof-of-concept chapter, validation of this hypothesis described in chapter 1 was conducted. Utilizing 1,12 diaminododecane, an aliphatic chemical crosslinker. In-depth investigations were carried out to assess the potential of 1,12 diaminododecane to arrest (or crosslink) CS. Defining this preliminary crosslinked network is crucial as it determines if 1,12 diaminododecane is a suitable future candidate for CS arresting (before incorporating into advanced drug delivery systems for *in vitro* cell studies). In 1994, 1,12 diaminododecane was reported to form crosslinked products with CS,

however, the study lacked chemical integrity characterizations, stability, morphological evaluations and thermal analysis (Sintov et al., 1995). Utilizing more advanced technology, the CS-1,12 diaminododecane crosslinking via amide formation between the amine group from the crosslinker with the abundant carboxylic acid moieties of CS to yield a stable CS-1,12 diaminododecane crosslinked networks with reduced water solubility and anionic groups at 37 °C was proved (Figure 5.2).

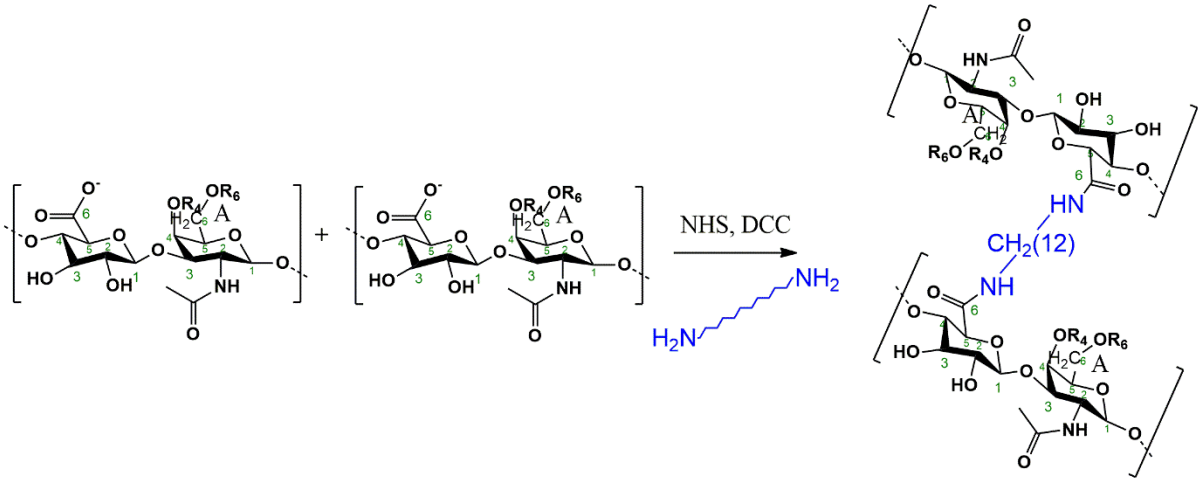

Figure 5.2. Proposed mechanism of 1,12 diaminododecane crosslinking CS, forming an arrested CS-1,12 diaminododecane network.

5.3. Materials and Methods

5.3.1. Materials

1,12 diaminododecane (98%, 200.36 g/mol), Chondroitin Sulphate sodium salt from shark cartilage, with a carboxylic acid and sulphate anionic content (determined via spectrophotometric mapping analysis) of 0.746 mmoL/g, *N*,*N*′-Dicyclohexylcarbodiimide (99%, 206.33 g/mol) and *N*-Hydroxysuccinimide (98%, 115.09 g/mol) were all purchased from Sigma Aldrich including (St. Louis, Missouri, United States), Methylene blue (MB) was purchased from BDH chemicals (Ltd, England).

5.3.2. Synthesis of CS-1,12 Diaminododecane Crosslinked Networks

A total of 300 mg CS was completely dissolved in 4 mL of distilled water, whilst 1,12 diaminododecane and DCC was dissolved with 2 mL of methanol. The crosslinker solution was rapidly introduced to the solution containing CS and allowed to react for 24 hours at ambient temperature. The residual methanolic content was removed via rotary evaporation (Rotavapor® RII, BüchiLabortechnik AG, Switzerland) and dialysed overnight. The mixture was then transferred to a cellulose dialysis membrane (MW cut-off: 14 000) and dialysed over three consecutive days. Finally, the pure mixture was then freeze-dried before storing at room temperature. The amount of DCC and 1,12 diaminododecane used is summarised in Table 5.1.

Table 5.1. Showing the various amounts of DCC and 1,12 diaminododecane used for chemical synthesis of CS networks.

Molar % of crosslinker	CS (mg)	DCC (mg)	1,12 diaminododecane (mg)
30	300	88.5	40
50	300	117.6	65
90	300	265.8	112

***The molar percentage of the 1,12 diaminododecane crosslinker was calculated according to an average molecular weight of 0.3 g of CS over 458 (which is the molecular weight of one dimer unit of the polysaccharide) (Sintov et al., 1995).

5.3.3. Physicochemical and Thermal Analysis of the CS-1,12 Diaminododecane Crosslinked Network

5.3.3.1. Chemical Integrity Characterization of the CS-1,12 Diaminododecane Crosslinked Network.

Fourier Transmission Infrared (FT-IR) spectrophotometry was performed in order to characterize the chemical structure of the crosslinked CS. Analyses were undertaken at high resolution with wavenumbers ranging from 650-4000 cm^{-1} on a FTIR Spectrophotometer using PerkinElmer® spectrum quant software (Perkin Elmer Inc. MA, USA).

5.3.3.2. Thermal Analysis of the CS-1,12 Diaminododecane Crosslinked Network CS.

Differential Scanning Calorimetry (DSC) analysis was undertaken (Mettler Toledo DSC1 STARe System, Switzerland) in order to determine the changes in heat flow between pristine 1,12 diaminododecane and CS and crosslinked CS-1,12 diaminododecane networks. Indium was used to calibrate the instrument and samples were weighed in standard DSC aluminium pans and analysed within a temperature gradient of 25-300 °C under an 8kPa nitrogen atmosphere. A bare pan served as a reference for all DSC scans.

5.3.3.3. Evaluation of Phase Transitions of the CS-1,12 Diaminododecane Crosslinked Networks

X-ray diffraction was employed in order to determine the phase changes (crystallinity or amorphous) between CS polymers after crosslinking to 1,12 diaminododecane crosslinking. This characterisation technique was performed on the Rigaku MiniFlex 600 Benchtop X-ray Diffractometer (Rigaku Corporation, Tokyo, Japan). A powdered sample secured on a sample holder and was scanned at a rate of 15° per minute with a diffraction angle range of 03-90° 2 θ with a degree step of 0.02, a voltage of 40 kV and a current of 15 mA.

5.3.3.4. Thermal Stability analysis by Thermogravimetric Experimentation of the CS-1,12 Diaminododecane Crosslinked Network

Thermogravimetric analysis (TGA) of the native CS, 1,12 diaminododecane and CS-1,12 diaminododecane crosslinked networks PEC was carried out using the TGA software (PerkinElmer STA 6000, Beaconsfield, United Kingdom) in order to elucidate the chemical reactions and/or weight changes relating to thermal stability. The following parameters were employed for the analysis: heat from 35-900 °C at a rate of 10 °C/min and nitrogen gas (N_2). The percentage mass loss was calculated using

Delta Y software against maximum decomposition temperature-initial decomposition temperature.

5.3.4. Size, Zeta Potential, Polydispersity Index and Morphological Analysis of the CS-1,12 Diaminododecane Crosslinked Network

5.3.4.1. Morphological Characterization by Scanning Electron Microscopy Imagery on the CS-1,12 Diaminododecane Crosslinked Network.

Scanning electron microscopy (SEM) (Zeiss Sigma FEG, Jena, Germany) was undertaken to establish the surface morphology of the newly formed CS-1,12 diaminododecane crosslinked network at various 1,12 diaminododecane molar concentrations. Each dry lyophilized sample was secured on a metallic sample stub using tape, following sputter-coating with a one layer of carbon and two layers of gold palladium. The sample was viewed under varying magnifications at an accelerating voltage of 20 kV.

5.3.4.2. Network Size Determination

Determination of the average particle size and polydispersity index (PDI) of the CS-1,12 diaminododecane was analysed using a Zetasizer NanoZS instrument (Malvern Instruments (PTY) LTD, Worcestershire, UK) at 25 °C. Approximately 1 mg/mL crosslinked samples or pristine CS and 1,12 diaminododecane were sonicated (bath sonication) and filtered (0.22 µm) into a plastic cuvette. Each test was performed in triplicate and the average value in each case was reported accordingly.

5.3.4.3. Network Zeta Potential Determination

In order to certify the expected surface charge modifications of CS induced by 1,12 diaminododecane arresting, zeta potential analysis was conducted using the Zetasizer NanoZS instrument (Malvern Instruments (PTY) LTD, Worcestershire, UK). CS (1 mg/ 1mL), 1,12 diaminododecane (1 mg/ 1mL), and CS-1,12 diaminododecane

crosslinked networks (1 mg/ 1mL), was utilized for the experimentation. Each test was performed in triplicate and the average value in each case was reported accordingly.

5.3.5. Degree of 1,12 Diaminododecane Crosslinking onto CS Backbones

The degree of 1,12 diaminododecane crosslinking to CS was determined via selective adsorption of MB onto the various concentrations of CS crosslinked networks as reported by Fras and co-workers and Sintov and co-workers. To a solution of 25 mL of MB chloride (150 mg/L), CS (50 mg) and 1,12 diaminododecane network (50 mg) was dissolved and the solution was buffered to a pH 8,5 with borate buffer (25 mL). The resulting solution was left to react for 1 hour at room temperature in a 100 mL Erlenmeyer flask. The MB content was determined spectrophotometrically at 668 nm. The extent of crosslinking was assessed by measuring the relative percentage of MB which was adsorbed onto the various crosslinked networks relative to free CS. The relative percentage of MB that adsorbed onto the available CS groups was calculated as follows:

Eq. 5.1. $$Relative\ MB\ adsorption\ factor = \frac{(\mathrm{Ao}-\mathrm{Am})}{(Ao-Ac)} \times 100$$

Where *Am*, is the absorbance value of MB solution containing the various CS-1,12 diaminododecane crosslinked networks; *Ac* is the absorbance value of the MB solution containing non-crosslinked CS; and *Ao* is the initial absorbance value of the MB solution before any adsorption occurred (Sintov et al., 1995).

5.4. Results and Discussion

5.4.1. Physico-Chemical Analysis of the CS-1,12 Diaminododecane Crosslinked Network

5.4.1.1. Chemical Integrity Characterization of the CS-1,12 Diaminododecane Crosslinked Network

FT-IR was used to assess the changes in the chemical structure of CS when crosslinked with 1,12 diaminododecane (Figure 5.3). The FT-IR spectra of CS confirms the presence of –OH and -NH stretching vibration at 3321 cm^{-1}, where the –OH stretching vibration is overlapped by -NH stretching; the absorption of -CH stretching of methyl or methylene group is at 2886 cm^{-1}; the peak at to 1612 cm^{-1} were assigned to -NH bending of amide II (Amruktar et al., 2009) and 1026 cm^{-1} are assigned to -CO vibration stretching; the bands at 1410 and 1375 cm^{-1} are due to the coupling of the -CO stretch vibration and -OH variable-angle vibration and suggests the existence of the free carboxyl group. The peak at 1219 cm^{-1} corresponds to the stretching vibrations of S=O bond of N-acetyl-d-galactosamine (-$OSO3^{2-}$), which is the characteristic peak of CS (Fejardo et al., 2012), whilst 1,12 diaminododecane shows -NH stretch at 3330 cm^{-1}, methylene stretching at 2916 cm^{-1} and the -NH bending at 1606 cm-1; the peak at 1192 cm^{-1} is associated with -CN alkyl stretching. For the crosslinked CS (30,50 and 90 Molar % 1,12 diaminododecane), an increase in the intensity of the amide peaks at 1612 and 1026 cm^{-1} is observed, suggesting the formation of additional amide bonds. In addition, the methylene stretch from the crosslinker is present amongst all concentrations of crosslinked networks. Furthermore, it is worthy to note that as the concentration of crosslinker increases, the intensity of the peak corresponding to the amide (1612 and 1026 cm^{-1}) increases, suggesting greater formation of additional amide bonds, with a higher degree of crosslinking. The latter statement is in accordance with the findings observed in the zeta potential and the relative MB adsorption factor on the crosslinked network, suggesting higher degree of crosslinking as 1,12 diaminododecane concentration increases in the network. In addition, we observe a decrease in the peaks at 3300, 1606 and1192 cm^{-1} corresponding to -NH stretching, -NH bending and -CN alkyl

stretching respectively, inferring that the free -NH_2 group of 1,12 diaminododecane is diminished during the crosslinking synthesis. Furthermore, a decrease in the intensity of the peak at 1410 cm^{-1} in relation to the peak at 1375 cm^{-1} is seen in all crosslinked products relative to pristine CS, this could potentially be associated with a decrease in the free carboxylic acid moieties available due to their reaction with -NH_2 from the crosslinker. Furthermore, this difference in peak height between 1410 and 1375 cm^{-1} appears more pronounced in the 65 mg and 112 mg crosslinked networks, suggesting a higher degree of crosslinking. Lastly, the characteristic peak of CS at 1219 cm^{-1} (-$OSO3^{2-}$) confirmed the presence of CS in the crosslinked network (Amruktar et al., 2009).

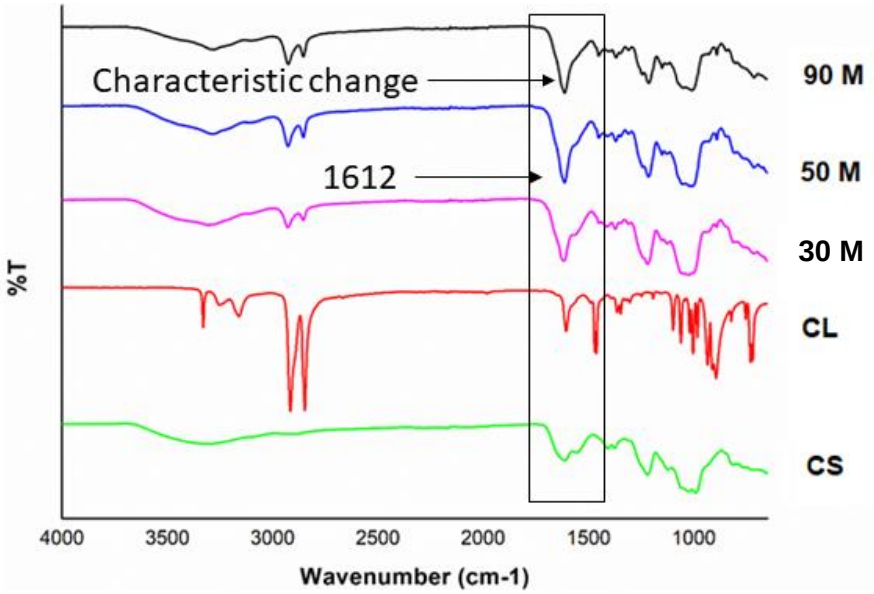

Figure 5.3. FT-IR spectra for pristine CS, CL = 1,12 diaminododecane, and the various crosslinked networks represented on the graph by the total molar % of 1,12 diaminododecane used (30, 50 and 90 Molar percentage).

5.4.1.2. Thermal Analysis of CS-1,12 Diaminododecane Crosslinked Network

The DSC thermograms of the crosslinked products (C), (D) and (E) compared to the pristine (A) (Figure 5.4) CS reveals that as the crosslinker concentration increases, the endothermic peak related to water evaporation (116. 5 °C) decreases and shifts towards a lower temperature range (90-105 °C). These results indicate that the

crosslinked products display smaller amounts of absorbed water, suggesting that this water is weakly bonded to the crosslinked networks (Cavalcanti et al., 2005). This trend correlates to the DSC thermograms obtained for crosslinked CS, when trisodium trimetaphosphate (TMFS) was used as the crosslinking agent presented by Cavalcanti and co-workers.

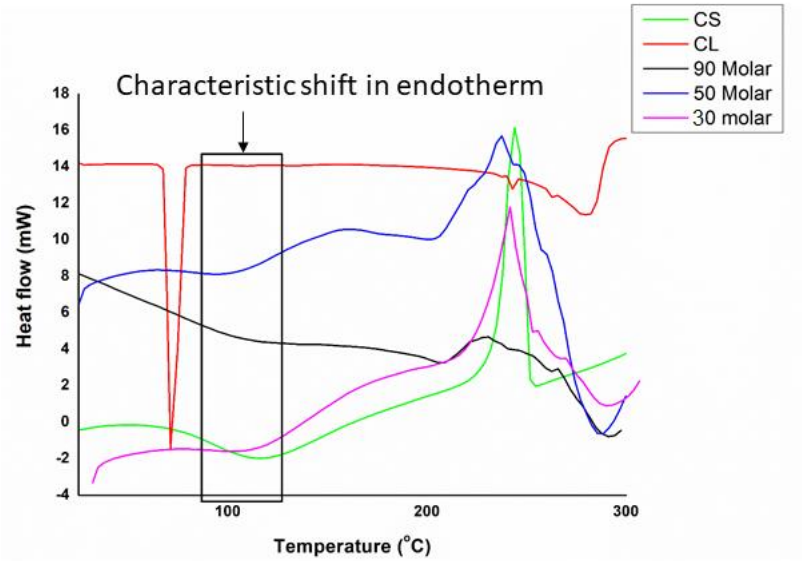

Figure 5.4. DSC thermograms for pristine CS, CL = 1,12 diaminododecane, and the various crosslinked networks represented on the graph by the total molar % of 1,12 diaminododecane used (30, 50 and 90 Molar percentage).

5.4.1.3. Phase Transition determination of 1,12 Diaminododecane Crosslinking to CS

XRD characterizations were conducted to evaluate the microstructural modifications of CS due to the physical crosslinking with 1,12 diaminododecane to yield CS-1,12 diaminododecane crosslinked networks (Figure 5.5). Morphological studies were performed to determine the phase transitions between 1,12 diaminododecane, CS polymer, and the resultant crosslinked networks out. Diffractograms of CS confirmed the amorphous nature of the polymer. It was evident from diffractograms that 1,12 diaminododecane demonstrated sharp peaks at ~ 25 2θ confirming the crystalline nature of the crosslinker. For the CS-1,12 diaminododecane crosslinked network, a loss in the crystallinity of 1,12 diaminododecane is observed due to crosslinking on

polymeric backbone and amorphous behavior of crosslinked network (Ali et al., 2019). In addition, the physical crosslinking of CS chains did not significantly change its diffraction patterns. This amorphic nature is favored as it infers a denser network, which has great utility for blocking nutritional suppliers from the tumour vasculature to the OC cell surfaces *in situ* (Ferjado et al., 2013).

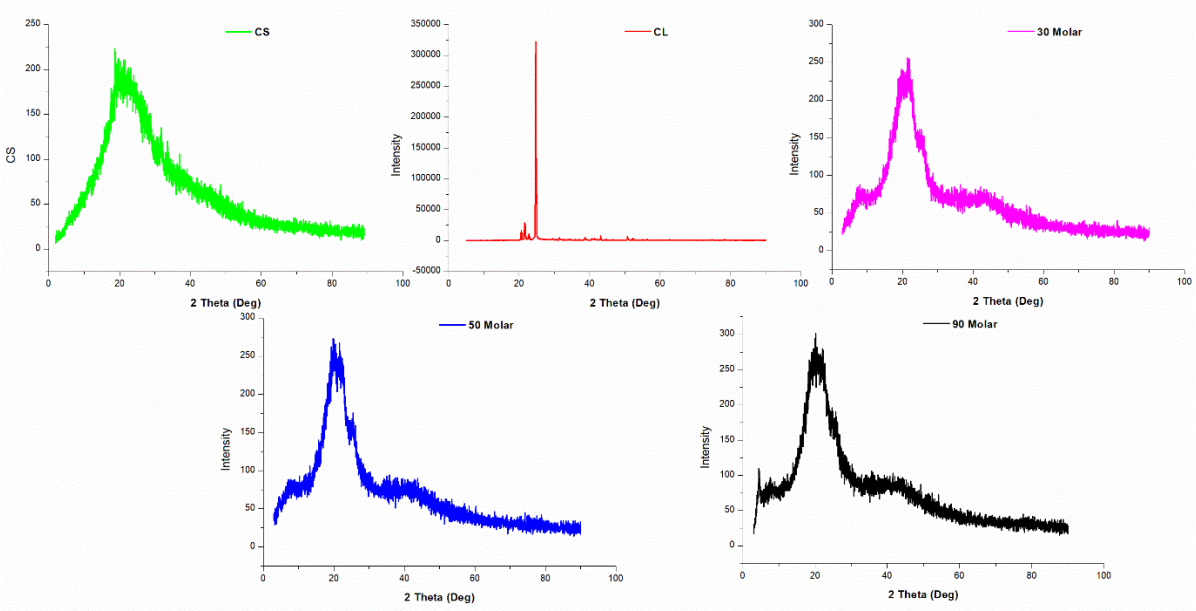

Figure 5.5. XRD patterns for pristine CS, CL = 1,12 diaminododecane, and the various crosslinked networks represented on the graph by the total molar % of 1,12 diaminododecane used (30, 50 and 90 Molar percentage).

5.4.1.4. Thermogravimetric Analysis of the CS-1,12 Diaminododecane Crosslinked Network

In order to determine the thermal stability of the CS; thermogravimetric analysis (TGA) was utilized. Weight loss vs. temperature curves for CS, 1,12 diaminododecane and the various concentrations of CS-1,12 diaminododecane crosslinked networks are presented in figure 5.6. It is evident that the weight loss from CS occurs in three major segments. First segment starts at 100 °C and counts for approximately 10% weight loss (before reaching a temperature of 205 °C). This resultant weight loss relates to the loss of moisture, which occurs due to anhydride formation through polymer chains. Second stage commences at 205 °C and ends at 255 °C, which counts for

approximately 30% weight loss. This weight loss may be attributed to initial degradation of carboxylate and sulfonate groups in polymer backbone. Degradation continues further in the third stage which starts from 255 °C and lasts up to complete degradation of the polymer (Khalid et al., 2018).

The TGA thermograms of CS-1,12 diaminododecane crosslinked networks revealed that this first stage of weight loss (moisture loss) occurs at an earlier stage (approximately 90 °C) for all crosslinked networks, supporting the claims that less water is absorbed onto these crosslinked networks (seen during the DSC analysis). It is further observed that as the crosslinker concentration increases to 90 Molar %, a decrease in the weight loss percentage is observed relative to the 30 Molar % of 1,12 diaminododecane crosslinked networks and pristine CS. This suggests that the higher concentration of 1,12 diaminododecane increases the thermal stability of the network relative to CS at this temperature range, as less weight loss is observed. This implies that within the tumour microenvironment (37 °C), the network stability is assured, with negligible dissociation into smaller weight fragments.

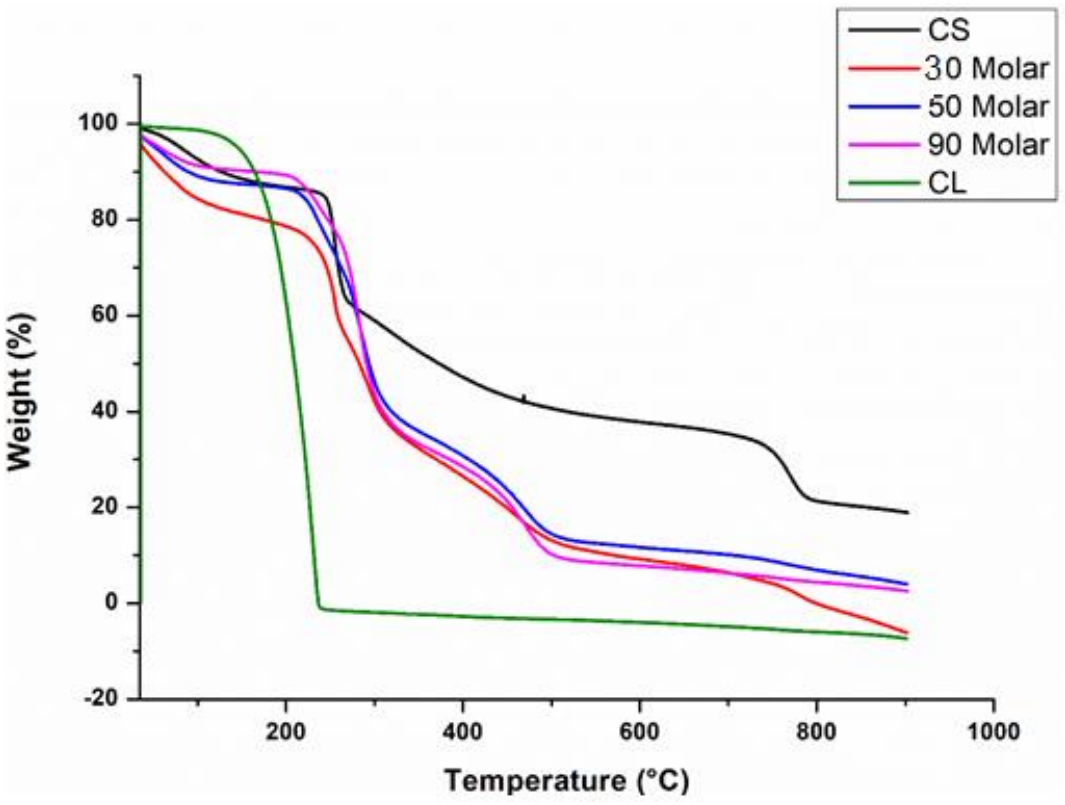

Figure 5.6. Thermogravimetric curves for pristine CS, CL = 1,12 diaminododecane, and the various crosslinked networks represented on the graph by the total molar % of 1,12 diaminododecane used (30, 50 and 90 Molar percentage).

5.4.2. Morphological Characterization of the CS-1.12 Diaminododecane Crosslinked Network

5.4.2.1. Size and Zeta potential Determination of the CS-1,12 Diaminododecane Crosslinked Network

The size and zeta potential of the CS-1,12 diaminododecane crosslinked networks at varying concentrations of 1,12 diaminododecane was determined to observe what effect chemical crosslinking has on the CS polymer macromolecule (Figure 5.7). Pristine CS (2887 nm ± 1466.29) drastically decreased in size after crosslinking with 30 Molar % of 1, 12 diaminododecane (550 nm ± 49,7). This trend was further continued as the concentration of 1,12 diaminododecane in the crosslinked network increased (50 Molar % = 417 nm ± 23.61; 90 Molar % = 307 nm ± 8.66) and approached the size of pristine 1,12 diaminododecane (214 nm). An identical trend with respect to zeta potential was additionally observed. Briefly, as the crosslinker concentration increased, the zeta potential decreased approaching neutral. The presence of higher density of reacting groups, such as free carboxylic acids causes electrostatic repulsion and, consequently, an increase in the hydrodynamic diameter of the polymer network and the zeta potential, thus, the decrease in these reacting groups by means of crosslinking reduces the size and potential, further suggesting a favourable interaction between the two moieties (Jardim et al., 2015). The potential reasoning for the wide range of error for CS in the figure relates to the chain length and macro-size nature of the CS polymer upon detection using DLS on the Zetasizer NanoZS instrument, which is primarily designed to test nanomaterials. A major fluctuation was generated amongst the biological replicates as a result, which ultimately led to the wider standard deviation. Nevertheless, as the long pristine polysaccharide chains of CS are crosslinked into more stable networks, a reduction in the chain length and size of the polymer was observed.

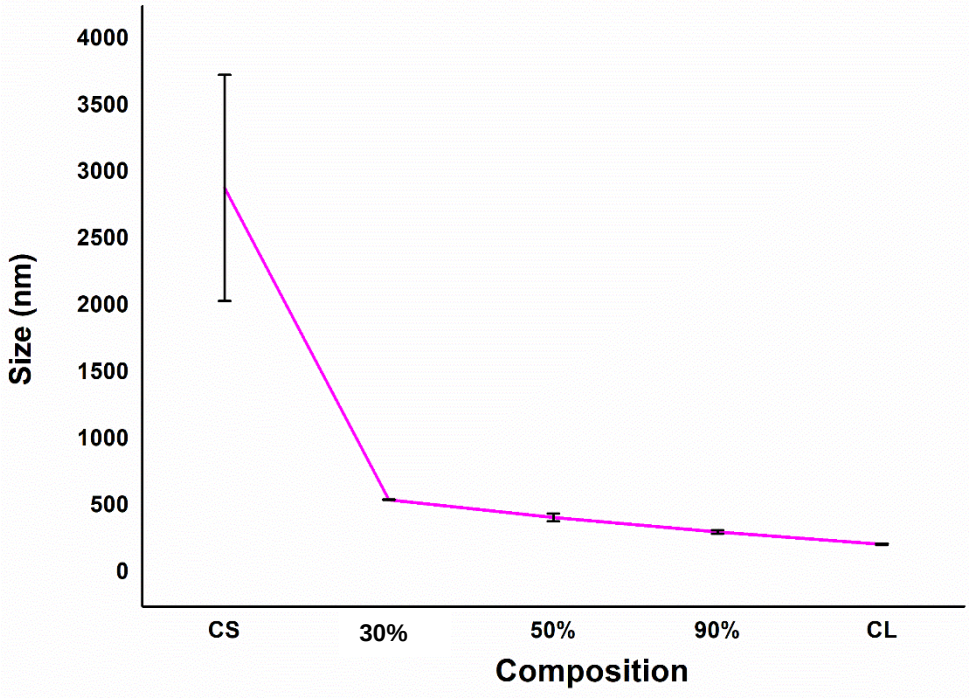

Figure 5.7. Graphical illustration of the size trends of CS and the various sizes of structurally modified CS backbones with various concentrations of 1,12 diaminododecane forming crosslinked networks.

5.4.2.2. Evaluation of the Morphology of the CS-1,12 Diaminododecane Crosslinked Networks

The CS-1,12 diaminododecane crosslinked network topology was evaluated using SEM imagery (Figure 5.8). In addition to confirming the architectures within the network microstructure. Confirmation of the morphological variations of the different molar concentrations of 1,12 diaminododecane utilized in the synthesis was performed revealing no significant changes between them. The imagery suggests a high network of crosslinked fibers, with regions of perfectly spherical orientated crosslinked CS nanostructures. CS has been commonly crosslinked with chitosan producing nanoparticles (Tsai et al., 2011), though the formation of CS crosslinked to CS nanoparticles is rarely reported in literature, and could thus be a novel finding, for additional niche CS nanoparticle applications for future drug delivery systems.

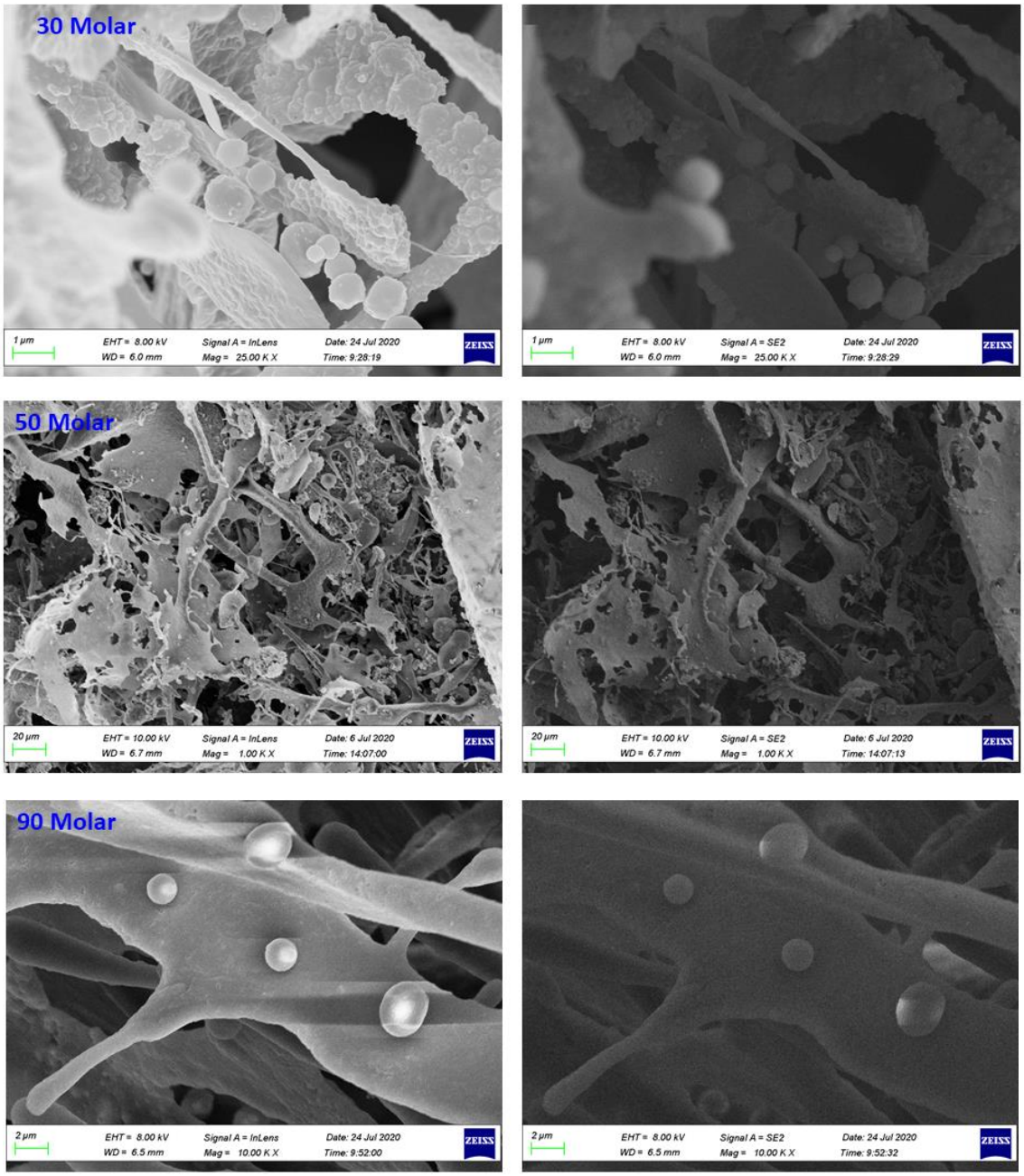

Figure 5.8. Typical SEM imagery of the CS-1,12 diaminododecane crosslinked networks.

5.4.3. Degree of 1,12 Diaminododecane Crosslinking on CS

Methylene blue (MB) is a cationic dye that has the ability to associate on the crosslinked CS by strong ionic binding (adsorption). This MB probe technique was established to characterize the degree of crosslinking within the CS-1,12 diaminododecane crosslinked network. The degree of CS crosslinking was evaluated

by measuring the residual ability of CS polymer to adsorb MB from aqueous solutions. The adsorption process involves three crucial processes: (1) dissociation of the MB-water (MB-H_2O) interaction; (2) de-solvation of the hydrated U sites of the swollen crosslinked CS networks, namely, dissociation of the CS-water (CS- H_2O) interactions; and (3) attraction and binding of the water-dissociated MB by the free U sites of the CS (CS-MB). The adsorption process can be expressed in terms of enthalpy (ΔH°) and entropy (ΔS°) as follows:

Eq. 5.2. $$\Delta H° = \Delta H°CS - MB + \Delta H°MB - W + \Delta H°CS - W$$

Eq. 5.3. $$\Delta S° = \Delta S°CS - MB = \Delta S°MB - W + \Delta S°CS - W$$

It was found experimentally that the values of the adsorptive factor of the adsorbate decreased with the extent of crosslinking. As shown in figure 5.9, less MB molecules are adsorbed on the crosslinked polymer network when the degree of crosslinking (i.e., lower Relative MB adsorption factor) is higher. This occurs as MB cations lose its ability to penetrate through the denser crosslinked network with the lower relative MB adsorption factors. In addition, there are less available anionic carboxylic acid groups for MB cationic adsorption as a result of amide formation between the NH_2 of 1,12 diaminododecane.

It may be assumed that in the aqueous environment, the CS-MB complex is arranged in a more orderly way than the CS or the MB. Therefore, both the enthalpy (ΔH°CS-MB) and the entropy (ΔS° CS-MB) changes of the binding process are negative. The overall enthalpy change is also negative because of the low energy required to dissociate the interactions with water (i.e., hydrogen bonds). As for the entropy considerations, the dissociation of water-bound molecules may contribute only a positively low entropy change to the overall entropy change. However, the more crosslinked (and less hydrophilic) CS is, the more ordered its hydrated state is, thus possessing higher entropy values. This results in an increase in the entropy change associated with freeing U in the hydrated CS chains and a decrease in the overall entropy change of MB adsorption (Sintov et al., 1995).

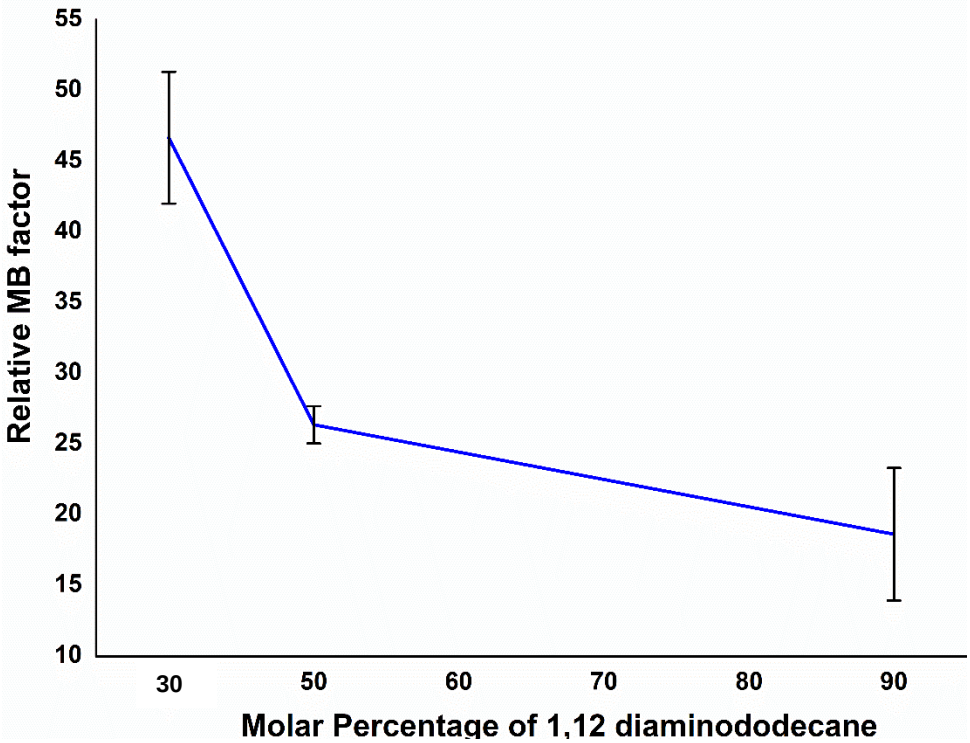

Figure 5.9. Graphical illustrations of the relative MB adsorption factor for the various molar % of the crosslinked CS networks where 30 molar = 46.67 ± 8.07; 50 Molar= 26.36 ± 2.28; 90 Molar= 18.63 ± 4.68).

5.5. Conclusion

Crosslinked CS networks using 1,12 diaminododecane were synthesized successfully by an inhouse chemical crosslinking technique. The novel technique led to fabricated networks which exhibited physicochemical, thermal, and morphological traits strongly confirming the advanced modifications of the polymer suitable to disturb *in situ* cell-cell signalling and nutritional supplies. The microstructural modifications on CS polymer backbone by 1,12 diaminododecane seen by FT-IR and XRD analysis are in favour of an altered state polymeric network, leading to changes in recognition and potential disturbances in the CS structure. These disturbances reduce the ability of the ECM to have a structural and supportive role for OC dissemination. The relative MB factor displayed high a degree of crosslinking, which suggests that considerable modifications of the CS polymer backbone by 1,12 diaminododecane is possible, which is a favourable preliminary finding for the future usage of 1,12 diaminododecane

in the *in situ* crosslinking of CS-E. Further studies are however required, such as the incorporation of the crosslinker into nanoarchetype formulations with subsequent anti-cancer testing in CS-E over-expressed cell lines.

5.6. References

Afratis, N., Gialeli, C., Nikitovic, D., Tsegenidis, T., Karousou, E., Theocharis, A.D., Pavão, M.S., Tzanakakis, G.N., Karamanos, N.K., 2012. Glycosaminoglycans: Key players in cancer cell biology and treatment. FEBS J. 7, 1177-97.

Ali, A., Khalid, I., Usman, M., Barkat, K., Ullah Khan, I., Khalid Syed, H., & Umar, A., 2019. Preparation and in vitro evaluation of chondroitin sulfate and carbopol based mucoadhesive controlled release polymeric composites of loxoprofen using factorial design. European Polymer Journal. 121, 109312.

Amrutkar, J. and Gattani, S., 2009. Chitosan–Chondroitin Sulfate Based Matrix Tablets for Colon Specific Delivery of Indomethacin. AAPS PharmSciTech. 10, 670-677.

Anttila MA, Tammi RH, Tammi MI, Syrjänen KJ, Saarikoski SV, Kosma VM., 2000. High levels of stromal hyaluronan predict poor disease outcome in epithelial ovarian cancer. CANCER RESEARCH. 60, 150–155.

Asimakopoulou, A. P., Theocharis, A. D., Tzanakakis, G. N., Karamanos, N. K., 2008. The biological role of chondroitin sulphate sulphate in cancer and chondroitin – based anti- cancer drugs. In Vivo. 3, 385 – 389.

Bai, D. P., Zhang, X. F., Zhang, G. L., Huang, Y. F., & Gurunathan, S., 2017. Zinc oxide nanoparticles induce apoptosis and autophagy in human ovarian cancer cells. International journal of nanomedicine. 12, 6521–6535.

Bourguignon, L. Y. W.; Zhu, H.; Chu, A.; Iida, N.; Zhang, L.; Hung, M. C., 1997. Interaction between the adhesion receptor, CD44, and the oncogene product,

p185(HER2), promotes human ovarian tumor cell activation. J. Biol. Chem. 272, 27913–27918.

Cavalcanti, O. A., Silva, C.C., Pineda, E. A.G., Hechenleitner, A. A. W., 2005. Synthesis and Characterization of Phosphated Crosslinked Chondroitin Sulfate: Potential Ingredient for Specific Drug Delivery. Acta Farm. Bonaerense. 24, 234-8.

Fajardo, A., Lopes, L., Pereira, A., Rubira, A. and Muniz, E., 2012. Polyelectrolyte complexes based on pectin–NH2 and chondroitin sulfate. Carbohydrate Polymers. 87, 1950-1955.

Fajardo, A. R., Fávaro, S. L., Rubira, A. F., & Muniz, E. C., 2013. Dual-network hydrogels based on chemically and physically crosslinked chitosan/chondroitin sulfate. Reactive and Functional Polymers. 73, 1662–1671.

Fras, L., Stana-Kleinschek, K., Ribitsch, V., Sfiligoj-Smole, M. and Kreze, T., 2004. Quantitative Determination of Carboxyl Groups in Cellulose Polymers Utilizing Their Ion Exchange Capacity And Using A Complexometric Titration. Materials Research Innovations. 8, 145-146.

Hiltunen, E. L. J., Anttila, M., Kultti, A., Ropponen, K., Penttinen, J., Yliskoski, M., Kuronen, A. T., Juhola, M., Tammi, R., Tammi, M., Kosma, V. M., 2002. Elevated hyaluronan concentration without hyaluronidase activation in malignant epithelial ovarian tumors. Cancer Res. 62, 6410–6413.

Jardim, K.V., Joanitti, G.A., Azevedo, R.B., Parize, A.L., 2015. Physico-chemical characterization and cytotoxicity evaluation of curcumin loaded chitosan/chondroitinsulfate nanoparticles, Materials Science and Engineering: C. 56, 294-304.

Khalid, I., Ahmad, M., Minhas, M.U., Barkat,K., 2018. Synthesis and evaluation of chondroitin sulfate based hydrogels of loxoprofen with adjustable properties as controlled release carriers. Carbohydrate Polymers. 181,1169-1179.

Kulhari, H., Pooja, D., Kota, R., Reddy, T.S., Tabor, R.F., Shukla, R., Adams, D.J., Sistla, R., Bansal, V., 2016. Cyclic RGDfK Peptide Functionalized Polymeric Nanocarriers for Targeting Gemcitabine to Ovarian Cancer Cells. Mol. Pharm. 13, 1491–1500.

Pradeep, P., Choonara, Y. E., Kumar, P., Pillay, V., 2016. “On-the-spot” arresting of chondroitin sulphate proteoglycans: Implications for ovarian adenocarcinoma recognition and intervention. Int. J. Mol. Sci. 17.

Qiao, H., Tang, T., 2018. Engineering 3D approaches to model the dynamic microenvironments of cancer bone metastasis. Bone Res. 6, 3.

Sintov, A., Di-Capua, N. and Rubinstein, A., 1995. Cross-linked chondroitin sulphate: characterization for drug delivery purposes. Biomaterials. 16, 473-478.

Tsai, H.Y., Chiu, C.C., Lin, P.C., Chen, S.H., Huang, S.J. and Wang, L.F., 2011. Antitumor Efficacy of Doxorubicin Released from Crosslinked Nanoparticulate Chondroitin Sulfate/Chitosan Polyelectrolyte Complexes. Macromol. Biosci. 11, 680-688.

Vallen, M., Schmidt, S., Oosterhof, A., Bulten, J., Massuger, L., Kuppevelt, T., 2014. Primary Ovarian Carcinomas and Abdominal Metastasis Contain 4,6-Disulfated Chondroitin Sulfate Rich Regions, Which Provide Adhesive Properties to Tumour Cells. PLoS ONE. 9, e111806.

Vallen, M.J.E., Massuger, L.F.A.G., Ten Dam, G.B., Bulten, J., Van Kuppevelt, T.H., 2012. Highly sulfated chondroitin sulfates, a novel class of prognostic biomarkers in ovarian cancer tissue. Gynecol. Oncol. 127, 202–209.

Vallen, M.J., van der Steen, S., van Tiborg, A., Massuger, L., van Kuppevelt, T., 2014. Sulfated sugars in the extracellular matrix orchestrate ovarian cancer development: ‘when sugars turn sour’. Gynaecologic oncology.135, 371-381.

van der Steen, S.C.H.A., Raav, R., Langerak, S., van Houdt, L., van Duijnhoven, S.M.J., van Lith, S.A.M., Massuger, L.F.A.G., Daamen, W.F., Leenders, W.P., van Kuppevelt, T.H., 2017. Targeting the extracellular matrix of ovarian cancer using functionalized, drug loaded lyophilisomes. Eur. J. Pharm. Biopharm. 113, 229–239.

Van Der Steen, S.C.H.A., Van Tilborg, A.A.G., Vallen, M.J.E., Bulten, J., Van Kuppevelt, T.H., Massuger, L.F.A.G., 2016. Prognostic significance of highly sulfated chondroitin sulfates in ovarian cancer defined by the single chain antibody GD3A11. Gynecol. Oncol. 140, 527–536.

Xiao, K., Li, Y., Lee, J.S., Gonik, A.M., Dong, T., Fung, G., Sanchez, E., Xing, L., Cheng, H.R., Luo, J., Lam, K.S., 2012. “OA02” peptide facilitates the precise targeting of paclitaxel-loaded micellar nanoparticles to ovarian cancer In Vivo. Cancer Res. 72, 2100–2110.

Wegrowski, Y., Maquart, F.X., 2004. Involvement of stromal proteoglycans in tumour progression, Crit. Rev. Oncol. Hematol. 49, 259–268.

CHAPTER 6:

Novel Anti-MUC 16 Functionalized Didodecyldimethyl Ammonium Bromide Cationic Nanoliposomes for Inhibition of Ovarian Cancer Activity In Vitro

6.1. Synopsis of this Chapter

OC is the most lethal gynecologic malignancy, implicated with high rates of relapse and inefficacious chemotherapy. Current treatment strategies are flawed by a myriad of challenges, which lead to adverse effects and drug resistance. This drastically hinders the clinical performance of medicines, escalating the demand for a non-pharmacological-personalized-treatment approach for OC-targeted therapy**.** In aims to deter conventional drugs, a preliminary proof of concept of our groups internationally recognized hypothesis was undertaken (Detailed in Chapter 4). The purpose of this chapter is to further validate the integrity of the hypothesis, by designing, formulating, and characterizing an OC targeted nanosystem. Didodecyldimethyl ammonium bromide (DDAB) cationic nanoliposomes (NLs) were synthesized and functionalized with the anti-MUC 16 antibody for OC active targeting. Particle size, zeta potential, DDAB residual content, cytotoxicity, and various biological assays that link CS-E to OC dissemination were performed (proliferation, migration, and apoptosis assays) on CS-E over-expressed-SKOV3 and healthy HEK293 cell lines. Lastly, cellular uptake studies were undertaken. The experimental findings concluded that the anti-MUC 16 NLs display advanced selectivity for a precision non-pharmacological approach to OC therapy.

Keywords: Ovarian Cancer; SKOV3 cell lines; Chondroitin sulphate; Nanotechnology.

6.2. Introduction

OC is a major global health concern, particularly in South Africa (Smith et al., 2009). In the past five-year survey, statistics reflected that approximately 21.9 million new

patients were clinically diagnosed with OC annually (Menyhárt et al., 2019). OC typically exhibits an overly aggressive and rapidly growing nature, which causes patients to present with a major tumour load throughout the abdomen. The high proliferative activity in ovarian carcinomas is correlated to poor prognosis (Yoon et al., 2002), causing late-stage diagnosis and multiple failed therapies.

Nanotechnological approaches to combat OC have displayed tremendous performances in curbing the rate of mortalities and enhancing the existing therapeutic efficacies of conventional chemotherapeutics (Hoosen et al., 2018; Pantshwa et al., 2020). This particularly relates to the development of nanoparticles (NPs) which are able to efficiently encapsulate and specifically deliver drugs, dyes, or other desired substances to a variety of target sites (Borlan et al., 2020). In this way, liposomal nanoparticles or nanoliposomes (NLs) have aroused considerable attention in drug delivery research and serve a major asset in fighting against cancerous conditions. Briefly, NLs are lipid-based NPs that are composed of an inner aqueous reservoir surrounded by one or more concentric bilayer phospholipids (Wang et al., 2012). They possess excellent features such as biocompatibility, biodegradability, and considerably low toxicity. Furthermore, NLs exhibit features that allow versatility, due to their diverse ability to encapsulate both hydrophilic and hydrophobic drugs with active targeting functionalization for advanced site-specific delivery of anti-cancer agents (Kopel et al., 2015; Ebrahimifar et al., 2017; Hoosen et al., 2018).

MUC 16 (previously known as CA125) is a transmembrane protein that is over-expressed on OC cells (Liu et al., 2017). MUC 16 has been extensively used as a molecular target for OC detection (Chauhan et al., 2006) as its expression has been correlated with the disease progression (Felder et al., 2014). Studies have demonstrated the protein's role, structure, and function in fundamental processes, including protection of the epithelium and their contributions to human carcinogenesis. The expression of mucins in healthy polarized cells is intricately balanced, with the expression restricted on the apical membranes of exposed epithelia. Following the loss of cell polarity during ovarian carcinogenesis, mucins are widely expressed on the cell surface, promoting interactions with growth factor receptors that are usually restricted to the basolateral surface, and modulate downstream signalling in various

cancers (Joshi et al., 2014; Chaturvedi et al., 2008; Kufe et al., 2009). The aberrant over-expression of MUC 16 has been observed in several human malignancies, including OC. Previous studies have demonstrated that MUC 16 promotes cancer cell proliferation and metastasis and could potentially contribute to chemoresistance. MUC 16 is further responsible for shielding ovarian and breast cancer cells from the destructive cytolysis by human natural killer (NK) cells (Felder et al., 2019). In addition, MUC 16 modulates cell growth, motility, and invasiveness of OC cells (Coelho et al., 2018). Due to their over-expression and functional involvement, MUC 16 and MUC 16 ligands have gained the spotlight as potential targets for therapeutic intervention using monoclonal antibodies and immunotherapy (Aithal et al., 2018).

To This end, the Anti-MUC 16 antibody was selected for its dual role in synergistically reducing OC metastasis and actively transporting the CS-E PEC agent; DDAB to the OC sites specifically (Pantshwa et al., 2018) (Figure 6.1.).

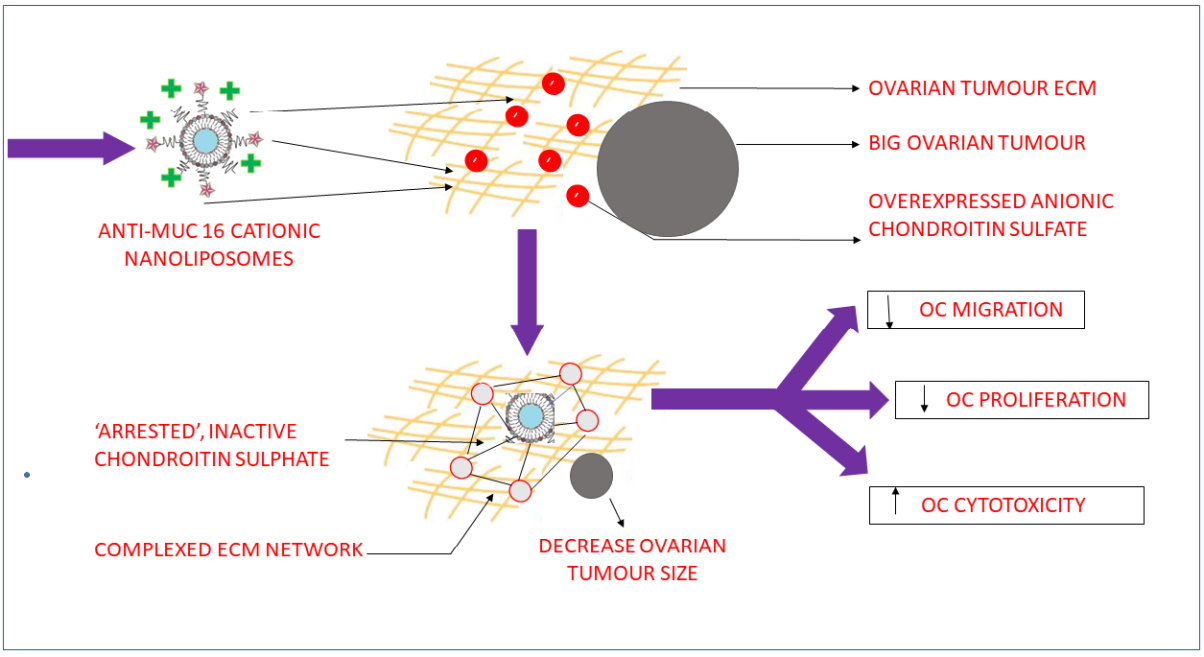

Figure 6.1. Illustration of the Anti-MUC 16 DDAB NLs, which directly targets the OC cells. *In situ*, knockdown of the CS-E GAGs occurs as a consequence of PEC, resulting in a reduction of the ovarian tumour size (Pradeep et al., 2016).

In this study NLs served as the delivery platform to engineer DDAB (as the complexing agent) and the anti-MUC 16 antibody (as an active surface targeting moiety) on the

periphery of the NLs for advanced site-specific conveyance. The functionalized DDAB-active NLs were morphologically and architecturally characterized, following size and zeta potential definition. In-depth *in vitro* cell studies were undertaken on the hallmark pathogenic traits of CS-E to OC (proliferation and migration; Vallen et al., 2014) in both CS-E over-expressed OC (SKOV3; Vallen et al., 2014; ten Dam et al., 2007) and healthy cell lines (HEK 293). Experimental findings angle the application of the novel system towards its utility in advanced stage OC therapy.

6.3. Materials and Methods

6.3.1. Materials

Didodecyldimethylammonium bromide (DDAB) (≥98%; Mw= 462.63), Chondroitin Sulphate sodium salt from shark cartilage (CS), Fluorescein Isothiocyanate isomer 1 (FITC) (≥97.5%; Mw= 389.38), *N*,*N*′-Dicyclohexylcarbodiimide (DCC)(99%, 206.33 g/mol) and *N*-Hydroxysuccinimide (NHS)(98%, 115.09 g/mol) were all purchased from Sigma Aldrich (St. Louis, Missouri, United States). Lipids including cholesterol (CHOL) (≥99%; Mw= 386.65), 1,2-Distearoyl-sn-glycero-3-phosphocholine (DSPC)(≥99%; Mw= 790.15) and L-α-Phosphatidylethanolamine distearoyl methoxypolyethylene glycol conjugate (L-α PEDM) was purchased from Sigma Aldrich (St. Louis, Missouri, United States). Methylene blue (MB) was purchased from BDH chemicals (Ltd, England) and bromothymol blue which was purchased from Protea Laboratory services (PTY, South Africa). All MUSE^{TM} assay reagents were purchased from Merck (Kenilworth, New Jersey, United States). CIM plates were purchased from Anatech (PTY, South Africa). Cancer cell lines including SKOV3 were purchased from Fox Chase Cancer Centre, (Philadelphia, USA) and served as a positive control over-expressing CS-E, whilst the HEK 293 was generously donated by Dr Clement Penny and served as the healthy control. All cells were cultured in RPMI, supplemented with 10 % fetal bovine serum and penicillin/streptomycin, which were purchased from Sigma Aldrich (St. Louis, Missouri, United States).

6.3.2. Formulation of DDAB Cationic Nanoliposomes

Surface present DDAB-active NLs were prepared using an adapted method of Safari and Hosseinkhani (Safari et al., 2013). The lipids (with or without FITC) were mixed in varying amounts and dissolved in chloroform. The chloroform was subsequently evaporated utilizing a rotary evaporator which was set to 65 °C at 40 rpm for 2 h period, leading to a thin lipid film formation. The lipid films were allowed to air dry for an additional 24 h at room temperature which ensured complete exclusion of the residual chloroform. A total of 10 mL of double distilled water (DDW) at 70 °C (±5 °C) was added to the dried lipid films and mixed vigorously for 30.0 min at 70 °C to obtain a dispersion. Primary homogenization was performed by bath sonication for 20.0 min at 65 °C, following probe sonication (Sonics & Materials, Inc., CT, USA; pulse on for 5.0 s and pulse off for 10.0 s) for 3 min. NLs were then subjected to a freeze-thawing process before filtration through a 0.22 µm syringe filter and stored at 4 °C.

6.3.3. Surface-Engineering of Anti-MUC 16 Antibody onto the Nanoliposomes

The Anti-MUC 16 antibody was surface engineered to the NLs as previously described by our research group (Mufamadi et al., 2013). Briefly, NLs were allowed to react with 46 mg of N-Hydroxysuccinimide (NHS) and 87 mg of Dicyclohexylcarbodiimide (DCC) in the presence of methanol and PBS at pH 7.2. After maintenance at room temperature for 1 h, 5 µL (0.124 mg/mL) of synthetic peptide was added to the treated NLs suspension and allowed to react overnight at room temperature. Thereafter, the NLs suspension was dialyzed against PBS (pH 7.4) using SnakeSkin™ Pleated dialysis tubing of (3.500 MWCO; Sigma-Aldrich, St. Louise, MO, USA) for 24 hours to remove excess reagents. The anti-MUC 16 functionalized NLs were further stabilized by a second freeze-thawing process following filtration through a 0.22 µm syringe filter and storage at 4 °C (Mufamadi et al., 2013).

6.3.4. Optimization of the DDAB Cationic Nanoliposomes

A series of 18 nanoliposomal formulations were developed in order to select the ideal lipid ratio composition (DSPC: CHOL) that yielded the optimal surface presence of

DDAB. Zeta potential measurements are directly affected by the chemical composition and lipid ratios within NLs and was thus a critical determinant for the optimal nanoliposomal formulation (Safari et al., 2013). Zeta Size, polydispersity index (PDI) and conductivity were additional output measurements that were analysed. The 18 nanoliposomal lipid compositions are detailed in Table 6.1 below.

Table 6.1. Typical formulation design template for producing the nanoliposomes with the optimal size, zeta potential, PDI and surface antibody peptide attachment.

ID	DSPC (mg)	CHOL (mg)	DDAB (mg)	L-α PEDM (mg)	Antibody
1.	20	20	3	2	NO
2.	20	15	3	2	NO
3.	20	10	3	2	NO
4.	20	5	3	2	NO
5.	20	0	3	2	NO
6.	15	20	3	2	NO
7.	10	20	3	2	NO
8.	5	20	3	2	NO
9.	0	20	3	2	NO
10	20	20	3	2	YES
11	20	15	3	2	YES
12	20	10	3	2	YES
13	20	5	3	2	YES
14	20	0	3	2	YES
15	15	20	3	2	YES
16	10	20	3	2	YES
17	5	20	3	2	YES
18	0	20	3	2	YES

6.3.5. Physicochemical Characterization of the Anti-MUC 16-Functionalized Nanoliposomes

Physicochemical characterizations of the NLs were undertaken, which were either analysed as suspended particles in DDW or as a lyophilized powder. Lyophilized powders of NLs were generated in the presence of a niche cryoprotectant (0.5 % w/v sucrose) to prevent destruction or leakage of NLs upon mechanical stress during freezing and dehydration. Briefly, 2.5 mL of cryoprotectant in DDW was mixed with 2.5 mL of PBS buffered at pH 7.4. and added to the NLs sample solutions, following both freeze-thaw and freeze-drying processes (Mufamadi et al., 2013).

6.3.6. Determination of Size and Zeta Potential of the Nanoliposomes

Determination of the average particle size, PDI and zeta potential of the NLs were analysed using a Zetasizer NanoZS instrument (Malvern Instruments (PTY) LTD., Worcestershire, UK) at 25 °C. A total of 100 µL of each sample was dispersed in 2 mL of DDW before addition in a plastic cuvette. Each test was performed in triplicate and the average value in each case was reported accordingly.

6.3.7. Assessment of Anti-MUC 16 Antibody Functionalization onto the Surface of the Nanoliposomes

In order to confirm the successful conjugation of the anti-MUC 16 antibody to the surface of the NLs, FT-IR was utilized. Samples of lyophilized unfunctionalized-NLs and anti-MUC 16 antibody NLs were compared to view a contrast in the molecular and structural interference created by the antibody on the NLs surface. Analysis was undertaken at high resolution with wavenumbers ranging from 650-4000 cm^{-1} on a FT-IR Spectrophotometer using PerkinElmer® Spectrum Quant Software (Perkin Elmer Inc. MA, USA).

6.3.8. Evaluation of the Surface Morphology and Architecture of the Nanoliposomes

Transmission Electron Microscopy examination (TEM) (FEI Tecnai T12 TEM. FEI, Oregon- USA) was used to generate photographic images of the NLs. Each NLs formulation was sparsely dispersed using bath sonication for 5 min. Using a 2 mL syringe, one drop of the diluted sample was placed on a carbon-coated copper grid and air-dried to obtain a NLs film. The films on the copper grid were then examined.

6.3.9. Determination of the DDAB Content that was Fixated on the Surface of Nanoliposomes

An innovative method employing a bromothymol blue complexation assay was performed as described by Gossman and co-workers (Gossman et al., 2015). The assay was performed by mixing 160 µL of the NLs dispersion with 25 µL NaOH (1 N). The mixture was then incubated for 15 min at 60 °C under agitation, following the addition of 25 µL HCl, 140 µL bromothymol blue 0.06 (% w/v)/ethanol and sufficient PBS (pH 7.5) to a volume of 2.0 mL. The samples were vigorously shaken for 1 hour at room temperature and centrifuged at 5000 rpm for 30 min to separate the supernatant containing excess bromothymol blue from the precipitated green DDAB-bromothymol blue complex stuck to the bottom of the centrifuge tube. The supernatant was diluted with distilled water at a ratio of 1:1 and measured photometrically at 610 nm using a Carry 50 Conc UV- Vis spectrophotometer (Varian (PTY) LTD, Australia). All samples were performed in triplicate. For linear assay calibration, 160 µL DDAB working solutions (0 to 300 µg/mL of DDAB) instead of the NLs dispersions were used.

6.3.10. Cytotoxic Performance of Nanoliposomes on SKOV3 Carcinoma and HEK293 Cell Lines (All three Assays were Performed on the MUSE™ Cell Analyser)

Samples were analysed by MUSE™ Cell Analyzer flow cytometry (EMD Millipore, Billerica, MA, USA) and by MUSE 1.4 Analysis software (EMD Millipore). Prior to analysis, the MUSE™ cell analyser underwent a complete clean**,** in addition, after

every replicate for each working sample, the quick clean function was used to ensure no contamination between samples occurred. The System Check procedure was undertaken prior to each experiment to verify the performance of the MUSE™ System by assessing counting accuracy and fluorescence detection.

6.3.10.1. Cell Viability Assay and IC_{50} Determination

Cell viability assays were performed in order to determine the cytotoxic potential of the anti-MUC 16 cationic NLs on SKOV3 OC cells. According to the American Type Culture Collection (ATCC), the SKOV3 cancer cells are resistant to tumour necrosis factor and to several cytotoxic drugs including diphtheria toxin, cis-platinum, and Adriamycin, in addition to over-expressing CS-E (Vallen et al., 2014), and was thus a robust model for anti-cancer screening.

The kit provides consistent staining and quantification of cell viability when the cell concentrations lie between the ranges of 1×10^5 to 1×10^7 cells/mL. T-25 culture flasks were seeded with approximately viable 6×10^4 cells and were allowed to reach 70-80% confluency. At confluency, cells were serum starved overnight and subsequently treated with various concentrations (100, 50, 25, 12,5 and 6,25 µg/ mL) of a) DDAB cationic NLs b) anti-MUC 16 Cationic NLs and c) media only and were consequently incubated for 48 hours before analysis on the MUSE™ utilizing the Count & Viability Kit (Millipore, USA cat.no MCH 100102) as per manufacturer's protocol. The final concentration of cells obtained after treatment was approximately 3×10^6 on average. A total of 20 µL of cell suspension at various DDAB concentrations were mixed with 380 µL of cell count and viability reagent ($<5 \times 10^5$ cells/mL cell concentration) and incubated for 5 minutes before analyses. The IC_{50} values were then determined using GraphPadPrism version 8 software for each nanoliposomal formulation and administered in further studies below.

6.3.10.2. Apoptosis Assay

Degree of apoptosis was used to quantify the ability of the nanoliposomal formulations to selectively induce apoptosis in cancerous cell lines in comparison to the healthy

HEK 293 control. 6 well culture plates were seeded with approximately 1 x 10^4 viable cells and were allowed to reach 60-70% confluency. At confluency, cells were serum starved overnight and subsequently treated with various concentrations of a) DDAB cationic NLs b) anti-MUC 16 Cationic NLs and c) media only as a single dose at the IC_{50} 48 hours. Thereafter, the assay was performed by adding 100 µL of Annexin V reagent (Millipore, USA cat.no MCH 100105) to 100 µL of cell suspension and determination of total apoptosis was conducted.

6.3.10.3. Proliferation Assay

Proliferation assays were conducted using MUSE™ Ki67 Proliferation Kit (catalogue No. MCH100114) in order to evaluate the nanoliposomes ability to selectively reduce proliferation of cancerous cell lines in comparison to the healthy control (HEK 293 cells). 12 well plates seeded with approximately 5 x 10^3 viable cells and were allowed to reach 70-80% confluency. At confluency, cells were serum starved overnight and subsequently treated with various concentrations of a) DDAB cationic NLs b) anti-MUC 16 Cationic NLs and c) media only as a single dose at the IC_{50} 48 hours. Thereafter the cells were stained according to the manufacturer's protocol. Briefly, 1.0 x 10^4 cells were fixed, permeabilized and treated with either MUSE Hu IgG1-PE or MUSE ki67-PE antibodies for 30 minutes before determining the percentage of Ki67(+) cells and Ki67(–) cells.

6.3.11. Cellular Migration Assays using xCELLigence System

Migration assays were performed using the xCELLigence RTCA (Real-Time Cell Analyser) DP (Dual Plate) instrument according to manufacturers' instructions (Roche Applied Science, Mannheim, Germany and ACEA Biosciences, San Diego, CA) on the cell invasion and migration plate 16 (CIM-plate 16). The lower well was supplemented with 160 µL of media with or without serum, the upper well was seeded with approximately 30 000 SKOV3 cells and was allowed to evenly settle at the bottom surface for 1 hour before treatment with nanoliposomes at their respective IC_{50} for 48 hours. Cell index values, which were the indices used to measure the relative change

in electrical impedance to represent cell migration, was calculated for each sample by the RTCA Software Package 1.2.

6.3.12. In vitro Uptake of FITC Labelled Anti-MUC 16 NLs

In order to visualize the cellular uptake of FITC labelled anti-MUC 16 NLs into SKOV3 cells, 1 x 10^4 viable were cultured on a glass slide and allowed to grow until 60-80 % confluency. At confluence, cells were serum starved overnight following incubation with either non-FITC labelled NLs (negative control) or FITC labelled NLs at the IC_{50} for 24 h. Lastly, cells were washed for a total of three times with PBS and fixed with 4% paraformaldehyde in PBS for 10 min. The nuclei of the cells were then stained with 0.5 µg/mL of DAPI in PBS for 3-5 min in order to visualize the NLs in relation to the nucleus, following mounting and viewing on the Zeiss LSM 780 confocal microscope at 630x magnification.

Statistical Analysis

All samples were performed in 3 biological replicates and their mean and standard deviations we recorded as computed. An unpaired student T-test, two-tailed was performed for all biological assays, where the performance of the NLs treated cells were compared against the untreated control cells, this was performed to verify the statistical significance of the obtained data. All statistics and calibration curves were analysed using Microsoft Excel. All graphs were plotted using OriginPro 8.5 Software and or GraphPadPrism 8 Software.

6.4. Results and Discussion

6.4.1. Characterization and Determination of Particle Size and Zeta Potential of the Nanoliposomes

The optimal CHOL-DSPC lipid ratio was selected from nine NLs formulations. The selection criteria were based on the physicochemical characterization of the NLs surface. The average particle size and zeta potential output measurements of the

individual formulations were then used to select the optimal formulation composition and are summarized in Table 6.2. From the nine systems in the design, Formulation #1 yielded the ideal size and high positive zeta potential. The equal quantities of CHOL and DSPC added a feature of robustness and stability to the outer lipid membrane, providing strong (and stable) particles that support the surface presence of DDAB. This finding led to the subsequent development of NLs using equal CHOL-DSPC ratio (Table 6.3).

Zeta potential analysis indirectly reflects particle surface net charge (Safari et al., 2013). Thus, it was essential to validate the cationic rich surface of the NLs as an indicator for successful PEC predictions (Safari et al., 2013). The reduction in zeta potential is well in agreement with the reductions in physical stability. A minimum zeta potential of greater than $\pm$60 mV is required for excellent stability, or greater than $\pm$30 mV for a good physical stability (Riddick et al., 1968). The enhanced formulation (Figure 6.2, Table 6.3) exhibited an average size of $\sim$125 nm (N=3), with a positive zeta potential of +39.9 mV. This confirmed that the DDAB cationic lipids were fixated onto the surface regions of the NLs with strong cationic repulsion between individual particles which suggested a stable cationic system.

Following functionalization with anti-MUC 16 antibodies, an increase in the size (from 125 nm to 149 nm) and decrease in zeta potential (from +39.9mV to -9.51mV) was observed. This resultant increase in size and decrease in the zeta potential is a key feature implying the successful attachment of the antibody to the cationic NPs (Srinivasan et al., 2014; Eck et al., 2008), preliminary inferring successful anti-MUC 16 antibody-nanoliposomal functionalization.

Table 6.2. Showing the various sizes, zeta potential, PDI and conductance of the various nanoliposomal formulations.

ID	Zeta Size (mV)	SD	PDI	SD	Zeta Potential	SD	Conductance (mS/cm)	SD
1	106.36	0.80	0.24	0.01	38.23	2.44	0.01	0.003
2	132.83	1.67	0.18	0.009	24.63	0.40	0.02	0.001
3	100.31	1.11	0.24	0.01	37.7	0.56	0.02	0.003
4	102.96	0.90	0.22	0.009	32.63	0.47	0.03	0.006
5	94.83	0.22	0.24	0.008	40.46	0.60	0.03	0.003
6	111.73	0.90	0.24	0.01	37.13	0.45	0.05	0.20
7	110.1	1.85	0.23	0.009	30.97	1.04	0.03	0.006
8	134.83	1.40	0.21	0.01	36.4	0.17	0.02	0.003
9	129.33	1.79	0.24	0.006	25.63	0.76	0.01	0.001
10	132.8	0.9	0.11	0.005	-24.4	0.95	0.05	0.003
11	156.03	2.94	0.13	0.03	-21	0.26	0.08	0.006
12	134.36	1.20	0.08	0	-15.16	0.38	0.04	0.001
13	153.13	0.55	0.11	0.02	-20.4	0.4	0.04	0.004
14	102.8	1.45	0.11	0.01	-12.9	1.01	0.04	0.006
15	196.9	3.15	0.26	0.06	-34.2	1.08	0.15	0.019
16	225.07	1.53	0.17	0.03	-36.93	0.68	0.03	0.001
17	239.3	12.13	0.30	0.05	-31.5	0.72	0.02	0.009
18	181.23	10.21	0.30	0.07	-26.73	0.15	0.01	0.007

DDAB loaded NLs Anti-MUC 16 DDAB loaded NLs

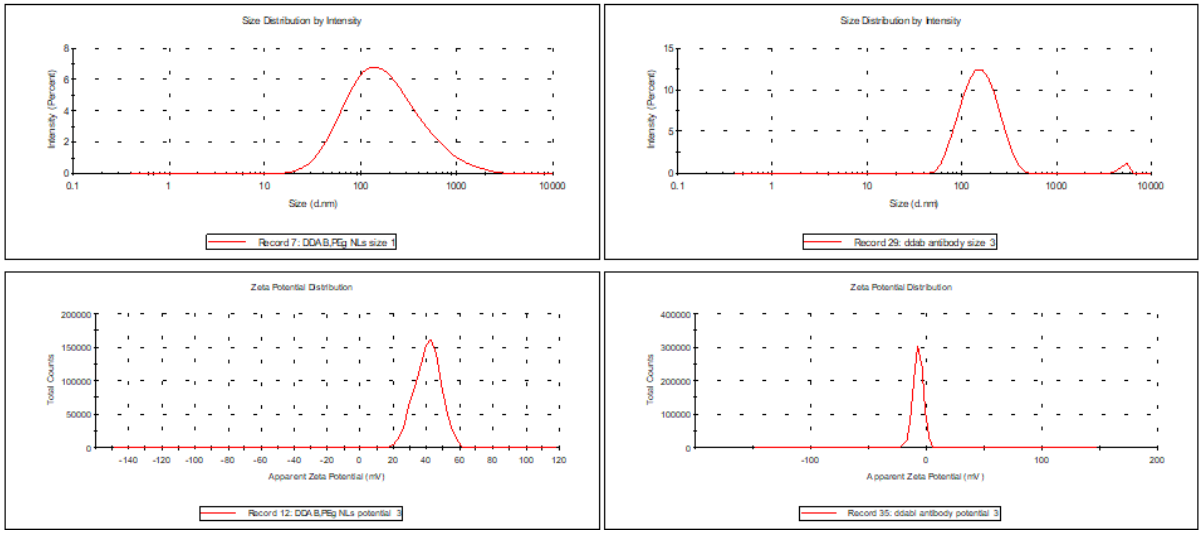

Figure 6.2. Depicting the size and zeta potentials of the various optimized nanoliposomal formulation.

Table 6.3. Showing the composition, average particle size and zeta potential of the optimized nanoliposomal formulation.

DDAB loaded NLs				
Composition of lipids (mg)		**Average size (nm)**	**PDI**	**Zeta potential (mV)**
DSPC, (21 mg)	CHOL, (21 mg)	125.03± 0,95	0.409	+39.9 ±1.31
DDAB, (3 mg)	L-α PEDM (2 mg)			
Anti-MUC 16 DDAB NLs				
DSPC, (21 mg)	CHOL, (21 mg)	149.9±2, 81	0.236	- 9.51±0.88
DDAB, (3 mg)	L-α PEDM (2 mg)			

6.4.2. Determination of Anti-MUC 16 Functionalization onto the Nanoliposome Surface

Spectroscopic analysis employing FT-IR was performed to verify the chemical integrity microstructural modifications to the nanoliposomal surface as a consequence of the antibody attachment. Covalent interactions between the -NH_2 groups of the anti-MUC 16 antibody and the -OH groups present on the NL surface yielding amide formation was evaluated (Figure 6.3). The FT-IR spectrum for the non-functionalized NLs showed a broad band between 3200-3600 cm^{-1} indicative of -OH an -NH_2 vibrational regions (Mohtashamian et al., 2018) and an absorption band at 1236 cm^{-1} indicative of free hydroxyl functional groups. The two bands present at 1236 cm^{-1} and 1045 cm^{-1} suggested the presence of free carboxyl groups. For the anti-MUC 16 NLs, a shift in the peak at 1625cm^{-1} and an additional peak at 1574 cm^{-1} was observed indicating amide bond formation during covalent linkage of anti-MUC 16 antibody. Furthermore, the spectra also confirmed an interaction between the -NH_2 groups of anti-MUC 16. This was observed by a decrease in intensity of the peak region 3200-3600 cm-1 and a decrease in peak intensity of the -OH group (1046 cm^{-1}) of L-α PEDM on the nanoliposomes. To this end, DLS and FT-IR served as conclusive data that suggested the successful conjugation of anti-MUC 16 to the surface of the NLs (Mufamadi et al., 2013; Safari et al., 2013).

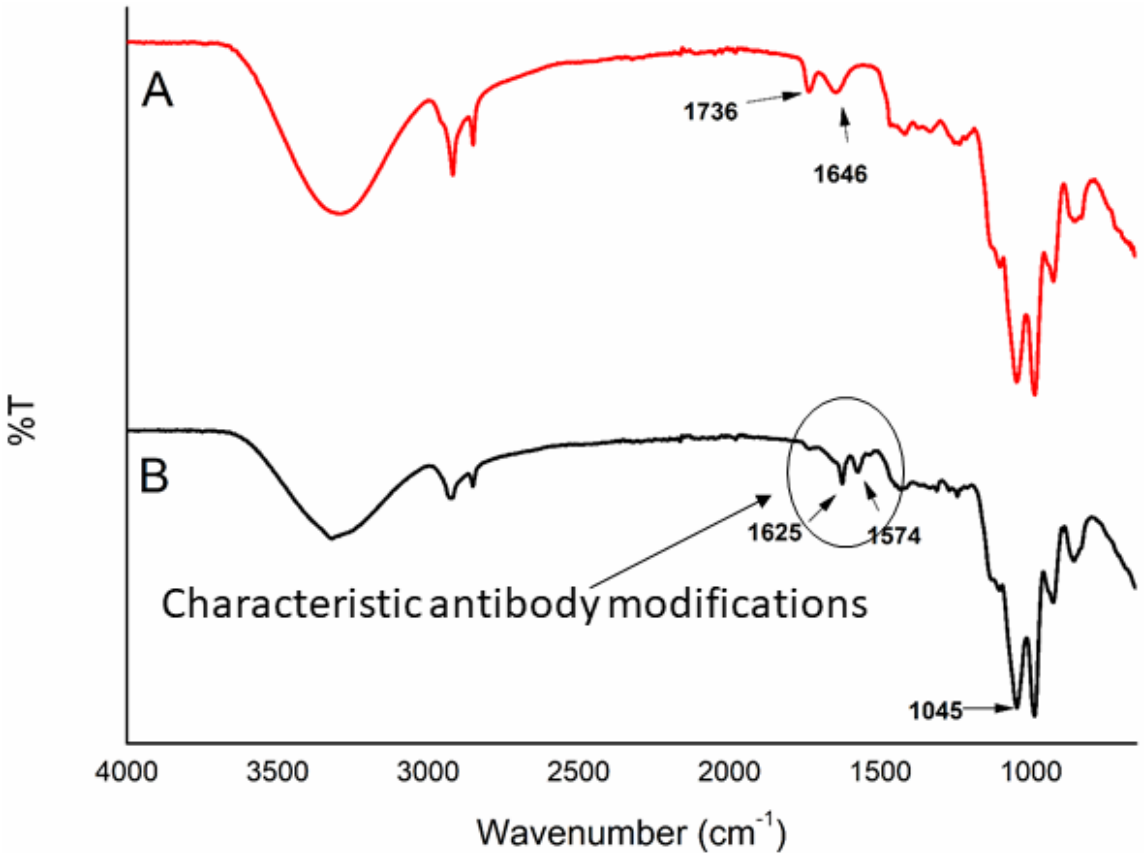

Figure 6.3. FT-IR spectrum of the successful conjugation of the Anti-MUC 16 antibody onto the surface of NLs, where A= unfunctionalized and B=functionalized.

6.4.3. Assessment of the N^+ fixation on the Surface of the Anti-MUC 16 Nanoliposomes by Zeta Potential Analysis.

Size and zeta potential analysis were utilized to confirm that the stable N^+ moieties were fixated onto the functionalized NLs surface and were not lost following antibody attachment. The N^+ from the DDAB surface lipid was protected by the presence of the anti-MUC 16 antibody, giving an overall neutral charge to the system upon formulation. In order to assess the positive nature of the NLs following antibody attachment, NLs were stored up to 21 days and recorded for size and zeta potential measurements (Table 6.4). The shielding effect of the surface antibody to the NLs was observed 21 days after the formulation was synthesized, where a size decrease from 149.9 nm to 139.7 nm occurred (implying some loss of antibody) and a dramatic change in the zeta potential was observed (-9.5 on day 0 to +19.7 on day 21), yielding a highly positively charged surface. Possible explanations for this include the loss of stability of the

antibody at 4 °C (as the antibody remains stable up to 3-15 days at this temperature; Johnson, 2012). Once the antibody starts to denature, the surface of the NLs (containing a rich presence DDAB) are exposed, which explains the highly positive potential observed after 21 days (Figure 6.4).

Table 6.4 further displays the size and potential outputs for the unfunctionalized DDAB NLs, which showed an increase in the hydrodynamic size of 2.67 nm, and a drop in the zeta potential from 39.9 to 34.5. These results are still in the range of good physically stable nanosystems (as described in section 6.4.1).

Table 6.4. Displaying the differences in size, zeta potential and PDI of the various nanoliposomal formulations 21 days after synthesis and storage at 4 °C.

Time (days)	Formulation	Size (nm)	Zeta Potential (mV)	PDI
0	DDAB-loaded NLs	125.03±0.95	+39.9 ±1.31	0.41
0	Anti-MUC16 DDAB NLs	149.9±2.81	- 9.51±0.88	0.24
21	DDAB-loaded NLs	127.7±0.51	+ 34.5±0.85	0.28
21	Anti-MUC16 DDAB NLs	139.67±1.4	+ 20.47±0.67	0.21

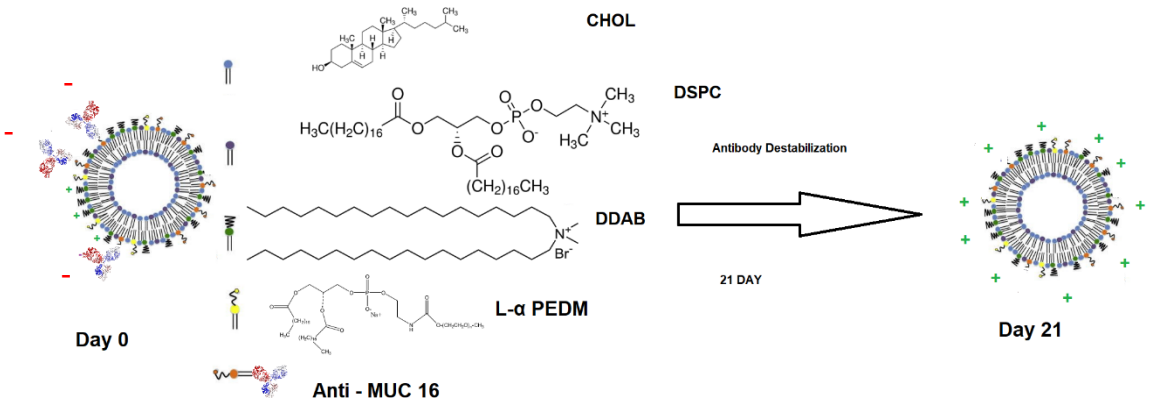

Figure 6.4. Illustration of the cationic shielding contributed by the Anti-MUC 16 localized on the NLs periphery (adapted from Mitchell et al., 2013).

6.4.3. Evaluation of the Surface Morphology and Architecture of the Anti-MUC 16 Nanoliposomes

TEM was used to validate the morphology, architecture, and dimensions of the anti-MUC DDAB NLs seen in Figure 6.5. The structural architecture of the nanostructures are in line with the typical formation of NLs, seen by a clearly demarcated unilamellar lipid membrane, generated from the probe sonication step in the synthesis of the formulation. The size of the NLs, which was extrapolated from the TEM micrographs directly reflect the size dimensions seen above (using the zetasizer instrument), which further supports the presence of well-formed lipid nanoparticles.

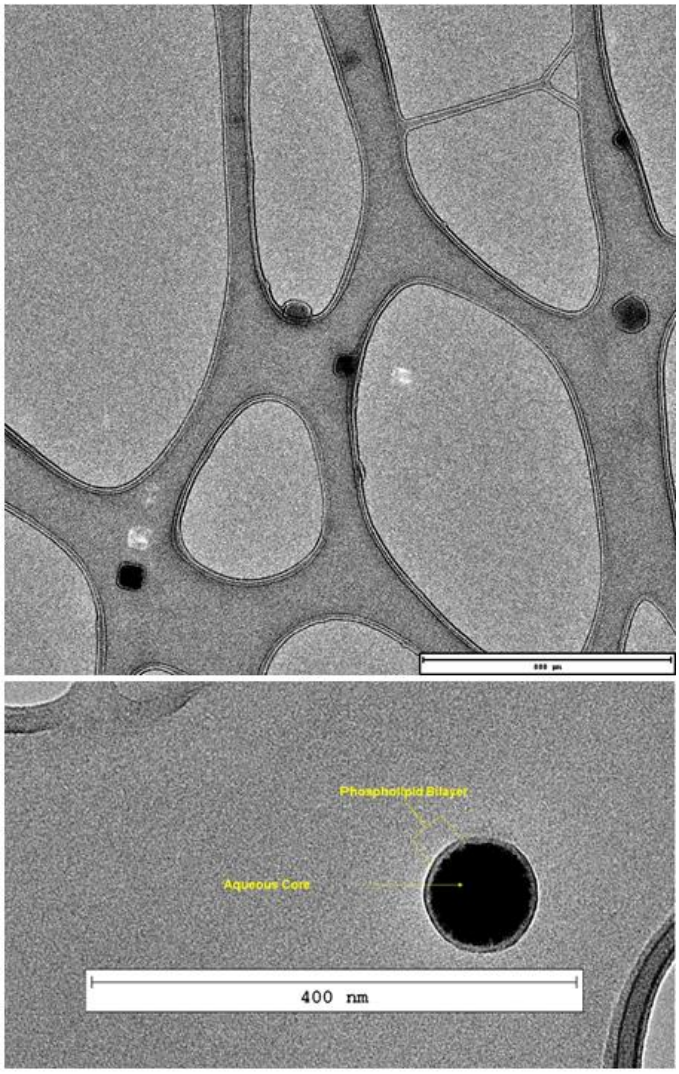

Figure 6.5. Typical TEM micrographs of Anti-MUC 16 functionalized DDAB NLs.

6.3.4. Determination of the Residual DDAB Content on the Surface of Nanoliposomes

DDAB mimics the active pharmaceutical ingredient (API) role typically convoyed with conventional drug delivery systems. Determining the concentration of DDAB fixated on to the surface of the nanoliposomes is paramount to correlate the quantity of NLs required for adequate degree of CS-E PEC, and will also inform dose requirements for cytotoxicity at the tumour microenvironment in OC. A bromothymol blue assay was used as a rapid method to determine the DDAB content on the surface of the NLs. The method was adapted from Lowry and co-workers (Lowry et al., 1979) and Gossmann and co-workers (Gossmann et al., 2015), which involved the formation of a PEC between the cationic DDAB lipids and anionic bromothymol blue probe buffered at pH 7,5. In addition, it proved the presence of cationic DDAB localized onto the surface of the NLs yielding a precipitated green complex. DDAB content was computed from the calibration curve (N=3) (Table 6.5) to be 2.9 mg in 10 mL. This correlates to the total 3 mg in 10 mL initially added during preparation with a loss of 0,1 mg of DDAB (97% DDAB recovery).

Table 6.5. A summary of the calibration curve parameters and DDAB quantifications

Experimental Parameters	Outputs
Correlation coefficient (r^2)	097
Slope	- 0.0026
Y intercept	0.97
Number of samples (n)	3
Residual concentration of DDAB	290 µg/mL ± 0.11

6.4.5 *In vitro* Cell Viability, Apoptosis and Proliferation Assays

6.4.5.1. IC_{50} Determination of the DDAB Nanoliposomes on SKOV3 Cell Lines

The primary aim of this study is to explore the potential of DDAB-NLs to serve as a pharmacological avenue that detours conventional chemotherapy. This section of the chapter thus investigated the chemo-sensitivity of OC SKOV3 cells (over-expressing CS-E) upon short-term (48 h) single treatment dose treatment utilizing the DDAB

nanoliposomal systems. Each biological assay performed within this chapter (proliferation, apoptosis, viability, and migration) relates to key pathogenic contributions of CS-E to OC dissemination. Thus, the decrease or increase in a specific assay validates the anti-cancer success of the system, relative to the untreated control and health HEK 293 cells.

Cell viability assays were performed on SKOV3 OC cells to ensure adequate cell death induced by the system, mediated by chemical complexation of the over-expressed CS-E. The Anti-MUC 16 functionalized DDAB-NLs and non-functionalized DDAB-NLs both displayed considerably low concentrations required to facilitate cancerous cell death in a dose dependent manner. The targeted system, which directly stimulated OC cells by its selective transport mechanism, displayed a lower IC_{50} value compared to the non-functionalized DDAB-loaded NLs (Figure 6.6). Whereas the non-functionalized DDAB-NLs produced a considerably lower IC_{50} when compared to pristine DDAB/DDW seen in chapter 4. The incorporation of DDAB onto the surface of the NLs provided an increased surface area for the fixation of the positively charged N^+ moiety on the periphery of the NLs (Bertrand et al., 2014), potentially allowing for more PEC to occur *in situ*. In addition, the smaller size of the DDAB-NLs compared to the larger pristine DDAB favours a higher cellular uptake in cancerous cell lines (Hu et al., 2007). Furthermore, the incorporation of DDAB into lipid-based NLs are associated with an increase in the hydrophobicity of the system, leading to the elevated production of ROS and subsequent loss of cell viability (Chompoosor et al., 2010). The cytotoxicity of the anti-MUC 16 DDAB NLs was higher than the unfunctionalized system which can be attributed to active MUC 16 receptor targeting and functionalization with anti-MUC 16 antibody (Pantshwa et al., 2017). MUC 16 has been shown to promote cancer cell dissemination, in addition to modulating OC cell growth, motility, and invasiveness of OC cells (Coelho et al., 2018). Thus, the delivery

of the anti-MUC 16 antibody and the cationic effects of DDAB synergically enhanced the cytotoxic performance of the system, potentially leading to the low IC_{50} obtained.

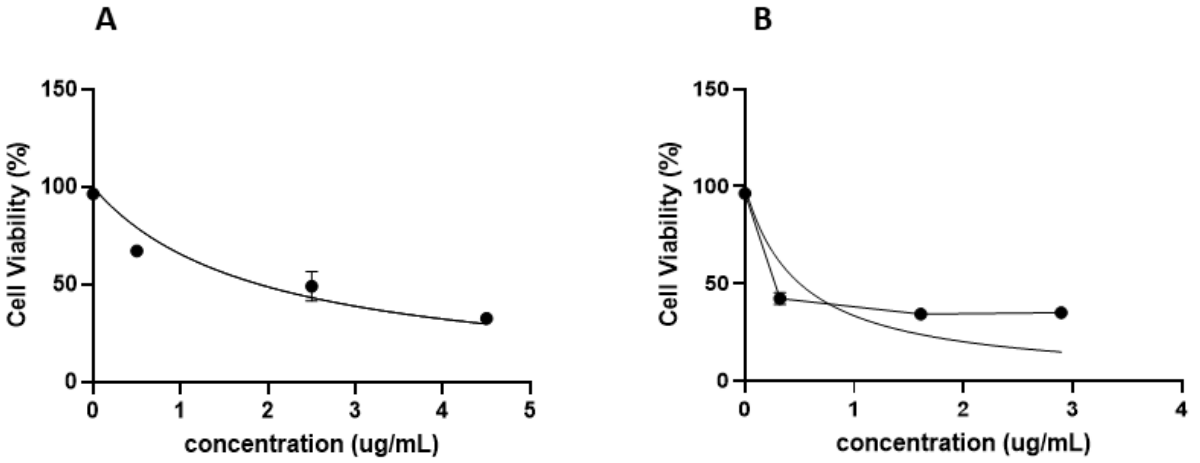

Figure 6.6. Cell viability profiles showing IC_{50} values of **A)** DDAB-loaded NLs (1.905 µg/mL) and **B)** anti- MUC 16 functionalized NLs (0.5031 µg/mL). A student T-test (unpaired) for the cell viability for the anti-MUC 16 DDAB NLs (at 4.5 µg/mL) and DDAB (at 4.5 µg/mL) NLs against the untreated controls showed a significance of $P= 2.7 \times 10^{-9}$ and $P= 7.8 \times 10^{-8}$ respectively.

6.4.5.2. Evaluation of the Apoptotic Potential of the DDAB Nanoliposomes on SKOV3 and HEK 293 Cell Lines

Programmed cell death is an important regulatory pathway of cell growth and proliferation. Cells respond to specific induction signals by initiating intracellular processes that result in characteristic physiological changes including externalization of phosphatidylserine (PS) to the cell surface, cleavage and degradation of specific cellular proteins, compaction and fragmentation of nuclear chromatin, and loss of membrane integrity (Halicka et al., 2019). A majority of anti-tumour therapies primarily act by inducing apoptosis in cancer cells through various mechanistic means mentioned above (Herr et al., 2001; Johnstone et al., 2002). Furthermore, down-regulating the expression of chondroitin sulphate proteoglycan 4 (CSPG4) by intratumoral injection of a lentivirally encoded shRNA induced considerable apoptosis in SKOV3 cells (Vallen et al., 2014). To this end, at this elementary exposure of these

nanoliposomal systems with cancer cells, it was paramount to screen for their selective apoptotic potentials.

For the non-functionalized DDAB NLs, a higher percentage of live cells were observed in HEK 293 (83.46%±1.88) compared to SKOV3 (74.63%±2.57) (Figure 6.7). In addition, a lower percentage of apoptotic cells in HEK cell lines was achieved (HEK 293=15.21%±1.90 and SKOV3=17.23%±0.65).

Comparison of the anti-MUC 16 functionalized DDAB NLs on HEK 293 and cancerous cells revealed a significant difference in the total percentage of apoptotic cells (P=0.003), where the HEK cells were minimally affected (3.83%±1.28) in contrast to the 12.2%±1.80 of apoptotic cells produced in the SKOV3 cell line at the same dose and incubation time.

These results confirmed the targeted induction of apoptosis in cancer cells for the anti-MUC 16 DDAB NLs.

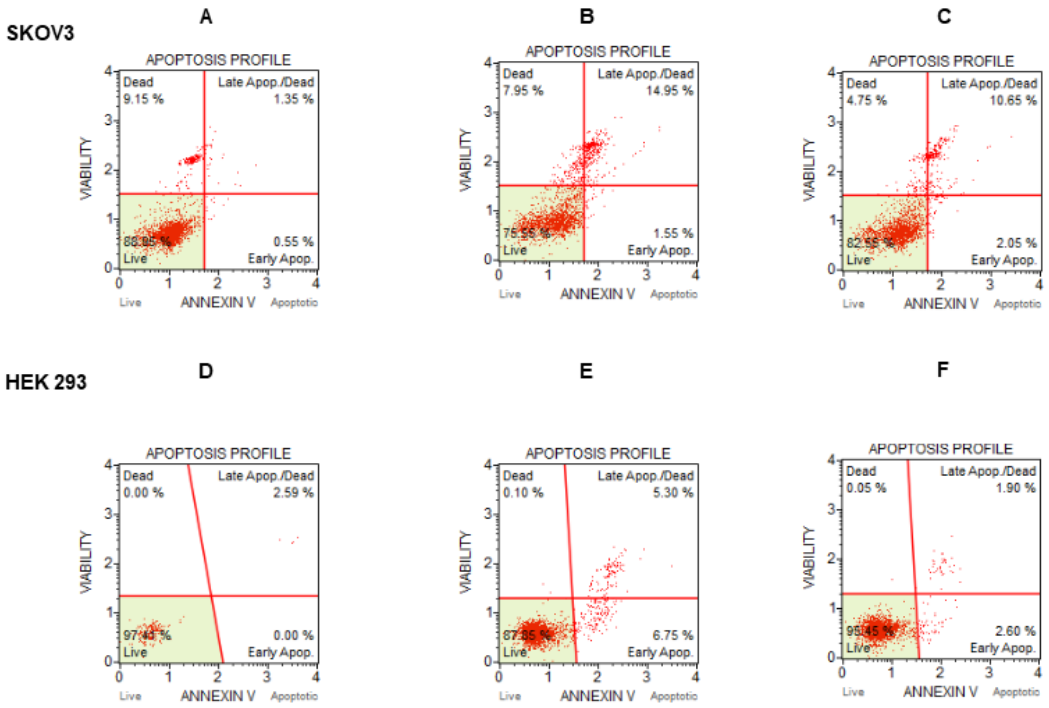

Figure 6.7. Graphical representation of apoptosis profiles, where A and D are untreated, B and E are treated with DDAB-loaded NLs and C and F are treated with

anti-MUC 16-DDAB-loaded NLs. A student T-test (unpaired) for the total apoptotic percentages of the anti-MUC 16 DDAB NLs and DDAB NLs against the untreated controls showed no significance for the HEK 293 cell line (P=0.23 and P=0.017 cells respectively), whilst for the SKOV3 cells, the anti-MUC 16 NLs displayed a significance of P=0.0007 and the unfunctionalized DDAB NLs displayed a significance of P=5.794 $X10^{-6}$.

6.4.5.3. Evaluation of the Anti-Proliferative Potential of the DDAB Nanoliposomes on SKOV3 and HEK 293 Cell Lines

The over-expression of CS-E proteoglycans such as versican and enzymes including metalloproteinases (MPs) elevate the proliferation, migration and metastatic states of SKOV3 cell lines (Ghosh et al., 2010), which are directly activated by over-expressed CS-E in the tumour microenvironment (ten Dam et al., 2007). Studies have previously shown that the knockdown of CS-E by chondroitinase ABC treatment adversely affects the proliferation and migration of OC cells (Vallen et al., 2014). To this end, a proliferation assay was performed to assess if the disturbance of CS-E chains by means of PEC to DDAB could potentially reduce the ability of OC cells to proliferate.

Figure 6.8. displays the resultant percentages of proliferating cells in SKOV3 and HEK 293 cell lines following nanoliposomal exposure (at the IC_{50} values obtained on SKOV3 cells). In the healthy cell lines, no significant reductions in the percentage of proliferating cells were noted when treated with non-functionalized DDAB-NLs (96.01%±1.72) and functionalized DDAB-loaded NLs (98.96%±1.18) relative to the untreated control (99.5%). However, in the SKOV3 cell line, a considerable reduction in the percentage of proliferating cells was achieved in the non-functionalized DDAB-NLs (45.62%±1.36) and anti-MUC 16 functionalized DDAB-NLs (77.21%±0.95) relative to the untreated control (84.28%±2.17). This was indicative of CS-E complexation leading to a decrease in proliferation. These results are in line with the elimination of CS-E by the chondroitinase ABC treatment, which showed a reduction in the percentage of proliferating cells in Lewis lung carcinomas (Denholm et al., 2001; Faassen et al., 1993).

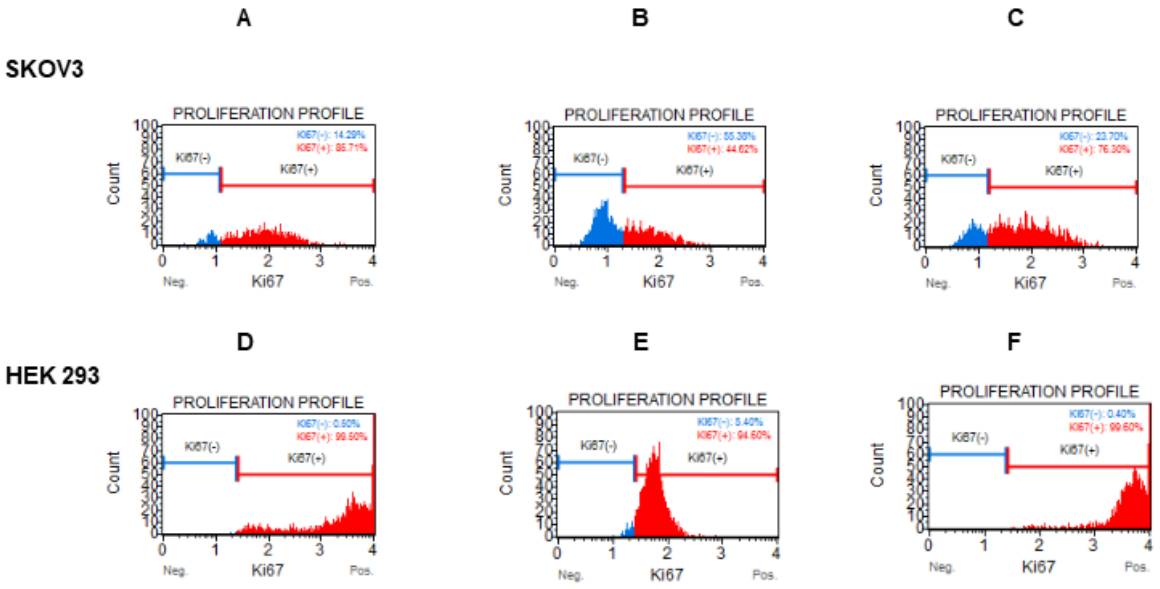

Figure 6.8. Graphical representation of proliferation profiles, where A and D are untreated, B and E are treated with DDAB-loaded NLs and C and F are treated with anti-MUC 16 DDAB-loaded NLs. A student T-test (unpaired) for the percentages of proliferating cells for the anti-MUC 16 DDAB NLs and DDAB NLs against the untreated controls in the HEK 293 cell lines showed no significance (P=0.50 and P=0.02 respectively), whilst for the SKOV3 cells, the systems displayed a significance of P=0.006 for the anti-MUC 16 NLs and P=1.28 x 10^{-5} for the DDAB NLs.

6.4.6. Evaluation of Cell Migration Assays using xCELLigence System

MPs are a group of enzymes that respond virulently (and promptly) to the signals received by the over-expressed CS-E within the stromal regions of the OC sites, which lead to enhanced OC cell migration (Vallen et al., 2014). The hypothesis which navigates the angle of this project, strongly encouraged that the blockage of CS-E will result in a disturbance of these pro-cancerous interactions leading to tumour dissemination hindrances (Pradeep et al., 2016). Thus, the assessment of the system to reduce OC migration, to infer GAG disturbance was conducted. Figure 6.9. displays the migratory patterns for the SKOV3 cell lines, treated with functionalized and unfunctionalized NLs (at the IC_{50}). These migratory patterns are represented by the cell index values obtained at 35 hours treatment exposure. The patterns show an inhibitory effect on migration of the OC cells. The functionalized NLs (cell index = 0.62

± 3.0) displayed a higher anti-migratory capability over the unfunctionalized system (cell index = 1.28 ± 0.12) relative to the untreated control (2.87 ± 0.75). Possible explanations for this are associated with the targeted stimulation of OC cells and the synergistic effects of the anti-MUC 16 antibody.

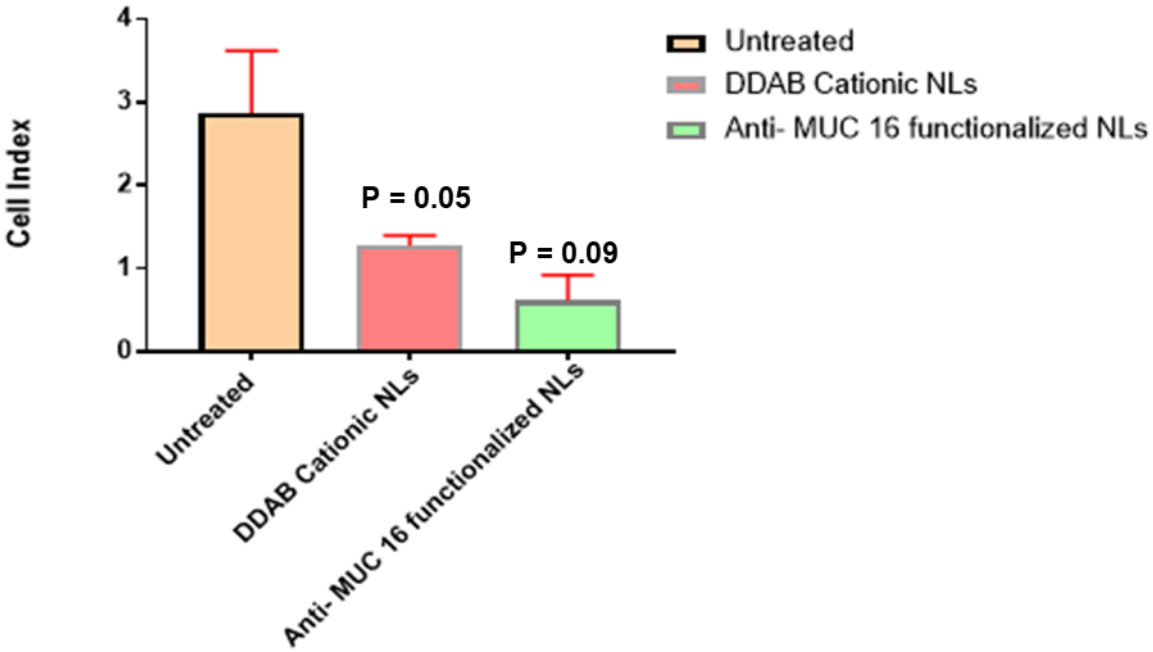

Figure 6.9. Graphical representation of the migration patterns for the various NLs formulations on SKOV3 cell lines. A student T-test (unpaired) for the cell index values representing the migratory patterns of the anti-MUC 16 DDAB NLs and DDAB NLs against the untreated controls displayed a significance of P=0.09 and P=0.05, respectively.

6.4.7. Cellular Uptake Studies of FITC Tagged Anti-MUC 16 DDAB NLs on SKOV3 cells

Cellular uptake studies were undertaken to visualize the intracellular entry, localization and distribution of the FITC tagged anti-MUC 16 DDAB NLs into and on the CS-E rich SKOV3 cancer cellular surface (Vallen et al., 2014). NLs were labelled with non-FITC labelled NLs (negative control) (Figure 6.10.A) or FITC labelled NLs (positive control) (Figure 6.10.B). The nucleus of both groups was stained with 4′,6-diamidino-2-phenylindole (DAPI). For the experimental group, NLs appeared in aggregates,

situated in close proximity or on the nucleus (circled), suggesting the successful receptor binding of the anti-MUC 16 antibody, which lead to endocytosis of the NLs, inferring a definite involvement of DDAB to the cell surface. The interaction of DDAB with other cell surface proteoglycans such as CD44 (CS proteoglycan) has potential to block mesothelial attachment of cancerous cells, reducing the spread of OC. In addition, the "*on-the-spot"* ability of DDAB to arrest surface CS-E is also possible, which changes the cellular surface for host recognition and further reduces the available amount of the tumour promoting CS-E (Vallen et al., 2014).

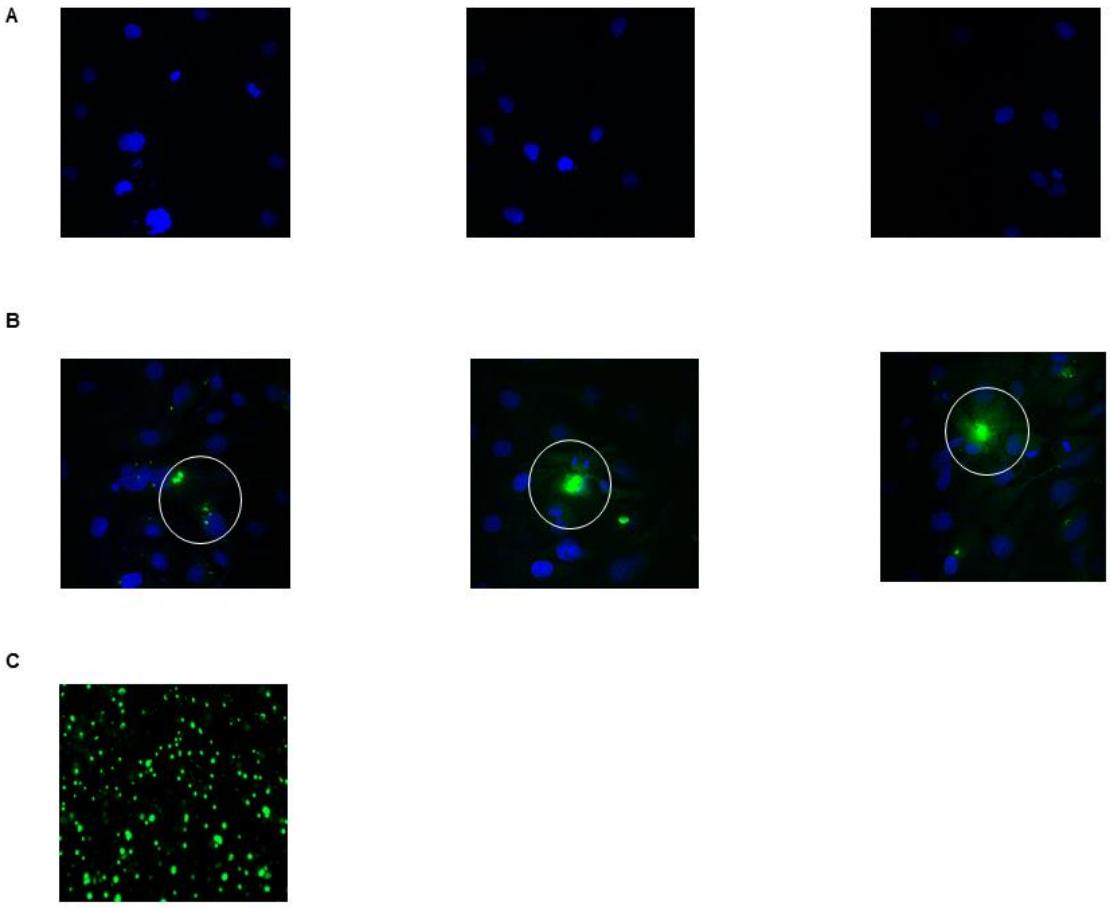

Figure 6.10. Fluorescent imagery showing the SKOV3 cellular uptake of **(A)** non-FITC labelled anti-MUC 16 DDAB-loaded NLs; **(B)** showing the FITC tagged NLs on SKOV3 cells (as circled in the figure) and **(C)** showing the pristine FITC labelled anti-MUC 16 DDAB-NLs without cells.

6.5. Conclusions

In the present study, *in situ* polyelectrolyte complexation was presented as an innovative mechanism of action to arrest the over-expressed CS-E present within the OC tumour microenvironment (as described by the mentioned hypothesis in Chapter 4). Following the establishment of DDAB as a suitable CS complexing agent, the subsequent formulation, characterization and *in vitro* testing of the DDAB NLs was performed. A series of nanoliposomal formulations were prepared in order to assess the optimum lipid ratio. The equal CHOL-DSPC quantities (21 mg) was the ideal ratio to stabilize the anchorage of DDAB on the periphery of the NLs. The optimized NLs displayed a high zeta potential and nanosized diameters. To enhance the site-specific delivery of DDAB, the anti-MUC 16 antibody was surface engineered using covalent attachment chemistry. Size, zeta potential and FT-IR successfully confirmed the interaction between the surface of the NLs and the reactive moiety on the antibody. Although these functionalized NLs displayed an overall neutral charge initially, degradation of the antibody revealed the cationic DDAB remained steadily anchored to the NLs surface. Thus, the antibody aided in the protection of the N^+ charge during the transportation of DDAB to the OC sites. Upon *in vitro* testing, the functionalized system displayed a selective proliferatory, apoptotic and migratory effects in the highly drug resistant (and CS-E over-expressed) SKOV3 cell lines, relative to the healthy HEK 293 control. This further concluded the preliminary utilization of this system as a targeted chemotherapy approach. Further studies are however required to ensure the CS-E targeting of the NLs is achieved, using a more robust and clinically relevant model for anticancer testing.

6.6. References

Aithal, A., Rauth, S., Kshirsagar, P., Shah, A., Lakshmanan, I., Junker, W. M., et al., 2018. MUC16 as a novel target for cancer therapy. Expert Opinion on Therapeutic Targets. 22, 675–686.

Bertrand, N., Wu, J., Xu X., Kamaly, N., Farokhzad, O.C., 2014. Cancer nanotechnology: The impact of passive and active targeting in the era of modern cancer biology. Adv. Drug Deliv. Rev 66, 2-25.

Borlan, R., Tatar, A.-S., Soritau, O., Maniu, D., Marc, G., Florea, A., Astilean, S., 2020. Design of fluorophore-loaded human serum albumin nanoparticles for specific targeting of NIH:OVCAR3 ovarian cancer cells. Nanotechnology. 31, 315102.

Chaturvedi, P., Singh, A.P., Batra, S.K., 2008. Structure, evolution, and biology of the MUC4 mucin. Faseb j. 22, 966-981.

Chompoosor, A., Saha, K., Ghosh, P.S., Macarthy, D.J., Miranda, O.R., Zhu, Z.-J., Arcaro, K.F. and Rotello, V.M., 2010. The Role of Surface Functionality on Acute Cytotoxicity, ROS Generation and DNA Damage by Cationic Gold Nanoparticles. Small. 6, 2246-2249.

Coelho, R., Marcos-Silva, L., Ricardo, S., Ponte, F., Costa, A., Lopes, J. M., & David, L., 2018. Peritoneal dissemination of ovarian cancer: role of MUC16-mesothelin interaction and implications for treatment. Expert Review of Anticancer Therapy. 18, 177-186.

Denholm, E., Lin, Y., Silver, P., 2001. Anti-tumor activities of chondroitinase AC and chondroitinase B: inhibition of angiogenesis, proliferation and invasion. European Journal of Pharmacology. 416, 213-221.

Eck, W., Craig, G., Sigdel, A., Ritter, G., Old, L., Tang, L., et al., 2008. PEGylated Gold Nanoparticles Conjugated to Monoclonal F19 Antibodies as Targeted Labeling Agents for Human Pancreatic Carcinoma Tissue. ACS Nano. 2, 2263-2272.

Felder, M., Kapur, A., Rakhmilevich, A.L., Qu, X., Sondel, P.M., Gillies, S.D., Connor, J., Patankar,M.S., 2019. MUC16 suppresses human and murine innate immune responses. Gynecologic Oncology. 152, 618-628.

Faassen, A.E., Mooradian, D.L., Tranquillo, R., Dickinson, R.B., Letourneau, P.C., Oegema, T.R., et al., 1993. Cell surface CD44-related chondroitin sulfate proteoglycan is required for transforming growth factor-beta-stimulated mouse melanoma cell motility and invasive behavior on type I collagen. J Cell Sci. 105, 501–11.

Ghosh, S., Albitar, L., LeBaron, R., Welch, W., Samimi, G., Birrer, M., et al., 2010. Up-regulation of stromal versican expression in advanced stage serous ovarian cancer. Gynecologic Oncology.119, 114-120.

Gossmann, R., Langer, K., Mulac, D., 2015. New Perspective in the Formulation and Characterization of Didodecyldimethylammonium Bromide (DMAB) Stabilized Poly (Lactic-co-Glycolic Acid) (PLGA) Nanoparticles. PLOS ONE.10, e0127532.

Halicka, H.D., Li, J., Zhao, H. and Darzynkiewicz, Z., 2019. Concurrent detection of lysosome and tissue transglutaminase activation in relation to cell cycle position during apoptosis induced by different anticancer drugs. Cytometry, 95, 683-690.

Hu, Y., Xie, J., Tong, Y, W., Wang, C, H., 2007. Effect of PEG conformation and particle size on the cellular uptake efficiency of nanoparticles with the HepG2 cells. Journal of Controlled Release. 118, 7-17.

Joshi, S., Kumar, S., Choudhury, A., et al., 2014. Altered Mucins (MUC) trafficking in benign and malignant conditions. Oncotarget. 5, 7272-7284.

Liu, J.F., Moore, K.N., Wang, J.S., Patel, M., Birrer, M.J., Hamilton, E., et al., 2017. Abstract CT009: Targeting MUC16 with the THIOMAB^{TM}-drug conjugate DMUC4064A in patients with platinum-resistant ovarian cancer: a Phase I escalation study. Cancer Research. 77(13 Supplement): CT009-CT.

Kufe, D.W., 2009. Mucins in cancer: function, prognosis, and therapy. Nat Rev Cancer. 9, 874-885.

Lowry, J., 1979. Direct Spectrophotometric Assay of Quaternary Ammonium Compounds Using Bromthymol Blue. Journal of Pharmaceutical Sciences. 68, 110-111.

Menyhárt, O., Fekete, J.T., Gyorffy, B., 2019. Gene expression indicates altered immune modulation and signaling pathway activation in ovarian cancer patients resistant to Topotecan. Int. J. Mol. Sci. 20, 2750.

Mitchell, N., Kalber, T. L., Cooper, M. S., Sunassee, K., Chalker, S. L., Shaw, K. P., et al ., 2013. Incorporation of paramagnetic, fluorescent and PET/SPECT contrast agents into liposomes for multimodal imaging. Biomaterials. 34, 1179–1192.

Mohtashamian, S., Boddohi, S., Hosseinkhani, S., 2018. Preparation and optimization of self-assembled chondroitin sulfate-nisin nanogel based on quality by design concept. International Journal of Biological Macromolecules. 107, 2730-2739.

Mufamadi, M., Choonara, Y., Kumar, P., Modi, G., Naidoo, D., van Vuuren, S., et al., 2013. Ligand-functionalized nanoliposomes for targeted delivery of galantamine. International Journal of Pharmaceutics. 448, 267-281.

Pantshwa. J., Choonara. Y.E., Kumar, P. du Toit, L.C., Penny, C., Pillay, V., 2017. Synthesis of novel amphiphilic poly(N-isopropylacrylamide)-b-poly(aspartic acid) nanomicelles for potential targeted chemotherapy in ovarian cancer. Journal of Drug Delivery Science and Technology. 39, 308-323.

Pantshwa, J. M., Rhoda, K., Clift, S. J., Pradeep, P., Choonara, Y. E., Kumar, P., du Toit, L. C., Penny, C., & Pillay, V., 2018. Chemotherapeutic Efficacy of Implantable Antineoplastic-Treatment Protocols in an Optimal Mouse Model for Human Ovarian Carcinoma Cell Targeting. International journal of molecular sciences. 19, 3030.

Pantshwa, J.M., Kondiah P.P.D., Choonara, Y.E., Marimuthu T., Pillay, V., 2020. Nanodrug delivery systems for the treatment of ovarian cancer. Cancers. 12, 213.

Pradeep, P., Choonara, Y., Kumar, P., Pillay, V., 2016. “On-The-Spot” Arresting of Chondroitin Sulphate Proteoglycans: Implications for Ovarian Adenocarcinoma Recognition and Intervention. International Journal of Molecular Sciences. 17, 1136.

Riddick, T., 1968. Control of colloid stability through zeta potential. Wynnewood, Pa: Published for Zeta-Meter, Inc., by Livingston Pub. Co.

Safari, M.G., Hosseinkhani, S., 2013. Lipid composition of cationic nanoliposomes implicate on transfection efficiency. Journal of Liposome Research. 23,174-186.

Smith, T., Guidozzi, F., 2009. Epithelial ovarian cancer in Southern Africa. SA J. Gynaecol. Oncol. 1, 23–27.

Srinivasan, A., Shoyele, S., 2014. Influence of Surface Modification and the pH on the Release Mechanisms and Kinetics of Erlotinib from Antibody-Functionalized Chitosan Nanoparticles. Industrial & Engineering Chemistry Research. 53, 2987-2993.

ten Dam, G. B., van de Westerlo, E. M. A., Purushothaman, A., Stan, R. V, Bulten, J., Sweep, F. C. G. J., Massuger, L. F., Sugahara, K., van Kuppevelt, T. H., 2007. Antibody GD3G7 selected against embryonic glycosaminoglycans defines chondroitin sulfate-E domains highly up-regulated in ovarian cancer and involved in vascular endothelial growth factor binding. Am. J. Pathol. 171, 1324–1333.

Vallen, M., Schmidt, S., Oosterhof, A., Bulten, J., Massuger, L., Kuppevelt, T., 2014. Primary Ovarian Carcinomas and Abdominal Metastasis Contain 4,6-Disulfated Chondroitin Sulfate Rich Regions, Which Provide Adhesive Properties to Tumour Cells. PLoS ONE. 9, e111806.

Vallen, M. J. E., Van Der Steen, S. C. H. A., Van Tilborg, A. A. G., Massuger, L. F. A. G., Van Kuppevelt, T. H., 2014. Sulfated sugars in the extracellular matrix orchestrate ovarian cancer development: “When sweet turns sour.” Gynecol. Oncol. 135, 371–381.

Yoon, H., Liyanarachchi, S., Wright, F.A., Davuluri, R., Lockman, J.C., de la Chapelle, A., et al., 2002. Gene expression profiling of isogenic cells with different TP53 gene dosage reveals numerous genes that are affected by TP53 dosage and identifies CSPG2 as a direct target of p53. Proc Natl Acad Sci U S A. 99, 5632–7.

CHAPTER 7:
Novel Anti-MUC 16 Functionalized 1,12 Diaminododecane Loaded Nanoliposomes for Targeted Ovarian Cancer Therapy

7.1. Synopsis of this Chapter

OC is a lethal gynaecological malignancy, to the extent that despite major initiatives being invested into drug research and development, OC remains steadfast and incurable, to date. Consequently, efforts to circumvent the lethal characteristics requires investigations into an approach which detour conventional pharmacological avenues. Inherent with this research was a mechanistic forecast of a crosslinker based nanoarchetype that adversely compromises chondroitin sulphate-E (CS-E) activity *in situ* by means of chemical crosslinking. Herein, the *first-of-its-kind*, 1,12 diaminododecane loaded nanoliposomes (NLs) was formulated and characterized for their loading, entrapment, and release behaviours. The morphology of the NLs revealed unilammelar lipid vesicle archetypes that were in the nanosized range. The NLs displayed moderate 1,12 diaminododecane entrapment, with zero order release kinetics. The anti-MUC 16 antibody was functionalized to the surface of the NLs, and their cytotoxicity was tested on SKOV3 OC cell lines (cell viability, apoptosis, proliferation and oxidative stress) and compared to healthy HEK 293 cell lines, displaying remarkable selectivity and efficacy.

Key words: Crosslinking; Nanoliposomes; Ovarian cancer; Chondroitin Sulphate.

7.2. Introduction

OC has gained the most fatal gynaecological malignancy status, affecting millions of females worldwide (Pantshwa et al., 2020). According to the global statistics data, OC

is the 7th most common cancer and 8th most common cause of mortality amongst cancer in females globally. The Globocan Study predicts that by 2035 there will be a worldwide escalation in the incidence of OC to 3, 71,000 and an increase in mortality to 254,000 (Bray et al., 2018). OC's high death rates are primarily due to its ability to bypass early detection, consequently leading to low cure rates and failed therapies (Coleman et al., 2013).

This chapter follows on from the preliminary research detailed in Chapter 5, where the tumour extracellular matrix was identified as a promising region for OC therapeutic targeting (Pradeep et al., 2016; Hoosen et al., 2018). In this remote portion of the tumour, houses a promising molecular target: CS-E (ten Dam et al., 2007), to which we aimed to target (by means of crosslinking) and hinder the rapid dissemination of OC (Vallen et al., 2014; Pradeep et al., 2016).

Crosslinking is the process of forming tridimensional networks by linking polymer chains by covalent (chemical bonds; accomplished by irradiation, sulfur vulcanization, or chemical reactions) (Bhattacharya et al., 2009) or noncovalent bonds (physical bonds; accomplished ionic interactions, hydrogen bonding and hydrophobic interactions) (Hennink et al., 2012). Conventional applications for polysaccharide-polysaccharide crosslinking includes the development of film and coatings in the food industry. These crosslinked networks display enhanced water resistance and superior mechanical and barrier properties, reduced water vapor permeability, low water solubility and increased tensile strength which adds a unique feature to the polymer for a diverse field of applications (Azeredo et al., 2016). In this study, we utilized crosslinking as a mechanism to impede OC by physically restricting CS-E mediated OC cell dissemination, in addition to blocking of nutritional supplies from peripheral blood vessels to the tumour (as described in the hypothesis, Pradeep et al., 2016, Chapter 5). To this end, crosslinking of CS-E in the stroma adds an incredibly unique feature to the polymer that can potentially reduce OC metastasis by restoring normal ECM function.

CA125 is a prominent OC antigen commonly employed for serum assay detection in OC diagnostics. CA125 is a repeating peptide epitope of the mucin 16 and is widely

over-expressed on OC cells. Consequently, promoting cancer cell proliferation and inhibiting anti-cancer immune responses (Felder et al., 2014). In the past, anti-MUC 16 antibodies such as Oregovomab (Mab B43.13, a murine monoclonal antibody) displayed great binding affinities to MUC 16 with high affinity, able to induce a dual humoral and cellular immune responses against OC (Ehlen et al., 2005). In addition, anti-MUC 16 Chimeric Antigen Receptor T Cells have demonstrated cytotoxic activity *in vitro* and delayed progression or eradicated disease states in xenograft models (Chekmasova et al., 2010). Thus, the anti-MUC 16 antibodies were selected to synergistically (in conjunction with 1,12 diaminododecane) treat and target OC (Pantshwa et al., 2018). Thus, a dual approach to OC therapy.

In this study, NLs were employed as a crosslinker delivery reservoir for the optimal 1,12 diaminododecane pharmacokinetics and to ensure that off target crosslinking was minimized. The system was functionalized with the anti-MUC 16 antibody to actively transport the crosslinker to OC sites specifically. Lastly, the cytotoxic performance of the crosslinker nano-formulations we assessed on SKOV3 OC cell lines (cell viability, apoptosis, proliferation and oxidative stress) and compared to healthy HEK293 cell lines, showing remarkable selective anti-cancer activity.

7.3. Methods and Materials

7.3.1. Materials

1,12 diaminododecane (98%, 200.36 g/mol), Chondroitin Sulphate sodium salt from shark cartilage *N*,*N*′-Dicyclohexylcarbodiimide (99%, 206.33 g/mol), *N*-Hydroxysuccinimide (98%, 115.09 g/mol), Cholesterol (CHOL) (99%, 386.65 g/mol), 1,2-Distearoyl-sn-glycero-3-phosphocholine (DSPC) (99%, 790.15 g/mol), L-α-Phosphatidylethanolamine distearoyl methoxypolyethylene glycol conjugate (L-α PEDM) and Triton X (laboratory grade) were all purchased from Sigma Alrich (St. Louis, Missouri, United States). Methylene blue was purchased from BDH chemicals (Ltd, England). Cancer cell lines including SKOV3 were purchased from Fox Chase Cancer Centre (Philadelphia, USA) and served as a positive control, over-expressing CS-E. HEK 293 cells derived from human embryonic kidney was generously donated

by Clement Penny and served as a CS negative control and was also deficient in other GAGs for example, hyaluronan. Muse Cell count and viability kit (MCH100102), Muse™ Annexin V & Dead Cell Kit (MCH100105), Muse® Ki67 Proliferation Kit (MCH100114) and Muse™ Oxidative Stress Kit (MCH100111) were purchased from Merck (Kenilworth, New Jersey, United States). The Anti-MUC 16 antibody [EPR1020(2)] ab110640, was purchased from Abcam (Cambridge, United Kingdom). Cells were cultured in RPMI, supplemented with 10 % fetal bovine serum and penicillin/streptomycin, which were purchased from Sigma Aldrich (St. Louis, Missouri, United States).

7.3.2. Synthesis and Characterization of the Anti-MUC 16 1,12 Diaminododecane NLs

7.3.2.1. Formulation of the 1,12 Diaminododecane Loaded Nanoliposomes

a) Unloaded and b) 1,12 diaminododecane loaded NLs were prepared using an adapted method of Safari et al., 2013. The lipids were dissolved in varying amounts (Table 7.1) using chloroform following homogenization with a probe sonicator for 30 s-1 min (Sonics & Materials, Inc., CT, USA). The chloroform was removed via rotary evaporation (Rotavapor® RII, Büchi Labortechnik AG, Switzerland) at 65 °C and 40 rpm for 2 hours, producing a thin lipid film. The residual solvents were removed by air drying at ambient temperatures overnight. A total of 10 mL of double distilled water (DDW) or 0.07 %(w/v) solution of 1,12 diaminododecane in water at 70 °C was added to the dried lipid films and mixed vigorously for 30.0 min at 65 °C to obtain a dispersion. Primary homogenization was performed by bath sonicator for 20.0 min at 65 °C and was then sonicated by probe sonication (pulse on for 5.0 s and pulse off for 10.0 s, for 3 min). The dispersion was centrifuged to remove the un-entrapped 1,12 diaminododecane in the pellet. Lastly the NLs solution was freeze-thawed at 37 °C and filtered through a 0.22 µm pore size membrane filter and stored at 4 °C until further use.

Table 7.1. Varying amounts of lipids and hydration mediums used for the nanoliposomal formulation.

.

Composition	Unloaded (mg)	1,12 diaminododecane NLs (mg)
DSPC	21	21
CHOL	21	21
L-α PEDM	0	2
Hydration with DDW	YES	NO
Hydration with 1,12diaminododecane	NO	YES

7.3.3.2. Determination of Size, Zeta Potential and Polydispersity Index of the 1,12 Diaminododecane Loaded NLs

Determination of the average particle size, polydispersity index (PDI) and zeta potential of the 1,12 diaminododecane NLs were analysed using a Zetasizer NanoZS instrument (Malvern Instruments (Pty) Ltd., Worcestershire, UK) at 25 °C. A total of 100 µL of each sample was dispersed in 2 mL of DDW and gently mixed, before addition in a plastic cuvette. Each test was performed in triplicate and the average value in each case was reported accordingly.

7.3.3.3. Surface-Engineering of Anti-MUC 16 Antibody onto the Nanoliposomes

Conjugation of the anti-MUC 16 antibodies was performed as described previously in our group (Mufamadi et al., 2013). Briefly, native NLs were allowed to react with 46 mg of and 87 mg of DCC in 100 µL of methanol and 4 mL of PBS buffer at pH 7.2. After maintenance at room temperature for 45 min, 5 µL (0.124 mg/mL) of synthetic peptide was added to the treated NLs suspension and allowed to react overnight at

room temperature, following solvent removal via rotary evaporation. Thereafter, The anti-MUC 16 functionalized NLs were further stabilized by a freeze-thawing processes and filtered through a 0.22 µm filter to remove any excess undissolved NHS and DCC, and then stored at 4 ˚C for further use (Mufamadi et al., 2013).

7.3.3.4. Chemical Integrity Assessment of the Surface Architecture of the Nanoliposomal Formulations Following Anti-MUC 16 Antibody Conjugation

FT-IR spectrophotometry was utilized to evaluate the microstructural modifications of the NLs as a result of anti-MUC 16 antibody attachment. This study provided a physicochemical insight into the successful surface engineering of the NLs. Samples of lyophilized 1,12 diaminododecane NLs and anti-MUC 16 functionalized 1,12 diaminododecane NLs were analysed to determine the molecular interactions between the antibody and the surface of the NLs. Analysis was undertaken at high resolution with wavenumbers ranging from 650-4000 cm^{-1} on a FTIR Spectrophotometer using PerkinElmer® spectrum quant software (Perkin Elmer Inc. MA, USA).

7.3.3.5. Microscopic Evaluation of the Surface Morphology and Architecture of the Nanoliposomes

Transmission Electron Microscopy examination (TEM) (FEI Tecnai T12 TEM. FEI, Oregon, USA) was used to generate photographic images of the NLs. Each NLs formulation was homogenised using bath sonication for 5 minutes. A total one drop of the diluted sample was placed on a carbon-coated copper grid and air-dried. The films on the copper grid were examined.

7.3.3.6. Determination of the 1,12 Diaminododecane Loading Capacity and Entrapment Efficacy of the Nanoliposomes

In order to quantify the amount (mg) of 1,12 diaminododecane entrapped within the core regions of the NLs, a ninhydrin assay probe technique was employed. Ninhydrin reacts positively in the presence of primary amine groups (present on the crosslinker) resulting in Ruhemann's purple colour change (Friedman et al., 2004). The method involved the use of a Kaiser test kit (Sigma Aldrich) and instructions detailed in the kit. The entrapment efficiency (EE%) was assessed on both freshly prepared liquid samples and dry lyophilized powders. Briefly, three samples of lyophilized NLs or liquid samples were used. For the dry powder samples, each lyophilized powder was weighed and suspended in ethanol, following the addition of 0.5 %(v/v) triton X. Samples were allowed to homogenise using a vortex for 5 mins. The dispersion was then reacted with 1 mL of ninhydrin solution (made up of equal amounts of 1- 500 mg ninhydrin in 10 mL ethanol, 2-80 mg phenol in 20 mL ethanol and 3- 2 mL of 0.001 M solution of KCN diluted to 100 ml with pyridine) at 120 °C for 10 min before dilution with 3 mL of ethanol. The solution was diluted before addition into quartz cuvettes. For the liquid sample, aliquots of 300 µL of NLs were dispersed in 700 µL of DDW. A total of 1 mL of 0.5 %(v/v) triton X was added and vigorously mixed for 10 min to ensure complete release of the entrapped material. Finally, the dispersion was reacted with 1 mL of the ninhydrin cocktail and diluted several times in ethanol before addition into the quartz cuvette. Concentrations were determined photometrically at 570 nm. For linear assay calibrations, working solutions were made from a stock solution of 1,12 diaminododecane in ethanol. The drug entrapment efficiency (DEE) was calculated using Equation 7.1:

Eq. 7.1. $\mathrm{DEE}\ \% = \frac{\mathrm{Aq}}{\mathrm{Tq}} \mathrm{x} 100$ (Mufamadi et al., 2013)

Where Aq is the actual quantity of 1,12 diaminododecane obtained and Tq is the theoretical quantity of 1,12 diaminododecane added in the NLs formulation.

And drug loading (DL) was calculated based on Equation 7.2:

Eq. 7.2. $DL\% = \frac{amount\ of\ drug\ in\ nanoliposomes}{amount\ of\ total\ nanoliposomes}\ x\ 100$ (Tong et al., 2010)

7.3.3.7. In Vitro Release of 1,12 Diaminododecane from the Nanoliposomes and Mathematical Modelling of the Release Kinetics

The *in vitro* crosslinker release from the NLs was investigated using dialysis tubing method (10,000 MWCO; Sigma-Aldrich, St. Louise, MO, USA) and performed at pH 7.4 and 5.5. Briefly, a total of 3 NLs samples were prepared in order to obtain the average release from the 1,12 diaminododecane system. A total of 2 mL of each crosslinker-loaded NLs were transferred to the dialysis tubing and placed in a vessel containing 40 mL of release medium, which was maintained in an orbital shaker at 30 rpm at 37 °C. At predetermined sampling times, 300 µL medium containing the released crosslinker was drawn and replaced the same volume of fresh medium. The 300 µL of release media was then diluted with 700 µL of ethanol and reacted with 1 mL of ninhydrin at 120 °C for 10 min. Each measurement was performed in triplicate and the average percentage of drug release was determined photometrically from a standard curve at 570 nm.

The release kinetics of 1,12 diaminododecane from the formulated NLs were computed into the zero-order (Equation 7.3), first-order (Equation 7.4), Higuchi (Equation 7.5), Korsmeyer Peppas (Equation 7.6), and Hixson-Crowell (Equation 7.7) kinetic models to assist in the elucidation of the primary crosslinker release mechanisms.

Eq. 7.3. $C = k_0 t$

where K_0 is the zero-order release constant at time t.

Eq. 7.4. $\log C = \log C_0 - Kt/2.303$

where C0 is the initial drug concentration and K is the first order rate constant at time t.

Eq. 7.5. $$Q = K_{t^{1/2}}$$

where Q reflects percent drug release and K is the design variable of the system at time t.

Eq. 7.6. $$Q_0{}^{1/3} - \ Q_t{}^{1/3} = K_{HC}t$$

where Q_0 is the initial quantity of crosslinker in the formulations, Q_t is the residual quantity of 1,12 diaminododecane at time t and KHC is the rate constant.

Eq.7.7. $$\frac{M_t}{M_\infty} = Kt^n$$

where M_t/M_∞ is the fractional drug release at time t, K is the release rate constant, and n is the release exponent.

7.3.3.9. Validation of the In Vitro Crosslinking Ability of the 1,12 Diaminododecane Nanoliposomes on CS Over-Expressed Simulated Environment

A total of 0.47 and 0.933 mg/mL of 1,12 diaminododecane loaded NLs reacted with 5 mL of CS (0.01 %w/v) at 37 °C in an orbital shaker. This experiment was performed to assess the ability of the 1,12 diaminododecane NLs to crosslink a free CS solution (NLs-1,12 diaminododecane-CS crosslinked networks). Samples of NLs-1,12 diaminododecane-CS crosslinked networks were removed at 16 h and 120 h intervals and lyophilized to obtain a solid network. The 16 h interval served to assess the level of CS crosslinking after the rapid burst release of the NLs, whilst the 120 hours served to assess the degree of crosslinking of CS following complete release of the crosslinker. Chemical integrity characterization analysis of the NLs-1,12 diaminododecane-CS crosslinked network was assessed using FT-IR spectrophotometry. Briefly, analyses were undertaken at high resolution with

wavenumbers ranging from 650-4000 cm^{-1} on a FT-IR Spectrophotometer using PerkinElmer® spectrum quant software (Perkin Elmer Inc. MA, USA).

The degree of CS crosslinking mediated by the 1,12 diaminododecane NLs was further assessed using the methylene blue (MB) probe assays described in Chapter 5. Briefly, each lyophilized sample was weighed and reacted with 25 mL of MB (150 mg/L) and 25 mL of borate buffer at pH 8.5. The contents were allowed to react for 2 hours. The MB content was determined spectrophotometrically at 668 nm. The extent of crosslinking was assessed by measuring the relative percentage of MB which was adsorbed onto the various crosslinked networks relative to free CS. The relative percentage of MB that adsorbed onto the available CS groups was calculated as follows:

Eq. 7.8. $$Relative\ MB\ adsorption\ factor = \frac{(\mathrm{Ao}-\mathrm{Am})}{(Ao-Ac)} \times 100$$

Where Am, is the absorbance value of MB solution containing the various CS-1,12 diaminododecane crosslinked networks; Ac, is the absorbance value of the MB solution containing non-crosslinked CS; and Ao, is the initial absorbance value of the MB solution before any adsorption occurred (Sintov et al., 1995).

7.3.4. In Vitro Cytotoxic Performance of the Nanoliposomes on SKOV3 Carcinoma and HEK293 Cell Lines (All three Assays were Performed on the MUSETM Cell Analyser)

Samples were analysed by MUSE™ Cell Analyzer flow cytometry (EMD Millipore, Billerica, MA, USA) and by MUSE™ 1.4 Analysis software (EMD Millipore). Prior to analysis, the MUSE™ cell analyser underwent a complete clean**,** in addition, after every replicate for each working sample, the quick clean function was used to ensure no contamination between samples occurred. The System Check procedure was undertaken prior to each experiment to verify the performance of the Muse™ System by assessing counting accuracy and fluorescence detection.

7.3.4.1. Cell Viability Assay and IC_{50} Determination

Cell viability assays were performed in order to determine the cytotoxic potential of the anti-MUC 1,12 diaminododecane NLs on SKOV3 OC cells. According to the American Type Culture Collection (ATCC), the SKOV3 cancer cells served as a robust model, as these cells are resistant to tumour necrosis factor and to several cytotoxic drugs including diphtheria toxin, cis-platinum and adriamycin, in addition to over-expressing CS-E (Vallen et al., 2014; ten Dam et al., 2007), thus this cell line served as a robust model for anti-cancer testing.

The kit provides consistent staining and quantification of cell viability when the cell concentrations lie between the ranges of 1 x 10^5 to 1 x 10^7 cells/mL. T-25 culture flasks were seeded with approximately viable 6 x 10^4 cells and were allowed to reach 70-80 % confluency. At confluency, cells were serum starved overnight and subsequently treated with various concentrations (100, 50, 25, 12.5 and 6.25 µg/mL) of a) 1,12 diaminododecane NLs b) anti-MUC 16 1,12 diaminododecane NLs and c) media only and incubated for 48 h before analysis on the MUSE™ utilizing the Count & Viability Kit (Millipore, USA cat.no MCH 100102) as per manufacturer's protocol. The final concentration of cells obtained after treatment was approximately 3 x 10^6 on average. A total of 20 µL of cell suspension at various DDAB concentration were mixed with 380 µL of cell count and viability reagent (<5 x 10^5 cells/mL cell concentration) and incubated for 5 minutes before analyses. The IC_{50} values were then computed using GraphPadPrism version 8 software for each nanoliposomal formulation and administered in further studies below.

7.3.4.1. Apoptosis Assay

Degrees of apoptosis were used to quantify the ability of the nanoliposomal formulations to selectively induce apoptosis in cancerous cell lines in comparison to the healthy HEK 293 control. 6 well culture plates were seeded with approximately 1 x 10^4 viable cells and were allowed to reach 70-80% confluency. At confluency, cells were serum starved overnight and subsequently treated a) 1,12 diaminododecane NLs b) anti-MUC 16 1,12 diaminododecane NLs and c) media only as a single dose at the

IC_{50} for a 48 h exposure period. Thereafter, the assay was performed by adding 100 µL of Annexin V reagent (Millipore, USA cat.no MCH 100105) to 100 µL of cell suspension and determination of total apoptosis was conducted.

7.3.4.2. Proliferation Assay

Proliferation assays were conducted using MUSE™ Ki67 Proliferation Kit (catalogue No. MCH100114) in order to evaluate the NLs ability to selectively reduce proliferation of cancerous cell lines in comparison to the healthy control (HEK 293 cells). 12 well culture plates were seeded with approximately 5 x 10^3 viable cells and were allowed to reach 70-80% confluency. At confluency, cells were serum starved overnight and subsequently treated a) 1,12 diaminododecane NLs b) anti-MUC 16 1,12 diaminododecane NLs and c) media only as a single dose at the IC_{50} for a 48 h exposure period. Thereafter the cells were stained according to the manufacturer's protocol. Briefly, 1,0 x 10^4 cells were fixed, permeabilized and treated with either Muse Hu IgG1-PE or Muse ki67-PE antibodies for 30 minutes before determining the percentage of Ki67(+) cells and Ki67(–) cells.

7.3.4.3. Oxidative Stress Assay

Oxidative stress assays were conducted on both HEK 293 and SKOV3 cell lines to quantify the reactive oxygen species (ROS) such as superoxide, induced by the nanoliposomal formulations. HEK 293 and SKOV3 cells were incubated with the formulations (at the IC_{50}) for 48 h. Briefly, a total of 1 x 10^6 were suspended in 1 mL assay buffer, to which 10 uL was reacted to 190 µL of MUSE™ Oxidative Stress working solutions and incubated at 37 °C for 30 min prior to analysis.

Statistical Analysis

All samples were performed in 3 biological replicates and their mean and standard deviations we recorded as computed. An unpaired student T-test, two-tailed was performed for all biological assays, where the performance of the NLs treated cells were compared against the untreated control cells, this was performed to verify the

statistical significance of the obtained data. All statistics and calibration curves were analysed using Microsoft Excel. All graphs were plotted using OriginPro 8.5 Software and or GraphPadPrism 8 Software

7.4. Results and Discussions

7.4.1. Synthesis and Characterization of the Anti-MUC 16 1,12 Diaminododecane NLs

7.4.1.1. Evaluation of the Morphology/Architecture, Size and Zeta Potential of the 1,12 Diaminododecane Nanoliposomal Formulations

TEM was utilized to verify the spherical morphology of the 1,12 diaminododecane and Anti-MUC 16 functionalized 1,12 diaminododecane NLs displayed in Figure 7.1. Both nanoliposomal systems present with varying size and shape distributions. Whilst some NLs are perfectly spherical, others contrast this by appearing with slightly oblong structures on the carbon copper grid. All NLs appear to be unilamellar, with clearly defined lipid membranous bilayers. The unilamellar structures are in line with the probe sonication technique used. The nano-size obtained from the TEM imaging correlates to the size obtained from dynamic light scattering (Table 7.2 and Figure 7.2).

Furthermore, an increase in size occurs after functionalization of the anti-MUC 16 antibodies onto the surface of the NLs, which is indicative of the surface attachment of the antibody (Eck et al., 2008), preliminary confirming the attachment of the antibody to the surface of the NLs structure.

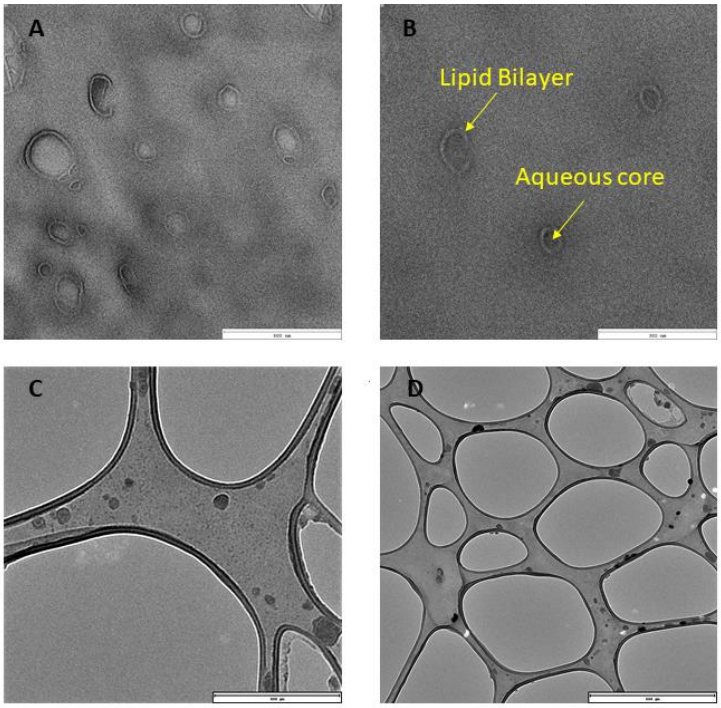

Figure 7.1. Typical TEM micrographs of the 1,12 diaminododecane NLs (A and B) and the Anti-MUC 16 functionalized 1,12 diaminododecane NLs (C and D).

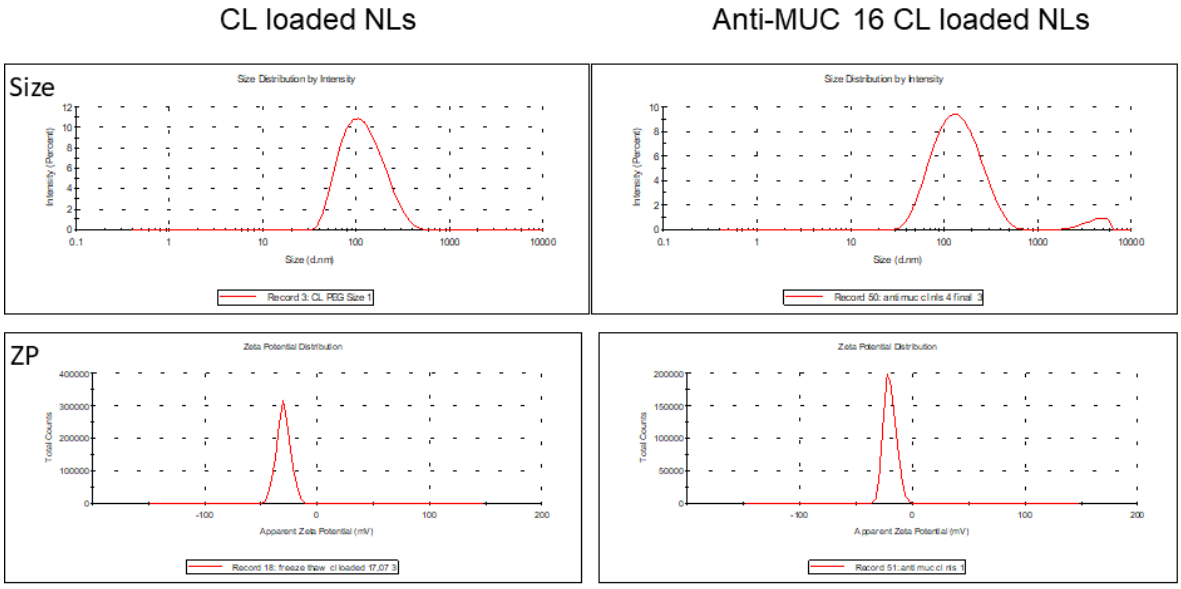

Figure 7.2. Graphical Illustration of the size and ZP =Zeta potential distributions of the CL=1,12 diaminododecane NLs, and anti MUC 16 1,12 diaminododecane NLs.

Table 7.2. Showing the average particle size, PDI and zeta potential for the various nanoliposomal systems.

Formulation	Average size (nm)	PDI	Zeta potential (mV)
Blank NLs	124.5 ± 0.87	0.159±0.017	-33.43 ± 2.65
1.12 diaminododecane-NLs	102.93 ±1.80	0.198±0.007	-30.03 ±0.05
Anti-MUC16 1.12 diaminododecane-NLs	135.16 ±3.25	0.231 ±0.01	-21.26 ±1.55

7.4.1.2. Assessment of the Anti-MUC 16 Antibody Attachment to the Nanoliposomes Surface

FT-IR spectroscopy was used to validate the microstructural modifications onto the NLs as a consequence of the antibody attachment. Conjugation of the antibody was based on covalent interactions between the NH_2 of the antibody and the OH group of L-α-PEDM on the NL surface. Figure 7.3. draws a contrast between the FT-IR spectrums of the NLs before functionalization (Figure 7.3A) and after functionalization (Figure 7.3B). For (A), the FT-IR spectrum confirms a broad band between 3200-3600 cm^{-1} and an absorption band at 1234 cm^{-1} suggesting the presence of free hydroxyl groups. Two bands at 2918 cm^{-1} and 2850 cm^{-1} confirms the $-CH_2$ and $-CH_3$ stretching vibrations. Bands at 1234 cm^{-1} and 1047 cm^{-1} are observed as a result of free carboxyl groups vibration and absorption. For (B), an absorption band at 1579 cm^{-1} newly forms, in addition, a slight shift in the peak position and height is observed from 1648 in the unfunctionalized to 1626 cm^{-1} in the functionalized with a stronger intensity. This indicates the formation of an amide (-NH) bond that was associated with the bending vibrations occurred during covalent attachment of the antibody (Mufamadi et al., 2013).

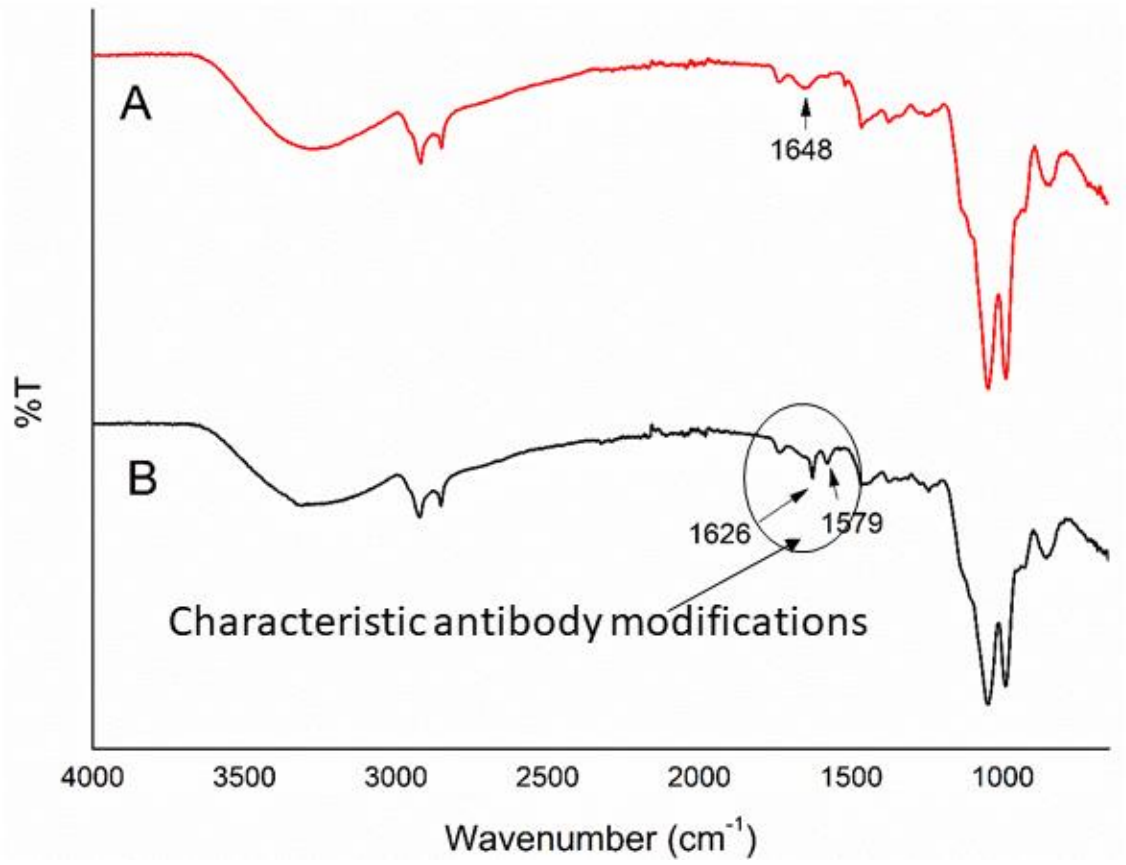

Figure 7.3. FT-IR spectrums showing the microstructural modifications of the anti-MUC 16 antibody on the nanoliposomal surface, where (A) Unfunctionalized 1,12 diaminododecane NLs and (B) Functionalized 1,12 diaminododecane NLs.

7.4.1.3. 1,12 Diaminododecane Entrapment Efficacy.

This study aims to provide confirming evidence that scientifically back the novel loading of 1,12 diaminododecane within NLs. The entrapment efficiency (EE%) and amount (mg) of 1,12 diaminododecane within the NLs are essential for understanding dosage requirements and to establish the amount of the crosslinker necessary to produce an adequate degree of crosslinked CS. The delivery of a crosslinker, encapsulated in a nano-vehicle for anti-cancer drug delivery purposes is the *first-of-its-kind*. 1,12 diaminododecane lacks a chromophore for detection, thus a ninhydrin assay was employed as a probe for UV detection. Ninhydrin reacts with the primary amine groups 1,12 diaminododecane in 1:1 ratio, producing a strong colour: Ruhemann's purple, detected photometrically at 570 nm (Friedman et al., 2004). In order to determine entrapment, NLs samples were ruptured to facilitate crosslinker

release and reacted with ninhydrin for quantification. The crosslinker entrapment efficiency (CEE%) was obtained using Equation 1 described above. Table 7.3. shows the various experimental parameters employed.

Due to the novel nature of the 1,12 diaminododecane loading into NLs, several initial amounts of 1,12 diaminododecane were preliminary mixed with a fixed ratio of lipids to yield large size particles (>1000 nm). In order to ensure the suitable nanosizes of the system required for enhanced cell internalization, the mixing of a 0.07 %(w/v) solution of 1,12 diaminododecane with the lipids in question yielded the optimal size. This led to a loading efficiency of 10.57% [regarded as an efficient loading % (Kouchakzadeh et al., 2014)] and a moderate CEE.

Table 7.3. Displaying the amount of 1,12 diaminododecane obtained from 3 NLs samples, with the experimental parameters.

Experimental parameters	Calibration curve obtained values
correlation coefficient (r^2)	0.9992
Slope	90.707
Number of samples (n)	3
Average Amount of 1,12 diaminododecane in NLs in solid sample (mg)	3.052 ± 1.9
Average Amount of 1,12 diaminododecane in NLs in liquid sample (mg)	3.8 ± 0,.53
1,12 diaminododecane loading (%)	10.57 ± 4.32
% 1,12 diaminododecane entrapment efficiency by solid sample (%)	43.6
% 1,12 diaminododecane entrapment efficiency by liquid sample (%)	54.03

7.4.1.4. *In vitro* Crosslinker Release Study and Release Kinetics Evaluations

Figure 7.4. describes the crosslinker release behaviour of 1,12 diaminododecane-loaded NLs investigated at pH 7.4 and 5.5 (physiologically relevant to tumour pHs) at 37 ˚C. The release of 1,12 diaminododecane from the NLs displayed an initial rapid/burst release phase, with approximately 60 % and 80 % of 1,12

diaminododecane released for the NLs within the first 6 hours at pH 7.4 and 5.5 respectively. This was subsequently followed by a period (8-60 h) of relatively sustained release. The fraction of crosslinker released in the initial burst is dictated by the lipid compositions (containing a relatively high concentration L-α PEDM) (Yousefi et al., 2009) and hydration processes (Avgoustakis et al., 2002). The sustained release phase was influenced by the CHOL concentration within the membranous lipid bilayers. CHOL possesses advanced lipid bilayer stabilizing properties, thus reducing the membrane fluidity, and limiting the exchange of crosslinker across the nanoliposomal membranes (Mufamadi et al., 2013; Betageri et al., 1992). The rapid burst of the crosslinker in the initial phase is highly favourable in order to flood the dense stromal regions of ovarian tumours with a surplus of crosslinker to facilitate an adequate degree CS crosslinking leading to proteoglycan activity knockdown.

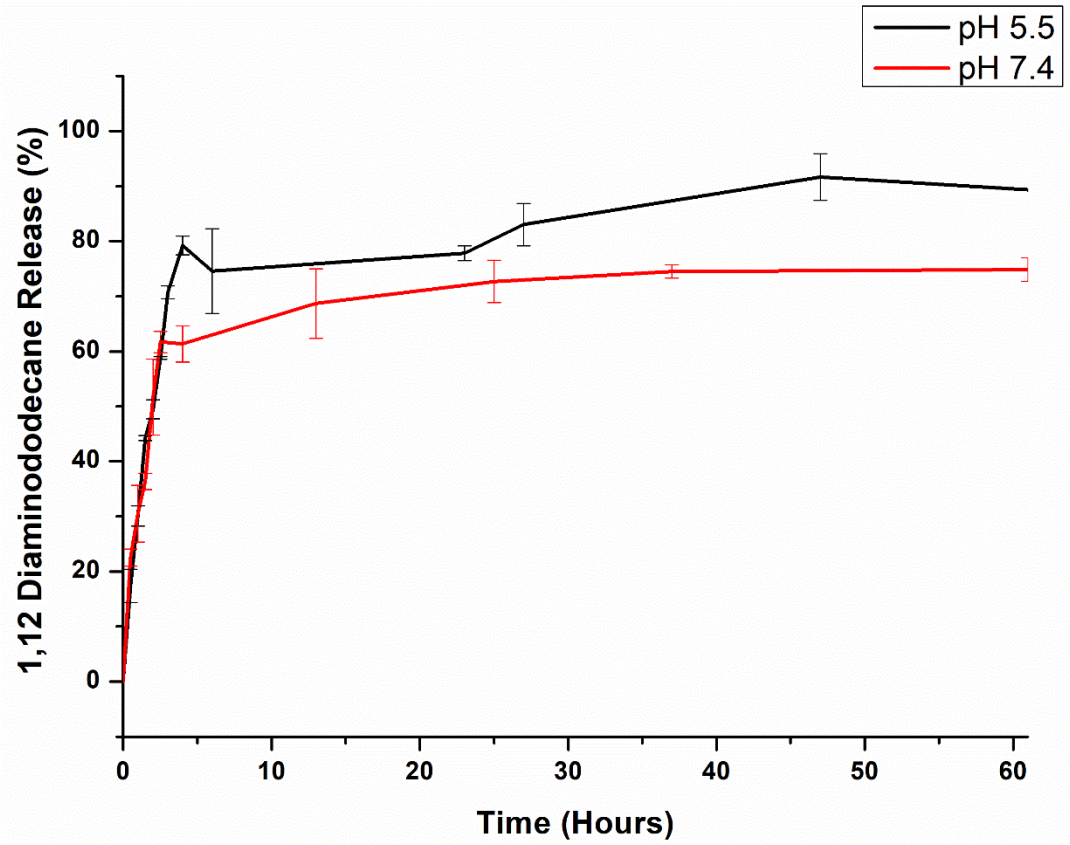

Figure 7.4. Graphical representation of the average 1,12 diaminododecane release from 3 NLs samples at pH 7.4 and 5.5 at 37 °C.

Mathematical modelling of the 1,12 diaminododecane release data (Table 7.4, Figure 7.5) was analysed to construct a series of best fit release kinetic curves which provide a deeper insight into the underlying 1,12 diaminododecane release mechanisms from the NLs. NLs at pH 7.4 and 5.5 followed a zero-order release profile (R^2= 0.9775; 0.9693 respectively). However, this would need further investigations as the rapid burst release within 4-5 h questions the zero-order release nature obtained from the mathematical modelling results. Nevertheless, zero-order release kinetics is advantageous in controlled release drug delivery systems as it provides constant (an essential) release over a period of time.

Lipid compositions making up the membranous bilayers play a key role in dictating the release of a drug molecule from the lipid membranes (Mufamadi et al., 2013). Avnir and co-workers highlighted the crucial role that membrane phosphatidylcholine species has on determining kinetic order and release rates (Anvir et al., 2011). The DSPC present in the formulation possesses a unique property to offer zero order and slow release to drug delivery systems. This can be explained by the neutral nature of 1,12 diaminododecane and its ability to extravasate from the lipid membranes to the extra-liposomal spaces resulting in release. To elaborate the latter, release rate depends on the level of membranous free volume, as high melting temperature phospholipids (i.e. greater than 55 °C such as DSPC) exhibit a minimal free volume in the membrane leading to highly saturated 1,12 diaminododecane release sites for maximal release velocity, subsequently leading to zero-order release kinetics (Anvir et al., 2011).

Table 7.4. Mathematical modelling for 1,12 diaminododecane release kinetics from the nanoliposomes.

Medium pH	Zero-Order		First-Order			Higuchi		Korsmeyer-Peppas				Hixson-Crowell	
	r^2	$k_0(h^{-1})$	r^2	m	$k_1(h^{-1})$	r^2	$kH(h^{-½})$	r^2	*n*	c	$KKP(h^{-n})$	r^2	$kHC(h^{-1´3})$
pH 7.4	0.977	20.03	0.952	0.15	-0.35	0.940	45.16	0.952	0.62	1.50	32.15	0.962	-0.45
pH 5.5	0.969	17.81	0.987	0.17	-0.39	0.991	49.14	0.991	0.74	1.47	30.13	0.990	-0.46

Medium pH	Best-Fit	Second	Third
pH 7.4	Zero-Order	Hixson-Crowell	First-Order
pH 5.5	Zero-Order	Higuchi	Hixson-Crowell

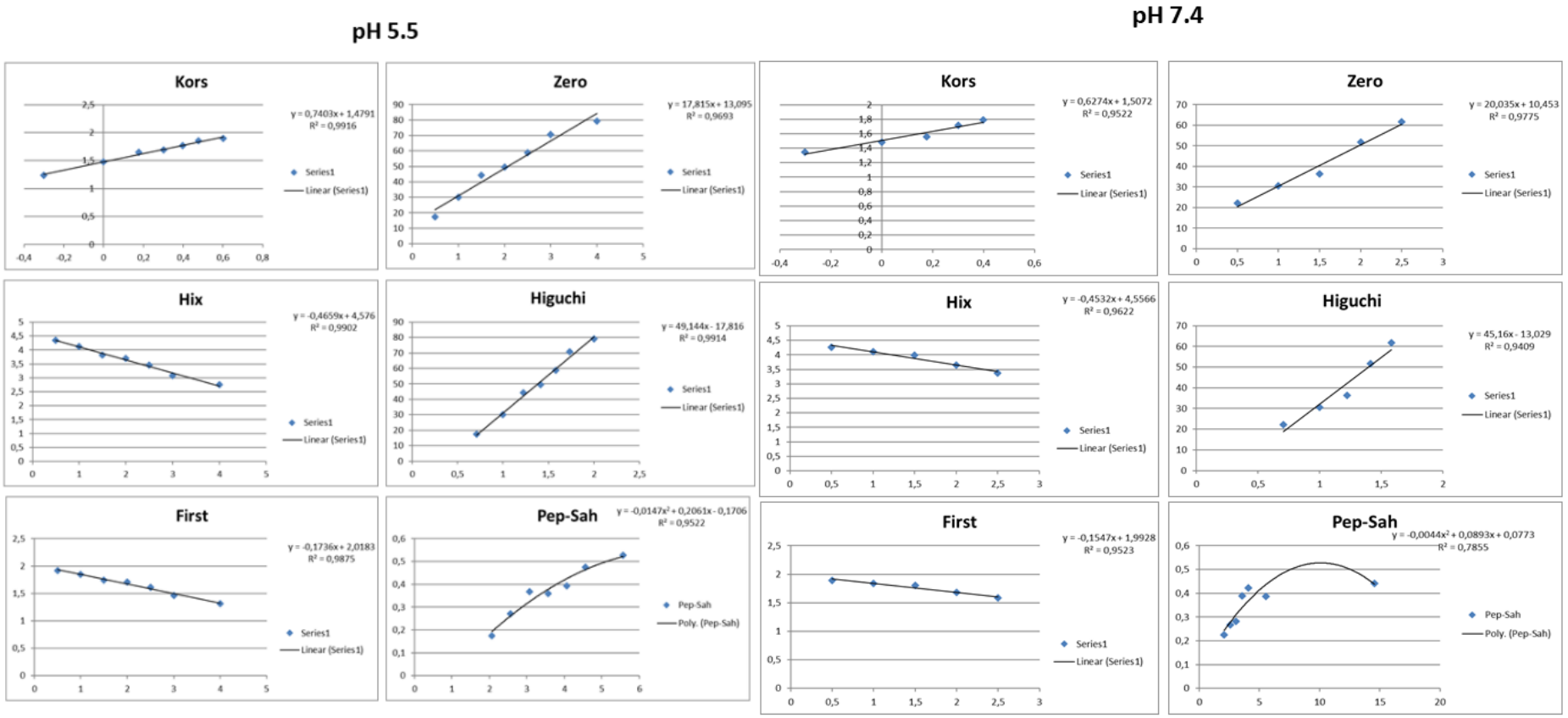

Figure 7.5. 1,12 diaminododecane kinetic profiles for the various mathematical models.

7.4.1.5. Degree of Crosslinking and Chemical Integrity Characterization of CS Following Exposure to 1,12 diaminododecane Nanoliposomes

FT-IR was used to assess the changes in the microstructural backbone of CS, facilitated by exposure to 1,12 diaminododecane NLs as a direct consequence of chemical crosslinking. Figure 7.6 shows the spectrums for unloaded NLs-CS and 1,12 diaminododecane loaded NLs-CS-crosslinked networks at various times and 1,12 diaminododecane doses.

For the FT-IR spectrum of CS exposed to 0.47 µg/ mL 1,12 diaminododecane NLs (left); a marked increase and shift in the intensity of the peaks corresponding to an amide is observed (1627 cm^{-1} from the 16 h time point to 1638 cm^{-1} at the 120 h time point). Furthermore, an increase in the intensity of the peak at 2919 and 2850 cm^{-1} of the 1,12 diaminododecane-CS-crosslinked network is observed, which corresponds to the methylene group of the crosslinker. These shifts in the peak suggest that a higher formation of amides was present at 120 h due to the complete release of the crosslinker, allowing more crosslinker in solution to facilitate more CS crosslinking.

A similar trend is observed for the 0.93 µg/mL dose, as an increase and shift in the peak corresponding to the amide region from 16 h to 120 h is observed. Affirming the time dependent release of 1,12 diaminododecane required to form crosslinked CS networks.

To validate these claims, the extent of 1,12 diaminododecane mediated CS crosslinking for 0.47 and 0.93 µg/mL doses at the exposure time was determined using methylene blue adsorption experimentation on the crosslinked CS surface and summarised in Table 7.5.

A lower MB absorbance factor corresponds to a higher degree of CS crosslinking, as less of the cationic MB is able to adsorb onto the anionic groups of CS utilized in the crosslinking process (Sintov et al., 1995). From the table, it can be deduced, that as the

concentration of 1,12 diaminododecane increases at a single time point (for e.g. 16 h) and increase in the extent of crosslinking occurs. In addition, for the same amount of crosslinker dosed to CS, as the exposure time of the NLs with CS increases (from 16 to 120 h), more crosslinker is released, subsequently leading to a greater extent of crosslinking.

To this end, these results collectively infer that 1,12 diaminododecane release rates from the NLs play a paramount role in the extent of crosslinking.

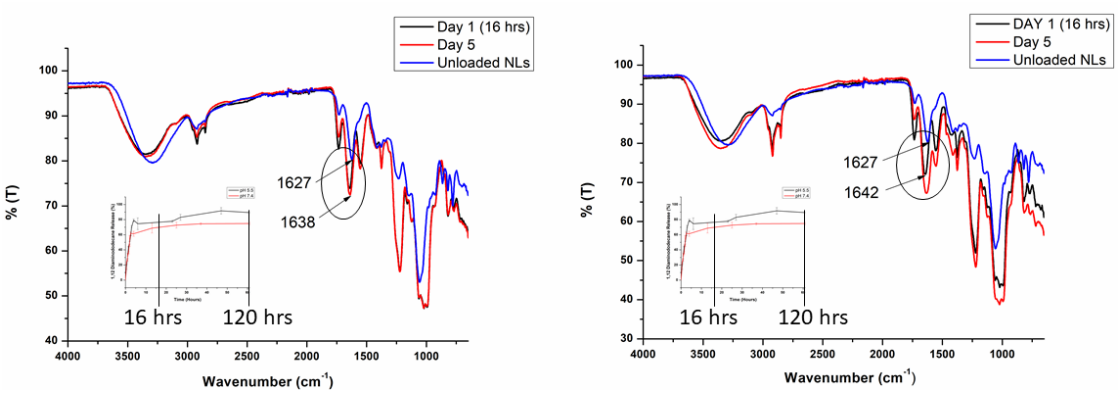

Figure 7.6. Describes the FTIR spectrum showing 1,12 diaminododecane nanoliposomal mediated crosslinking of CS *in vitro*. Left = 0.47 µg/mL dose and right =0.93 µg/ mL dose.

Table 7.5. Summarising the degree of crosslinking based on the relative MB adsorption factor for the various doses at various time points.

Sample	Relative MB adsorption factor (%)
0.47 µg/mL at T=16 h	96.03
0.47 µg/mL at T=120 h	50.13
0.93 µg/mL at T=16 h	74.48
0.93 µg/mL at T=120 h	27.23

7.4.2. Cytotoxic Evaluation of the Novel Anti-MUC 1,12 Diaminododecane Loaded Nanoliposomes

7.4.2.1. Cytotoxicity Analysis and IC_{50} Determination of the Nanoliposomes

Anti-cancer screening evaluations were performed on both the functionalized and unfunctionalized systems as a single short term (48 h) dose. It is worthy to note that both the targeted and non-targeted NLs display a significant cytotoxic characteristic on SKOV3 cell lines at considerably low concentrations (IC_{50} of 1,12 diaminododecane =2.036 µg/mL and functionalized 1,12 diaminododecane NLs = 0.4063 µg/mL (Figure 7.7)). MUC 16 has shown to promote cancer cell dissemination, in addition to modulating OC cell growth, motility, and invasiveness of OC cells (Coelho et al., 2018). Thus, the co-administration of the anti-MUC 16 antibody and 1,12 diaminododecane synergically enhanced the cytotoxic performance of the system, which produced the lowest IC_{50}. where the ant—MUC 16 antibody contributed to the dual humoral and cellular immune responses against OC cells (Ehlen et al., 2005), and 1,12 diaminododecane led to the arresting of CS-E (Pradeep et al., 2016). Table 7.6. summarises the concentrations employed, with their corresponding percentage of viable cells. It can be ascertained that the anti-MUC NLs displayed no significant differences in the cytotoxic effects between 2.5 and 4.5 µg/mL of 1,12 diaminododecane. Potential explanations for this finding relate to the saturation concentration of 1,12 diaminododecane within cells. For instance, it is proposed that the extent of CS crosslinking at 2.5 µg/mL of 1,12 diaminododecane approaches the saturation concentration of 1,12 diaminododecane in cells, causing a fixed level of CS crosslinking concentration leading to an approximate 25 % cell viability. When this dose is superseded to 4.5 µg/mL, no significant changes to the cell viability occurs as the 1,12 diaminododecane levels in the cells are saturated and the available CS present within the cells have already been crosslinked

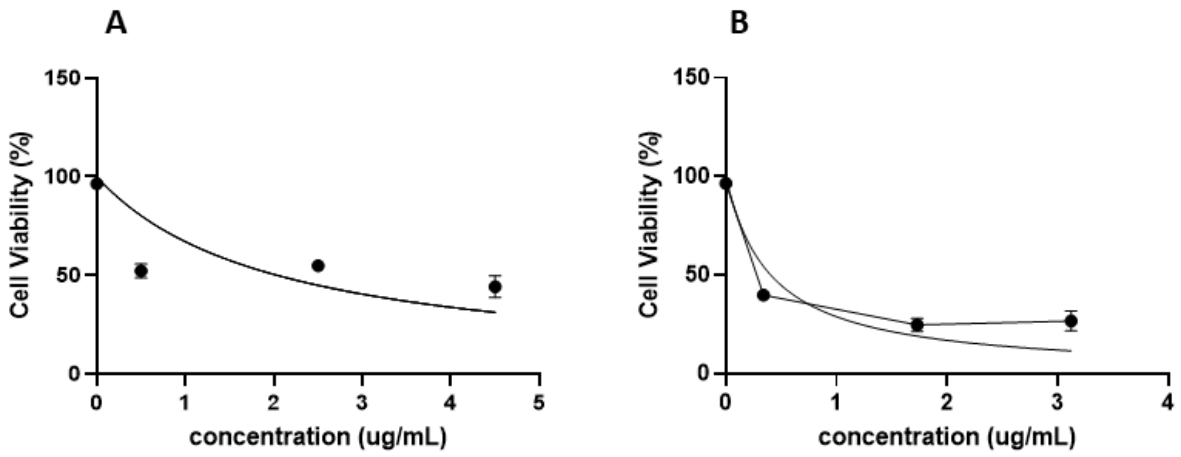

Figure 7.7. Cell viability profiles showing IC_{50} values of A) 1,12 diaminododecane loaded NLs (2.036 µg/ml) and B) anti- MUC 16 functionalized 1,12 diaminododecane loaded NLs (0.4063 µg/ml).

Table 7.6. Summarising the percentages of cell viability with the respective IC_{50} of CL-NLs (2.036 µg/mL) and anti-MUC 16 functionalized CL-NLs (0.4063 µg/mL) on SKOV3 cell lines.

Concentration (µg/ml)	Mean % viability of CL-NLs	Mean % viability of functionalized CL-NLs
0	96.4±0.72	96.4±0.72
0.5	52.16± 3.52	39.8± 0.70
2.5	54.85± 0.77	24.66± 3.30
4.5	44.23± 5.51	26.73± 5.07

7.4.2.2. Apoptosis Assay.

Apoptosis studies were conducted to ensure that these targeted nanosystems display a significant apoptotic potential on cancerous cells in contrast to healthy cell lines (HEK 293). The apoptosis observed is a potential consequence of 1,12 diaminododecane and

the anti-MUC 16 antibodies on CS-E over-expressed OC cells (Figure 7.8). For the cancerous SKOV3 cell line, the total apoptotic % of the anti-MUC 16 1,12 diaminododecane system was higher compared to the non-targeted system. In the HEK 293 cells, the targeted system displayed a similar apoptotic potential to the non-targeted system (Table 7.7). To this end, the anti-MUC 16 1,12 diaminododecane-NLs displayed a marked difference over the unfunctionalized NLs (P=0.0002) in the SKOV3 cell line, in addition, displayed a significant difference when administered to the HEK 293 cells at the same dose and incubation time ($P < 0.05$).

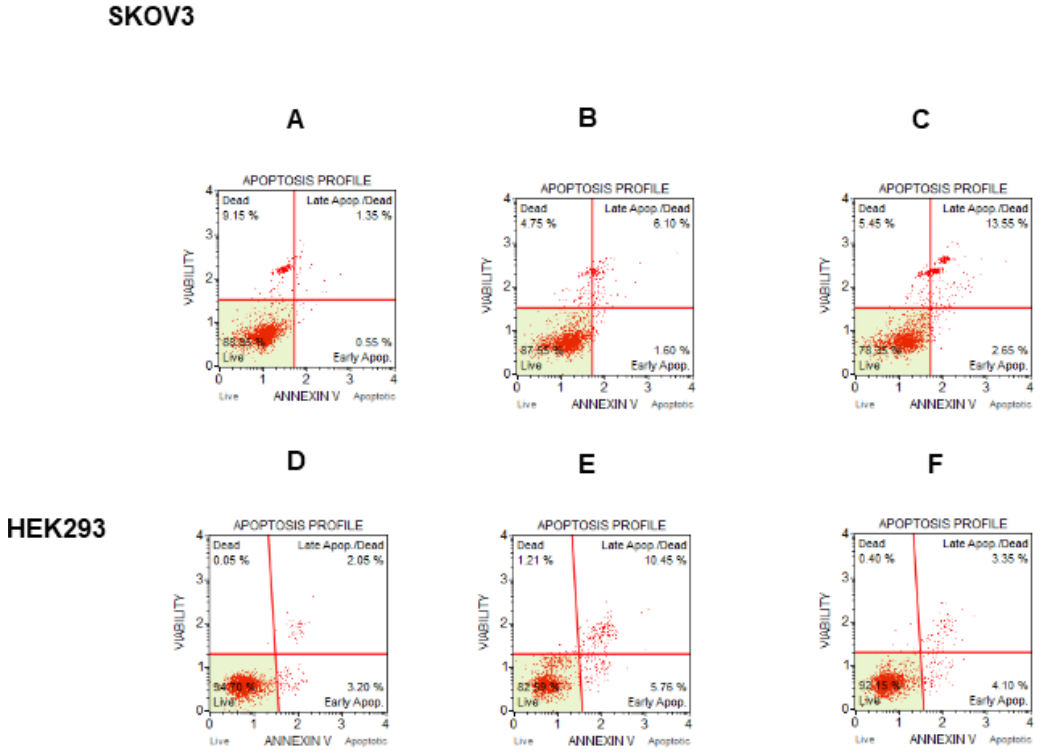

Figure 7.8. Graphical representation of apoptosis profiles generated from the MUSE™ cell analyser, where A and D are untreated, B and F are treated with 1,12 diaminododecane-NLs and C and E are treated with anti-MUC 16-1,12 diaminododecane NLs. A student T-test (unpaired) for the total apoptotic percentages of the anti-MUC 1,12 diaminododecane NLs and 1,12 diaminododecane NLs against the untreated controls showed no significance for the HEK 293 cell lines (P=0.14 and P=0.40, respectively) and for the SKOV3 cells; the anti-MUC 16 1,12 diaminododecane NLs showed a significance of P=0.0007 and the 1.12 diaminododecane NLs showed a significance of P=0.0003.

Table 7.7. Showing the percentages of live cells, Early and late apoptotic cell, and the total apoptotic cells, in both SKOV3 and HEK293 cell lines (with their standard deviations present), where Control=untreated, CL=1,12 diaminododecane NLs and F CL=anti-MUC 16 functionalized NLs.

N=3	SKOV3			HEK 293		
	Control	**CL**	**F CL**	**Control**	**CL**	**FCL**
% Live	87.85±1.03	85.08±3.48	80.03±1.45	93.35±0,17	87.91±5.2	88.06 ± 4.92
Early Apop	0.76±0.22	1.78±0.59	2.68±0.15	1.733 ±0.33	3.37±0.88	4.70± 0.91
Late Apop	1.56±0.21	6.13±0.10	12.8±0.7	4.76 ± 0.37	7.34±3.3	6.54±3.66
Total Apop	2.33±0.48	7.91±0.7	15.48±0.63	6.5 ±0.086	10.71±4.1	11.22±4.50

7.4.2.3. Proliferation Assay.

Previous studies demonstrate that the proliferation of OC cells within the tumour microenvironment is up-regulated by the over-expression of CS-E (Vallen et al., 2014). A proliferation assay was conducted to validate the ability of 1,12 diaminododecane to reduce the rapid ability of CS-E rich cell lines (SKOV3) to proliferate, relative to healthy control (HEK 293). In the SKOV3 cell lines, a remarkable ∼59% reduction in cell proliferation induced by the anti-MUC16 1,12 diaminododecane-NLs (Figure 7.9, Table 7.8). In contrast, HEK 293 cell lines were minimally affected by 1,12 diaminododecane ($P>0.05$). These findings support the ideology of *in situ* CS-E crosslinking in over-expressed cancerous cells, leading to a reduction in OC cell proliferation. In addition, the results infer enhanced targeting capabilities of these systems with minimal anti-proliferative effect on healthy cells.

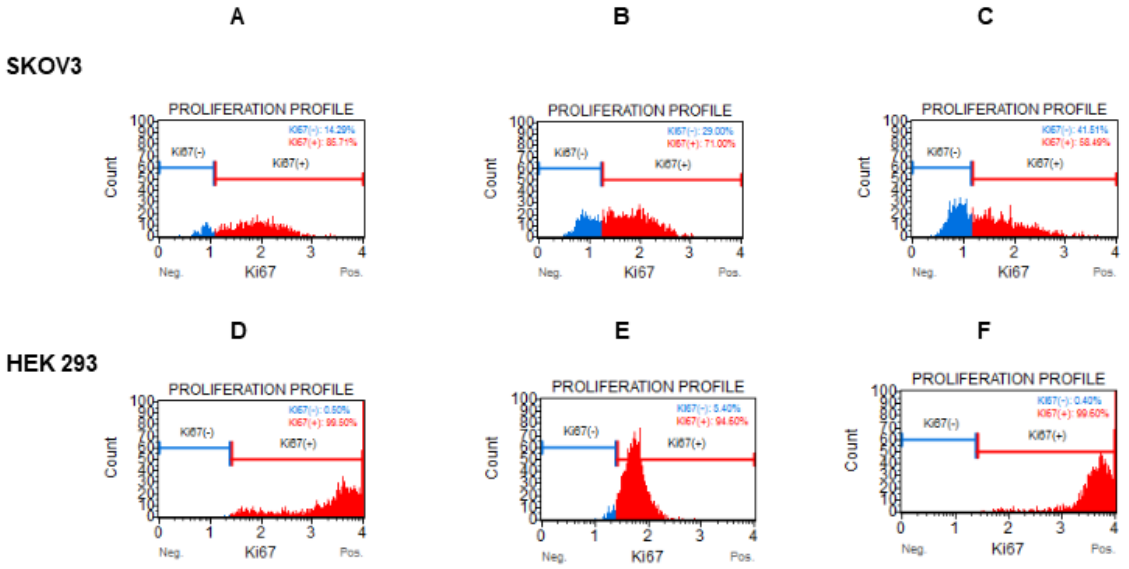

Figure 7.9. Graphical representation of profiles, where A and D are untreated, B and E are treated with CL-NLs and C and F are treated with anti-MUC 16 CL-NLs. A student T-test (unpaired) for the percentages of proliferating cells for the anti-MUC 16 1.12 diaminododecane NLs and 1,12 diaminododecane NLs against the untreated controls in the HEK 293 cell lines showed no significance (P=0.04 and P=0.84, respectively) and for the SKOV3 cells; the anti-MUC 16 1,12 diaminododecane NLs showed a significance of P=0.0003 and the 1.12 diaminododecane NLs showed a significance of P=0.02.

Table 7.8. Showing the various percentages of proliferating and non-proliferating cells in both SKOV3 and HEK 293 cell lines, where Control=untreated, CL=1.12diaminododecane NLs and F CL=anti-MUC 16 1.12 diaminododecane NLs.

	SKOV3			**HEK293**		
	Control	**CL**	**F CL**	**Control**	**CL**	**F CL**
% Proliferating	84.28±2.17	75.55±3.9	59.26±3.1	99.5	99.45±0.1	99.73±0.1
% Non-Proliferating	15.72±2.17	24.45±3.9	40.73±3.1	0.5	0.55±0.13	0.26±0.16

7.4.2.4. Oxidative Stress Assay.

Oxidative stress analysis was conducted in order to determine the ability of the NLs to generate reactive oxidation species such as superoxides. Due to the novel nature of the crosslinking application described in this study, determination of the ROS states in healthy cells is vital as their accumulations adversely affects the equilibrium of cells which lead to cell death and apoptosis (Matés et al., 2012). Figure 7.10 and Table 7.9. summarises the ROS profiles and percentages of ROS+ and ROS- cells. In the SKOV3 cell line, 47.4% of cells contained ROS states induced by the anti-MUC 16 1,12 diaminododecane-NLs which was favourable relative to the ~8% generated in the HEK 293 cells ($P>0.05$). The interaction between 1,12 diaminododecane and anti-MUC 16 on the over-expressed CS-E in SKOV3 cells lead superior production of ROS. It is also evident that HEK 293 cells were minimally affected, as these cells lack CS-E or MUC 16 over-expression. To this end, these systems display a greater anti-cancer potential in favour of cells that over-express CS-E.

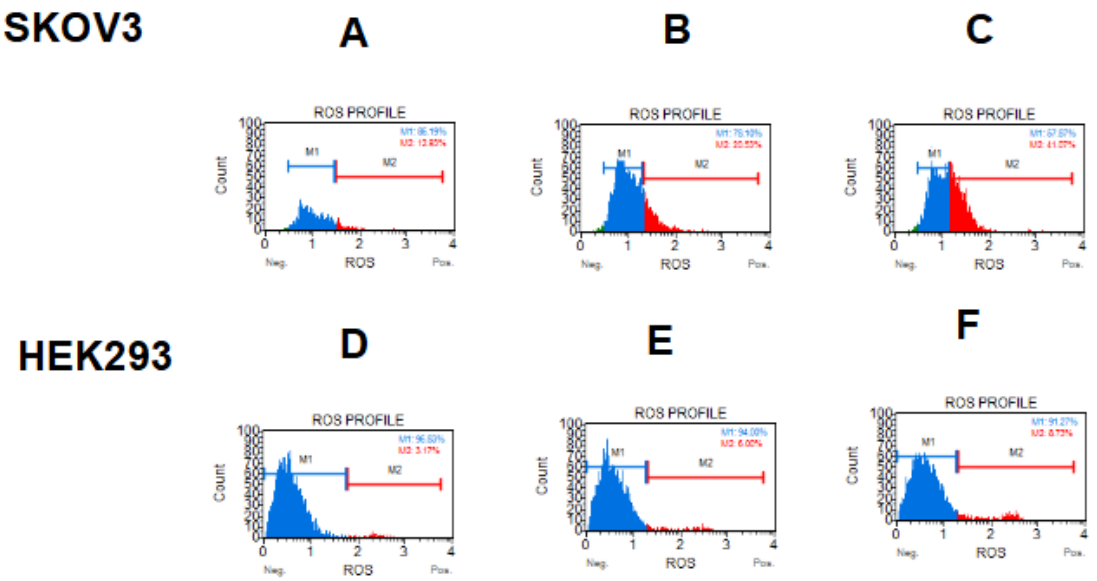

Figure. 7.10. Graphical representation of ROS profiles, showing the various percentages of ROS + and ROS – cells treated. Where A and D are untreated, B and E are treated

with 1,12 diaminododecane-NLs and C and F are treated with Anti-MUC 16 1,12 diaminododecane -NLs. A student t test (unpaired) for the percentages of ROS - cells for the anti-MUC 16 1,12 diaminododecane NLs and 1,12 diaminododecane NLs against the untreated controls in the HEK 293 cell lines showed a significance of P = 0.0019 and P= 0.07, respectively, and for the SKOV3 cells; the anti-MUC 16 1,12 diaminododecane NLs showed a significance of P = 0.003 and the 1,12 diaminododecane NLs showed a significance of P= 0.004.

Table. 7.9. Summarising the percentages of ROS negative and ROS positive cells in both SKOV3 and HEK 293 cell lines, where Control = untreated, CL = unfunctionalized 1,12 diaminododecane NLs and F CL = Anti-MUC 16 1,12 diaminododecane NLs.

	SKOV3			**HEK 293**		
	Control	**CL**	**F CL**	**Control**	**CL**	**F CL**
% ROS (-) Cells (M1)	86.37±0.77	75.93±3	51.93±10.05	95.66±1.02	94.2±0.17	91.38±0.10
% ROS (+) Cells (M2)	12.49±0.92	22.8±3.34	47.4±10.19	4.33±1.02	5.8±0.17	8.62±0.10

7.5. Conclusion

This chapter was conducted to verify the scientific feasibility of our previously published hypothesis following on from the preliminary discoveries presented in Chapter 5. The crosslinking of CS utilizing 1,12 diaminododecane proved successful, rationalizing further anti-cancer testing. This led to the formulation of crosslinker loaded nanoliposomes, characterization and subsequent testing in 2D cancer models on over-expressed CS-E OC cell lines. The 1,12 diaminododecane NLs were successfully formulated and showed favourable nano-sized and zeta potential distributions which placed the formulation in the category of good physical stability. The favourable zero-order release kinetics achieved was, which allowed for the constant release of 1,12 diaminododecane. This released 1,12

diaminododecane further displayed abilities to crosslink a solution of CS, in a time dependent manner. More crosslinked CS networks formed for the same amount of 1,12 diaminododecane at the longer time points (function of release). This was confirmed by FT-IR spectroscopy and MB degree of crosslinking quantifications. The novelty of the system was further enhanced by the surface engineering of the anti-MUC 16 antibodies onto these NLs, for its dual targeting and anti-cancer properties. These OC targeted-functionalized-NLs display superior selectivity when tested in OC cell lines (SKOV3), decreasing cell proliferation, increasing apoptosis and stimulating the accumulation ROS, in contrast to the healthy cell lines (HEK 293), which served as a negative control to ensure the OC selective characteristics of the system. The findings of this study infer successful preliminary anti-cancer abilities of the 1,12 diaminododecane nanoliposomal concept, *A world's-first*. However, further testing in more physiologically relevant models and gene expression studies are required to prove GAG knockdown for OC therapy.

7.6. References

Avnir, Y., Turjeman, K., Tulchinsky, D., Sigal, A., Kizelsztein, P., Tzemach, D., et al., 2011. Fabrication Principles and Their Contribution to the Superior In Vivo Therapeutic Efficacy of Nano-Liposomes Remote Loaded with Glucocorticoids. PLoS ONE. 6, e25721.

Bhattacharya, A., Rawlins, J.W., Ray, P., 2009. Polymer grafting and crosslinking John Wiley, Hoboken, NJ, USA. 341.

Breimer, D.D., 1999. Future challenges for drug delivery. J Control Release. 62, 3–6.

Avgoustakis, K., Beletsi, A., Panagi, Z., Klepetsanis, P., Karydas, A.G., Ithakissios, D.S., 2002. PLGA–mPEG nanoparticles of cisplatin: in vitro nanoparticle degradation, in vitro drug release and in vivo drug residence in blood properties. Journal of Controlled Release. 79, 123-135.

Azeredo, H.M.C., Waldron, K.W., 2016. Crosslinking in polysaccharide and protein films and coatings for food contact – A review, Trends in Food Science & Technology. 52, 109-122.

Betageri, G., and Parsons, D., 1992. Drug encapsulation and release from multilamellar and unilamellar liposomes. International Journal of Pharmaceutics. 81, 235-241.

Bray, F., Ferlay, J., Soerjomataram, I., Siegel, R.L., Torre, L.A., Jemal, A., 2018. Global cancer statistics 2018: GLOBOCAN estimates of incidence and mortality worldwide for 36 cancers in 185 countries. CA Cancer J. Clin. 68, 394–424.

Chekmasova, A.A., Rao, T.D., Nikhamin, Y., et al., 2010. Successful eradication of established peritoneal ovarian tumors in SCID-Beige mice following adoptive transfer of T cells genetically targeted to the MUC16 antigen. Clin Cancer Res. 16, 3594-606.

Coelho, R., Marcos-Silva, L., Ricardo, S., Ponte, F., Costa, A., Lopes, J. M., & David, L., 2018. Peritoneal dissemination of ovarian cancer: role of MUC16-mesothelin interaction and implications for treatment. Expert Review of Anticancer Therapy. 18, 177-186.

Coleman, R.L., Monk, B.J., Sood, A.K., Herzog, T.J., 2013. Latest research and treatment of advanced-stage epithelial ovarian cancer. Nat Rev Clin Oncol. 10, 211–24.

Eck, W., Craig, G., Sigdel, A., Ritter, G., Old, L., Tang, L., Brennan, M., Allen, P and Mason, M., 2008. PEGylated Gold Nanoparticles Conjugated to Monoclonal F19 Antibodies as Targeted Labeling Agents for Human Pancreatic Carcinoma Tissue. ACS Nano. 2, 2263-2272.

Ehlen, T.G, Hoskins, P.J., Miller, D., Whiteside, T.L., Nicodemus, C.F., Schultes, B.C., Swenerton, K.D., 2005. A pilot phase 2 study of oregovomab murine monoclonal antibody to CA125 as an immunotherapeutic agent for recurrent ovarian cancer. Int J Gynecol Cancer. 15, 1023-1034.

Felder, M., Kapur, A., Gonzalez-Bosquet, J. et al., 2014. MUC16 (CA125): tumor biomarker to cancer therapy, a work in progress. Mol Cancer. 13, 129.

Fras, L., Stana-Kleinschek, K., Ribitsch, V., Sfiligoj-Smole, M. and Kreze, T., 2004. Quantitative Determination Of Carboxyl Groups In Cellulose Polymers Utilizing Their Ion Exchange Capacity And Using A Complexometric Titration. Materials Research Innovations. 8, 145-146.

Friedman, M., 2004. Applications of the Ninhydrin Reaction for Analysis of Amino Acids, Peptides, and Proteins to Agricultural and Biomedical Sciences. Journal of Agricultural and Food Chemistry. 52, 385-406.

Hennink, W.E., van Nostrum, C.F., 2012. Novel crosslinking methods to design hydrogels. Advanced Drug Delivery Reviews. 64, 223-236.

Hoosen, Y., Pradeep, P., Kumar, P., du Toit, L.C., Choonara, Y.E., Pillay, V., 2018. Nanotechnology and glycosaminoglycans: Paving the way forward for ovarian cancer intervention. Int. J. Mol. Sci. 19, 253.

Kouchakzadeh, H., Shojaosadati, S, A., Shokri, F., 2014. Efficient loading and entrapment of tamoxifen in human serum albumin based nanoparticulate delivery system by a modified desolvation technique,
Chemical Engineering Research and Design. 92, 1681-1692.

Matés, J., Segura, J., Alonso, F. and Márquez, J., 2012. Oxidative stress in apoptosis and cancer: an update. Archives of Toxicology. 86, 1649-1665.

Mufamadi, M., Choonara, Y., Kumar, P., Modi, G., Naidoo, D., van Vuuren, S., et al., 2013. Ligand-functionalized nanoliposomes for targeted delivery of galantamine. International Journal of Pharmaceutics. 448, 267-281.

Pantshwa, J. M., Rhoda, K., Clift, S. J., Pradeep, P., Choonara, Y. E., Kumar, P., du Toit, L. C., Penny, C., & Pillay, V., 2018. Chemotherapeutic Efficacy of Implantable Antineoplastic-Treatment Protocols in an Optimal Mouse Model for Human Ovarian Carcinoma Cell Targeting. International journal of molecular sciences. 19, 3030.

Pantshwa, J.M., Kondiah, P.P.D., Choonara, Y.E., Marimuthu, T., Pillay, V., 2020. Nanodrug delivery systems for the treatment of ovarian cancer. Cancers. 12, 213.

Pradeep, P., Choonara, Y., Kumar, P., Pillay, V., 2016. “On-The-Spot” Arresting of Chondroitin Sulphate Proteoglycans: Implications for Ovarian Adenocarcinoma Recognition and Intervention. International Journal of Molecular Sciences. 17, 1136.

Safari, M.G., Hosseinkhani, S., 2013. Lipid composition of cationic nanoliposomes implicate on transfection efficiency. Journal of Liposome Research. 23,174-186.

Sintov, A., Di-Capua, N., Rubinstein, A., 1995. Cross-linked chondroitin sulphate: Characterization for drug delivery purposes. Biomaterials. 16, 473–478.

ten Dam, G. B., van de Westerlo, E. M. A., Purushothaman, A., Stan, R. V, Bulten, J., Sweep, F. C. G. J., Massuger, L. F., Sugahara, K., van Kuppevelt, T. H., 2007. Antibody GD3G7 selected against embryonic glycosaminoglycans defines chondroitin sulfate-E domains highly up-regulated in ovarian cancer and involved in vascular endothelial growth factor binding. Am. J. Pathol. 171, 1324–1333.

Vallen, M. J. E., Van Der Steen, S. C. H. A., Van Tilborg, A. A. G., Massuger, L. F. A. G., Van Kuppevelt, T. H., 2014. Sulfated sugars in the extracellular matrix orchestrate ovarian cancer development: “When sweet turns sour.” Gynecol. Oncol. 135, 371–381.

Yousefi, A., Esmaeili, F., Rahimian, S., Atyabi, F., Dinarvand., 2009. Preparation and In Vitro Evaluation of A Pegylated Nano-Liposomal Formulation Containing Docetaxel. Scientia Pharmaceutica. 77, 453-464.

CHAPTER 8:

Anti-MUC 16 Functionalized DDAB and 1,12 Diaminododecane Nanoliposomes Arrest Chondroitin Sulphate-E Activity in 3D Ovarian Tumourospheres

8.1. Synopsis of this chapter

In this chapter, the cytotoxic ability of the 1,12 diaminododecane and Didodecyldimethyl ammonium bromide (DDAB) nanoliposomes (NLs) against an innovative 3D tumourosphere model was investigated. These tumourospheres better mimic physiological tumours and present as a more robust model for OC drug testing. The cytotoxic potential of the NLs was announced by disturbing tumourosphere formation and destruction of intact tumourospheres. The ability of these nanosystems to produce ROS in cancerous cell lines, later leading to apoptosis and reductions in cell viability was also determined and compared to healthy cells. The hallmark pathogenic contribution of CS-E to OC, i.e., elevated vascular endothelial growth factor (VEGF) levels, was also evaluated via selective VEGF ELISA testing. This yielded promising reductions in VEGF in cells treated with the various nanoliposomal formulations relative to the healthy control cells. Lastly, quantitative polymerase chain reactions (qPCR) for the gene expression analysis of GalNAc4S-6ST was undertaken (SKOV3, HEK 293 and OVCAR-5). GalNAc4S-6ST is the sole sulfotransferase responsible for the rapid CS-E biosynthesis. It was revealed experimentally that a selective knockdown in the gene expressions of GALNAc4s-6ST on SKOV3 cell lines was induced by these NLs relative to the comparison cell lines.

Keywords: Tumourospheres, GalNAc4S-6ST, Vascular Endothelial Growth Factor, Polyelectrolyte Complexation.

8.2. Introduction

Great advances in research and development aimed at discovering novel biomarkers for OC therapy have been conducted in recent times (Enroth et al., 2019; Simmons et al., 2019). Efforts to identify and determine a niche area of the tumour environment with suitable molecular targets are essential for rationale based targeted chemotherapy. In light of the above, the extracellular matrix (ECM) is paramount for maintaining all functioning organs. A healthy ECM encapsulating cancer cells has a potential to restrain and hinder cancer progression (Bissell et al., 2002; Kenny et al., 2003), by retaining malignant tumours from disseminating to adjacent healthy regions. Conversely, the ECM also provides a scaffold for tumour cell adhesion, attachment and migration, and is therefore an essential supporter and intermediate player in tumour progression (Bissell et al., 2002; Kenny et al., 2003). In contrast to a healthy ECM, cancerous ECM contains higher concentrations of various growth factors (such as VEGF) and elevated amounts of specific proteoglycans and glycosaminoglycans (GAGs) such as chondroitin sulphate-E (CS-E) (Pradeep et al., 2016; detailed in Chapter 6), solidifying the tumour ECM of OC as a highly niche region for drug targeting.

The consequence of CS-E over expression has been detailed greatly throughout this thesis. The final step in the *de-novo* biosynthesis of the CS-E subtype relies solely on enzymatic addition of a free sulphate group to CS-A by N-acetyl galactosamine 4-sulphate 6-O-sulfotransferases (GalNAc4S-6ST) (Ohtake et al., 2001). A considerably elevated expression of GalNAc4S-6ST mRNAs was present in patients with colorectal and astrocytic tumours (Kobayashi et al., 2012; Ito et al., 2007), which consequently lead to failures in clinical therapies. Furthermore, it was observed that down regulating the expression of GalNAc4S-6ST in Lewis lung carcinomas reduced the adhesive properties of cells to the ECM surface leading to a considerable suppression of metastatic lung carcinoma (Mizumoto et al., 2013). In addition to this, it was further established in SKOV3 OC cells that the knockdown of GalNAc4S-6ST caused a similar reduction in the adhesive properties which restricted tumour noduli formation. To this end, the ability of both nanoliposomal systems to induce a knockdown effect on the CS-E biosynthesis by down-

regulating GalNAc4S-6ST was investigated. The rationale for this is based on the availability of the CS-A substrate; as CS-A forms a PEC with DDAB or crosslinked networks with 1,12 diaminododecane, it potentially restricts CS-A from its interaction with the GalNAc4S-6ST, leading to the aggressive production of the CS-E species.

The application of monolayer 2D cell cultures have been established for decades for its utility as a model in a diverse spectrum of research. The ‘go to’ 2D cultures are low cost, high throughput and relatively easy to control. However, major criticisms relating to their reliability in comparison to *in vivo* models are frequently presented. The culture geometry of a flat 2D model restricts the number of neighbouring cells, resulting in reduced inter-cellular contact and communication relative to *in vivo* cells. Furthermore, 2D culture conditions have increased surface area for direct exposure to oxygen and growth nutrients (Brüningk et al., 2020), in addition to missing the trademark features of cancer including hypoxia, altered cell–cell contacts, and rewired metabolisms (Han et al., 2020). However, for *in vivo* scenarios, existing models are useful for defining the biological properties of cancer, though not flawless. Genetically engineered xenografted mouse models mimic tumour growth and their microenvironment, but are limited by large scalability, prolonged incubations, and laborious surgical procedures which require expert personnel related to extreme costs. This highlights the importance of targeting cancer cells in a setting that is more biologically mimetic and encompasses the 3D architecture of an original tumour (Ketchen et al., 2020). Among the 3D cell culture models, multi-cellular spheroids are commonly used as they accurately mimic tumour structures (Cheryl Jia Le, C., 2019). 3D tumour models, such as the SKOV3 tumourospheres established in this chapter are said to bridge the gap between 2D cell studies and *in vivo* models. Cells grow in close proximity within a 3D environment which facilitates mandatory cell–cell interactions. To this end, it is vital to focus on the establishment of 3D models for future cancer studies, especially in reducing the discrepancies between *in vivo* and *in vitro* research environments (Brown et al., 2019).

In this chapter, the key questions in light of potential genetic reasonings surrounding the anti-proliferation and anti-migratory effects of the systems were addressed (i.e. does the

systems reduce CS-E, seen by a reduction in CS-E biosynthesis). We thus analysed the reductions in GalNAc4S-6ST in SKOV3 OC cell lines (over-expressing CS-E) and compared these expressions to that of OVCAR-5 cells (comparison group) and HEK 293 cell lines (healthy control group). Furthermore, a more suitable and biologically replicating, 3D spheroidal architecture of SKOV3 cells was established, to which we termed "*Tumourospheres*" for determining the potential cytotoxicity of both nanoliposomal formulations. Lastly, a Vascular Endothelial Growth Factor A (VEGF-A) ELISA assay on both systems was performed to determine if the cytotoxicity can be correlated to reductions in VEGF, a hallmark feature caused by the over-expression of CS-E in OC.

8.3. Materials and Methods

8.3.1. Materials

1,12 diaminododecane (98%, 200.36 g/mol), Chondroitin Sulphate sodium salt from shark cartilage, *N*,*N*′-Dicyclohexylcarbodiimide (99%, 206.33 g/mol), *N*-Hydroxysuccinimide (98%, 115.09 g/mol) and Didodecyldimethylammonium Bromide (DDAB) (≥98%; Mw= 462,63), Lipids including cholesterol (≥99%; Mw= 386.65), 1,2-Distearoyl-sn-glycero-3-phosphocholine (≥99%; Mw= 790.15) and L-α-Phosphatidylethanolamine distearoyl methoxypolyethylene glycol conjugate were all purchased from Sigma Aldrich (St. Louis, Missouri, United States). Muse™ assay reagents including the Oxidative Stress Kit (MCH100111) were purchased from Merck (Kenilworth, New Jersey, United States). Cancer cell lines including SKOV3 were purchased from Fox Chase Cancer Centre, (Philadelphia, USA) and served as a positive control; over-expressing CS-E, whilst HEK 293 was generously donated by Dr Clement Penny and served as a negative control, OVCAR5 were purchased from Biocom (Torreyana Rd, San Diego, CA, USA) and served as a comparison control for the gene expression analysis study. All cells were cultured in RPMI, supplemented with 10 % fetal bovine serum and penicillin/streptomycin, which were purchased from Sigma Aldrich (St. Louis, Missouri, United States). Kits for the gene expression analysis include RNAeasy Mini Kit was purchased from Qiagen (Hilden,

Germany). Both High-Capacity RNA-to-cDNA and Power SYBR Green PCR Master Mix were purchased from Applied Biosystems (Foster City, California, United State). Primers were purchased from Inqaba Biotech (Pretoria, Gauteng, South Africa). Live/dead™ viability cytotoxicity kit was purchased from ThermoFisher Scientific (Waltham, Massachusetts, United states). Corning® Spheroid Microplates were purchased from Sigma Aldrich. Lastly the Human VEGF-A (Vascular Endothelial Growth Factor A) ELISA Kit (cat numb: E-TSEL-H0026) was purchased from Elabscience® (Wuhan, Hubei, China).

8.3.2. Formulation of DDAB Cationic Nanoliposomes

Surface present DDAB-active NLs were prepared using an adapted method of Safari and Hosseinkhani (Safari et al., 2013). The lipids were mixed in varying amounts and dissolved in chloroform (Table 8.1). The chloroform was subsequently evaporated utilizing a rotary evaporator which was set to 65 °C at 40 rpm for a 2-h period, leading to a thin lipid film formation. The lipid films were allowed to air dry for an additional 24 h at room temperature which ensured complete exclusion of the residual chloroform. A total of 10 mL of double distilled water (DDW) at 70 °C (±5°C) was added to the dried lipid films and mixed vigorously for 30.0 min at 70 °C (±5°C) to obtain a dispersion. Primary homogenization was performed by bath sonication for 20.0 min at 65 °C, following probe sonication (Sonics & Materials, Inc., CT, USA; pulse on for 5.0 s and pulse off for 10.0 s) for 3 min. NLs were then subjected to a freeze-thawing process before filtration through a 0.22 µm syringe filter and stored at 4°C.

Table 8.1. Showing the various compositions of the optimized nanoliposomal formulation.

Composition	DDAB active (mg)
DSPC	21
CHOL	21
DDAB	3
L-α PEDM	2

8.3.3. Formulation of the 1,12 Diaminododecane Loaded Nanoliposomes.

1,12 diaminododecane loaded NLs were prepared using an adapted method of (Safari et al., 2013). The lipids were dissolved in varying amounts (Table 8.2.) using chloroform following homogenization with a probe sonicator for 30 s – 1 min (Sonics & Materials, Inc., CT, USA). The chloroform was removed by rotary evaporation (Rotavapor® RII, Büchi Labortechnik AG, Switzerland) at 65 °C and 40 rpm for 2 hours, producing a thin lipid film. The residual solvents were removed by air drying at ambient temperatures overnight. A total of 10 mL of DDW or 0.07 %(w/v) solution of 1,12 diaminododecane in DDW at 70 °C was added to the dried lipid films and mixed vigorously for 30.0 min at 65 °C to obtain a dispersion. Primary homogenization was performed by bath sonicator for 20.0 min at 65 °C and was then sonicated by probe sonication (pulse on for 5.0 s and pulse off for 10.0 s, for 3 min). The dispersion was centrifuged to remove the un-entrapped 1,12 diaminododecane in the pellet. Lastly the NLs solution was freeze-thawed at 37 °C and filtered through a 0.22 µm pore size membrane filter and stored at 4 °C until further use.

Table 8.2. Amounts of lipids used and hydration fluids for each NLs formulation.

Composition	(mg)
DSPC	21
CHOL	21
L-α PEDM	2
Hydration with 1,12diaminododecane	0,07 %(w/v)

8.3.4. Surface-Engineering of Anti-MUC 16 Antibody onto the Nanoliposomal Surfaces.

The anti-MUC 16 antibody was surface engineered to the NLs following a method previously described (Mufamadi et al., 2013). Briefly, NLs were allowed to react with 46

mg of N-Hydroxysuccinimide (NHS) and 87 mg of Dicyclohexylcarbodiimide (DCC) in 100 µL of methanol and 4 mL of PBS at pH 7.2. After maintenance at room temperature for 1 hour, 5 µL (0.124 mg/mL) of synthetic peptide was added to the treated NLs suspension and allowed to react overnight at room temperature, following solvent removal via rotary evaporation. Thereafter, the DDAB NLs suspension was dialyzed against PBS (pH 7.4) using SnakeSkinTM Pleated dialysis tubing of (3.500 MWCO; Sigma-Aldrich, St. Louise, MO, USA) for 24 hours to remove excess reagents whilst the 1,12 diaminododecane system was rotavated at 40 °C and extensively filtered. The anti-MUC 16 functionalized NLs were further stabilized by a second freeze-thawing process following filtration through a 0.22 µm syringe filter.

8.3.5. Oxidative Stress Assay.

Oxidative stress assay was conducted on both HEK 293 and SKOV3 cell lines to quantify the reactive oxygen species (ROS) accumulation such as superoxide, induced by the nanoliposomal formulations. T-25 culture flasks were seeded with approximately 6 x 10^4 viable cells and were allowed to reach 70-80% confluency (approximately 3 x 10^6 cells). At confluency, cells were serum starved overnight and subsequently treated with various concentrations of a) DDAB cationic NLs b) anti-MUC 16 cationic NLs and c) media only as a single dose at the IC_{50} 48 hours and stained according to the manufacturer's protocol. Briefly, 1 x 10^6 cells were suspended in 1 mL assay buffer, to which 10 µL was reacted to 190 µL of MUSE^{TM} Oxidative Stress working solutions and incubated at 37 °C for 30 min prior to analysis

8.3.6. Anti-VEGF Assessment of the Nanoliposomal Systems

Quantitative determination of the VEGF expressions (ng/mL) were evaluated using the Human VEGF-A ELISA test kit (E-EL-H0111) conducted on SKOV3 and HEK 293 cell lines. The levels of VEGF were determined over 48 hours (0, 24 and 48 h) and performed as described by the manufacturer's protocol. Briefly, a 24 well plate was seeded with

173840 SKOV3 (test group) and 69700 HEK 293 (healthy control group) and allowed to reach 70-80% confluency. At T=0 h, wells were treated with the nanoliposomal systems at the IC_{50}. At each time interval, 100 µL of each sample was added to a 96 well ELISA test plate, OD was obtained according to the instructions on the manufacturer's protocol at 450 nm using a BioTek 800TS Microplate Absorbance Reader (BioSPX B.V. | Bovenkamp 9 | 1391 LA Abcoude, Netherlands). For linear assay calibrations, a stock solution of a known 2000 ng/mL VEGF from the supplier was utilized to create several working dilutions, from which, the amount of VEGF of the cell samples were determined.

8.3.7. Cytotoxic Evaluation of the Anti-MUC 16 Nanoliposomal Systems on 3D Tumourosphere Models

Two parameters were assessed to conclude the cytotoxicity of the nanoliposomal formulations on 3D spheroidal models. The first assessment analysed the development of spheroid formation in the presence of the nanoliposomal formulations, whilst the second experiment assessed the effect of the nanoliposomes on the intact spheroid. Briefly, a total of 5 x 10^3 SKOV3 cancer cells/ 300 µL of complete media was seeded in a Corning® Spheroid Microplate (used to generate spheroids) with or without the various nanoliposomal formulations at the IC_{50} value. Spheroids were allowed to grow for 48 hours with incubation of the nanoliposomes. Lastly, cells were fluorescently stained with Live/dead™ viability cytotoxicity kit (Thermofisher) for 35 minutes and analysed microscopically.

8.3.8. Assessment of CS-E Biosynthesis by Gene Expression Analysis

Quantitative polymerase chain reactions (qPCR) on GalNAc4S-6ST was conducted on SKOV-3 (test group), HEK 293 (healthy control group) and OVCAR-5 (comparison group) in order to assess the ability of the described systems to knockdown GalNAc4S-6ST gene expression, the primary gene responsible for the biosynthesis of CS-E. Briefly, approximately 2.5 x 10^6 cells in triplicate T25 culture flasks were obtained at confluency,

following serum starvation overnight. Cells were subsequently administered with media only and the various nanoliposomal systems at their respective IC_{50} values for 48 hours as a single dose. RNA was extracted from cell lines using the RNA isolation kit (RNeasy Mini Kit, Qiagen) in accordance with the manufacturer's protocol. Each mRNA sample was quantified using a nanodrop instrument, following visual assessment of the 260/280 and 260/230 ratios which provided insight on the RNA quality. Each cDNA was synthesized from ~2000 ng/µL of the purified total RNA using High-Capacity RNA-to-cDNA™ Kit (Applied biosystems) and an oligo(dT) primer (Inqaba Biotech). Primer sequences used were as follows: GalNAc4S6st (sense: 5-CATCCCCAACAAATTCCTTCC- 3; anti-sense: 5-GCGCAGTGAATAATCAAGCATGC-3) or the GAPDH primers (sense: 5-GGTATCGTGGAAGGACTCAT- 3 anti-sense: 5-ACCACCTGGTGCTCAGTGTA-3). Samples were amplified using the following protocol: 1 minute at 94 °C, 1 minute at 60 °C, and 1 minute at 72 °C for 35 cycles. Quantitative real-time PCR was performed using a *Power* SYBR™ Green PCR Master Mix (applied biosystems) in a Bio RAD C1000 CFX96 Real-time System. The level of GalNAc4S-6ST mRNA was normalized to that of the transcript of GAPDH (ten Dam et al., 2007).

8.4. Results and Discussion

8.4.1. Reactive Oxygen Species (ROS) Determination of the Anti-MUC 16 DDAB Nanoliposomes on SKOV3 cells

The accumulation of ROS in cells induce reactions with a plethora of cellular targets that results in a wide range of pathologies associated with cancer (Waris et al., 2006), featured by structural alterations in DNA sequencing. Such alterations lead to cell death through apoptosis. In addition, ROS may also facilitate the activation of several pro-oncogenes leading to mutations and tumours (Matés et al., 2012). An oxidative stress assay was thus undertaken to ensure the nanoliposomal formulations had minimal ROS accumulation in healthy cells, and to determine if these formulations induced the production of ROS in cancer cells leading to apoptosis. Figure 8.1 highlights the percentages of ROS positive

and negative cells (at the IC_{50} values obtained on SKOV3 cells above). These results suggest the radical-mediated generation of ROS by specific interactions of the NLs and SKOV3 cells. In HEK 293 cells, we observe a considerable change in the percentage of ROS + cells between unfunctionalized DDAB NLs treated cells (21.93%±1.98) and untreated control cells (4.33%±1.02). However, cells treated with anti-MUC 16 functionalized NLs displayed no significant differences in the percentages of ROS+ cells (5%±0.08) ($P>0.05$) when compared to the untreated control (4.33%±1.02). The latter findings strongly validate the targeting and synergistic capabilities of the anti-MUC 16 system in decreasing the production of ROS in healthy cell lines. In the SKOV3 cell lines, an increase in the ROS+ cells between the control (12.49%±0.93) compared to the unfunctionalized DDAB NLs (50.57%±1.17) and functionalized DDAB NLs (20.91±1.57). The generation of ROS can be attributed to the cationic DDAB, as studies have demonstrated that cationic liposomes containing cetyltrimethylammonium bromide (CTAB) can stimulate the formation of oxygenated species, which induce degranulation, release of lactatedehydrogenase, and promote the release of DNA into the external medium (Lotosh et al., 2019). To this end, the anti-MUC 16 DDAB NLs showed a significant difference in the percentages of ROS+ cells between the SKOV3 and HEK 293 cell lines ($P < 0.05$), which suggest the selective induction of cytotoxicity on the more robust cancer cell lines.

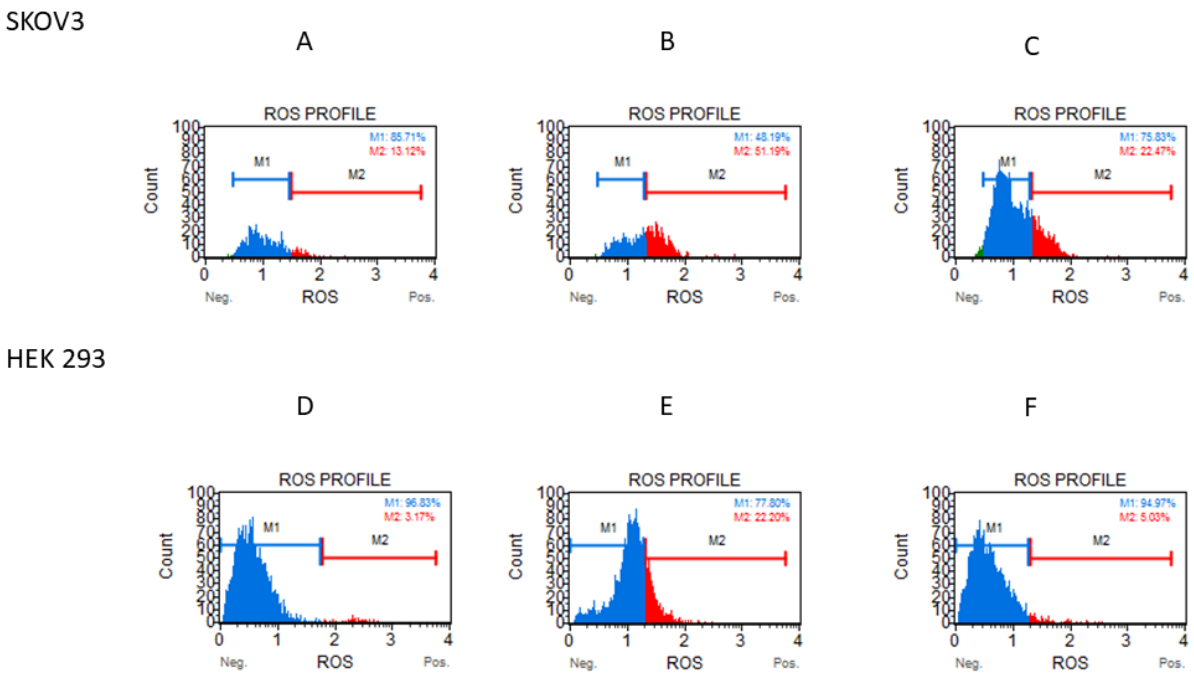

Figure 8.1. Graphical representation of ROS profiles, showing the various percentages of ROS + and ROS – cells treated with the various nanoliposomal formulations. Where A and D are untreated, B and E are treated with DDAB NLs and C and F are treated with Anti-MUC 16 DDAB NLs. A student t test (unpaired) for the percentages of ROS - cells for the anti-MUC 16 DDAB NLs and DDAB NLs against the untreated controls of showed a significance of P = 0.002 and P= 0.00019 for the HEK 293 cell lines respectively, and for the SKOV3 cells; the anti-MUC 16 DDAB NLs displayed a significance P = 0.0001 and the DDAB NLs displayed a significance P= 1.66×10^{-6}.

8.4.2. Determination of the Anti-VEGF Capabilities of Anti-MUC 16 DDAB and 1,12 Diaminododecane Nanoliposomes by ELISA Testing

Growth factor binding to CS in the ECM is an important mechanism regulating tumour growth (Pradeep et al., 2016). CS-E is implicated in VEGF biology by serving as an important binding site for VEGF attachment which is significant for OC angiogenesis. A large variety of growth factors bind to CS-E with strong affinity, these include fibroblast growth factor (FGF)2, FGF10, FGF16, FGF18, heparin-binding epidermal growth factor-

like growth factor (HBEGF), hepatocyte growth factor (HGF), midkine (MDK), pleiotrophin (PTN), platelet derived growth factor (PDGF), and vascular endothelial growth factor (VEGF) (Vallen et al., 2014). This binding of CS-E to VEGF is essential for tumorigenesis and has been associated with the virulent metastatic potential of ovarian tumour cells (Vallen et al., 2012). To this end, assessment of the nanoliposomal potential to arrest and disturb CS-E chains leading to a reduction in VEGF binding was determined (Pradeep et al., 2016). For the SKOV3 cell lines, all nanoliposomal systems showed potential anti-VEGF capabilities seen by a reduction in the amount of VEGF relative to the untreated control (Figure 8.2) at 48 h, with the DDAB NLs and anti-MUC DDAB NLs exhibiting the best reductions in VEGF. Whilst the 1,12 diaminododecane system possessed slightly weaker anti-VEGF capabilities. This could be a consequence of the time dependent process of the crosslinker release and crosslinking mechanism, as opposed to the spontaneous "*on-the-spot*" interactions of DDAB with CS, leading to a PEC. Furthermore, it is also possible for the DDAB system to cause more destructive disturbances to CS-E compared to 1,12 diaminododecane, due to the ability of DDAB to form inclusion complexes seen from ^{1}H NMR data in Chapter 4. To this end, studies have concluded that the effect of CS on the binding and signalling to growth factors is complicated and likely dependent on the CS fine structure (Vallen et al., 2014), which supports the ideology that disturbing CS architectures in addition to HA, which also aids in the accelerated expressions of VEGF (Vitale et al., 2018) has occurred, leading to decreases in the VEGF expressions and cell viabilities observed. Table 8.3 summarises the linear calibration curve parameters.

Table 8.3. Experimental parameters utilized to quantify the expression of VEGF by OD ELISA measurements and VEGF expressions (ng/mL).

Experimental Parameters	Outputs	
Correlation coefficient (r^2)	0.9913	
Slope	0.0009	
Accuracy (%)	99.2%	
Number of samples (n)	2	
	SKOV3 (ng/mL)	**HEK 293 (ng/mL)**
Control	1179.85 ±171.48	190.55±16.49
DDAB	81.11±12.57	
F. DDAB	319.96±342.6	226.11±82.49
CL	638.33±212.92	
F.CL	981.66±291.49	73.88±8.64

where DDAB = DDAB NLs; F. DDAB = Anti-MUC 16 DDAB NLs; CL= 1,12 diaminododecane NLs and F.CL = Anti-MUC 16 1,12 diaminododecane NLs.

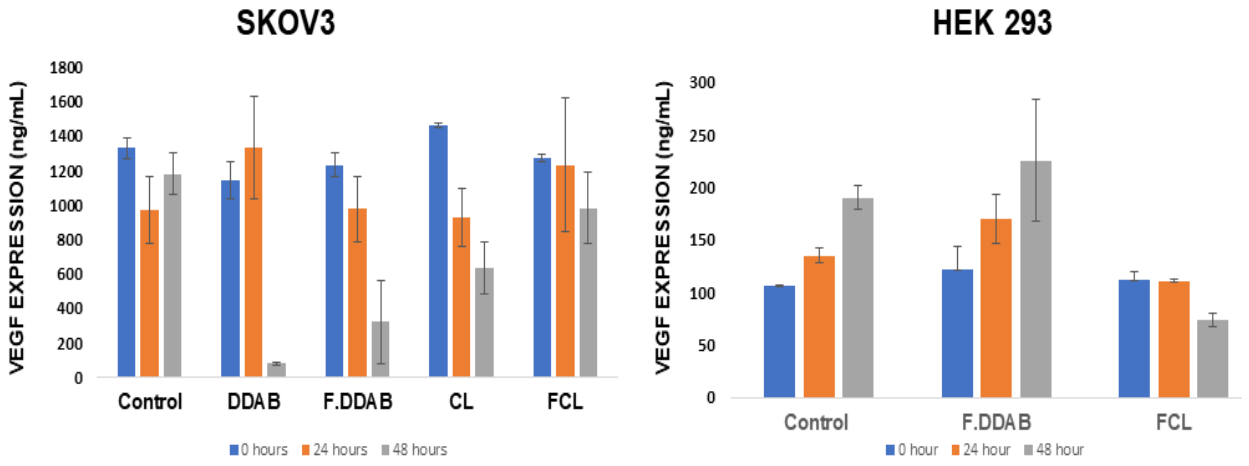

Figure 8.2. Graphical representations of the VEGF levels (ng/mL) of SKOV3 and HEK 293 cell treated with or without the various nanoliposomal formulations (where DDAB = DDAB NLs; F.DDAB = Anti-MUC 16 DDAB NLs; CL= 1,12 diaminododecane NLs and F.CL = Anti-MUC 16 1,12 diaminododecane NLs).

8.4.3. Cytotoxic Evaluation of the Anti-MUC 16 DDAB and 1,12 Diaminododecane Nanoliposomes on 3D Tumour Spheroid Models

Fluorescent microscopy employing the Live/dead™ viability cytotoxicity kit was utilized to identify regions of dead/live cells in the spheroidal architectures (Figure 8.3a and 8.3b). The kit is based on the simultaneous determination of live and dead cells with two probes that measure the recognized parameters of cell viability i.e., intracellular esterase activity and plasma membrane integrity. Ethidium homodimer enters cells with damaged membranes and undergoes a 40-fold enhancement of fluorescence upon binding to nucleic acids, thereby producing a bright red fluorescence in dead cells, with an exclusion of cells that possess intact plasma membranes (live). Each system was administered at the IC_{50} on two models i.e., 1) the effect of tumour spheroid formation in the presence of these systems and 2) the effect of intact tumour spheroidal damage induced by these systems. ImageJ software was utilized to identify the % area of regions of red (dead), which was employed for semi-quantitative analysis to support the imagery (Table 8.4.a and 8.4b). This semi-quantitative analysis is based on the total area of the spheroid which was mapped out using tracing tools in the software, thus, for spheroids that are whole structures (1 single structure) a more accurate measurement as a result of less background, was obtained.

The rationale for developing tumourosphere architectures was to bridge the gap between 2D cell studies and animal models. Malignant cells in advanced OC patients float in ascitic fluid as small cell 3D aggregates, rationalizing the use of 3D cell models to better mimic physiologically relevant scenarios. These cancer cells aggregate metastasis at the surface of internal organs. Therefore, these novel nanoliposomal formulations that displayed prevention of growth of aggregates and control ascites could be of great use in the treatment of advanced OC. The performance of the nanoliposomal formulations revealed that these systems have the ability to interfere with tumourosphere formation and the potential to damage intact stable spheroids, seen by an increase in the amount of non-viable regions (red), reduction in spheroid size and change in the spheroidal morphology. The dead regions seen in the figures below are not a true representation of

the total amount of dead cells. As intact tumourospheres begin to die, the dead cells dislodge from the primary tumourosphere and are lost from the well during the staining process. Nevertheless, a clear change in tumourosphere morphology and size are seen correlating to reductions in viability. This finding could be linked to the arresting of CS-E, as the aggressive CS-E species (and their over-expression in OC) correlates to the development of spheroid formation and metastasis (Pradeep et al., 2016). Thus, inferring that these NLs alter the structural architecture of CS-E, leading to reduction in spheroid formation and cell viability.

Table 8.4.a Semi-Quantitative analysis of the percentage of dead regions (red) in the SKOV3 Tumourospheres, where DDAB= DDAB-NLs and F. DDAB= anti-MUC 16 DDAB NLs.

Intact Spheroid		**Spheroid Formation**	
Sample	**% of red area**	**Sample**	**% of red area**
Untreated	4.643	Untreated	1.518
DDAB	0.665	DDAB	5.677
F. DDAB	27.592	F. DDAB	25.010

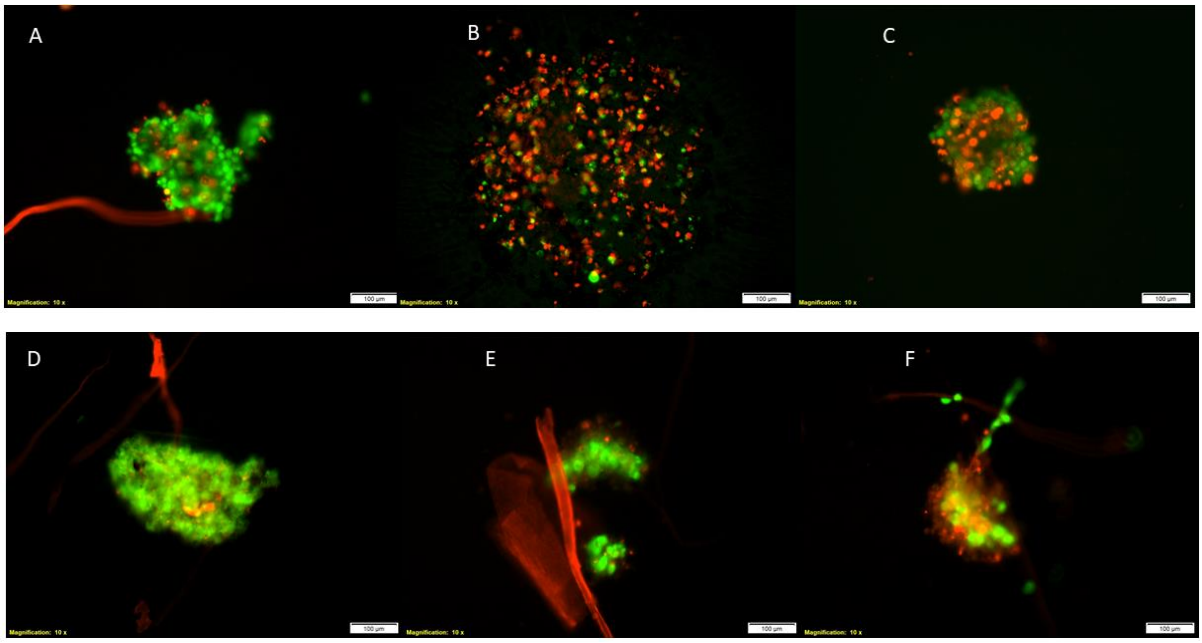

Figure 8.3.a. Photographic illustration SKOV3 Tumourospheres, where A) untreated spheroid, B) DDAB-NLs @ IC_{50} treated spheroid and C) anti-MUC 16 DDAB NLs at IC_{50} was analysed for the effects of spheroid formation in the present of these systems and D) untreated spheroid, E) DDAB-NLs at IC_{50} treated spheroid and F) anti-MUC 16 DDAB NLs at IC_{50} was analysed for the anti-cancer effect of the following systems on intact spheroids (N=1).

Table 8.4.b Semi-Quantitative analysis of the percentage of dead regions(red) in the SKOV3 Tumourospheres, where CL= 1,12 diaminododecane-NLs and F. CL= Anti-MUC 16 diaminododecane-NLs.

Intact Spheroid		**Spheroid Formation**	
Sample	**% of red area**	**Sample**	**% of red area**
Untreated	4.643	Untreated	1.518
CL	29.137	CL	16.134
F. CL	11.98	F. CL	10.89

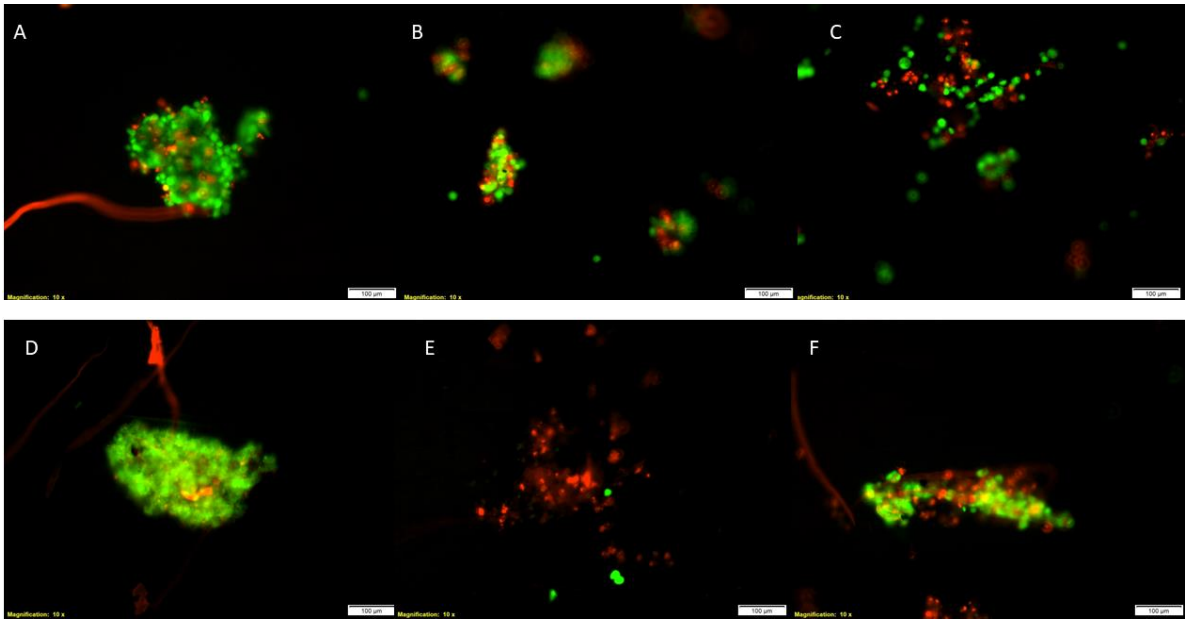

Figure 8.3.b. Photographic illustration SKOV3 Tumourospheres, where A) untreated spheroid, B) diaminododecane -NLs at IC_{50} treated spheroid and C) anti-MUC 16 diaminododecane NLs at IC_{50} was analysed for the effects of spheroid formation in the present of these systems and D) untreated spheroid, E) 1,12 diaminododecane NLs at IC_{50} treated spheroid and F) anti-MUC 16 1,12 diaminododecane NLs at IC_{50} was analysed for the anti-cancer effect of the following systems on intact spheroids (N=1).

8.4.4. GALNAc4S-6ST Gene Expression Analysis

To confirm whether the anti-migratory, proliferative and VEGF effects on SKOV3 cells seen above correlates to the reductions in CS-E levels. The expression of GALNAc4S-6ST in SKOV3 cells was determined and compared to OVCAR-5 and HEK 293 cells. SKOV3 cells were noted previously to have higher expressions of GALNAc4S-6ST when compared to other OVCAR series cell lines (ten Dam et al., 2007). The rationale for this experiment was to determine if GALNAc4S-6ST can interact with the arrested state of CS-A to produce CS-E. In addition, if the CS substrate is less available for GALNAc4S-6ST, it may lead to down regulations of the enzyme. All cells were treated with DDAB-NLs, anti-MUC 16 DDAB-NLs, 1,12 diaminododecane NLs and anti-MUC 16 1,12

diaminododecane NLs in triplicate and at their respective IC_{50} values. At a first glance (Figure 8.4), it is observed that all systems treated on SKOV3 cells show a considerable knockdown in the GalNAc4S-6ST expression compared to the other cell lines. The anti-MUC 16 DDAB-NLs-SKOV3 treated cells produced an 8-fold reduction compared to and 1.3-fold knockdown in HEK293 and a 3-fold reduction in OVCAR 5 cell lines. The 1,12 diaminododecane loaded NLs showed the highest down regulation in SKOV3 cells (10-fold), whilst having the lowest down regulation potential in HEK 293 (1-fold) and OVCAR-5 (1.2-fold), highlighting the usefulness of CS crosslinking in the over-expressed CS cell lines. Therefore, this knockdown of GalNAc4s-6st can be potentially associated with the reductions in CS-E mediated tumour cell viability presented in this and above chapters.

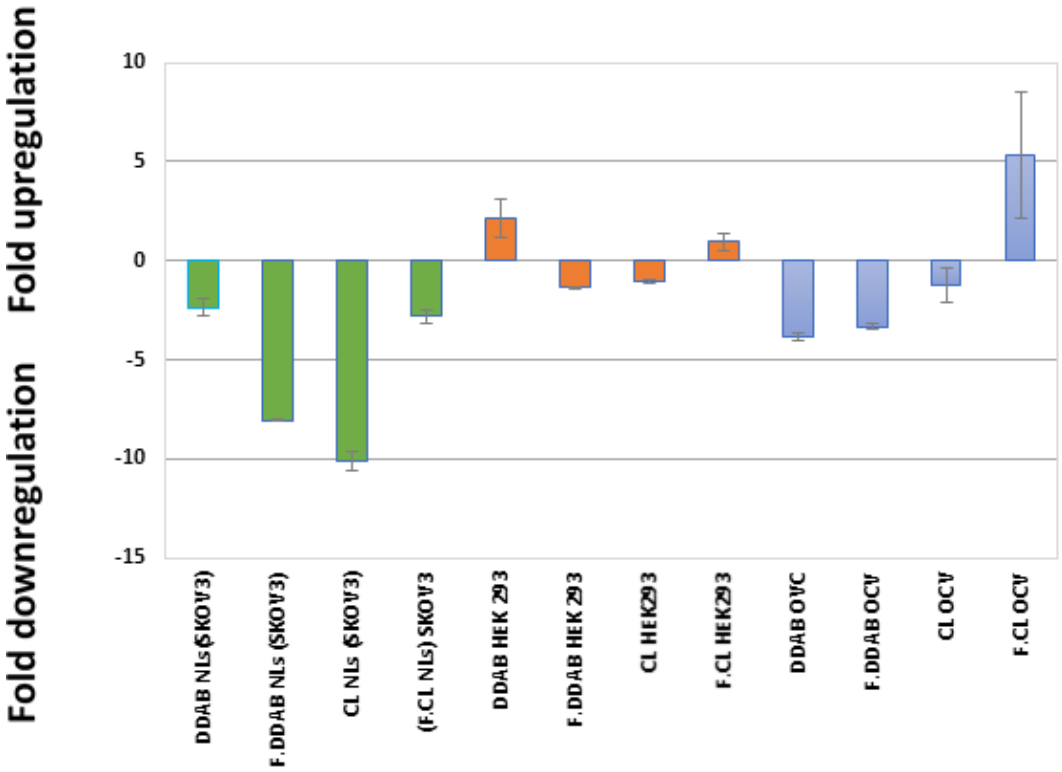

Figure 8.4. Graphical illustration of GalNAc4S-6ST expressions initiated by the various nanoliposomal formulations.

8.5. Conclusions

DDAB and 1,12 diaminododecane were selected as potential against CS-E by an arresting mechanism hypothesized to impede the progression of OC. At this final stage in the establishment of the concept, a dramatic impact of the nanoliposomal formulations on the tumourosphere models was observed. The ability of the systems to inhibit 2D to 3D cell formation is ideal *in vivo*, particularly as tumours assemble in 3D cell aggregates before metastasizing to other organs, yielding an anti-metastasizing effect for the NLs. A further tumour spheroidal deteriorating capability for the NLs was observed, highlighted by a destructive alteration in the size, shape and morphology. The dead cells (seen by red fluorescents) further proved the loss of cell viability and disturbances in the tumourosphere integrity. The hallmark finding was the selective knockdown of these nanoliposomal systems induced on the GalNAc4S-6ST gene expressions in SKOV3 cells (in contrast to OVCAR-5 and HEK 293). This gave insight into the less freely available CS-A species, by their unitization in the chemical arresting mechanism, leading to a down expression in the CS-E biosynthesis and subsequent down expression of CS-E. Reductions in proliferation, migration, and VEGF (seen in Chapters 6 and 7) can thus be correlated to this finding. Overall, a noteworthy cytotoxic performance of the formulated NLs was observed. To this end, there are considerably favourable anti-cancer traits for this system to motivate its utility in a more advanced preclinical animal model.

8.6. References

Bissell, M.J., Radisky, D.C., Rizki, A., Weaver, V.M., Petersen, O.W., 2002. The organizing principle: microenvironmental influences in the normal and malignant breast. Differentiation. 2002, 70, 537–46.

Brown, M.J., Bahsoun, S., Morris, M.A., Akam, E.C., 2019. Determining Conditions for Successful Culture of Multi-Cellular 3D Tumour Spheroids to Investigate the Effect of Mesenchymal Stem Cells on Breast Cancer Cell Invasiveness. Bioengineering. 6, 101.

Brüningk, S. C., Rivens, I., Box, C., Oelfke, U., & Ter Haar, G., 2020. 3D tumour spheroids for the prediction of the effects of radiation and hyperthermia treatments. Scientific reports. 10, 1653.

Cheryl Jia Le, C., 2019. Formation of miniaturized 3D tumour spheroids for drug screening. http://hdl.handle.net/10356/77993.

Enroth, S., Berggrund, M., Lycke, M., et al., 2019. High throughput proteomics identifies a high-accuracy 11 plasma protein biomarker signature for ovarian cancer. Commun Biol. 2, 221.

Han, K., Pierce, S.E., Li, A., et al., 2020. CRISPR screens in cancer spheroids identify 3D growth-specific vulnerabilities. Nature. 580, 136–141.

Huilin, Z., Bingjian, L., 2020. microRNAs as biomarkers of ovarian cancer, Expert Review of AnticancerTherapy. 20, 5, 373385.

Ito, Y., Watanabe, M., Nishizawa, T., Omachi, T., Kobayashi, T., et al., 2007. The utility of formalin-fixed and paraffin-embedded tissue blocks for quantitative analysis of N-acetylgalactosamine 4-sulfate 6-O-sulfotransferase mRNA expressed by colorectal cancer cells. Acta Histochem Cytochem. 40, 53–59.

Kenny, P.A., Bissell, M.J., 2003. Tumor reversion: correction of malignant behavior by microenvironmental cues. Int J Cancer. 107, 688–95.

Ketchen, S., Rohwedder, A., Knipp, S et al., 2020. A novel workflow for three-dimensional analysis of tumour cell migration. Interface Focus. 10, 2042-8898.

Kobayashi, T., Yan, H., Kurahashi, Y., Ito, Y., Maeda, H., et al., 2013. Role of GalNAc4S-6ST in astrocytic tumor progression. PLoS One. 8, e54278.

Lotosh, N.Y., Aliaseva, S.O., Malashenkova, I.K. et al., 2019. Cationic Liposomes Cause ROS Generation and Release of Neutrophil Extracellular Traps. Biochem. Moscow Suppl. Ser. A. 13, 40–49.

Matés, J., Segura, J., Alonso, F. and Márquez, J., 2012. Oxidative stress in apoptosis and cancer: an update. Archives of Toxicology. 86, 1649-1665.

Mizumoto, S., Watanabe, M., Yamada, S., Sugahara, K., 2013. Expression of Nacetylgalactosamine 4-sulfate 6-O-sulfotransferase involved in chondroitin sulfate synthesis is responsible for pulmonary metastasis. Biomed Res Int. 656319.

Mufamadi, M., Choonara, Y., Kumar, P., Modi, G., Naidoo, D., van Vuuren, S., et al., 2013. Ligand-functionalized nanoliposomes for targeted delivery of galantamine. International Journal of Pharmaceutics. 448, 267-281.

Ohtake, S., Ito,Y., Fukuta, M., Habuchi, O., 2001. Human N-acetylgalactosamine 4-sulfate 6-O-sulfotransferase cDNA is related to human B cell recombination activating gene-associated gene. J Biol Chem. 276, 43894–43900.

Pradeep, P., Choonara, Y., Kumar, P., Pillay, V., 2016. “On-The-Spot” Arresting of Chondroitin Sulphate Proteoglycans: Implications for Ovarian Adenocarcinoma Recognition and Intervention. International Journal of Molecular Sciences. 17, 1136.

Safari, M.G., Hosseinkhani, S., 2013. Lipid composition of cationic nanoliposomes implicate on transfection efficiency. Journal of Liposome Research. 23,174-186.

Simmons, A.R., Fourkala, E.O., Gentry-Maharaj, A., Ryan, A., Sutton, M.N., Baggerly K., et al., 2019. Complementary Longitudinal Serum Biomarkers to CA125 for Early Detection of Ovarian Cancer. Cancer Prevention Research. 2019,12, 391-400.

ten Dam, G. B., van de Westerlo, E. M., Purushothaman, A., Stan, R. V., Bulten, J., Sweep, F. C., Massuger, L. F., Sugahara, K., & van Kuppevelt, T. H., 2007. Antibody GD3G7 selected against embryonic glycosaminoglycans defines chondroitin sulfate-E domains highly up-regulated in ovarian cancer and involved in vascular endothelial growth factor binding. The American journal of pathology. 171, 1324–1333.

Vallen, M. J. E., Massuger, L. F. A. G., Ten Dam, G. B., Bulten, J., Van Kuppevelt, T. H., 2012. Highly sulfated chondroitin sulfates, a novel class of prognostic biomarkers in ovarian cancer tissue. Gynecol. Oncol. 127, 202–209.

Vallen, M. J. E., Van Der Steen, S. C. H. A., Van Tilborg, A. A. G., Massuger, L. F. A. G., Van Kuppevelt, T. H., 2014. Sulfated sugars in the extracellular matrix orchestrate ovarian cancer development: “When sweet turns sour.” Gynecol. Oncol. 135, 371–381.

Vitale, D. L., Spinelli, F. M., Del Dago, D., Icardi, A., Demarchi, G., Caon, I., García, M., Bolontrade, M. F., Passi, A., Cristina, C., & Alaniz, L., 2018. Co-treatment of tumor cells with hyaluronan plus doxorubicin affects endothelial cell behavior independently of VEGF expression. Oncotarget. 9, 36585–36602.

Waris, G., & Ahsan, H., 2006. Reactive oxygen species: role in the development of cancer and various chronic conditions. Journal of carcinogenesis. 5, 14.

CHAPTER 9:

1. In vivo Assessment of the Dose Tolerability and Tumour Retardation Potential of DDAB using a SKOV3 Ovarian Cancer Xenografted *Floxn1^{nu}* Athymic Nude Mice Model.

2. In vivo Tumour Growth Retardation Assessment of the Anti-MUC 16 Functionalized DDAB Nanoliposomes on an Advanced Stage Ovarian Cancer Xenografted *Floxn1^{nu}* Athymic Nude Mice Model

9.1. Synopsis of this Chapter

In Chapter 9, an innovative two-model SKOV3 OC cell xenograft pilot study utilizing *Floxn1^{nu}* athymic nude mice was established. The model was designed to validate the potential of the anti-MUC 16 DDAB nanoliposomes (NLs) to retard the growth of ovarian tumours by inhibiting chondroitin sulphate-E (CS-E) glycosaminoglycan (GAG) activity. Two models were employed to screen for therapeutic activity:

Model 1: Assessment of the high (20 mg/kg), medium (10 mg/kg) and low (5 mg/kg) intratumoural (IT) inserts of DDAB using three separate delivery systems viz 1) Anti-MUC 16 functionalized NLs 2) non-functionalized NLs and 3) pristine DDAB in PBS was evaluated for the preferred delivery system based on tolerability and tumour retardation potential. The optimized anti-MUC 16 DDAB NLs at 5 mg/kg yielded the most significant anti-cancer potential (tumour volume = 64 mm^3 for targeted NLs at 5 mg/kg and 305 mm^3 for the unfunctionalized NLs at 5 mg/kg dose at day 21) and most tolerable to mice (with no adverse effects seen to the surrounding organs and local skin reactions in contrast to

the comparison groups). The unfunctionalized delivery of DDAB NLs and pristine DDAB in PBS were both associated with severe skin reactions, histological changes to the surrounding organs and failure to retard the growth of tumours. Thus the 5 mg/kg DDAB incorporated on the anti-MUC 16 functionalized NLs surface was concluded as the preferred delivery system of choice. The hallmark finding, which motivated the utilization of the anti-MUC 16 DDAB NLs at 5 mg/kg for further studies was noted upon histological examination of the tumour tissue for the mouse that received this therapy, showing no signs neoplasm after the 21-day treatment period, in addition to a reduced tumour volume (5 times smaller) than that of the non-functionalized system.

Model 2: Evaluated the chemotherapeutic potential differences between the preferred IT insert of the anti-MUC 16 DDAB NLs and an equivalent dose of IV administered anti-MUC 16 DDAB NLs on late stage ovarian tumours. Tumour inhibition rate (%TIR) analysis revealed that the preferred IT insert inhibited the growth of advanced tumours by 58% in comparison to the IV injection at 5 mg/kg of DDAB, with an overall improved survival time of the mice (1 week increase in mice survival when using the IT insert). In addition, the mice had no considerable histological changes to the surrounding tissue which suggest no significant toxicities for both routes of administration. To this end, the chemotherapeutic potential of DDAB was concluded, as a CS-E targeting nano-injectable insert for paving the way for future OC therapy.

9.2. Introduction

The overall 5-year survival rate of OC is approximately 25% due to disease recurrence and rapid metastasis (Kim et al., 2020). Owing to the complications of conventional chemotherapy discussed at length in the prequel chapters (4,5,6 and 7). A novel anti—MUC 16 functionalized DDAB cationic nanoliposomal archetype was formulated, which was hypothesized to reduce OC activity by inhibiting CS-E proteoglycan activity. The system displayed as a suitable candidate for further studies, thus the crucial question was to ascertain whether the success of this system *in vitro* (seen in chapters 6,7 and 8) can be correlated to an *in vivo* animal model, with specific regard to a retardation of tumour

growth volume (Lu et al., 2010). Furthermore, as a consequence of the novel nature of the delivery system, the subsequent testing in *in vivo* models are vital for new medicine evaluations, with *in vivo* tolerability and targeting of the system as the primary subject/aim of concern (Cohen et al., 2010).

Human derived tumour xenografts implanted subcutaneously into immunosuppressed mice has served an important preclinical stage for the drug development lifecycle for decades (Kelland et al., 2004). Xenograft models are frequently developed by the injection or implantation of human cancer cell lines that thrive in *in vitro* growth cultures (Jin et al., 2010), or by the insertion of primary tumour fragments directly into immunodeficient mice ($Foxn1^{nu}$ are the commonly used species)(HogenEsch et al., 2012). Following novel medicine tolerability establishment, mice models serve as a beneficial predictive indicator for probing of clinical activity by validating new medicines for cytotoxicity and anti-cancer activity (Kelland et al., 2004). In the past, mice xenografts of SKOV3 cells were established (Tong et al., 2014), which gave insight on the system's ability to prolong survival times.

In vivo studies are particularly significant for the local distribution of nanoparticles (NPs) (Xu et al., 2015) and their targeted delivery to tumour sites specifically following IV administration (Panthswa et al., 2020). A plethora of intricate factors dictate the transport of NPs from the tip of the needle to the target sites within the tumour. To elaborate, NPs must firstly enter the bloodstream and evade clearance by renal filtration and the reticuloendothelial system (RES), extravasate through the enlarged endothelial gaps within tumours and penetrate through the dense stroma in the tumour ecosystem to reach the target cells, where an additional factor of retention comes to light (Ernsting et al., 2013). These innate bodily processes add the bulk of the complexity that hinders the systemic delivery and transport of drugs. Furthermore, in contrast to normal blood vessels which feature a tightly sealed endothelium, the tumour vasculature presents with abnormal permeability to NPs with an altered lymphatic drainage system. In addition, low molecular weight drugs can non-selectively diffuse through the endothelial layer of normal tissues, inducing significant toxicity at therapeutic doses (Ernsting et al., 2013). These

factors collectively modulate the ability of NPs to reach the tumour, which are bypassed by intratumoural (IT) insertions (Celikoglu et al., 2008), the latter further supports why *in vivo* models are essential in drug delivery testing for an optimal clinical rather than *in vitro* anticancer significance.

In this two-model pilot study, the preliminary dose tolerability and anticancer activity of DDAB delivered using 1. The anti-MUC 16 NLs, 2. Unfunctionalized DDAB NLs and 3. DDAB in PBS was established in model 1, where a conclusion of the preferred system, based on the least off target effects and most promising chemo potentials (seen by a decrease in tumour volume) was evaluated. The second model involved the testing of the preferred system in an advanced stage tumour. Mesiano and co-workers defined the specifications of advanced SKOV3 ovarian tumours in mouse models (10 to 15 mm in diameter with blood-filled cysts). These tumours are overly aggressive and representative of a late stage III-IV OC patient (Mesiano et al., 1998). This model therefore resembles an ideal clinical simulation, as the majority (>75%) of hospital cases are diagnosed in the advanced stages (Eisenkop et al., 2001). Advanced tumours present as highly virulent, aggressive and widespread (Vallen et al. 2014). The conventional treatment of these tumours is prompt surgery which includes cytoreduction or tumour debulking. Thus, the aim of this chapter was to achieve a delay in the progression of these advanced tumours to allow for an increase in the survival times in order for prompt surgical procedures to be selected and conducted (Lengyel et al., 2010).

9.3 Materials and Methods

9.3.1. Animal Husbandry and Athymic Nude Mice Specifications

Female athymic nude mice (15-20 grams, n=16) were obtained from University of Cape Town (UCT) animal unit. These mice were sourced from the Jackson Laboratory as NU/J (002019) and maintained in the SPF Rodent Production Unit. The mice have a specific *Floxn1*^{nu} genotype. Mice were housed in a sterile unit at the Central Animal Services (CAS) Unit of the University of the Witwatersrand (Wits) in individual cages, with free access to food and water at all times. All mice were maintained in a temperature and

humidity-controlled environment in a 12 h light/12 h dark cycle. Mice were monitored twice a day and weighed once a week to indicate their general state of well-being. All the animal procedures including surgeries were conducted in accordance with stringent SOPs established by the CAS Unit, in addition to practices prescribed by the Animal Ethics Screening Committee (AESC) of Wits University.

9.3.2. *In Vivo* Experimental Design

Two pilot studies were conducted on the same human-derived SKOV3 ovarian carcinoma xenograft athymic nude mice models, both of which were intervention studies shown in Tables 9.1.a and b. Study 1 (Figure 9.1) aimed to select the ideal DDAB delivery system/Vehicle and dose, based on tolerability and anti-cancer activity of an IT insertion (5,10 and 20 mg/kg) loaded into separate formulations (i.e. pure DDAB in PBS, DDAB-loaded NLs and anti-MUC 16 functionalized DDAB NLs) on 9 mice (n=3). Study 2 (Figure 9.2) was conducted to assess the effect of the anti-MUC 16 DDAB NLs at 2.5 mg/kg and 5 mg/kg on Stage 4 OC tumours. At random, each dose was administered to two mice (n=2) either IV or IT.

Table 9.1.a. Showing the various mice, dose and form and formulation types used in model 1.

Mice ID	Dose (mg/kg)	Formulation Type
5,6, 7	5,10,20 respectively	DDAB in Anti-MUC 16 NLs
8,9,10	5,10,20 respectively	DDAB in NLs
11,12,14	5,10,20 respectively	DDAB in PBS
25	Untreated control	Untreated control

Table 9.1.b. Showing the various mice, DDAB dosages and routes of administrations used in model 2.

Mice Number	Dose (mg/kg)	Formulation type	Injection site
1	5	DDAB in Anti-MUC 16 NLs	IT
2	5	DDAB in Anti-MUC 16 NLs	IV
3	2.5	DDAB in Anti-MUC 16 NLs	IT

4	Control	Untreated Control	Untreated Control
5	2.5	DDAB in Anti-MUC 16 NLs	IV

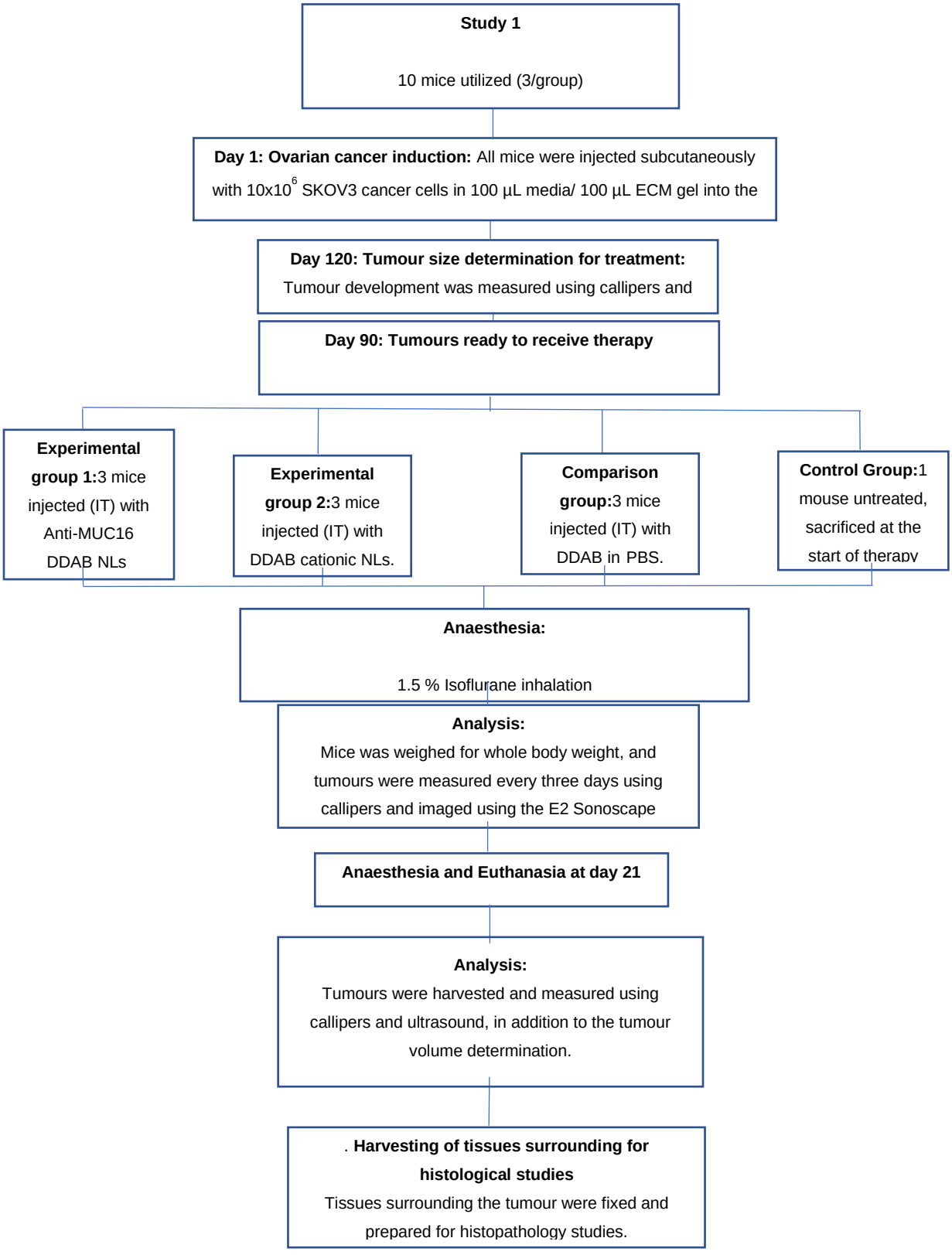

Figure 9.1. Study outline/protocol for model 1.

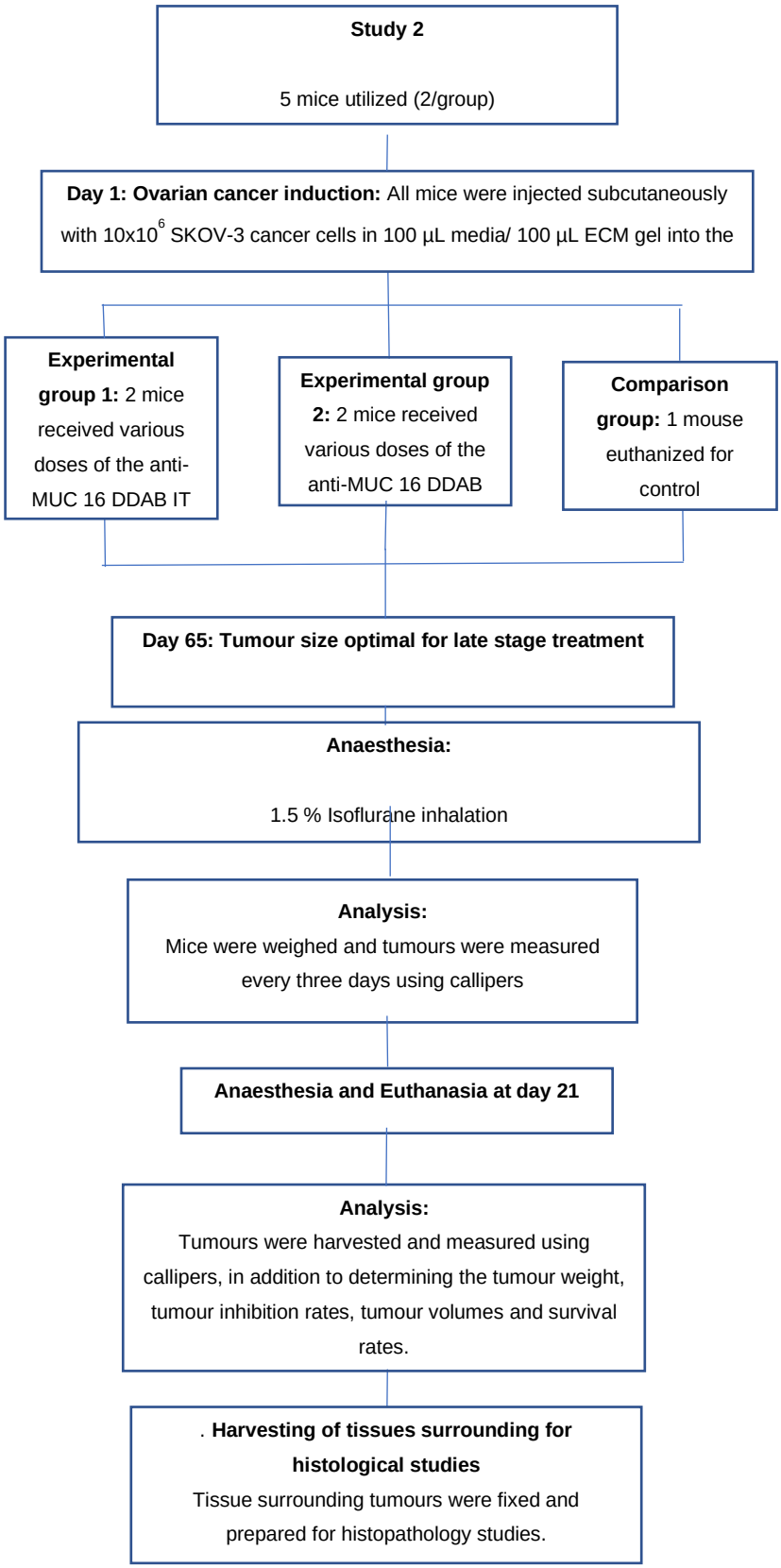

Figure 9.2. Study outline/protocol for model 2.

9.3.3. Induction of Human Ovarian Carcinoma in Athymic Nude Mice by SKOV3 Subcutaneous Xerograph

All mice were restrained and injected subcutaneously with approximately 10 x 10^6 SKOV3 cancer cells in 100 µL media and 100 µL of matrigel (Sigma Aldrich, St. Louis, Missouri, United States) into the peri-tumoural regions of the mice (Noori et al., 2014). This was to establish an *in vivo* tumour for the chemotherapeutic efficacy evaluation of the designed nanosystems. SKOV3 inoculation was achieved using a 26 G needle attached to a 0.5 mL syringe. Following injections (three times for study 1, once for study 2) the mice were maintained in the CAS unit until tumours developed to a target volume of 30-60 mm3 measured using pre-calibrated digital v callipers (accuracy of 0.02 mm) and ultrasound (Zhou et al., 2007).

9.3.4. Assessment of the Tumour Volume, Ultrasound Imagery and Mice Weight Transition Analysis

Mice were assessed twice a week for tumour growth based on visual assessments and volume measurements. For all subcutaneous tumours, two perpendicular measurements were obtained from which an estimate of tumour radius was derived. The tumour volume was calculated using Equation 9.1:

Eq. 9.1. $$tumour\ volume\ = L\ x\ W^2\ x\ 0.52 \ldots$$

Where L and W are the longest and shortest diameters of the tumour respectively (Noori et al., 2014) for constructing tumour growth curves (Shen et al., 2015).

Following the 21-day treatment period and surgical removal of the tumours, tumours were fixed in formalin until histopathological evaluation. The anti-tumour activity from each

treatment was evaluated on the basis of the tumour inhibition rate (TIR [%]) calculated using Equation 9.2 (Liu et al., 2011):

Eq. 9.2. $$TIR\ (\%) = \frac{mean\ weight\ of\ tumour\ in\ treatment\ group\ mean\ (g)}{weight\ of\ tumour\ in\ comparison\ group\ (g)} \times 100$$

To confirm and monitor the presence of tumours, the internal growth of tumours were noninvasively assessed using ultrasound imagery (Wirtzfeld et al., 2005). Briefly, mice were anesthetized using 1.5 % isoflurane and imaged using the E2 Sonoscape Ultrasound (SonoScape, Co., Ltd, Shenzhen, China).

Mice were weighed weekly and assessed twice a day to ascertain behavioural and physical changes before and after tumour/treatment induction to gain insight into the overall wellbeing of the tumour-bearing mice. Mice that decreased in weight >15% were prematurely terminated from study. Sickly behaviour and clearly noticeable side-effects such as neutropenia, uncontrolled anaphylaxis or physical distress also lead to the premature termination of the mice.

9.3.5. Chemotherapeutic activity of DDAB in Ovarian Carcinoma Athymic Mice Models

For the intervention study in Model 1, mice were treated when the tumour volume ranged between 30-60 mm^3. Mice were restrained and injected with 5,10 and 20 mg/kg of DDAB into a palpable tumour mass in 200 µL of sterilized PBS (Table 9.1A). Mice were injected every 3rd day for a period of 21 days (7 treatments in total) and the tumour volumes were measured. For the second intervention study in Model 2, tumours were allowed to grow until a size >200 mm^3.The mice were divided into 2 groups (i.e. IV and IT dosing) and administered 2.5 and 5 mg/kg of DDAB in the anti-MUC 16 NLs in 100 µL of sterilized PBS. Mice were assessed daily for side-effects or adverse reactions.

9.3.6. Histopathological Analysis of Tumours and Overall Dose Tolerability

Following the 21-day treatment period, mice were euthanized by phenobarbital overdose and organs viz. the heart, liver, kidney and tumours were harvested for histopathological analysis. Formalin-fixed, paraffin-embedded (FFPE) organs from the treatment groups were sectioned at 3-4 μm and routinely stained with Haematoxylin and Eosin (H&E) and analysed for histological changes relative to the untreated mouse.

9.4. Results and Discussion

9.4.1. Assessment of the Chemotherapy Efficacy and Dose Tolerability of DDAB in Separate Delivery Systems and Doses (Model 1)

The chemotherapeutic efficacy of the anti-MUC 16 DDAB NLs was compared against the non-functionalized DDAB NLs and pure DDAB in PBS, dosed via a IT insertion. A variety of indices were assessed to conclude the performances of the system including 1. tumour volume measurements 2. mouse weight transitions and 3. histopathology of the tumours and surrounding organs (liver, kidney and heart tissue).

9.4.1.1. Tumour Volume Retardation Potential of DDAB on Human Ovarian Carcinoma Mice Model

The chemotherapeutic efficacy of 3 doses of DDAB from 3 different formulations (Anti MUC 16 Functionalized DDAB NLs, Non-functionalized NLs and DDAB in PBS) administered to 9 mice were assessed by measuring tumour volumes (Table 9.2). Tumour volume comparison of mice that received the 5 mg/kg DDAB dose at day 21 is shown in Figure 9.3 with the photographic and ultrasound imagery in Figures 9.4 and 9.5, respectively. The mouse that received the 5 mg/kg dose of DDAB-loaded anti-MUC 16 NLs outperformed the equivalent dose of the non-functionalized NLs (64 mm3 vs. 305 mm^3 at day 21). Aggressive tumour growth between day 16 and day 21 of the treatment period was observed for the unfunctionalized DDAB mouse receiving 5 mg/ kg, further

revealing a tumour volume 5 times larger than the mouse receiving an equivalent dose of the anti-MUC 16 NLs at day 21, demonstrating the enhanced chemotherapeutic efficacy of the optimized (and functionalized) nanosystem.

9.4.1.2. Tumour histological examinations

Upon histological analysis (Figure 9.6) of the tumours, the mouse that received the optimized 5 mg/kg-anti-MUC 16 DDAB NLs did not present with signs of neoplasm in the tissue samples presented for analysis. This confirmed the chemotherapeutic potential of the nanosystem. In contrast, the mass within the connective tissue of the mouse that received the 5 mg/kg DDAB non-functionalized-NLs presented with a -demarcated and thinly encapsulated wall. It further displayed cuboidal to oval epithelial cells with multifocally forming tubular structures. Tubules and ribbons were present, separated by fine fibrovascular stroma. Palisading around blood vessels was present and nuclei were apically arranged in these areas. The neoplastic cells displayed moderate anisonucleosis with round to oval vesicular euchromatic nuclei containing single or double small nucleoli and showing fine chromatin stippling. Approximately 2 to 4 mitoses were present per high-power field (Figure 9.6). The cytoplasm was scant to moderate in amount and moderately eosinophilic in appearance. However, necrosis was not visible in the mass, potentially suggesting there was no significant cytotoxic effect of the system to the tumour. The adjacent connective tissue contained focal haemorrhages, which is potentially due to the non-targeting nature of the NLs. The tumour sample for the mouse that received 5 mg/kg-DDAB/PBS presented with a tumour mass similar to the mouse that received the unfunctionalized DDAB system, with highly prominent tubular structures. The mitotic rate was between 5 and 6 per high-power field with several abnormal mitoses present.

Overall assessment of the histology of the tumours indicated that features of the masses in the mice were typical for solid epithelial neoplasia, thus concluding the virulent carcinoma model. It is thus compatible with the cell line utilized in the study (ovarian carcinoma, SKOV3). The features of the neoplastic cells and growth pattern (solid) were similar in all individuals, with mild or absent tubule formation including the untreated control.

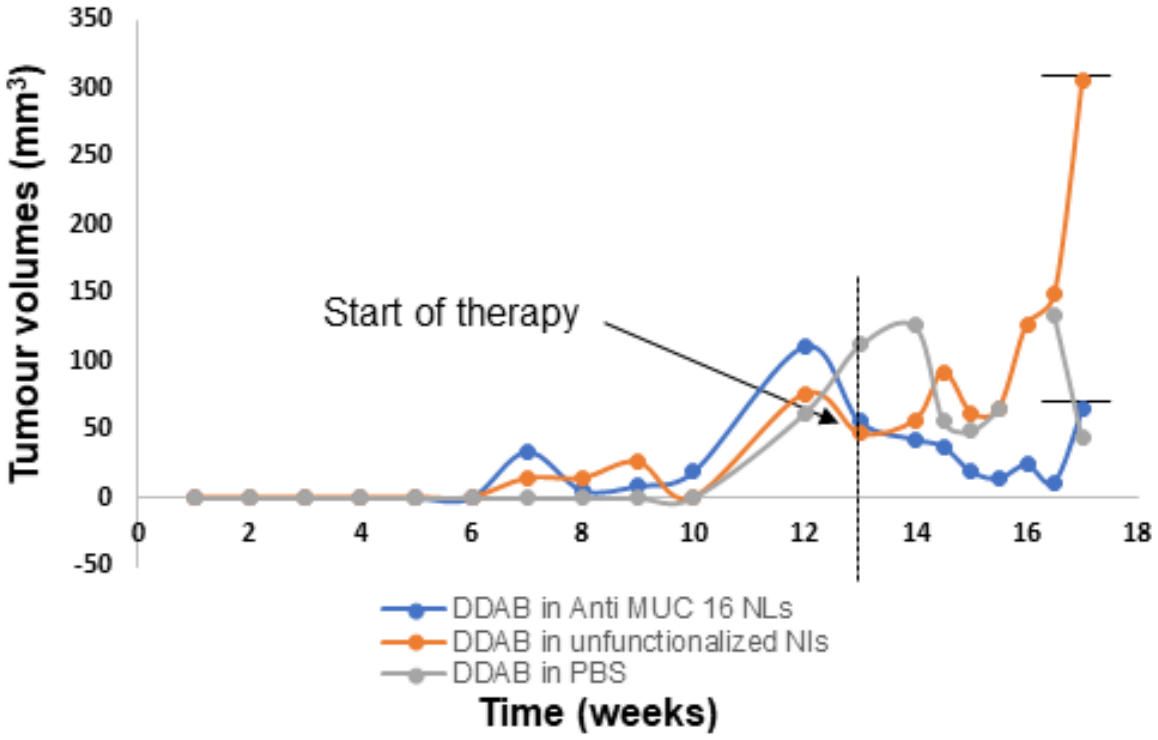

Figure 9.3. Graphical comparison of tumour volumes of mice that received 5 mg/kg DDAB within the various formulations.

Table 9.2.a. Tumour volumes and physical assessment of the mice in response to the anti-MUC16 DDAB NLs therapy.

	Mouse ID #5 (5 mg/kg)		Mouse ID #6 (10 mg/kg)		Mouse ID #7 (20 mg/Kg)	
Injection number	**Tumour Volume**	**Response**	**Tumour Volume**	**Response**	**Tumour Volume**	**Response**
1	V= 43.3 mm^3	NR	53.7 mm^3	NR	755 mm^3	NR
2	V= 37,72 mm^3	NR	67.7 mm^3	NR	1090 mm^3	NR
3	V = 19.7 mm^3	NR	45.45 mm^3	NR	898 mm^3	NR
4	V = 14.4 mm^3	NR	19.9 mm^3	NR	1318 mm^3	NR
5	V= 24.5 mm^3	NR	Terminated	abdominal distension	1123 mm^3	NR
6	V = 11.7 mm^3	NR	Terminated		1730 mm^3	NR
7	V= 64.74 mm^3	NR	Terminated		2554 mm^3	NR

***NR** = No response based on behaviour or physical signs of distress.

Table 9.2.b. Tumour volumes and physical assessment of the mice in response to the unfunctionalized DDAB NLs therapy.

	Mouse ID #8 (5 mg/kg)		**Mouse ID #9 (10 mg/kg)**		**Mouse ID #10 (20 mg/Kg)**	
Injection number	**Tumour Volume**	**Response**	**Tumour Volume**	**Response**	**Tumour Volume**	**Response**
1	V= 57.5 mm^3	NR	123 mm^3	NR	71.5 mm^3	NR
2	V= 92 mm^3	Local Hematoma around the tumour	101 mm^3	NR	35.67 mm^3	NR
3	V =62 mm^3	Necrotic skin reaction around the tumour	110 mm^3	NR	43mm^3	NR
4	V =65 mm^3	Healed	65 mm^3	NR	24 mm^3	NR
5	V= 127 mm^3	NR	65 mm^3	NR	147 mm^3	NR
6	V =149 mm^3	NR	352 mm^3	NR	336 mm^3	NR
7	V= 305 mm^3	NR	608 mm^3	NR	253 mm^3	NR

***NR** = No response based on behaviour or physical signs of distress.

Table 9.2.c. Tumour volumes and physical assessment of the mice in response to the DDAB in PBS therapy.

	Mouse ID #11 (5 mg/kg)		Mouse ID #12 (10 mg/kg)		Mouse ID #14 (20 mg/Kg)	
Injection number	**Tumour Volume**	**Response**	**Tumour Volume**	**Response**	**Tumour Volume**	**Response**
1	V= 126 mm^3	NR	137 mm^3	NR	0 mm^3	NR
2	V= 56.3 mm^3	NR	137 mm^3	NR	90 mm^3	NR
3	V = 49 mm^3	Severe local scab		Sever local skin reaction	132 mm^3	NR
4	V =65mm^3	Scab	26mm^3	local skin reaction	24 mm^3	NR
5		Scab	229 mm^3	local skin reaction		Severe skin reaction and abdominal distension
6	V =134 mm^3	Healed	406 mm^3	Healing	97 mm^3	Severe skin reaction and abdominal distension
7	V=44 mm^3	NR	143 mm^3	NR	Terminated	

***NR** = No response based on behaviour or physical signs of distress.



Figure 9.4. Photographic imagery of mice that received 5 mg/kg of DDAB in different delivery systems. Where **A** represents the mouse that received the anti-MUC 16 NLs; (left image = day 1 of therapy, middle image = day 21 and right image = post-mortem image of tumour at day 21). **B)** represents the mouse that received the DDAB in unfunctionalized NLs; (left image = day 1 of therapy, middle image = day 21 and right image = post-mortem image of tumour at day 21). **C)** represents the mouse that received DDAB in PBS; (left image = day 1 of therapy, middle image = day 21 and right image = post-mortem image of tumour at day 21).

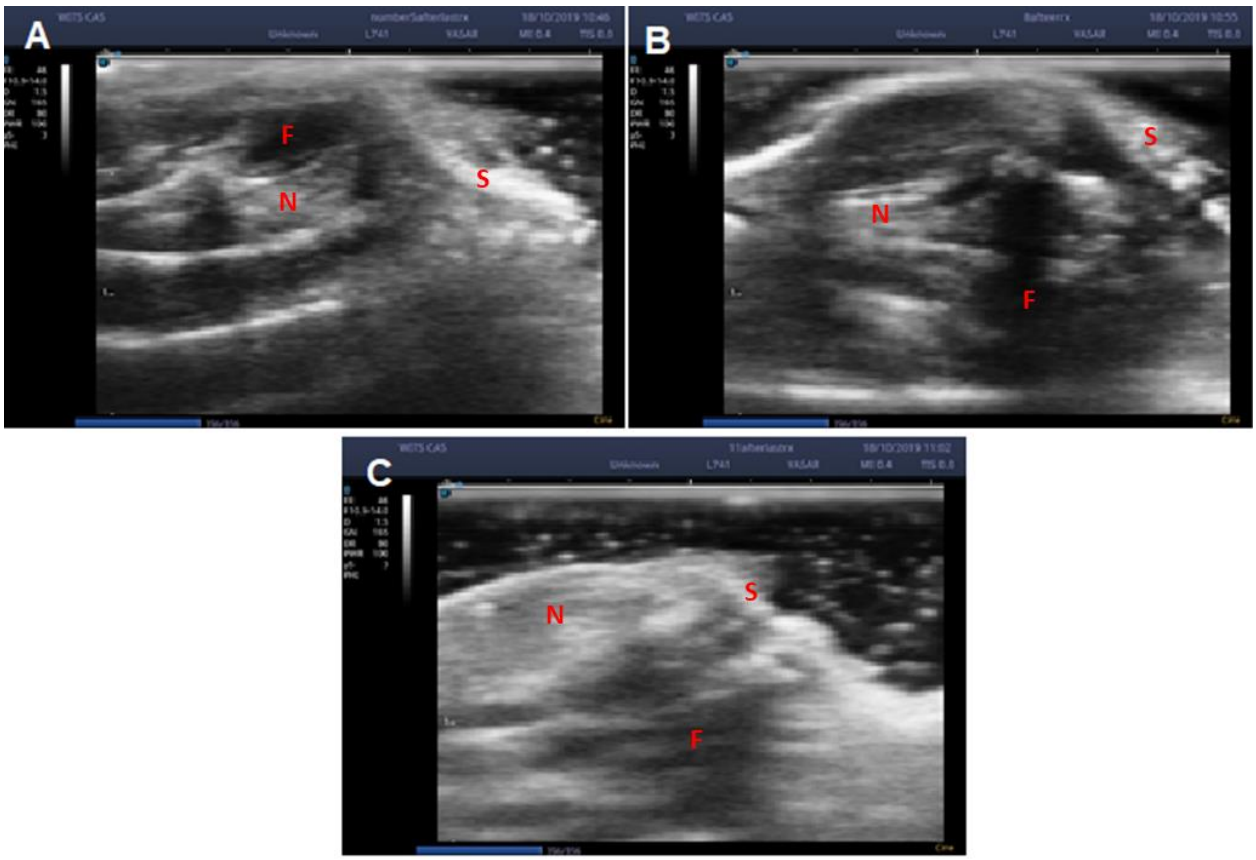

*__N__= Solid Nodule, __S__= Septa and __F__ = Fluid layer

Figure 9.5. Ultrasound imagery for the detection of the internal formation of tumour development between the mice that received the 5 mg/kg of DDAB in the various formulations following the 21-day treatment period. Where **A** represents the mouse that received the anti-MUC 16 NLs, **B** represents the mouse that received the DDAB in unfunctionalized NLs and **C** represents the mouse that received DDAB in PBS. The overlying subcutaneous fat demarcating the tumour appeared relatively hyperechoic on the sonogram (seen to outline the tumour). The tumour mass shows distinct signs of echogenicity changes represented by the letters annotated on the image. This image served to preliminary prove that the tumours were present internally before classification by means of histology.

9.4.1.3. Dose Toxicity and Tolerability Evaluation of DDAB on Athymic Nude Mice by Means of Physical Appearance and Histological Analysis

This section of the study aimed at assessing the effects of the DDAB therapy utilizing separate means of delivery to select the delivery approach with the least disturbances to healthy organs such as the kidney and liver (Table 9.3; Figure 9.6)

Table 9.3. A summary of the various histological changes of the mice that received the 5 mg/kg of DDAB using separate systems.

Untreated Control			
Physical signs of treatment adverse effects	**Liver**	**Kidney**	**Heart**
Normal Appearance	Normal Appearance	Normal Appearance	Normal Appearance
Mice ID #5 (5 mg/kg IT insert dose of the Anti-MUC 16 DDAB NLs)			
Normal appearance	Normal Appearance	Normal Appearance	Normal Appearance
Mice ID #9 (5mg/kg IT insert dose of the unfunctionalized DDAB NLs)			
Skin rash on the face and abdomen (Fig 9.7A)	Hepatocytes appeared mildly and diffusely swollen with mildly granular cytoplasm. In one area the attached mesenteric adipose tissue contains mild focal lymphocytic interstitial infiltration (Fig 9.6)	The kidney tissue displayed scattered bowman's spaces and few tubular lumens containing eosinophilic proteinaceous material. The hepatocytes appeared mildly and diffusely swollen with a mildly granular cytoplasm.	A few areas, the endocardium and underlying myocardial interstitium contain scattered single lymphocytes. In areas myocardial fibres are mildly hyalinised with increased eosinophilia and a smudged appearance of the cytoplasm

Mouse ID #11 (5 mg/kg IT dose of DDAB/PBS)			
Local skin irritation seen by a scab like rash	Normal appearance	The kidney appeared to have scattered tubular epithelial cells with increased eosinophilic cytoplasm, although they were not swollen. A granular appearance of the cytoplasm of hepatocytes diffusely appeared in the liver	scattered fibres had a mildly hyalinised cytoplasm

---

From the above table, the anti-MUC 16 DDAB NLs IT insert showed to have minimal effects on the surrounding tissue, which is essential for its role as a targeted drug delivery system. A clear benefit of targeting was observed.

The 10 and 20 mg/kg dose of unfunctionalized DDAB NLs

- *Adverse skin reactions*

no considerable changes to the organs was noted

- *The kidney*

No significant changers

- *The liver*

No significant histological changes

- *The heart*

Normal histological appearance was observed for the mice in the 10 mg/kg group, with an presence of scattered fibres that have mildly hyalinised cytoplasmic region for the 20 mg/kg

The lack of significant changes seen by the higher doses of unfunctionalized DDAB NLs can be potentially explained by the surfactant nature of DDAB, and their ability to form micelles and aggregate to different components of affinity, based on their state (Mehta et al., 2008). Once DDAB comes into contact with the aqueous portion of the tumour, the hydrophilic parts of DDAB are exposed and concentrate in the hydrophilic compartments. At low DDAB concentrations (below the critical micelle concentrations), DDAB dissociates from the NLs and could potentially be taken up in the serum as single stranded DDAB chains. The higher DDAB concentrations facilitates the orientation of DDAB into a lower free energy and stable micelle state (Owen et al., 2012), which could potentially explain the reduced adverse effects at higher DDAB concentrations due to the higher tumour retention potential of the micelle (Xiao et al., 2017).

The 10-20 mg/kg dose of DDAB/PBS

- *Adverse skin reaction*

For mice receiving DDAB in PBS, all doses (3/3) reacted with severe adverse skin conditions, which lead to the development of scab formation. For the mouse that received the 5 mg/kg, this was seen early in the injection period (within the first week). However, the mouse was shortly able to recover. The mouse that received the 10 mg/Kg of DDAB in PBS showed a severe skin reaction that was presented with scar-like tissue on the lower abdomen (Figure 9.7B).

- *The kidney*

These mice appeared to have scattered tubular epithelial cells with increased eosinophilic cytoplasm, although they were not swollen.

- *The liver*

Appeared normal

- *The heart*

Presented with scattered fibres which have mildly hyalinised cytoplasm.

Mouse #14 was immediately terminated due to a severe skin reaction and was consequently euthanized based on overall behavioural changes and weight loss. The post-mortem revealed a severely distended abdomen, with abnormal lung and liver congestion. A study reported by Zhang and co-workers discovered that lipoplex's (a positively charged complex) formed aggregates in serum, leading to transient embolism in the lungs (Zhang et al., 2005), this may have been caused when DDAB leaked out of the tumour and entered the bloodstream and extravasated into the lung of the mouse. Furthermore, the leaking and evading of DDAB into the gastrointestinal tract lead to abdominal distension and faecal impaction.

The 10-20 mg/kg dose of the anti-MUC 16 DDAB NLs

The mouse that received 10 mg/kg was also euthanized during the study, despite being treated with a targeted system. The DDAB dose of 10 mg/kg was likely associated with adverse effects. Upon post-mortem, this mouse was seen to have faecal impaction, and was terminated due to abdominal discomfort, however all other organs presented with a normal appearance.

To this end, it was concluded from these findings that the anti-MUC 16 delivery vehicle was associated with the least adverse effects to surrounding tissue (dose of 5 mg/kg) and the most suitable and preferred choice for chemotherapy.

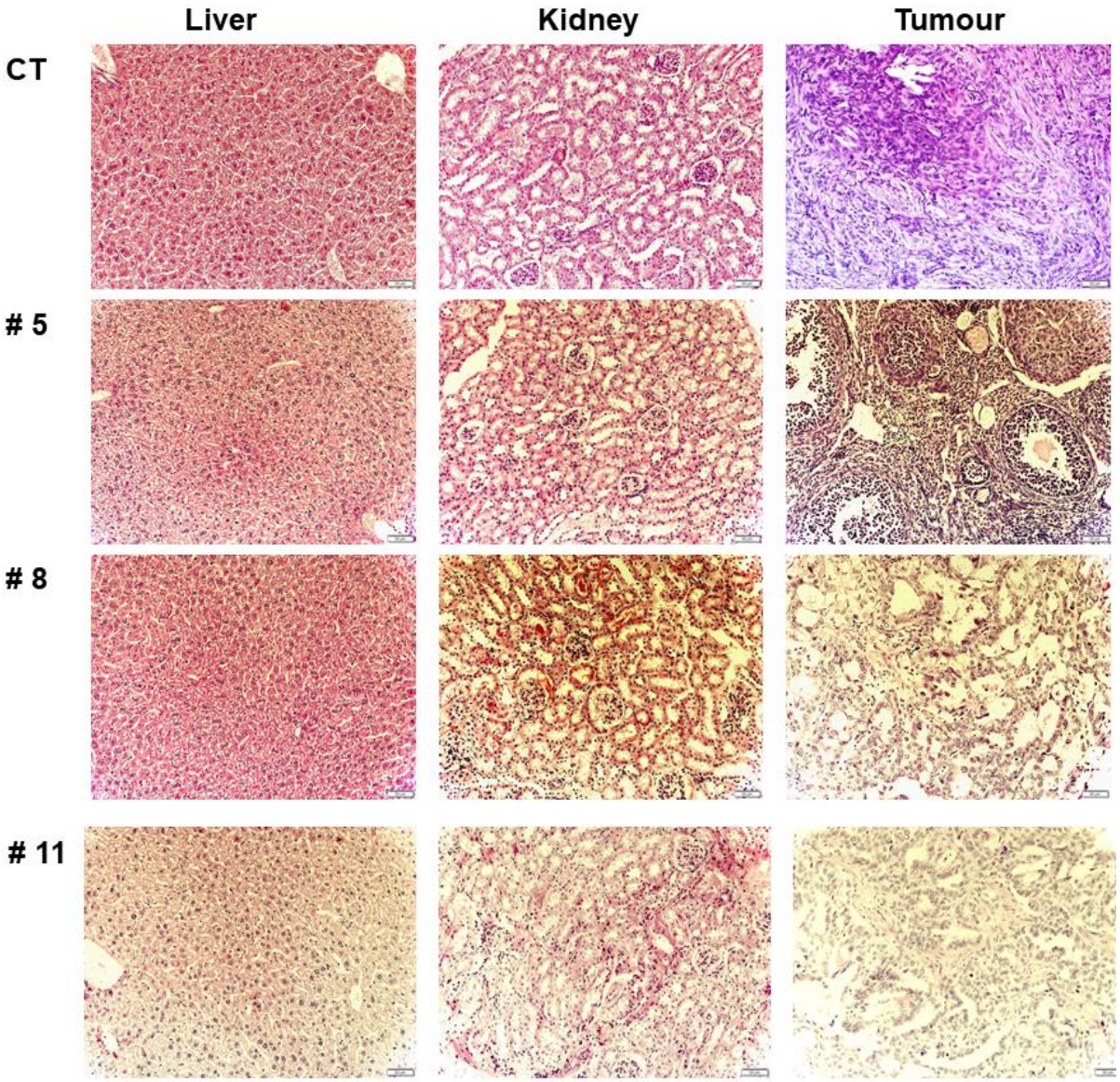

Figure 9.6. Histopathological images of the liver, kidney and tumour tissue of the mice that received the 5 mg/kg DDAB in separate delivery systems at 20x magnification. Where CT= untreated mouse.

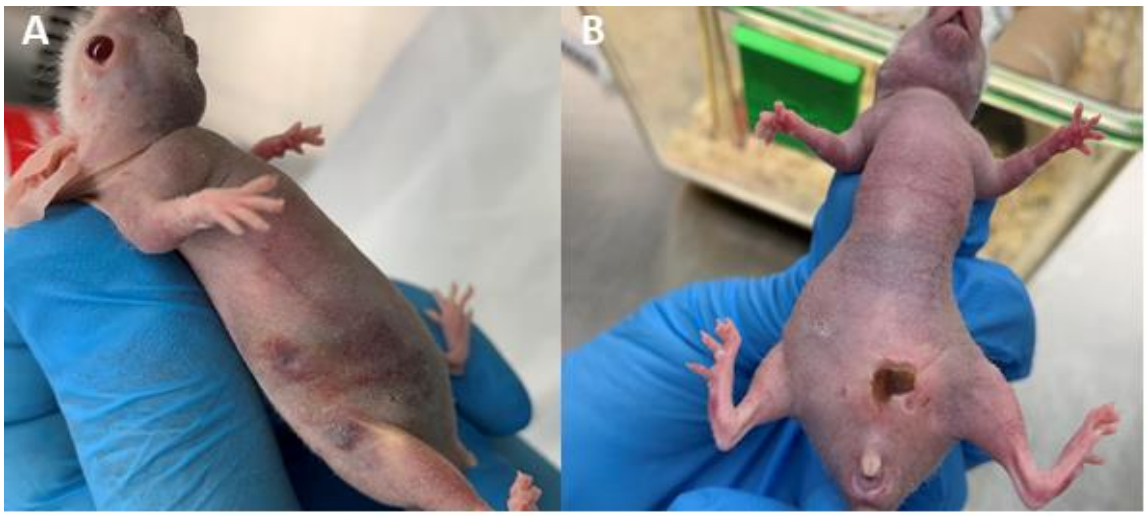

Figure 9.7. A) Photographic imagery of the mouse that received 5 mg/kg-DDAB unfunctionalized NLs which presented with a skin reaction and **B)** the mouse that received 10 mg/kg of DDAB/PBS that presented with a severe skin reaction.

9.4.1.3. Mice Weight Evaluations on Athymic Mice

Body weight of newly born mice typically increases in the early and late postnatal development up to 1 year of age (Rudolph et al., 1999), thus these 4-6-week-old mice are expected to show a healthy and gradual increase in weight as part of their normal growth and development. Table 9.4. summarises the various weights of each mice that are receiving DDAB therapy at various doses and means delivery systems. Mouse #14 (20 mg/kg; DDAB/PBS group) revealed a massive reduction in weight, observed since therapy began (~3 g loss in weight [~17%]), this mouse was thus promptly terminated before the end of the study as a result. This mouse was further associated with a severe skin reaction and abdominal distension, which was possibly due to the toxic nature of the unprotected (not housed in NLs) DDAB. This highlights the effectiveness of the anti-MUC 16 DDAB NLs therapy. All other mice in the study appeared to have a steady increase or maintenance of weight as a function of age throughout the 21-day period (Kapla-Lefko et al., 2003).

Table 9.4.A. Showing the various mice weights in the anti-MUC 16 DDAB NLs treatment group.

Week	Mice weight (g) in the anti-MUC 16 DDAB NLs group		
	Mouse #5 (5 mg/kg)	Mouse #6 (10 mg/kg)	Mouse #7 (20 mg/kg)
1 (before therapy)	24.79	22.2	22.7
2 (start therapy)	24.75	23.22	23.12
3 (middle therapy)	25.54	Terminated	23.3
4 (end therapy)	24.53	Terminated	26.5

Table 9.4.B. Showing the various mice weights in the unfunctionalized DDAB NLs treatment group.

Week	Mice weight (g) in the DDAB NLs group		
	Mouse #8 (5 mg/kg)	Mouse #9 (10 mg/kg)	Mouse #10 (20 mg/kg)
1 (before therapy)	24.3	24.12	21.96
2 (start therapy)	25.22	24.17	22.93
3 (middle therapy)	25.68	24.57	23.16
4 (end therapy)	23.39	24.54	23.96

Table 9.4.C. Showing the various mice weight in the DDAB/PBS treatment group.

Week	Mice weight (g) in the DDAB/PBS group		
	Mouse #11 (5 mg/kg)	Mouse #12 (10 mg/kg)	Mouse #14 (20 mg/kg)
1 (before therapy)	21.42	24.14	20.7
2 (start therapy)	22.48	25.82	22.4
3 (middle therapy)	22.89	25.55	22.75
4 (end therapy)	23.11	25.50	17.2

9.4.2. Assessment of the Chemotherapeutic Potential of the Anti-MUC 16 DDAB NLs on Advanced Stage 4 OC Tumours (Model 2)

The chemotherapeutic efficacy of the IT insert of the preferred anti-MUC 16 DDAB NLs was compared against an equivalent dose (i.e., 2.5 mg/kg and 5 mg/kg) of an IV administration of the same anti-MUC 16 DDAB NLs. A variety of indices was assessed including 1. tumour volume (measured with callipers), 2. tumour inhibition rates (%TIR), 3. histopathology of the tumour tissues and 4. survival analysis curves.

9.4.2.1. Determination of the Tumour Retardation Potential of the Anti-MUC 16 DDAB NLs in both IV and IT Administrations

The growth retardation of the optimized IT anti-MUC 16 DDAB nanoliposomal insert was compared against an equivalent IV dose (Figure 9.8 and 9.9). Despite identical systems, the path for the NLs to reach the target stroma and cellular surface differs considerably as described in section 9.1. At a glance (Figure 9.8), the IT group outperformed the IV group in retarding the growth of advanced ovarian tumours, which can be observed by the decline in the tumour volumes for both doses in the last 10 days of therapy

With particular attention to the mice in the IV group

Both tumours grew rapidly, showing a steady increase in the tumour volume and size. These tumours aggressively doubled in size despite receiving treatment, leading to their premature termination from the study. Potential explanations for the aggressive growth of these tumours relate to the inability of these systems to reach the stromal compartments and cellular surface in therapeutic concentrations. Various reasons may present, including the lack of an adequate surface composition of the NPs. Sadzuko and co-workers reported that PEGylation of NPs led to a 3-fold reduction in RES uptake, a 6-fold increase in plasma area under the curve (AUC), and a 3-fold increase in tumour uptake of a liposomal drug, leading to enhanced antitumor efficacy (Sadzuka et al., 1998). Despite the NLs in this study containing a PEGylated lipid, the

functional groups of this moiety were utilized in the attachment of the antibody. Thus, PEG failed to adequately contribute to a reduction in RES, seen by a decreased blood circulation time of the system. Another crucial factor affecting the transport of NPs to tumours is due to the highly irregular tumour vasculature compared to healthy tissues, with features including heterogeneous spatial distribution and uneven perfusion and permeability. Lee and co-workers reported that NP uptake occurred mainly in the perfused tumour peripheries, suggesting that perfusion rather than permeability is the main limiting factor for tumour penetration of NPs (Lee et al., 2010). In addition, other factors adversely influencing the movement of the NPs in tumours are abnormal drug permeability, lymphatic vessel malfunction, interstitial fibrosis, contraction of interstitial tissues mediated by stromal fibroblasts (compression from multiplying tumour cells) and elevated interstitial fluid pressure (IFP) (up to 60 mmHg). This increased IFP disrupts normal convective flow, thus, NPs that rely on this transportation will subsequently fail to move within the tumour compartments (Ernsting et al., 2013).

With particular regards to the mice in the IT group

A considerably slower progression of advanced tumours at both doses was observed. The tumour volumes did not exceed 2000 mm^3 (Figure 9.8), and a marked reduction in the tumour size was seen during the last 5 days of the treatment period (Figure 9.8). The prolonged survival times observed in Figure 9.10 subsequently allows for the establishment and conductance of the niche surgical interventions necessary to fully eradicate the tumour. In addition, these IT inserts have a potential application to be administered synergistically with other potent chemotherapeutics to enhance the overall anticancer performance. Assessment of the TIR at the 5 mg/kg dose revealed that the IT insert displayed a 58% rate of inhibition over the equivalent IV dose and a 48% TIR for the IT insert at 2.5 mg/kg treatment dose (Table 9.5). This further highlights the effectiveness of the 5 mg/kg dose.

The advantageous ability of the system can be explained due to the favourable zeta potential. Studies have revealed that within tumours, neutral NPs (± 10 mV) are transported three times more than charged particles and are distributed more homogeneously within tissue. Cationic particles tend to interact with negatively

charged matrix polymers such as chondroitin sulphate (CS), this however is crucial in the study, as this interaction i.e. the cationic NLs with anionic matrix polymers is the baseline of the hypothesis that was proposed to retard OC progression (Stylianopoulos et al., 2010; Hoosen et al., 2018; Pradeep et al., 2016). This was overcome by the intelligent surface design modifications of the cationic NLs surface by the shielding effect of the anti-MUC 16 antibody, which gives an overall neutral zeta potential to the system (described in chapter 6). *In situ*, the anti-MUC 16 antibody is cleaved from the NLs surface and the cationic moieties are exposed for polyelectrolyte complexation of the matrix polymers.

Furthermore, it was reported by Nomura and co-workers that NLs carrying a nearly neutral charge were able to penetrate through tumours 14 times more effectively, relative to positively charged liposomes, which failed to sufficiently migrate (Nomura et al., 1998). The latter sentence could provide further explanations as to why the unfunctionalized system (zeta potential of + 39 mV, chapter 6) in the previous model failed to restrict the growth of small sized tumours despite seeing advanced anti-cancer effects on 2D and 3D cell cultures. Similarly, Stylianopoulos and co-workers demonstrated that highly positive particles exhibited reduced penetration and distributed less homogeneously in tumour masses (Stylianopoulos et al., 2010). Lastly neutral NLs possess higher diffusion coefficients than charged particles, explaining the success of the targeted system, which is neutral (zeta potential of – 9 mV; Chapter 6; Lieleg et al., 2009).

9.4.2.2. Histological Examination of Tumour Tissues

With respect to histological examinations of the tumours (Figure 9.11). The masses in all mice were observed to be consistent with that of a solid carcinoma (ovarian carcinoma). The neoplastic cells appeared similar in all mice. The untreated control mice only yielded a single small area of necrosis of a small group of neoplastic cells, no extensive central necrosis was present. The mice that received the 5 mg/kg and 2.5 mg/kg of the IT insert showed a large central area of necrosis present (annotated on the figure), which appeared liquefactive and caused a pseudocystic appearance.

This widespread necrosis was associated with the cytotoxic ability of DDAB on the tumour tissue.

A similar necrotic pattern was seen in the mouse receiving the 2.5 mg/kg IV dose, by a large central necrosis which appeared coagulative. These cases also show smaller foci of necrosis surrounding the central region scattered in the mass, which strongly suggested that DDAB did enter the tumour via the IV route to disturb and cause an altered necrotic state. When comparing the necrosis patterns of the 2.5 mg/kg IT insert dose to the 2.5 mg/kg IV dose, the IT dose showed marked degenerative changes in neoplastic cells surrounding the foci of necrosis, which were similar (yet slightly milder) for the IV dose.

Accompanying inflammation was associated with all mice that received treatment. Peripheral stromal reactions appeared mild to moderate and mostly consisting of neutrophils and lymphocytes. These changes were present only in the treatment mice, suggesting that the system delivered via the IV route did reach the tumour causing the local inflammation, however failed to reach in sufficient therapeutic concentrations to yield a significant reduction in tumour volume. This strongly validates the active targeting antibody of the system.

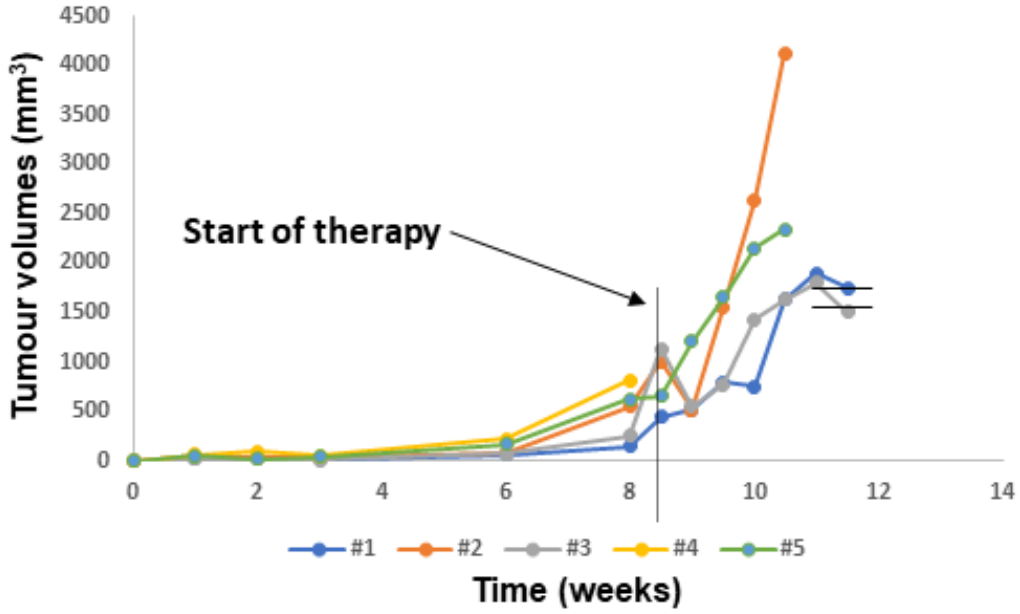

Figure 9.8. Graphical comparison of tumour volumes of mice, where 1 and 3 are the IT inserts of the anti-MUC 16 DDAB NLs at 5 mg/kg and 2.5 mg/kg respectively; 2 and 5 are IV administered of the anti-MUC 16 DDAB NLs at 5 mg/kg and 2.5 mg/kg respectively and 4 is the untreated control sacrificed at day 1 of treatment.

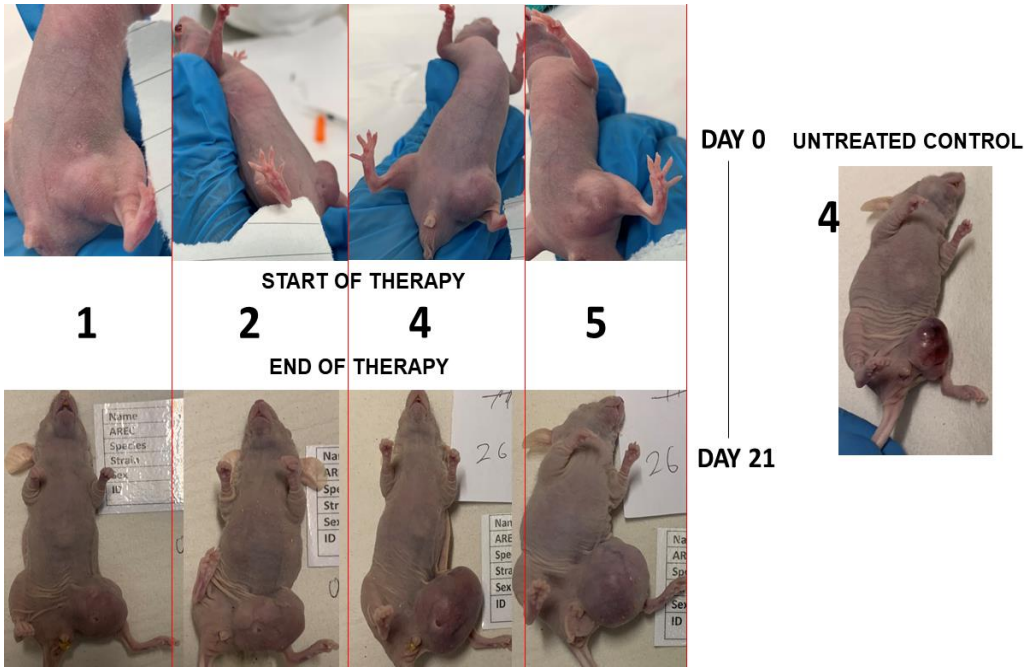

Figure 9.9. Photographical depictions of the increase in the tumours of the mice during the 21-day treatment period.

Table. 9.5. Summarising the tumour inhibition rates for both routes of administration of the anti-MUC 16 NLs.

MOUSE ID	Dose	Tumour Masses (g)	Tumour Inhibition Rate (%)
#1	5mg/kg (IT)	2.5	58
#2	5mg/kg (IV)	4.31	
#3	2.5 mg/kg (IT)	2.26	48
#5	2.5mg/kg (IV)	4.71	

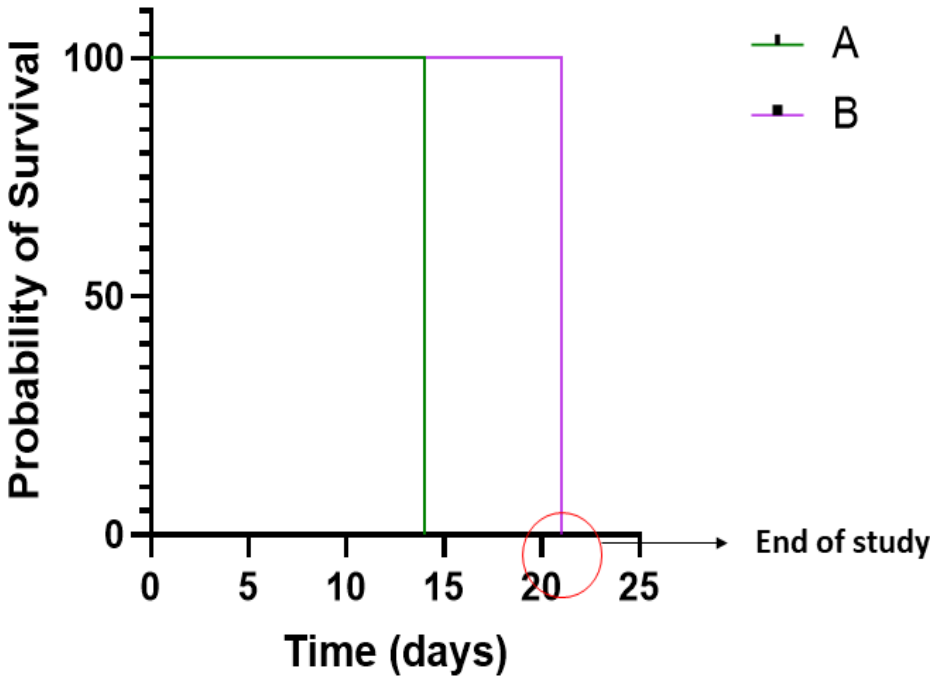

Figure 9.10. Representing the Kaplan-Meier Curve, where group A represents the mice that received both the IV doses and B represents the mice that received both the IT doses.

9.4.2.3. Safety Evaluations Based on the Histological Examinations of the Surrounding Organs and Behavioral Responses Initiated in Response to the Anti-MUC 16 DDAB NLs Therapy (both IV and IT)

- *Behavior*

All mice in the study presented with normal behavior. This was based on the mice physical appearance and eating patterns. No signs of the previously observed abdominal and skin adverse reaction was seen, highlighting the importance of targeted drug delivery platforms in curbing the adverse effect and toxicity potential of DDAB.

- *With respect to the kidney*

All mice showed minimal changes only. Deep cortical as well as proximal convoluted tubular changes were present, which were attributable to hypoxia caused by

blockages in the blood vessels feeding the kidney by the large presence of the tumour in the local vicinity (Figure 9.11).

- *With respect to the liver*

A similar non-significant histological change was observed in the liver of all mice.

- *With respect to the heart*

All mice showed myocardial changes that were minimal and likely incidental or at the most associated with mild hypoxia due to the presence of the large tumour.

Overall, there were no significant changes to the nearby organs relative to the necrotic changes seen within the tumour tissue. Thus, the preliminary safe use of the system as a targeted therapy against OC was concluded.

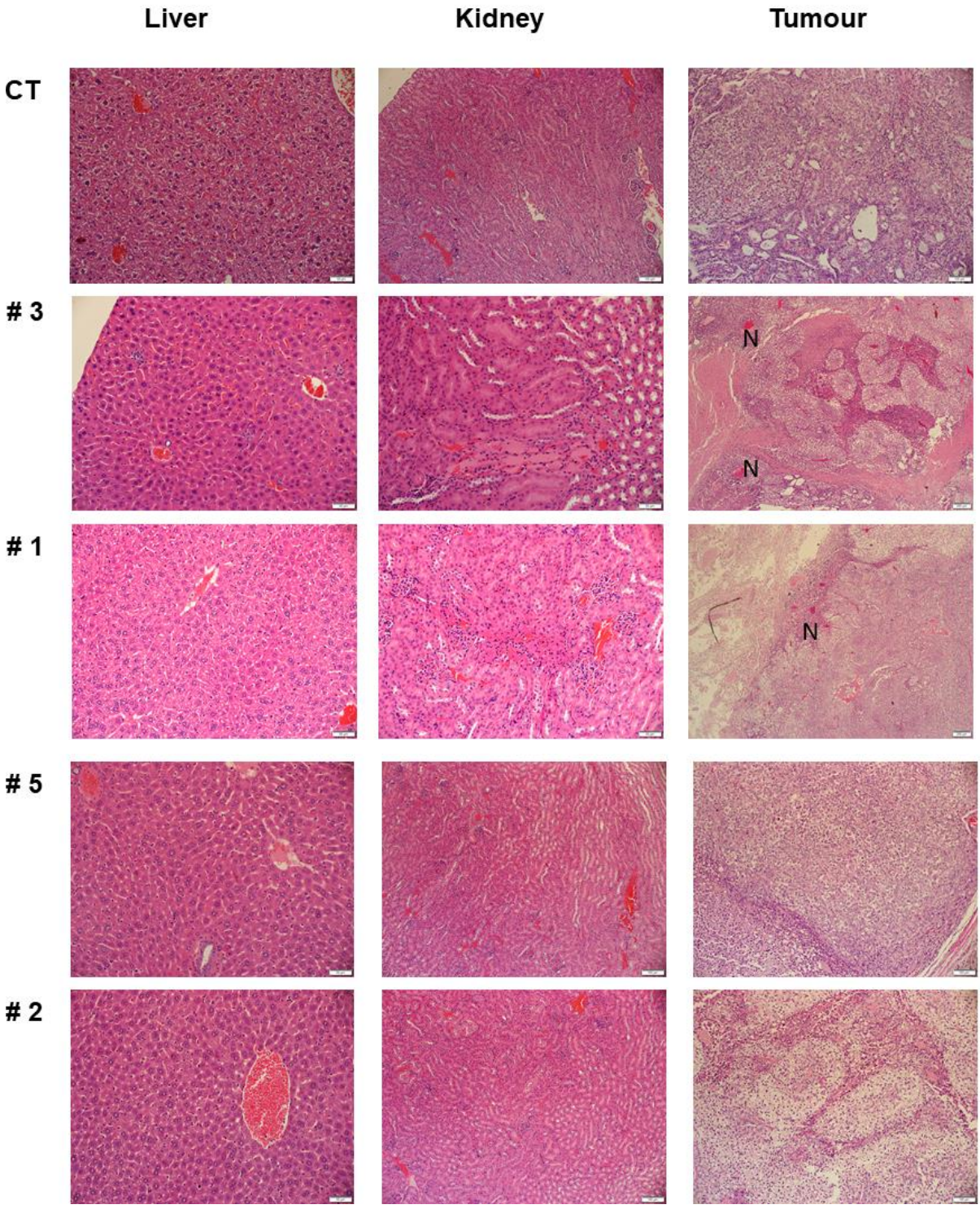

Figure 9.11. Histopathological images of the liver, kidney and tumour tissue of mice utilized in model 2. Where CT = untreated control and N = area of necrosis.

9.5. Conclusions

This phase of the study aimed to assess the anti-cancer potential, optimal dosage and tolerability of DDAB *in vivo*. From model 1, it was concluded that the DDAB molecule was highly toxic to the mice, observed during the delivery of pristine DDAB in PBS. A significant adverse skin reaction, severe abdominal distension and distinct changes to the heart, kidney and liver was observed by this treatment option of DDAB (DDAB injected with PBS). By delivering DDAB in a targeted drug delivery system such as the anti-MUC 16 DDAB NLs formulated in this study, evidently reduced the toxic effects to the skin and surrounding organs. In addition, the functionalized NLs outperformed the unfunctionalized NLs by a 5-fold reduction in tumour size at day 21 of therapy at an equivalent dose of DDAB. This was a consequence of the temporary neutral zeta potential of the NLs and targeting associated with the antibody. As the anti-MUC 16 NLs entered the tumour via IT insertion, they distributed freely within the tumour guided by the anti-MUC 16 antibody. As the antibody came into contact with their respective antigen, subsequently allowed for the exposure of DDAB to the adjacent stroma which contained the over-expressed CS-E, leading to spontaneous arresting of CS-E, which was hypothesized to reduce the tumour progression. Despite the unfunctionalized system producing a drastic loss in cell viability to 3D spheroids, their lack of ability to distribute homogeneously within tumours adversely affected the therapeutic outcome. These findings strongly suggest the necessity for tailor made drug delivery systems for enhancing the chemotherapeutic potential of the same drug at the exact same dose. Which concluded the anti-MUC 16 NLs as the preferred formulation choice of DDAB therapy.

The second model showed the favourable tumour retardation characteristics of the anti-MUC 16 DDAB NLs IT insert, over the IV administration. Despite the IV administration causing necrosis and inflammation to the tumour, without affecting nearby organs (evidence that the targeting was achieved), a lack of a therapeutic benefit was observed. To this end, a potential higher dose of DDAB following the IV administration of the targeted system could be a means to overcome the loss of DDAB due to the innate bodily processes.

The IT insert outperformed the IV admiration by an approximate 2-fold difference in the tumour inhibition rate potential and a longer survival time in advanced stage tumours was discovered. These advanced stage tumours represent a more clinical mimetic model. At this stage of OC, prompt surgery is the strategy of choice, thus, this system displayed a great potential to restrict/delay the exponential tumour growth at this stage where chemotherapy is not usually the first line option. The increase in the survival time allows for the opportunity for clinicians to slightly delay the onset of death (which is inevitable at this stage) to allow the strategic planning and conductance of the most appropriate surgical intervention, in hopes to save the patient.

This type of treatment approach speaks to a rationale-based drug design for tailor made anti-cancer therapy.

9.6. References

Celikoglu, F., Celikoglu, S. I., & Goldberg, E. P., 2008. Bronchoscopic intratumoral chemotherapy of lung cancer. Lung Cancer. 61, 1–12.

Eisenkop, S., Spirtos, N.M., 2001. The clinical significance of occult macroscopically positive retroperitoneal nodes in patients with epithelial ovarian cancer. Gynecol Oncol. 82, 143-149.

Ernsting, M.J., Murakami, M., Roy, A., Li, S.D., 2013. Factors controlling the pharmacokinetics, biodistribution and intratumoral penetration of nanoparticles, Journal of Controlled Release. 172, 782-794.

Ghassami, E., Varshosaz, J., Jahanian-Najafabadi, A., Minaiyan, M., Rajabi, P., & Hayati, E., 2018. Pharmacokinetics and in vitro/in vivo antitumor efficacy of aptamer-targeted Ecoflex® nanoparticles for docetaxel delivery in ovarian cancer. International journal of nanomedicine. 13, 493–504.

Ginsburg, G. S., Ginsburg, G. S., & J McCarthy, J., 2009. Transforming the practice of medicine using genomics. Clinical cases in mineral and bone metabolism: the

official journal of the Italian Society of Osteoporosis, Mineral Metabolism, and Skeletal Diseases, 6, 25–28.

Ginsburg, G.S., Willard, H.F., 2009. Genomic and personalized medicine: foundations and applications. Translational Research. 154, 277-287.

Lee, H., Hoang, B., Fonge, H., Reilly, R.M., Allen, C., 2010. In vivo distribution of polymeric nanoparticles at the whole-body, tumor, and cellular levels. Pharm. Res. 27, 2343-2355.

Lengyel, E., 2010. Ovarian Cancer Development and Metastasis. The American Journal of Pathology. 177, 1053-1064.

Lieleg, O., Baumgärtel, R. M., & Bausch, A. R. 2009. Selective Filtering of Particles by the Extracellular Matrix: An Electrostatic Bandpass. Biophysical Journal. 9, 1569–1577.

Liu, Z., Liu, D., Wang, L., Zhang, J. and Zhang, N., 2011. Docetaxel-loaded pleuronic P123 polymeric micelles: in vitro and in vivo evaluation. Int J Mol Sci. 12, 1684–1696

Mesiano, S., Ferrara, N., Jaffe, R.B., 1998. Role of Vascular Endothelial Growth Factor in Ovarian Cancer: Inhibition of Ascites Formation by Immunoneutralization. The American Journal of Pathology. 153, 1249-1256.

Nomura, T., Koreeda, N., Yamashita, F., Takakura, Y., Hashida, M., 1998. Effect of particle size and charge on the disposition of lipid carriers after intratumoral injection into tissue-isolated tumors. Pharm Res. 15, 128-132.

Noori Koopaei, M., Khoshayand, M.R., Mostafavi, S.H, et al., 2014. Docetaxel loaded PEG-PLGA nanoparticles: optimized drug loading, in-vitro cytotoxicity and in-vivo antitumor effect. J Pharm Res. 13, 819–833.

Owen, S. C., Chan, D. P. Y., & Shoichet, M. S.., 2012. Polymeric micelle stability. Nano Today. 7, 53–65.

Sadzuka, Y., Hirotsu, S., Hirota, S., 1998. Effect of liposomalization on the antitumor activity, side-effects and tissue distribution of CPT-11. Cancer Lett. 127, 99-106.

Shen, W., Liang, B., Yin, J. et al., 2015. Noscapine Increases the Sensitivity of Drug-Resistant Ovarian Cancer Cell Line SKOV3/DDP to Cisplatin by Regulating Cell Cycle and Activating Apoptotic Pathways. Cell Biochem Biophys. 72, 203.

Stylianopoulos, T., Poh, M. Z., Insin, N., Bawendi, M. G., Fukumura, D., Munn, L. L., & Jain, R. K., 2010. Diffusion of particles in the extracellular matrix: the effect of repulsive electrostatic interactions. Biophysical journal. 99, 1342–1349.

Xiao, W., Suby, N., Xiao, K., Lin, T., Al Awwad, N., Lam, K. S., & Li, Y., 2017. Extremely long tumor retention, multi-responsive boronate crosslinked micelles with superior therapeutic efficacy for ovarian cancer. Journal of Controlled Release. 264, 169–179.

Zhang, J.S., Liu, F., Huang, L., 2005. Implications of pharmacokinetic behavior of lipoplex for its inflammatory toxicity. Adv Drug Deliv Rev. 57, 689-698.

Zhou, W., Han, W. F., Landree, L. E., Thupari, J. N., Pinn, M. L., Bililign, T. and Kuhajda, F. P., 2007. Fatty AcidSynthase Inhibition Activates AMP-Activated Protein Kinase in SKOV3 Human Ovarian Cancer Cells. Cancer Research. 67, 2964–2971.

Rudolph, K.L., Chang, S., Lee, H,W., Blasco, M,Gottlieb, G.J., Greider, C., DePinho,R.A., 1999. Stress Response, and Cancer in Aging Telomerase-Deficient Mice. Cell. 96, 701-712.

Kapla-Lefko, P. J., Chen, T. M., Ittmann, M. M., Barrios, R. J., Ayala, G. E., Huss, W. J., et al., 2003. Pathobiology of autochthonous prostate cancer in a pre-clinical transgenic mouse model. The Prostate. 55, 219–237.

Kim, C.H., Kang, T.A., Kim, B.D., Lee, T.H., Yoon, H.Y., et al., 2020. Enhanced docetaxel delivery using sterically stabilized RIPL peptide-conjugated nanostructured lipid carriers: In vitro and in vivo antitumor efficacy against SKOV3 ovarian cancer cells. International Journal of Pharmaceutics. 583, 119393.

Lu, J., Liong, M., Li, Z., Zink, J. I., & Tamanoi, F., 2010. Biocompatibility, Biodistribution, and Drug-Delivery Efficiency of Mesoporous Silica Nanoparticles for Cancer Therapy in Animals. Small. 6, 1794–1805.

HogenEsch, H., & Nikitin, A. Y., 2012. Challenges in pre-clinical testing of anti-cancer drugs in cell culture and in animal models. Journal of Controlled Release. 164 183–186.

Kelland, L. R., 2004. “Of mice and men.” European Journal of Cancer. 40, 827–836.

Jin, K., Teng, L., Shen, Y., He, K., Xu, Z., & Li, G., 2010. Patient-derived human tumour tissue xenografts in immunodeficient mice: a systematic review. Clinical and Translational Oncology. 12, 473–480.

Cohen, A. F., 2010. Developing drug prototypes: pharmacology replaces safety and tolerability? Nature Reviews Drug Discovery. 9, 856–865.

Tong, L., Chen, W., Wu, J., & Li, H., 2014. Folic acid-coupled nano-paclitaxel liposome reverses drug resistance in SKOV3/TAX ovarian cancer cells. Anti-Cancer Drugs. 25, 244–254.

Xu, Q., Ensign, L. M., Boylan, N. J., Schön, A., Gong, X., Yang, J.C., et al., 2015. Impact of Surface Polyethylene Glycol (PEG) Density on Biodegradable Nanoparticle Transport in Mucus ex Vivo and Distribution in Vivo. ACS Nano. 9, 9217–9227.

CHAPTER 10:
Conclusion and Recommendations

10.1. Conclusion

Carbohydrate polymers implicated in cancerous conditions are structurally complex macromolecules with a high degree of heterogeneity and backbone variations. These sugars, however, contain typical functional groups that are accessible for simple chemical modifications, which alter their structure and chemical integrity. The anionic nature and virulent pathological contributions of chondroitin sulphate – E drove the current hypothesis, which was fundamental in anchoring the foundation of this project. Throughout this dissertation, the role and contribution of chondroitin sulphate – E in ovarian carcinomas was extensively discussed. Based on the structural architecture of the polymer, two molecules were selected to serve as chemotherapeutic entities.

The electrostatic interactions between chondroitin sulphate and didodecyldimethyl ammonium bromide was highly favourable. Utilizing advanced physicochemical characterization techniques (FT-IR, DSC, XRD and TGA), the successful "*on the spot*" interaction was clearly established. It was further observed through ^{1}H NMR and molecular docking simulations that the complete encapsulation of chondroitin sulphate was further possible. The establishment and synthesis of the complex was based on minimal external interference that usually drives reactions, for instance: no catalyst was used, the complex was not stirred, the pH of the environment was not manipulated, the ionization states of the poly-analytes were not optimized, and the temperature was not controlled, to name a few. This gave insight into their potential interactions in a more physiologically tailored environment. Despite the lack of optimization, a clear alteration in the structure and architecture of chondroitin sulphate was established. This innate interaction leads to the utilization and conclusion of Didodecyldimethyl ammonium bromide as a suitable chondroitin sulphate modifying agent.

Advanced drug delivery systems have various pharmaceutical specifications and traits. The combination of drugs within delivery systems provides an ultimate combination, as the delivery system is optimized to overcome the limitations of the drug in question and ensures the intact transport of the drug to a specific site. Nanoliposomes served as an ideal delivery platform, as their lipid nature coincides with the amphiphilic nature of Didodecyldimethyl ammonium bromide as the hydrophobic chains were securely anchored to the bulk lipids, whilst the stable N^+ moiety was exposed to the adjacent environment. In addition, the lipid nature of both the chemical agent and the delivery vehicle enhanced the overall stability of the system and reduced steric hindrances. The Didodecyldimethyl ammonium bromide nanoliposomes possessed suitable nano-sized specifications, which were essential to enhance the surface area of the periphery present N^+ charge in order to facilitate polyelectrolyte complexation with chondroitin sulphate. This was validated by a high zeta potential, leading to their quantifications on the nanoliposomes using the anionic bromothymol blue probe assay technique. The toxicity of these nanoliposomes was evident and a considerable reduction in cell viability was achieved in SKOV3 cell lines. The cytotoxicity, in terms of biological assay characterizations was observed in both SKOV3 and HEK 293 healthy cells (proliferation, reactive oxygen stress and apoptosis). In addition, these nanoliposomes retarded the formation of structurally durable 3D SKOV3 tumourospheres. The off-target toxicity of Didodecyldimethyl ammonium bromide was reduced by the surface engineering of the anti-MUC 16 antibody which has high affinity for the CA125 over expression presented on SKOV3 cell surfaces. Although these particles were bigger in size, the addition of the anti-MUC 16 antibodies synergistically aided the cytotoxic performance of Didodecyldimethyl ammonium bromide nanoliposomes and added a feature of active targeting to cancerous sites. The conjugation of the antibody to the nanoliposomal surface was assessed using size, zeta potential and FT-IR characterizations before testing in cell lines. Once optimized, an evident selective capability was observed, as the HEK 293 cells were minimally harmed. This finding correlates to the results achieved *in vivo*, as histological examinations of kidneys following the anti-MUC 16 Didodecyldimethyl ammonium bromide nanoliposomal treatment failed to contribute to any signs of abnormalities, though displaying clear therapeutic potentials. The chondroitin sulphate -E down regulation was confirmed using genetic quantification of

GALNAc4S-6ST, which is up-regulated in ovarian cancer and is responsible for the aggressive production of the virulent chondroitin sulphate – E species by enzymatic addition of a sulphate group onto chondroitin sulphate-A sites. As chondroitin sulphate-A is polyelectrolyte complex to Didodecyldimethyl ammonium bromide, less substrate is available for the enzymatic conversion to chondroitin sulphate - E, consequently leading to a down regulation of the enzyme.

1,12 diaminododecane also displayed a favourable interaction with chondroitin sulphate in Chapter 5, resulting in crosslinked linked chondroitin sulphate networks with a reduced water solubility. 1,12 diaminododecane was dissolved at high temperatures (>70°C) and entrapped within the stable walls of high phosphocholine and cholesterol content lipid membranes. These lipids provided sufficient interactions for zero order release kinetics behaviours of 1,12 diaminododecane, which is highly sought after in controlled drug delivery systems. The ability of 1,12 diaminododecane nanoliposomes to alter the chemical backbone of chondroitin sulphate was assessed using a methylene blue probe technique, which gave insight into the degree of crosslinking. These findings suggest that the degree crosslinking increases with an increase in the incubation times of these systems in chondroitin sulphate rich environments, owing to the time dependent crosslinker release process. It was further evident from FT-IR analysis that the longer incubation times was associated with a stronger intensity of the bands corresponding to an amide formation. Furthermore, upon GALNAc4S-6ST quantifications, a 10 fold reduction was observed at the IC_{50} single dose in SKOV3 cells and essentially no effects in HEK 293 cells, which support the ideology of chondroitin sulphate arresting.

To this end, we successfully delivered two non-pharmacological molecules to treat OC, using advanced drug delivery nanotechnology which displayed a promising potential to reduce the virulent tumour-bearing burden. We thus conclude that these two chemical entities play a tumoricidal role in the ECM of carbohydrate polymer over expressed cancers, with further clinical, translational, exploratory and development studies to be strongly encouraged in the future. These include future testing in a more robust animal model, where advanced genetic and protein experimentations are required to understand the complete biological mechanisms implicated.

10.2. Recommendations

Cancer is a disease that requires a multidisciplinary knowledge-based approach in order to yield any significant impact on the global burden. This statement motivated the literature review presented in chapter 3, where AI technologies were described to pave the way forward for cancer treatment and drug development. I thus strongly recommend the use of existing drug delivery data in order to generate super optimized delivery systems that provide patient specific therapy.

Patient-specific-personalised-therapy is essential in heterogeneous disorders. The biological mapping of an individual tumour is the only approach (opinionated) for the successful selection of drugs. A combinational drug therapy cocktail, which provides synergistic and additive chemo potential is mandatory. For e.g.: the use of doxorubicin; to target topoisomerase II, the use of 5-fluorouracil to targeted thymidylate synthase, which has an additive chemotherapeutic effect when co-prescribed with leucovorin and methotrexate and the use of didodecyldimethyl ammonium bromide, targeting chondroitin sulphate activity and GALNAc4S-6ST expression for a hypothetical patient. Although polypharmacy practices are extremely discouraged in clinical pharmacy, by genetic screening of the various up-regulated pathways and molecular targets in a specific patient tumour, an informed regimen of existing drugs targeting each pathological contribution can be identified. With the aid of advanced drug delivery systems, such as the anti-MUC 16 Didodecyldimethyl ammonium bromide nanoliposomes, the potential to selectively deliver one or more drugs within this aqueous free revisor is possible. To this end, these systems have great potential to conjugate or entrap other conventional chemotherapies for an additive tumoricidal effect.

Furthermore, the ability chondroitin sulphate crosslinked to chondroitin sulphate to form spherical nanoparticles was serendipitous, which has great utility as an advanced drug delivery system targeting bone tissue engineering research agendas, with particular focus on site specific delivery of drugs to cartilage affected areas.

APPENDICES

11. 1. APPENDIX A

11.1.1. Review Publication

International Journal of *Molecular Sciences*

MDPI

Review

Nanotechnology and Glycosaminoglycans: Paving the Way Forward for Ovarian Cancer Intervention

Yasar Hoosen, Priyamvada Pradeep, Pradeep Kumar, Lisa C. du Toit, Yahya E. Choonara and Viness Pillay *

Wits Advanced Drug Delivery Platform Research Unit, Department of Pharmacy and Pharmacology, School of Therapeutic Sciences, Faculty of Health Sciences, University of the Witwatersrand, Johannesburg, 7 York Road, Parktown 2193, South Africa; yasar.hoosen@students.wits.ac.za (Y.H.); priyamvada.pradeep@wits.ac.za (P.P.); pradeep.kumar@wits.ac.za (P.K.); lisa.dutoit@wits.ac.za (L.C.d.T); yahya.choonara@wits.ac.za (Y.E.C.)

* Correspondence: viness.pillay@wits.ac.za; Tel.: +27-11-717-2274

Received: 19 January 2018; Accepted: 23 February 2018; Published: 4 March 2018

Abstract: Ovarian cancer (OC) has gained a great deal of attention due to its aggressive proliferative capabilities, high death rates and poor treatment outcomes, rendering the disease the ultimate lethal gynaecological cancer. Nanotechnology provides a promising avenue to combat this malignancy by the niche fabrication of optimally-structured nanomedicines that ensure potent delivery of chemotherapeutics to OC, employing nanocarriers to act as "intelligent" drug delivery vehicles, functionalized with active targeting approaches for precision delivery of chemotherapeutics to overexpressed biomarkers on cancer cells. Recently, much focus has been implemented to optimize these active targeting mechanisms for treatment/diagnostic purposes employing nanocarriers. This two-part article aims to review the latest advances in active target-based OC interventions, where the impact of the newest antibody, aptamer and folate functionalization on OC detection and treatment is discussed in contrast to the limitations of this targeting mechanism. Furthermore, we discuss the latest advances in nanocarrier based drug delivery in OC, highlighting their commercial/clinical viability of these systems beyond the realms of research. Lastly, in the second section of this review, we comprehensively discussed a focus shift in OC targeting from the well-studied OC cells to the vastly neglected extracellular matrix and motivate the potential for glycosaminoglycans (GAGs) as a more focused extracellular molecular target.

Keywords: ovarian cancer; nanomedicine; glycosaminoglycans; antibodies; chemotherapy

1. Introduction

8.2. APPENDIX B

8.2.1. Abstracts of Research Outputs at Conference Proceedings

8.2.1.1 School of Therapeutic Science Research Day, University of the Witwatersrand, Johannesburg, South Africa, 6th September,2018, (Poster Presentation)

Abstract Ovarian cancer (OC) has secured its position as the most lethal gynaecological malignancy. Current conventional chemotherapeutics suffer a myriad of downfalls including side effects and resistance, drastically hindering clinical success. Herein, we introduce and establish the potential of two bioactive chemical ingredients (BCIs), Didodecyldimethyl ammonium bromide (DDAB), a cationic lipid and 1,12 diaminododecane, a chemical crosslinker, as novel “arresters” of Chondroitin sulfate, an over-expressed glycosaminoglycan that is implicated in the progression of OC. In this study, we perform proof of concept groundwork to evaluate the novel “on the spot” polyelectrolyte complex between DDAB-CS, characterizing the complex using FTIR, DSC, XRD and SEM, revealing complex formation via the electrostatic interaction between the N^+ of DDAB and SO_4^{2-} of CS, in addition to characterizing the 1,12 diaminododecane-CS crosslinked product. Finally, we synthesise novel 1,12 diaminododecane loaded nanoliposomes and characterize them for size (98.82 nm), morphology, zeta potential (-34.4 mV) and crosslinker entrapment efficiency (90.3 %). We then further tested their potential to crosslink a solution of CS (0.1% w/v) invitro and further characterized this degree of nanoliposomal mediated crosslinking (38,72%). We then synthesized DDAB active NLs and characterized them for size (120,2 nm), morphology, zeta potential (16.5 mV), residual DDAB content (96%) and tested their ability to complex CS, resulting in the spontaneous “on the spot” complexation (33,9%). Following FTIR studies, we were able to prove chemical crosslinking and complexation of CS initiated by these NLs, confirming the concept, With further potential for optimization and cell studies.

See Poster Below.

"On the spot" Arresting of Chondroitin Sulphate for Inhibition of Glycosaminoglycan Activity in Ovarian Cancer

Yasar Hoosen[1], Pradeep Kumar [1], Priyamvada Pradeep [1], Thashree Marimuthu [1], Lisa C Du Toit [1], Yayha E Choonara [1], Clement Penny [2] and Viness Pillay [1]

[1] Wits Advanced Drug Delivery Platform Research Unit, Department of Pharmacy and Pharmacology, School of Therapeutic Sciences, Faculty of Health Sciences, University of Witwatersrand, Johannesburg, 7 York Road, Parktown 2193, South Africa

[2] Oncology Division, Department of Internal Medicine, Faculty of Health Sciences, University of Witwatersrand , 7 York Road, Parktown 2193, South Africa

INTRODUCTION

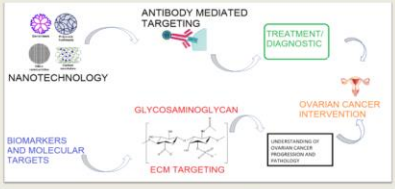

Schematic representation employing Nanotechnology and GAGs to combat OC

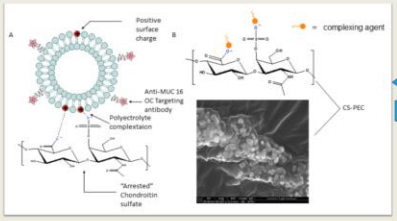

- Ovarian cancer (OC) is the most lethal gynaecological malignancy affecting thousands of females worldwide.
- Glycosaminoglycans (GAGs) including the anionic chondroitin sulphate-E (CS-E), are overexpressed in the ECM of OC patients and implicated in accelerated tumour cell growth and angiogenesis.
- CS-E has been targeted with a nano-conjugated complex composed of various cationic complexing agents.
- The complexation "arrests" CS-E forming a polyelectrolyte complex (PEC), a novel mechanism to impeding the progression of OC.

METHODS

- **Testing of Complexing agent – CS PEC**



- **Formulation of Nanoliposomes**

TABLE 1. Summary of NLs composition

Lipid	Function
Cationic lipid	Complexing agent
1,2 disteroeyl-glycerol-3-phosphocholine	Vesicle backbone
1,2-distearoyl-sn-glycero-3-phosphoethanolamine-N-[amino(polyethylene glycol)-2000]	Enhanced stability

- **Surface engineering of Anti-MUC 16 onto nanoliposomes**

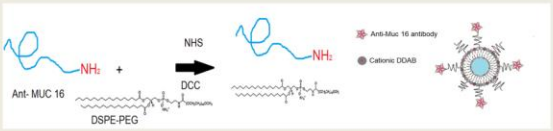

EXPERIMENTAL RESULTS

Characterization of novel CS complex

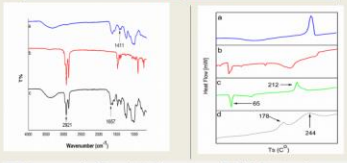

FTIR Spectrum (**Left**) and DSC Thermogram (**Right**) showing the physiochemical characterization of complexed CS.

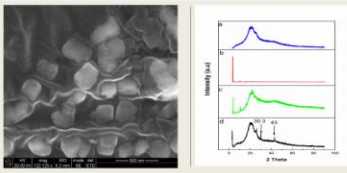

SEM micrograph (**Left**) and XRD patterns (**Right**) showing the morphology, size and diffraction peaks of complexed CS.

Characterization of Nanoliposomes

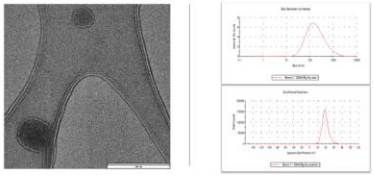

TEM (**Left**) and Zeta Size and Potential (**Right**) showing the morphology, size and cationic nature of NLs.

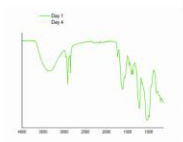

Time (hours)	Pristine lyophilized CS (λ)	Absorptions of DDAB NLs (λ)
0	0,1893	X
24	X	0,2878
96	X	0,2864

FTIR spectrum (**Left**) and Table of absorbances (**Right**) showing on the spot nanoliposomal mediated CS complexing.

Cell studies

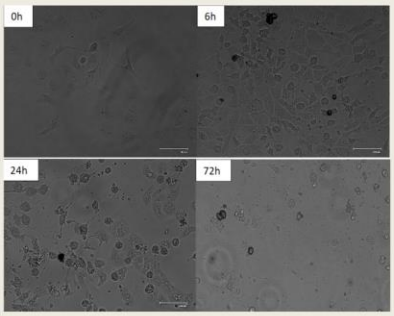

Fig. Showing SKOV-3 cell lines (overexpressing CS-E) before and 3 days after treatment with Anti-MUC 16 Cationic NLs. From the figure, we observed a change in the morphology of the cell lines suggesting apoptosis as early as 6 hours after treatment.

CONCLUSION AND FUTURE WORK

Anti-MUC 16 Cationic NLs show promising ability to complex CS invitro, in addition to high cell killing and targeting capabilities. Further cell studies will be conducted to determine the systems ability to inhibit cell apoptosis and migration.

Acknowledgements :

National Research Foundation

8.2.1.2. 9th Cross-Faculty Graduate Symposium, University of the Witwatersrand, Johannesburg, South Africa, September ,2019, (Poster presentation).

Tittle: Anti-MUC 16 functionalized Cationic Nanoliposomes, for "Arresting" of Chondroitin Sulfate in Ovarian Cancer

Authors: Yasar Hoosen*[a], Pradeep Kumar [a], Priyamvada Pradeep [a], Thashree Marimuthu [a], Lisa C Du Toit [a], Yahya E Choonara [a], Clement Penny[b] and Viness Pillay[a]

[a] Wits Advanced Drug Delivery Platform Research Unit, Department of Pharmacy and Pharmacology, School of Therapeutic Sciences, Faculty of Health Sciences, University of Witwatersrand, Johannesburg, South Africa
[b] Oncology Division, Department of Internal Medicine, Faculty of Health Sciences, University of Witwatersrand, Johannesburg, South Africa

E-mail: 714862@students.wits.ac.za

Keywords: Cancer, Nanotechnology, targeted drug delivery, chemotherapy

Introduction/purpose

Ovarian cancer (OC) is the leading cause of cancer associated deaths in females worldwide. Glycosaminoglycans (GAGs) including the anionic chondroitin sulfate-E (CS-E), are over-expressed in the ECM of OC patience and implicated in accelerated tumour cell growth and angiogenesis. By targeting CS with a nano-archetype conjugated with various cationic complexing agents, specifically and locally complex "arrest" CS-E forming a polyelectrolyte complex (PEC), a novel mechanism to impeding the progression of OC.

Methods

- **Preparation and characterization of polyelectrolyte complexed CS.** A novel didodecyldimethylammonium bromide (DDAB)-CS complex was synthesised and characterised (FTIR, SEM, DSC and XRD)**.**

- **Synthesis, functionalization and characterization of cationic nanoliposomes.** Cationic NLs were prepared by dissolving the complexing agent (DDAB) with various lipids, following solvent removal and sonication. We then functionalized the Anti-MUC16 antibody to the surface of the NLs and characterized.

Results and discussion

- **TEM.** NLs appear unilamellar, spherical to oblong in shape, and in the nano-range.
- **Zeta Size and Potential.** DDAB NLs and Anti-MUC16 DDAB NLs possessed a size of 125.3nm and 149.9nm, respectively, and a zeta potential of +39.9mV and –9.51, respectively.
- **Residual DDAB content.** 2.9 mg of DDAB (complexing agent) in 10 ml.
- **Degree of Nanoliposomal mediated complexation.** The NLs initiated 33,9 % complexation after four days of exposure to CS with 33% degree of complexation after 24 hours, suggesting on the spot complexation of CS.
- **Cytotoxicity**. Apoptosis in SKOV3 (over-expressing CS-E) cells as early as 6 hours of exposure is observed, suggesting on the spot complexation leading to decrease in cell survival
-

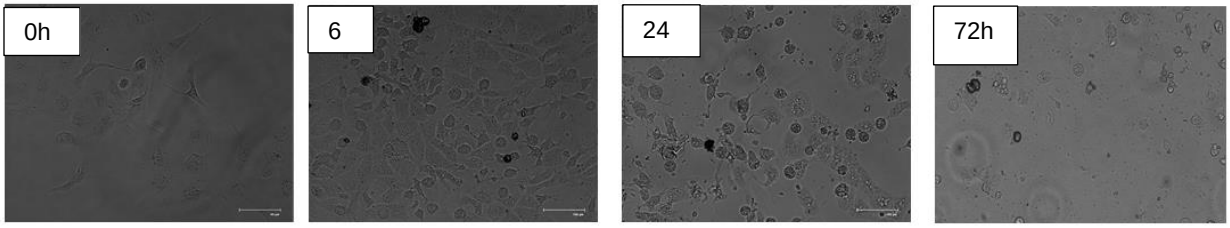

Figure 1 SKOV3 cell lines (over-expressing CS-E) before and 3 days after treatment with Anti-MUC 16 cationic NLs**.**

See Poster Below

Anti-MUC 16 Functionalized Cationic Nanoliposomes, for "Arresting" of Chondroitin Sulphate in Ovarian Cancer

Yasar Hoosen[1], Pradeep Kumar [1], Priyamvada Pradeep [1], Thashree Marimuthu [1], Lisa C du Toit [1], Yayha E Choonara [1], Clement Penny [2] and Viness Pillay [*1]

[1] Wits Advanced Drug Delivery Platform Research Unit, Department of Pharmacy and Pharmacology, School of Therapeutic Sciences, Faculty of Health Sciences, University of Witwatersrand, Johannesburg, 7 York Road, Parktown 2193, South Africa. E*: Viness.Pillay@wits.ac.za

[2] Oncology Division, Department of Internal Medicine, Faculty of Health Sciences, University of Witwatersrand , 7 York Road, Parktown 2193, South Africa

Introduction

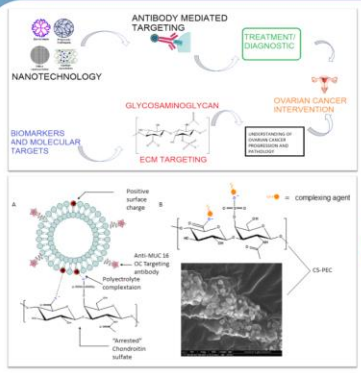

Schematic representation employing Nanotechnology and GAGs to combat OC

- Ovarian cancer (OC) is the most lethal gynaecological malignancy affecting thousands of females worldwide.
- Glycosaminoglycans (GAGs) including the anionic chondroitin sulphate-E (CS-E), are overexpressed in the ECM of OC patients and implicated in accelerated tumour cell growth and angiogenesis.
- CS-E has been targeted with a nano-conjugated complex composed of various cationic complexing agents.
- The complexation "arrests" CS-E forming a polyelectrolyte complex (PEC), a novel mechanism to impeding the progression of OC.

Methods

Testing of Complexing agent – CS PEC



Formulation of Nanoliposomes

TABLE 1. Summary of NLs composition

Lipid	Function
Cationic lipid	Complexing agent
1,2 disteroeyl-glycerol-3-phosphocholine	Vesicle backbone
1,2-distearoyl-sn-glycero-3-phosphoethanolamine-N-[amino(polyethylene glycol)-2000]	Enhanced stability

Surface engineering of Anti-MUC 16 onto nanoliposomes

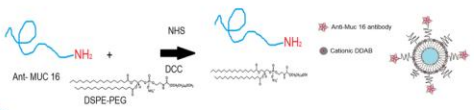

Results

Characterization of novel CS complex



FTIR Spectrum (**Left**) and DSC Thermogram (**Right**) showing the physiochemical characterization of complexed CS.



SEM micrograph (**Left**) and XRD patterns (**Right**) showing the morphology and diffraction peaks of complexed CS.

Characterization of Nanoliposomes

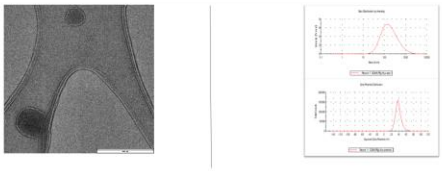

TEM (**Left**) and Zeta Size and Potential (**Right**) showing the morphology, size and cationic nature of NLs.

Cytotoxic Performance

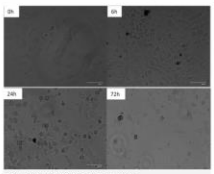

Fig. Showing SKOV-3 cell lines (overexpressing CS-E) before and 3 days after treatment with Anti-MUC 16 Cationic NLs resulting in cell death as early as 6 hours.

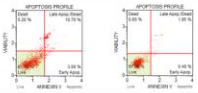

Apoptosis Profiles of SKOV3 cells (**Left**) and HEK 293 cells (**Right**).

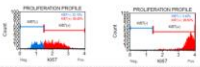

Proliferation Profiles of SKOV3 (**Left**) and HEK 293 (**Right**).

Conclusion and Future work

The anti-MUC 16 Cationic NLs show promising ability to complex CS invitro, in addition to selective reduction in cell viability and enhanced targeting capabilities. Further in vivo studies will be conducted to determine the systems ability to reduce tumour size and increase Survival in animal models.

Acknowledgments

WADDP | FACULTY OF HEALTH SCIENCES | NRF National Research Foundation

3. 43rd South African Chemical Institute National Convention, South Africa, Pretoria, September 6th, 2018 (oral presentation)

Tittle: Anti-MUC 16 functionalized Cationic Nanoliposomes, for "Arresting" of Chondroitin Sulfate in Ovarian Cancer

Authors: Yasar Hoosen*[a], Pradeep Kumar [a], Priyamvada Pradeep [a], Thashree Marimuthu [a], Lisa C Du Toit [a], Yahya E Choonara [a], Clement Penny[b] and Viness Pillay [a]

[a] Wits Advanced Drug Delivery Platform Research Unit, Department of Pharmacy and Pharmacology, School of Therapeutic Sciences, Faculty of Health Sciences, University of Witwatersrand, Johannesburg, South Africa

[b] Oncology Division, Department of Internal Medicine, Faculty of Health Sciences, University of Witwatersrand, Johannesburg, South Africa

E-mail: 714862@students.wits.ac.za

Keywords: Cancer, Nanotechnology, targeted drug delivery, chemotherapy

Introduction/purpose

Ovarian cancer (OC) is the leading cause of cancer associated deaths in females worldwide. Glycosaminoglycans (GAGs) including the anionic chondroitin sulfate-E (CS-E), are over-expressed in the ECM of OC patience and implicated in accelerated tumour cell growth and angiogenesis. By targeting CS with a nano-archetype conjugated with various cationic complexing agents, specifically and locally complex "arrest" CS-E forming a polyelectrolyte complex (PEC), a novel mechanism to impede the progression of OC.

Methods.

- **Preparation and characterization of polyelectrolyte complexed CS.** A novel didodecyldimethylammonium bromide (DDAB)-CS complex was synthesised and characterised (FTIR, SEM, DSC and XRD)**.**
- **Synthesis, functionalization and characterization of cationic nanoliposomes.** Cationic NLs were prepared by dissolving the complexing agent (DDAB) with various lipids, following solvent removal and sonication. We

then functionalized the Anti-MUC16 antibody to the surface of the NLs and characterized.

Results and discussion

- **TEM.** NLs appear unilamellar, spherical to oblong in shape, and in the nano-range.
- **Zeta Size and Potential.** DDAB NLs and Anti-MUC16 DDAB NLs possessed a size of 125.3nm and 149.9nm, respectively, and a zeta potential of +39.9mV and –9.51, respectively.
- **Residual DDAB content.** 2.9 mg of DDAB (complexing agent) in 10 ml.
- **Degree of Nanoliposomal mediated complexation.** The NLs initiated 33,9 % complexation after four days of exposure to CS with 33% degree of complexation after 24 hours, suggesting on the spot complexation of CS.
- **Cytotoxicity**. Apoptosis in SKOV3 (over-expressing CS-E) cells as early as 6 hours of exposure is observed, suggesting on the spot complexation leading to decrease in cell survival.

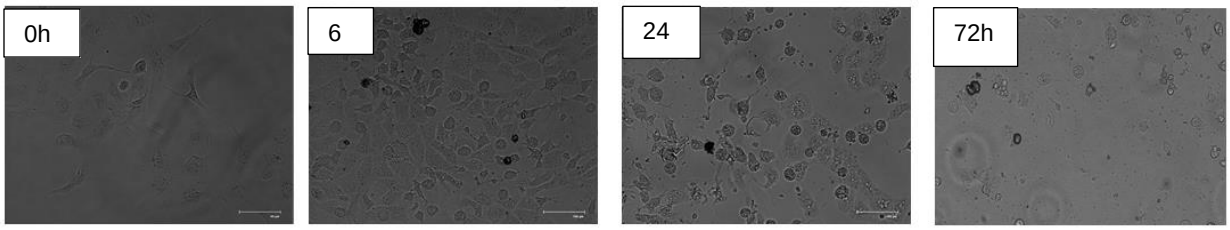

Figure 1 SKOV3 cell lines (over-expressing CS-E) before and 3 days after treatment with Anti-MUC 16 cationic NLs.

4. 10th Cross-Faculty Graduate Symposium, University of the Witwatersrand, Johannesburg, South Africa, September ,2019, (Poster presentation).

10th Wits Cross Faculty Postgraduate Symposium: Abstract

NAME/S: Yasar Hoosen
FACULTY: Pharmacy and Pharmacology
SCHOOL: Therapeutic sciences
STUDENT NUMBER: 714862
EMAIL: 714862@students.wits.ac.za
INDICATE YOUR CHOICE: Oral

TITLE: Anti-MUC 16 functionalized Cationic Nanoliposomes, for "Arresting" of Chondroitin Sulfate in Ovarian Cancer

Yasar Hoosen*[a], Pradeep Kumar [a], Priyamvada Pradeep [a], Thashree Marimuthu [a], Lisa C Du Toit [a], Yahya E Choonara [a], Clement Penny[b] and Viness Pillay [a]

[a] Wits Advanced Drug Delivery Platform Research Unit, Department of Pharmacy and Pharmacology, School of Therapeutic Sciences, Faculty of Health Sciences, University of Witwatersrand, Johannesburg, South Africa

[b] Oncology Division, Department of Internal Medicine, Faculty of Health Sciences, University of Witwatersrand, Johannesburg, South Africa.

Keywords: Nanotechnology, Ovarian Cancer, Glycosaminoglycans

Introduction/purpose

Ovarian cancer (OC) is the leading cause of cancer associated deaths in females worldwide. Glycosaminoglycans (GAGs) including the anionic chondroitin sulfate-E (CS-E), are over-expressed in the ECM of OC patience and implicated in accelerated tumour cell growth and angiogenesis. By targeting CS-E with nano-archetypes conjugated with various cationic complexing agents, specifically and locally complex (or "arrest") CS-E forming a polyelectrolyte complex (PEC), a highly innovative and *first-in-the-world* mechanism to impeding the progression of OC.

Methods.

- **Preparation and characterization of polyelectrolyte complexed CS.** A novel Didodecyldimethyl ammonium bromide (DDAB)-CS complex was synthesized and characterized (FTIR, SEM, DSC and XRD)**.**
- **Synthesis, surface engineering and characterization of cationic nanoliposomes (NLs).**
- **Cytotoxic analysis**. Cationic NLs were tested on SKOV3, HEK 293 and OVCAR-5 cells for viability, apoptosis, cell prefiltration, reactive oxidative stress and cellular migration assays. Cellular uptake and quantitative PCR was also performed.
- **Establishment of 3D SKOV3 (overexpressing CS-E) cancer cell architectures for morphological studies.**

Results and discussion

- **TEM.** NLs appear unilamellar, spherical to oblong in shape, and in the nano-range.
- **Zeta Size and Potential.** DDAB NLs and Anti-MUC16 DDAB NLs possessed a size of 125.3nm and 149.9nm, respectively, and a zeta potential of +39.9mV and –9.51 respectively.
- **Cytotoxicity**. Targeted cationic NLs showed selective reduction in cell viability, cell proliferation and migration in cancer cells relative to the healthy control cells. Increased cellular reactive oxidative stress and apoptosis on cancer cells were also noted. The targeted system shows superior knockdown in CHST-15, the gene responsible for the biosynthesis of CS-E.

This research was awarded the overall second-best oral presentation at the South African Chemistry Institute (SACI) 43th national convention

5. School of Therapeutic Science, Research Day 2019. Anti-MUC 16 functionalized Cationic Nanoliposomes, for “Arresting” of Chondroitin Sulfate in Ovarian Cancer. Yasar Hoosen, Pradeep Kumar, Priyamvada Pradeep, Thashree Marimuthu , Lisa C Du Toit , Yahya E Choonara , Clement Penny and Viness Pillay. (online abstract)

11.3. APPENDIX C

11.3.1. Award Certificate for SACI oral Presentation



43rd SACI NATIONAL CONVENTION



Oral Presentations

2nd Best Presenter
Yasar Hoosen



Chairperson

06 December 2018

DATE

11.3.2. Award for School of Therapeutic Science, Research Day 2019

School of Therapeutic Sciences

UNIVERSITY OF THE WITWATERSRAND JOHANNESBURG

Faculty of Health Sciences · Private Bag 3, Wits, 2050, South Africa
Tel: +27 11 717 2063/4 · Fax: 27 11 717 2066/086 553 5964 · E-mail: irene.jansevannoordwyk@wits.ac.za · www.wits.ac.za

18 September 2019

Mr Yasar Hoosen
Department of Pharmacy & Pharmacology
Faculty of Health Sciences

Dear Yasar

CONGRATULATIONS: RUNNER-UP – EMERGING RESEARCHER

Congratulations on being the Runner-Up for Emerging Researcher at the School's Biennial Research Day held on Tuesday, 10 September 2019 for your talk entitled: "*Anti-MUC 16 Functionalized Cationic Nanoliposomes, for "Arresting" of Chondroitin Sulfate in Ovarian Cancer*".

A Book Voucher to the value of R500 will be awarded to you and is available for collection from Mrs Irene Janse van Noordwyk, Room 4B02, Level 4, Health Sciences Building.

Once again, congratulations on your achievement.

Kind regards

Professor Hellen Myezwa
Head
School of Therapeutic Sciences

THERAPEUTIC Sciences

11.4. APPENDIX D

11.4.1. Animal Ethics Approval

UNIVERSITY OF THE WITWATERSRAND, JOHANNESBURG

STRICTLY CONFIDENTIAL

ANIMAL RESEARCH ETHICS COMMITTEE (AREC)

CLEARANCE CERTIFICATE NO. 2019/04/30/C

APPLICANT: Mr Y Hoosen

SCHOOL: Pharmacy
DEPARTMENT:
LOCATION:

PROJECT TITLE: In vivo Chemotherapeutic potential of novel nanoliposomes on Athymic nude mice cancer models

Number and Species

total of 98 (30 pilot + 68 main study) 4-8 weeks female Athymic nude mice

Approval was given for the use of animals for the project described above at an AREC meeting held on 2019/04/30. This approval remains valid until 2021/06/19.
Unreported changes to the application may invalidate the clearance given by the AREC
An annual progress report must be provided

The use of these animals is subject to AREC guidelines for the use and care of animals, is limited to the procedures described in the application form and is subject to any additional conditions listed below:

Signed: _____ (Chairperson, AREC) Date: 24/6/2019

I am satisfied that the persons listed in this application are competent to perform the procedures therein, in terms of Section 23 (1) (c) of the Veterinary and Para-Veterinary Professions Act (19 of 1982)

Signed: _____ (Registered Veterinarian) Date: 22/06/19

cc: Supervisor: Prof V Pillay
Director: CAS

Works 2000/lain0015/AESCCert.wps